Solution Processable Semiconductors for Opto-Electronic Applications

by Wentao Huang

A thesis submitted in partial fulfilment of the degree of
Doctor of Philosophy

Imperial College London
Department of Physics

Declaration

This thesis describes the work carried out between February 2015 and August 2018 within the Department of Physics at Imperial College London, under the supervision of Prof Thomas D. Anthopoulos. The material in this thesis has not been previously submitted for a degree at any University and except where explicitly stated is the product of my own work.

The copyright of this thesis rests with the author and is made available under a Creative Commons Attribution Non-Commercial No Derivatives licence. Researchers are free to copy, distribute or transmit the thesis on the condition that they attribute it, that they do not use it for commercial purposes and that they do not alter, transform or build upon it. For any reuse or redistribution, researchers must make clear to others the licence terms of this work.

Wentao Huang

London, March 2019

Abstract

This thesis focuses on the development of high-performance phototransistors based on several solution-processed semiconductors. After giving an outline of the relevant theory and experimental methods, the thesis is divided into three experimental chapters.

The first chapter presents the development of an ambipolar organic phototransistor based on [6,6]-phenyl-C61-butyric acid methyl ester ($PC_{61}BM$). The balanced electron and hole transport characteristics are achieved by fine-tuning of the injection electrode work function using a self-assembled monolayer. The ambipolar $PC_{61}BM$ phototransistor exhibits promising photoresponse in the UVA region, with maximum photosensitivity and responsivity of 9×10^3 and 3×10^3 A/W respectively. In addition, the phototransistor shows fast temporal response with switching times of <2 ms, validating the potential of ambipolar phototransistor for fast and sensitive photodetection.

The second chapter demonstrates a novel hybrid heterostructure transistor based on indium oxide (In_2O_3) and copper thiocyanate (CuSCN), which enables ambipolar operation while maintaining a high optical transparency. The ability of visible light detection is then enabled by the incorporation of a light-absorbing organic dye, resulting in an In_2O_3/dye/CuSCN trilayer phototransistor with remarkably enhanced photoresponse to green illumination. More interestingly, the trilayer phototransistor exhibits high switching speed with a response time of ~1 ms, indicating the hybrid method as an effective way to improve the speed of oxide-based phototransistors for efficient and fast photo-sensing application.

The third chapter is a study of hybrid perovskite-organic heterojunction phototransistors by integrating metal-halide perovskite (MHP) into a series of organic semiconductor transistor channels to form different types of heterojunction. Phototransistor characterisation shows that "straddling-gap" type-I heterojunction structure with preferential edge-on molecular orientation leads to more efficient photocarrier circulation and hence enhanced photoresponse, whilst transforming the heterojunction type by varying the organic composition allows tuneable photoresponse. This study provides important insights into the charge-transfer dynamics which can help the development of advanced device designs with "on-demand" optoelectronic properties. In addition, a novel evaluation method for phototransistors is proposed using a photo-inverter circuitry, which assesses phototransistors' amplification as well as asserts transistors' functionality for both linear and saturation operations.

Acknowledgement

First and foremost, I would like to express my deepest gratitude towards my supervisor Prof. Thomas Anthopoulos for offering the opportunity to pursue my PhD in his group and giving the continuous support and inspiration during this long journey. I would also like to thank Prof. Martin Heeney, my second supervisor, for all his helpful advice and support.

I would like to thank all the members of the Advanced Materials and Device group for all the good times we had at Imperial College London. I am particularly grateful to Dr.Yen-Hung Lin for his mentoring through my whole PhD life. I would also like to thank Satyajit Das, Julianna Panidi and Dr. Dimitra Georgiadou, who have accompanied me through most of my PhD journey, for all the precious memories in and out of the lab.

Last but not least, I have to thank my parents, Yuanrong Huang and Peihong Liao, for the unconditional support and consistent encouragement as always. It would not have been possible for me to have come this far without them. I would also like to thank my partner, Jiaing Wu, for her company and belief in me.

Lists of Publications

Wentao Huang, Yen-Hung Lin, Thomas D. Anthopoulos. "High Speed Ultraviolet Phototransistors based on an Ambipolar Fullerene Derivative", ACS Applied Materials and Interfaces, **10**, 10202–10210 (2018).

Yen-Hung Lin†, Wentao Huang†, Pichaya Pattanasattayavong, Jongchul Lim, Ruipeng Li, Nobuya Sakai, Julianna Panidi, Min Ji Hong, Chun Ma, Nini Wei, Nimer Wehbe, Zhuping Fei, Martin Heeney, John G. Labram, Thomas D. Anthopoulos, Henry J. Snaith. "Deciphering photocarrier dynamics for tuneable high-performance perovskite-organic semiconductor heterojunction phototransistors". Nature Communications, 10, 4475 (2019)

†Authors contributed equally.

Qiao He, Munazza Shahid, Julianna Panidi, Adam V. Marsh, Wentao Huang, Matyas Daboczi, Ji-Seon Kim, Zhuping Fei, Thomas D. Anthopoulos, Martin Heeney. "A versatile star-shaped organic semiconductor based on benzodithiophene and diketopyrrolopyrrole". Journal of Materials Chemistry C, **7**, 6622-6629 (2019)

Table of Contents

List of Figures 9
List of Tables 12
Chapter 1 Introduction 13
1.1 Flexible electronics 13
1.2 Photodetectors based on solution-processed semiconductors 15
1.3 Thesis Outline 17
Bibliography 19
Chapter 2 Theory 22
2.1 Non-traditional Semiconducting Materials 23
2.1.1 Organic semiconductor 23
2.1.2 Metal oxide semiconductors 26
2.2 Charge Transport in Non-Traditional Semiconductors 29
2.2.1 Electronic structure difference in crystalline and non-crystalline semiconductors 29
2.2.2 Band-like transport 31
2.2.3 Hopping transport 32
2.2.4 Multiple trapping and release model 32
2.3 Thin Film Transistors 33
2.3.1 Thin Film Transistors Architecture 34
2.3.2 Working Principle of TFTs 35
2.3.3 Current-Voltage Characteristics 37
2.3.4 Key Parameters Extraction 38
2.4 Ambipolar Transistor 40
2.4.1 Routes to ambipolarity 40
2.4.2 Operation of ambipolar transistor 41
2.5 Phototransistor 43
2.5.1 Operation principle of phototransistor 43
2.5.2 Photogain/dark current trade-off 44
2.5.3 Phototransistor structure 45
2.5.4 Characterisation of phototransistors 46
2.6 Integrated circuits 47
Bibliography 50
Chapter 3 Experimental Methods 58
3.1 Device Fabrication Techniques 59
3.1.1 Substrate Preparation 59
3.1.2 Solution Deposition of Organic/Inorganic Materials 59
3.1.3 Vacuum Deposition of Metal Contact 60

3.1.4 Application of Self-Assembled Monolayers 60
3.2 Material Characterisation 61
3.2.1 Atomic Force Microscopy 61
3.2.2 Ultraviolet-Visible-Near-infrared Spectroscopy 62
3.2.3 Scanning Kelvin Probe 62
3.3 Electrical Characterisation 63
3.3.1 Current-Voltage Measurements 63
3.3.2 Light-Response Measurements 63
Bibliography 65
Chapter 4 High Speed Ultraviolet Phototransistors based on an Ambipolar Fullerene Derivative 66
4.1 Introduction 67
4.2 Methods 68
4.2.1 Phototransistor Fabrication 68
4.2.2 Material Characterization 68
4.2.3 Optoelectronic Characterization 69
4.2.4 Temporal Response Measurements 69
4.3 Results and Discussion 70
4.3.1 Film Characterization 70
4.3.2. Transistor Design and Electrical Characterisation 71
4.3.3. Optoelectronic Characterisation of $PC_{61}BM$ Transistors 73
4.3.4. Dynamic Operation of $PC_{61}BM$ Phototransistors 82
4.4 Conclusions 84
Bibliography 85
Chapter 5 Hybrid Inorganic Ambipolar Transistors with Dye Functionalization for Efficient and Fast Photo-Sensing Application 92
5.1 Introduction 93
5.2 Methods 94
5.2.1 Film deposition 94
5.2.2 Film characterisation 95
5.2.3 Transistor fabrication 95
5.2.4 Electrical and optoelectronic characterisation 96
5.3 Hybrid Inorganic Transistor Based on $CuSCN/In_2O_3$ Heterostructure 96
5.3.1 Film characterisation 96
5.3.2 Transistor electrical characterisation 97
5.3.3 Transistor optoelectronic characterisation 99
5.4 Dye-Sensitized Hybrid Inorganic Phototransistor 100
5.4.1 Film characterisation 101
5.4.2 Trilayer transistor optoelectronic characterisation 103

5.4.3 Spectral characterisation 105
5.4.4 Dynamic characterisation 106
5.4.5 Gate-bias dependent figures of merit 107
5.4.6 Illumination dependent figures of merit 108
5.5 Opto-Electronic Circuits 111
5.6 Conclusions 112
Bibliography 113
Chapter 6 Tuneable, high-performance perovskite-organic heterojunction phototransistors 118
6.1 Introduction 119
6.1.1 Review of perovskite-based phototransistors 120
6.1.2 Perovskite-organic heterojunction phototransistors 122
6.2 Methods 124
6.2.1 Preparation of metal-halide perovskites and organic semiconductors 124
6.2.2 Fabrication of perovskite heterojunction phototransistors and bilayer structures 124
6.2.3 Film characterisation 125
6.2.4 Electrical and optoelectronic characterisations. 125
6.2.5 Photodetectors simulation 126
6.2.6 Photoluminescence spectroscopy 127
6.2.7 Time-resolved microwave conductivity 127
6.2.8 Transient photoconductivity 128
6.2.9 Impedance spectroscopy 128
6.3 Results and Discussion 129
6.3.1 Heterojunction Phototransistor Configuration 129
6.3.2 Film Characterisations 130
6.3.3 Phototransistor Optoelectronic Characterisations 133
6.3.4 Characterisation of Current Noise in HJPTs 139
6.3.5 Spectroscopic Analysis of Photoinduced Charge Carriers 141
6.3.6 Mott-Schottky Analysis and Perovskite-Organic Contact Diodes 143
6.3.7 Charge Transfer Mechanism 146
6.3.8 Assessing Performance Metrics via A Photo-Inverter 147
6.4 Conclusions 151
Bibliography 152
Chapter 7 Conclusions 160
Appendix A Content Reuse Permission 163

List of Figures

Figure 1.1: Examples of flexible electronics 14
Figure 2.1: Formation of semiconductivity in organic π-conjugated systems 25
Figure 2.2: Band structures and partial density of states plots of metal oxides 27
Figure 2.3: Schematics of electron orbitals in metal oxide 28
Figure 2.4: Schematic of density of states (DOS) in a non-crystalline semiconductor. 31
Figure 2.5: Schematic sketch of charge transport models 33
Figure 2.6: Schematic diagrams of four commonly used TFT architecture 35
Figure 2.7: Schematic illustration of different operation regimes for a transistor 37
Figure 2.8: Representative I-V characteristics of an n-channel transistor 39
Figure 2.9: Schematic of all operating regimes for an ambipolar transistor 41
Figure 2.10: Operation regimes of an ambipolar transistor with a positive V_D 42
Figure 2.11: Schematic illustrations of different types of photodetectors 43
Figure 2.12: Schematic illustrations of two phototransistor structures 46
Figure 2.13: Schematic illustration of inverter circuit 48
Figure 2.14: Illustration of inverter operation 49
Figure 3.1: Schematic illustration of an AFM system. 61
Figure 4.1: UV-Vis absorption spectrum of a $PC_{61}BM$ layer 70
Figure 4.2: AFM images of of $PC_{61}BM$ on glass 71
Figure 4.3: Schematic of $PC_{61}BM$ transistor and energy level band diagram 72
Figure 4.4: Transfer characteristics measured for a $PC_{61}BM$ transistor 72
Figure 4.5: Output characteristics measured for a $PC_{61}BM$ transistor 73
Figure 4.6: Absorption spectrum of $PC_{61}BM$ and EL spectrum of the UV LED 74
Figure 4.7: Transfer and output characteristics of a $PC_{61}BM$ phototransistor 75
Figure 4.8: Photosensitivity plots of a $PC_{61}BM$ phototransistor 76
Figure 4.9: Responsivity plots of a $PC_{61}BM$ phototransistor 77
Figure 4.10: Specific detectivity plots of a $PC_{61}BM$ phototransistor 78
Figure 4.11: Evolution of photocurrent versus incident optical power. 79
Figure 4.12: Photoresponse of a $PC_{61}BM$ phototransistor to three visible light LEDs 80
Figure 4.13: Calculated values for P, R and D_s* for four different wavelengths 81

Figure 4.14: Dynamic response of a $PC_{61}BM$ phototransistor. 83
Figure 5.1: UV-Vis spectra for In_2O_3 and CuSCN/In_2O_3 bilayer film..... 97
Figure 5.2: Schematics of CuSCN/In_2O_3transistor and energy level band diagram..... 98
Figure 5.3: Transfer characteristics measured for CuSCN/In_2O_3 transistor. 99
Figure 5.4: Photoresponse of the transistor under the green illumination 100
Figure 5.5: UV-Vis spectrum of the trilayer D102/In_2O_3 film 101
Figure 5.6: AFM images of CuSCN/D102/In_2O_3 film deposited on glass 103
Figure 5.7: Optoelectronic characterisation of transistors with green illumination. 105
Figure 5.8: Spectral response of the CuSCN/D102/In_2O_3 trilayer phototransistor..... 105
Figure 5.9: Temporal response of the CuSCN/D102/In_2O_3 trilayer phototransistor 107
Figure 5.10: Gate-voltage dependent figures of merit 108
Figure 5.11: Output characteristics of the trilayer phototransistor 109
Figure 5.12: Photocurrent evolution as a function of incident light 109
Figure 5.13: Illumination-intensity dependent figures of merit..... 110
Figure 5.14: Electro-optical NOT gate using trilayer phototransistor 111
Figure 6.1: Schematic of HJPT, chemical structures and energy band diagram 129
Figure 6.2: UV-vis absorption spectrum for OSCs and FACs. 130
Figure 6.3: AFM images for different MHP/OSC bilayer stacks 131
Figure 6.4: GIWAXS patterns for OSC films and FACs/OSC bilayer stacks..... 132
Figure. 6.5: Transfer characteristics of a FACs/OSC HJPT with C_8-BTBT only 134
Figure 6.6: Transfer characteristics of a FACs/OSC HJPT with a 3:1blend 135
Figure 6.7: Transfer characteristics of a FACs/OSC HJPT with a 1:1 blend 135
Figure 6.8: Transfer characteristics of a FACs/OSC HJPT with a 1:3 blend 136
Figure 6.9: Transfer characteristics of a FACs/OSC HJPT with C_{16}-IDTBT only 136
Figure 6.10: Gate-voltage dependent responsivity 138
Figure 6.11: Photogain as a function of dark current density for HJPTs..... 139
Figure 6.12: The dark current waveforms of FACs/OSC HJPTs 140
Figure 6.13: Analysis of noise spectral density of the HJPTs 140
Figure 6.14: PL spectroscopy results for FACs and FACs/OSC bilayer stacks 142
Figure 6.15: TRMC and TPC data for FACs and FACs/OSCs bilayer stacks. 143
Figure 6.16: I-V characteristics of diodes based on FACs/OSC heterostructure 144
Figure 6.17: Mott-Schottky plots for different FACs/OSC bilayer stacks 146
Figure 6.18: Photocarriers' charge transfer mechanisms for HJPTs 146
Figure 6.19: Transfer characteristics of FACs only phototransistors 147

Figure 6.20: Schematic of a PMOS-like HJPT photo-inverter 148
Figure 6.21: Inverter transfer characteristics 149
Figure 6.22: Corresponding A_i of HJPT photo-inverter 150
Figure 6.23: Effect of incident optical power density on photo-inverter V_{OUT} 150

List of Tables

Table 6.1: Summary of performance metrics of perovskite-based phototransistors. 123
Table 6.2: Transistor performance of FACs/OSC HJPTs. 133
Table 6.3: HJPTs figures of merit from current noise characterisation. 141

Chapter 1 Introduction

1.1 Flexible electronics

Electronic devices based on semiconducting materials have become an integral part of modern life. Conventional semiconductor materials are typically crystalline elemental materials from Group IV such as Silicon (Si), and compounds from Group III and V. The chemical bonding of these materials exhibits a strong covalent character. The strong intermolecular electron coupling contributes to the formation of physically robust structures that allow for superior thermal stability and high charge carrier mobilities. Microelectronics based on these materials has achieved great success in the past five decades, the development of which follows an exponential growth path doubling the number of transistors in an integrated circuit every 24 months, which is known as Moore's Law[1].

Despite the success of conventional semiconductors in microelectronics, emerging new applications like wearable integrated systems[2], artificial skins[3], smart labels[4] and intelligent packaging[5] require electronic devices to be flexible, stretchable, light-weight and even biocompatible. These technological demands create a field of applications inaccessible by conventional electronics as most of the crystalline semiconductors are by nature brittle materials and therefore only suitable for rigid substrates. This gives rise to the field of flexible electronics, the possibility of fabricating electronic circuits on flexible substrates thus making them bendable. To make flexible electronics devices, all components (e.g. the substrate, the back-plane and front-plane electronics) must comply with bending to some degree without losing their function[6]. Two basic approaches have been employed to make flexible electronics: i. transfer and bonding of completed circuits to a flexible substrate, ii. direct fabrication of functional circuits on the flexible substrate. The transfer-and-bond approach can date back to 1960s since the first flexible solar cell arrays were made by thinning single crystal silicon wafer to ~100 μm and then assembling them on a plastic substrate to realise flexibility[7]. This approach, however, is limited by small surface area coverage and high cost. On the other hand, direct fabrication approach relies on polycrystalline or amorphous semiconductors because these materials can be grown on foreign substrates. Hydrogenated amorphous silicon (a-SiH) and polycrystalline silicon (poly-Si) therefore have stimulated research on silicon-based thin-film circuits on novel substrates with successful demonstrations on flexible TFTs[8,9] and flexible solar cells[10,11]. In the past three decades, research in materials science has revealed that many

other materials also exhibit semiconducting properties, such as organic semiconductors[12], metal oxide semiconductors[13] and nanocrystal semiconductors[14]. The presence of these new semiconductor materials has significantly expanded the material families available for the direct fabrication of flexible electronics.

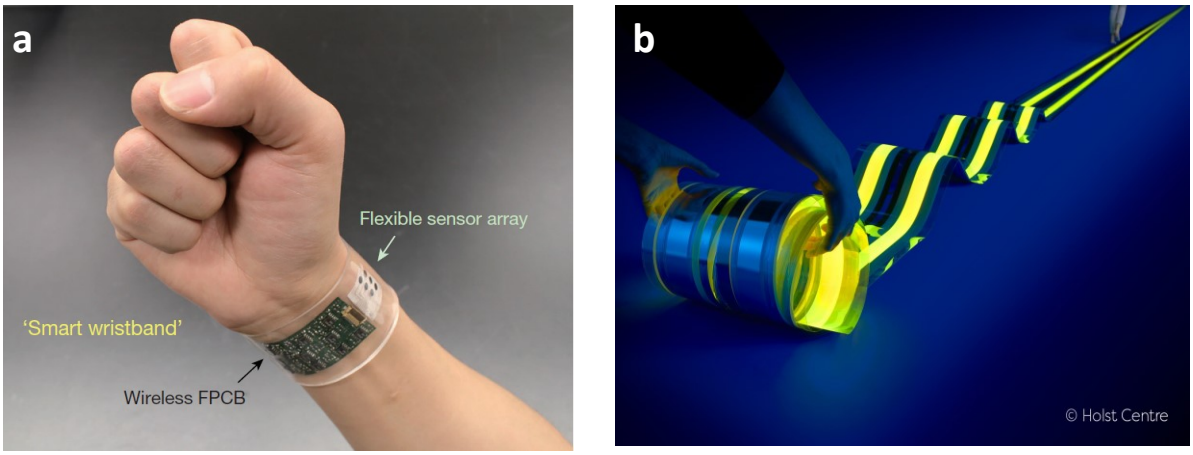


Figure 1.1: Examples of flexible electronics. (**a**) Photograph of a wearable flexible integrated sensing array on a subject's wrist, integrating the multiplexed sweat sensor array and the wireless flexible printed circuit board (FPCB). Taken from ref[15]; (**b**) Photograph of a record-breaking 15-metre single-device OLED strip produced by Holst Centre using a roll-to-roll (R2R) pilot line. Taken from ref[16].

Since the inspiring work in the 1970s by Chiang *et al.* on the discovery of doping-induced conductivity in polyacetylene[17], research interest in organic semiconductors has grown enormously. In the 1980s, functional electronic devices based on organic materials, such as organic light emitting didoes (OLEDs)[18] and organic field-effect transistors (OFETs)[19], were successfully demonstrated. Although the performances were found inferior to the conventional inorganic counterparts, the unique material properties of organic semiconductors provided new routes toward novel electronic device fabrication techniques and applications. For example, organic materials can be processed at lower temperatures, enabling fabrication on plastic substrates. This type of electronics devices has distinct advantages versus traditional electronics including low weight, low cost and high flexibility. Organic materials can also be processed from solution and hence allow various deposition techniques such as spin-coating[20], doctor blading[21], inkjet printing[22], and roll-to-roll printing[23] onto various types of substrates. Moreover, the structure versatility of organic compounds enables molecular design with tailor-made optoelectronic properties via the introduction of different chemical groups. One important example is that the ability to tune the energy bandgap of organic semiconductors leads to the realisation of full colour range emission of OLEDs.

Some inorganic semiconductors, particularly metal oxides, have also been demonstrated to be able to offer similar processability to organic materials with even better charge transport performance[13,24]. Studies on wide bandgap metal oxides as semiconductors can date back to 1960s since some demonstrations of field-effect transistor based on post-transition metal oxides such as tin oxide (SnO_2)[25] and zinc oxide (ZnO)[26]. These metal oxides with attractive properties like high transparency across the visible spectrum, high ambient stability and simple processing led to a surge of research in the early 2000s. A representative work is the first demonstration of thin-film transistor based on amorphous indium-gallium-zinc oxide (IGZO) in 2004 by Nomura *et al*.[27], which exhibits a nearly tenfold increase in mobility compared to amorphous silicon (a:Si). In addition to the high carrier mobility, the amorphous nature of IGZO ensures high device uniformity for large area fabrication. These appealing properties of IGZO TFTs combined with the drive for a replacement of traditional a:Si TFT backplane in flat panel display technology eventually has led to the rapid commercialisation of IGZO TFTs[28]. With significant advances in device performance, research interests then turned towards enriching the fabrication methods of metal oxides. Unlike conventional inorganic semiconductors, the chemical nature of metal oxides makes them possible for solution-based deposition methods[29]. With the research efforts in materials science and engineering, several new chemical routes have been proposed and demonstrated that allow low-temperature deposition of metal oxides on flexible plastic substrates[30–32].

1.2 Photodetectors based on solution-processed semiconductors

Photodetection technology, which has been one of the most important electronic applications in our daily lives, requires photodetectors with distinct electronic and optical properties[33]. Current photodetectors mainly use photodiodes or phototransistors made from conventional crystalline inorganic semiconductors, such as Si or GaAs. These conventional semiconductors possess some properties that restrict their ability to meet the ever-increasing demand for innovation in photodetection technology. For example, conventional semiconductors usually exhibit broadband absorption due to their relatively large bandgap, leading to a broad spectral photoresponse. This gives rise to the requirement of colour filters for colour imaging, which complicating the architecture and fabrication process of the image sensors. In addition, integration of rigid conventional semiconductors as photoactive materials with read-out integrated circuitry (ROIC) increases the complication of system design and poses significant limits on the achievable compactness and sensitivity[34]. Therefore, photodetectors based on

solution-processed light-absorbing materials such as organic semiconductors (OSCs), metal-halide perovskites (MHPs), and inorganic colloidal quantum dots (CQDs), have emerged as promising candidates for the next generation of photodetection[35].

These solution-processed materials possess several properties that are particularly attractive in photodetection applications. Firstly, the processing versatility enables the ease of integration with present sensing technologies like complementary metal-oxide-semiconductors (CMOS), allowing photodetection schemes such as top-surface photodetectors[36]. In the top-surface photodetection scheme, the photoactive layer is incorporated directly on top of the ROIC. The solution-based deposition method allows high coverage of photoactive material on the pixel area, hence delivers high-resolution imaging systems with improved-sensitivity and minimised crosstalk[36]. In addition to the fabrication-relevant benefits, another appealing property of the materials mentioned above is the ability to tune their optical bandgap during material synthesis, which enables photodetection for specific spectral ranges. The optical bandgap of OSCs can be tuned by varying the molecular structure as well as the solid-state assembly, enabling photodetection from the ultraviolet (UV) to the near-infrared (NIR) spectrum. The optical bandgap of MHPs can be tuned by varying the composition of the organic and inorganic fractions, allowing the modification of the bandgap from the visible to the near-infrared spectral range. In contrast, the tuning of the optical bandgap in CQDs is achieved by adjusting the nanocrystal size during growth. This quantum confinement in CQDs enables tuning of spectral response with an extremely wide range from X-ray to the short-wave infrared (SWIR) region. Advances in understanding the material science and device engineering have led to several applications with noteworthy state-of-the-art performance. For example, Adinolfi *et al.* reported a photovoltage field-effect transistor (PVFET)[37] by incorporating CQDs with Si, exhibiting a widely tuneable spectral response and significantly enhanced photodetection for Si-based electronics in the infrared region. Pierre *et al.* reported an all-organic phototransistor-based image sensor[38] processed on plastic substrate without photolithography, exhibiting a wide dynamic range competitive with state-of-the-art image sensors. Stijn *et al.* reported a broadband image sensor array[39] based on CQDs-graphene-CMOS integration, providing a perfect demonstration of incorporating 2D materials into the next-generation photodetection technologies.

Despite the considerable progress, several challenges remain from both scientific and engineering perspectives. From a scientific perspective, the electro-optical physics of these solution-processed materials are different from traditional crystalline inorganic counterpart due to the presence of charge traps and disorder. The latter is usually found to have a significant

influence on the electronic properties, which requires new physical models to be developed for describing the electro-optical mechanism in solution-based semiconductor and their related devices. In addition, the discrepancy in the underlying physics also means that the well-established assessing metrics for traditional photodetector characterization might need to be modified accordingly to avoid potential misinterpretation. From the point of view of device performance, although some performance metrics (such as responsivity and detectivity) of the solution-processed photodetectors have been reported to be competitive with or even exceeding those of Si-based devices, most of these values are measured under extremely low light condition, limiting the application of such photodetectors to low light detection. Solution-based photodetectors with detection sensitivity comparable to the conventional photodetectors under normal illumination conditions are still desired. Apart from the desire for detection sensitivity, there is also a demand for high detection speed which is crucial for the imaging system and determines the frame time of the read-out process in an optoelectronic circuit. Although several materials and architectures have been reported with response time in the range of sub-milliseconds, the temporal response of most of solution-processed photodetectors is still incomparable to that of their best crystalline semiconductor counterparts. All these requirements for solution-processed photodetectors mentioned above pose challenges at both material and device design levels.

1.3 Thesis Outline

This thesis focusses on the development and study of solution-processed semiconductors for phototransistor applications. Following this introductory chapter, Chapter 2 offers an overview of the theoretical foundation for non-traditional solution-processed semiconductors. It starts with the electronic structures of two major channel materials exploited in this work. Then the mechanism for charge transport in these solution-processed materials is discussed. The chapter finishes with a brief explanation of working principles of devices studied in this work, e.g. thin-film transistors, ambipolar transistors and phototransistors. Chapter 3 describes the electrical and material characterisation techniques employed in this work as well as the experimental methods used for film deposition and device fabrication. Chapters 4–7 report key experimental findings in this project with a brief introduction/conclusion given at the beginning/end of each chapter. Chapter 4 reports the development of ambipolar phototransistors based on a fullerene derivative $PC_{61}BM$ with balanced electron and hole transport characteristics. The ability of ambipolar transport is found to be critical for achieving fast operation speed. In chapter 5, the

concept of ambipolarity is applied to help oxide-based transistors which generally suffer from slow operation speed. The ambipolarity is realised by using a p-n heterojunction structure based on In_2O_3 and CuSCN. By the incorporation of an organic light absorbing dye a novel trilayer phototransistor is then demonstrated with a significantly enhanced response time of 1 ms. The last chapter of experimental result explores the route toward high performance hybrid phototransistor employing one of the most promising light absorbing family of materials, the metal halide perovskite. Important insights into the charge transfer dynamic within this hybrid structure are provided and realisation of device designs with "on-demand" optoelectronic properties are proposed. Finally, Chapter 8 summarises the key results of this research work and provides an outlook for future work.

Bibliography

(1) Mack, C. A. Fifty Years of Moore's Law. *IEEE Trans. Semicond. Manuf.* **2011**, *24* (2), 202–207.

(2) Gong, S.; Schwalb, W.; Wang, Y.; Chen, Y.; Tang, Y.; Si, J.; Shirinzadeh, B.; Cheng, W. A Wearable and Highly Sensitive Pressure Sensor with Ultrathin Gold Nanowires. *Nat. Commun.* **2014**, *5* (1), 3132.

(3) Bauer, S. Sophisticated Skin. *Nat. Mater.* **2013**, *12* (10), 871–872.

(4) Nathan, A.; Ahnood, A.; Cole, M. T.; Sungsik Lee; Suzuki, Y.; Hiralal, P.; Bonaccorso, F.; Hasan, T.; Garcia-Gancedo, L.; Dyadyusha, A.; Haque, S.; Andrew, P.; Hofmann, S.; Moultrie, J.; Daping Chu; Flewitt, A. J.; Ferrari, A. C.; Kelly, M. J.; Robertson, J.; Amaratunga, G. A. J.; Milne, W. I. Flexible Electronics: The Next Ubiquitous Platform. *Proc. IEEE* **2012**, *100* (Special Centennial Issue), 1486–1517.

(5) Makarov, D.; Melzer, M.; Karnaushenko, D.; Schmidt, O. G. Shapeable Magnetoelectronics. *Appl. Phys. Rev.* **2016**, *3* (1), 011101.

(6) *Flexible Electronics*; Wong, W. S., Salleo, A., Eds.; Electronic Materials: Science & Technology; Springer US: Boston, MA, 2009; Vol. 11.

(7) Ray, K. A. Flexible Solar Cell Arrays for Increased Space Power. *IEEE Trans. Aerosp. Electron. Syst.* **1967**, *AES-3* (1), 107–115.

(8) Theiss, S. D.; Wagner, S. Amorphous Silicon Thin-Film Transistors on Steel Foil Substrates. *IEEE Electron Device Lett.* **1996**, *17* (12), 578–580.

(9) Young, N. D.; Harkin, G.; Bunn, R. M.; McCulloch, D. J.; Wilks, R. W.; Knapp, A. G. Novel Fingerprint Scanning Arrays Using Polysilicon TFT's on Glass and Polymer Substrates. *IEEE Electron Device Lett.* **1997**, *18* (1), 19–20.

(10) Wronski, C. R.; Carlson, D. E.; Daniel, R. E. Schottky-barrier Characteristics of Metal–Amorphous-silicon Diodes. *Appl. Phys. Lett.* **1976**, *29* (9), 602–605.

(11) Okaniwa, H.; Nakatani, K.; Yano, M.; Asano, M.; Suzuki, K. Preparation and Properties of A-Si: H Solar Cells on Organic Polymer Film Substrate. *Jpn. J. Appl. Phys.* **1982**, *21* (S2), 239.

(12) Sirringhaus, H. 25th Anniversary Article: Organic Field-Effect Transistors: The Path Beyond Amorphous Silicon. *Adv. Mater.* **2014**, *26* (9), 1319–1335.

(13) Petti, L.; Münzenrieder, N.; Vogt, C.; Faber, H.; Büthe, L.; Cantarella, G.; Bottacchi, F.; Anthopoulos, T. D.; Tröster, G. Metal Oxide Semiconductor Thin-Film Transistors for Flexible Electronics. *Appl. Phys. Rev.* **2016**, *3* (2), 021303.

(14) Liu, Z.; Xu, J.; Chen, D.; Shen, G. Flexible Electronics Based on Inorganic Nanowires. *Chem. Soc. Rev.* **2015**, *44* (1), 161–192.

(15) Gao, W.; Emaminejad, S.; Nyein, H. Y. Y.; Challa, S.; Chen, K.; Peck, A.; Fahad, H. M.; Ota, H.; Shiraki, H.; Kiriya, D.; Lien, D.-H.; Brooks, G. A.; Davis, R. W.; Javey, A. Fully Integrated Wearable Sensor Arrays for Multiplexed in Situ Perspiration Analysis. *Nature* **2016**, *529* (7587), 509–514.

(16) Holst Centre. 15-meter roll-to-roll device is world's longest OLED https://www.holstcentre.com/news---press/2018/r2r-oled/.

(17) Chiang, C. K.; Fincher, C. R.; Park, Y. W.; Heeger, A. J.; Shirakawa, H.; Louis, E. J.; Gau, S. C.; MacDiarmid, A. G. Electrical Conductivity in Doped Polyacetylene. *Phys. Rev. Lett.* **1977**, *39* (17), 1098–1101.

(18) Tang, C. W.; VanSlyke, S. A. Organic Electroluminescent Diodes. *Appl. Phys. Lett.* **1987**, *51* (12), 913–915.

(19) Koezuka, H.; Tsumura, A.; Ando, T. Field-Effect Transistor with Polythiophene Thin Film. *Synth. Met.* **1987**, *18* (1–3), 699–704.

(20) Smith, J.; Hamilton, R.; Heeney, M.; de Leeuw, D. M.; Cantatore, E.; Anthony, J. E.; McCulloch, I.; Bradley, D. D. C.; Anthopoulos, T. D. High-Performance Organic Integrated Circuits Based on Solution Processable Polymer-Small Molecule Blends. *Appl. Phys. Lett.* **2008**, *93* (25), 253301.

(21) Knobloch, A.; Manuelli, A.; Bernds, A.; Clemens, W. Fully Printed Integrated Circuits from Solution Processable Polymers. *J. Appl. Phys.* **2004**, *96* (4), 2286–2291.

(22) Parashkov, R.; Becker, E.; Riedl, T.; Johannes, H.-H.; Kowalsky, W. Large Area Electronics Using Printing Methods. *Proc. IEEE* **2005**, *93* (7), 1321–1329.

(23) Søndergaard, R. R.; Hösel, M.; Krebs, F. C. Roll-to-Roll Fabrication of Large Area Functional Organic Materials. *J. Polym. Sci. Part B Polym. Phys.* **2013**, *51* (1), 16–34.

(24) Zhang, L.; Xiao, W.; Wu, W.; Liu, B. Research Progress on Flexible Oxide-Based Thin Film Transistors. *Appl. Sci.* **2019**, *9* (4), 773.

(25) Klasens, H. A.; Koelmans, H. A Tin Oxide Field-Effect Transistor. *Solid. State. Electron.* **1964**, *7* (9), 701–702.

(26) Boesen, G. F.; Jacobs, J. E. ZnO Field-Effect Transistor. *Proc. IEEE* **1968**, *56* (11), 2094–2095.

(27) Nomura, K.; Ohta, H.; Takagi, A.; Kamiya, T.; Hirano, M.; Hosono, H. Room-Temperature Fabrication of Transparent Flexible Thin-Film Transistors Using Amorphous Oxide Semiconductors. *Nature* **2004**, *432* (7016), 488–492.

(28) Wager, J.; Hoffman, R. Thin, Fast, and Flexible. *IEEE Spectr.* **2011**, *48* (5), 42–56.

(29) Thomas, S. R.; Pattanasattayavong, P.; Anthopoulos, T. D. Solution-Processable Metal Oxide Semiconductors for Thin-Film Transistor Applications. *Chem. Soc. Rev.* **2013**, *42* (16), 6910.

(30) Banger, K. K.; Yamashita, Y.; Mori, K.; Peterson, R. L.; Leedham, T.; Rickard, J.; Sirringhaus, H. Low-Temperature, High-Performance Solution-Processed Metal Oxide Thin-Film Transistors Formed by a 'Sol–Gel on Chip' Process. *Nat. Mater.* **2011**, *10* (1), 45–50.

(31) Kim, M.-G.; Kanatzidis, M. G.; Facchetti, A.; Marks, T. J. Low-Temperature Fabrication of High-Performance Metal Oxide Thin-Film Electronics via Combustion Processing. *Nat. Mater.* **2011**, *10* (5), 382–388.

(32) Kim, Y.-H.; Heo, J.-S.; Kim, T.-H.; Park, S.; Yoon, M.-H.; Kim, J.; Oh, M. S.; Yi, G.-R.; Noh, Y.-Y.; Park, S. K. Flexible Metal-Oxide Devices Made by Room-Temperature Photochemical Activation of Sol–Gel Films. *Nature* **2012**, *489* (7414), 128–132.

(33) Kufer, D.; Konstantatos, G. Photo-FETs: Phototransistors Enabled by 2D and 0D Nanomaterials. *ACS Photonics* **2016**, *3* (12), 2197–2210.

(34) Suzuki, T. Challenges of Image-Sensor Development. In *2010 IEEE International Solid-State Circuits Conference - (ISSCC)*; IEEE, 2010; Vol. 53, pp 27–30.

(35) García de Arquer, F. P.; Armin, A.; Meredith, P.; Sargent, E. H. Solution-Processed Semiconductors for next-Generation Photodetectors. *Nat. Rev. Mater.* **2017**, *2* (3), 16100.

(36) Armin, A.; Hambsch, M.; Kim, I. K.; Burn, P. L.; Meredith, P.; Namdas, E. B. Thick Junction Broadband Organic Photodiodes. *Laser Photon. Rev.* **2014**, *8* (6), 924–932.

(37) Adinolfi, V.; Sargent, E. H. Photovoltage Field-Effect Transistors. *Nature* **2017**, *542* (7641), 324–327.

(38) Pierre, A.; Gaikwad, A.; Arias, A. C. Charge-Integrating Organic Heterojunction Phototransistors for Wide-Dynamic-Range Image Sensors. *Nat. Photonics* **2017**, *11* (3), 193–199.

(39) Goossens, S.; Navickaite, G.; Monasterio, C.; Gupta, S.; Piqueras, J. J.; Pérez, R.; Burwell, G.; Nikitskiy, I.; Lasanta, T.; Galán, T.; Puma, E.; Centeno, A.; Pesquera, A.; Zurutuza, A.; Konstantatos, G.; Koppens, F. Broadband Image Sensor Array Based on Graphene–CMOS Integration. *Nat. Photonics* **2017**, *11* (6), 366–371.

Chapter 2 Theory

This chapter gives a brief overview of the theory behind non-traditional solution-processed semiconductors and the operating principles of several transistor-based electronic devices. The chapter starts with a brief description of two non-traditional semiconductors, namely organic semiconductors and metal oxides, that are primarily used in Chapter 4-6 as the conducting channel materials. There then follows a discussion on the models that are typically used to describe the charge transport in these non-tradition semiconductor systems. After the discussion of the charge transport theory, the operating principles and the relevant performance metrics extraction of several transistor-based devices, i.e. thin film transistor, ambipolar transistor, phototransistor and inverter are introduced.

2.1 Non-traditional Semiconducting Materials

The theory used to describe non-traditional semiconductors is based on the same solid-state physics as the conventional semiconductors such as Si or III-V compounds, where the interaction of electrons within the crystal lattice gives rise to an electronic structure containing energy bands and gaps specific to every material. However, the electronic structures in the case of non-traditional semiconductors can also be affected by the variations of the crystallinity, bonding and constituent component, resulting in an enormous difference in the physical and electronic properties. This section gives a brief introduction to two non-traditional semiconductor used in this work, namely organic semiconductors and metal oxide semiconductors. The focus of the discussion will be on the origin of electrical conductivity in these materials and their band structures which determines charge transport.

2.1.1 Organic semiconductor

In general, organic semiconductors are referred to a class of carbon-based compounds that show electrical and/or optoelectronic properties typically associated with semiconductor materials. Organic semiconductors come in many different forms, from allotropes of pure carbon (such as fullerenes), to small molecules and long chain polymers. Most of these compounds consist of a conjugated backbone, i.e. a system of alternating single and double bonds. Such a conjugated structure is the basis of semiconducting properties of organic systems.

To better explain how the conjugated structure results in semiconductor properties, we start with the basic building block of organic systems, i.e. the carbon atom. The orbital configuration of the most common carbon isotope in ground state can be described as $1s^2 2s^2 2p^2$. If an electron is excited from the 2s state to the 2p state, the orbital configuration is transformed to $1s^2 2s^1 2p^3$. In this configuration, it is possible for orbitals to hybridize through the combination of the 2p and 2s orbitals. The 2s orbital and two of the 2p orbitals hybridize to form three hybrid sp^2 orbitals. These highly directional sp^2 orbitals are energetically favourable to form a planar structure while the remaining unhybridised p_z orbital lies perpendicular to the sp^2 orbital plane[1]. The sp^2 orbitals of the neighbouring carbon atoms will overlap to form strong covalent σ-bonds, and the p-orbital of neighbouring atoms also overlap but will form weakly bound π-bonds. Considering the case of many carbon atoms being brought together, a long chain of σ-bonds and π-bonds between neighbouring atoms can be produced. The strong σ-bonds in the long chain form the backbone of the molecules providing the mechanical robustness of organic semiconductors. On the other hand, the π-bonded electrons in the p_z

orbital, which are described as being delocalised, can move freely across the chain, giving rise to the electrical conductivity of organic semiconductors.

According to the quantum theory, the behaviour of an electron in atoms can be described as a wavefunction. When the combination of different atomic orbitals occurs, the phase difference of the wavefunctions results in two different outcomes. Taking the p_z orbital combination as an example, if the unhybridized p_z orbitals overlap in phase with each other, π bonding orbitals with energies lower than the isolated p_z orbital are produced. In contrast, if the p_z orbitals overlap out of phase, π^* antibonding orbitals with higher energies are produced. Based on the Hückel approximation, the molecular orbitals can be described as the linear combination of the related atomic orbitals. Since all these discrete orbitals are filled by electrons from the lowest energy to the highest according to Hund's rules, the orbital combination eventually results in two distinct regions consisting of filled π bonding orbitals and unfilled π^* antibonding orbitals respectively. Within this structure, two orbitals are of particular interest in the organic chemistry, namely Highest Occupied Molecular Orbital (HOMO) and Lowest Unoccupied Molecular Orbital (LUMO). The HOMO and the LUMO, which correspond to the valence band and the conduction band of crystalline inorganic semiconductors respectively, act as pathways for the holes and the electrons to move through in organic conjugated systems.

Since the molecular orbitals can be described as the linear combination of the related atomic orbitals, increasing the length of the conjugated chain, therefore, increases the number of molecular orbitals. In the ideal case of an infinite π-conjugated chain, the number of molecular orbitals would be infinite such that the discrete energy levels become continuous and a band of π states is formed, which would cause metallic conduction. However, it has been found that the periodicity of the chain changes due to the distortion of bonds between adjacent atoms[2], which is a consequence of an instability of the Fermi level states breaking spontaneously the symmetry of distribution over the long chain. The resulting chain with alternating bonding lengths (dimerized chain) has lower potential energy than a chain with equidistant carbon-carbon spacing (non-dimerized chain), as was first proposed by Peierls in 1955 for the case of one-dimensional metals[3]. The so-called Peierls' distortion results in an energy gap that depends on the displacement in the dimerized chain (**Figure 2.1**). Moreover, the presence of disorder in organic semiconductors interrupts the wavefunctions over the chain, transforming the organic systems into a succession of segments. These segments, each has a specific energy gap, eventually lead to a broadened Gaussian distribution of the gap between

the HOMO and the LUMO[4]. This energy gap between the HOMO and the LUMO, also known as the band gap, gives rise to the semiconducting properties of π-conjugated organic systems.

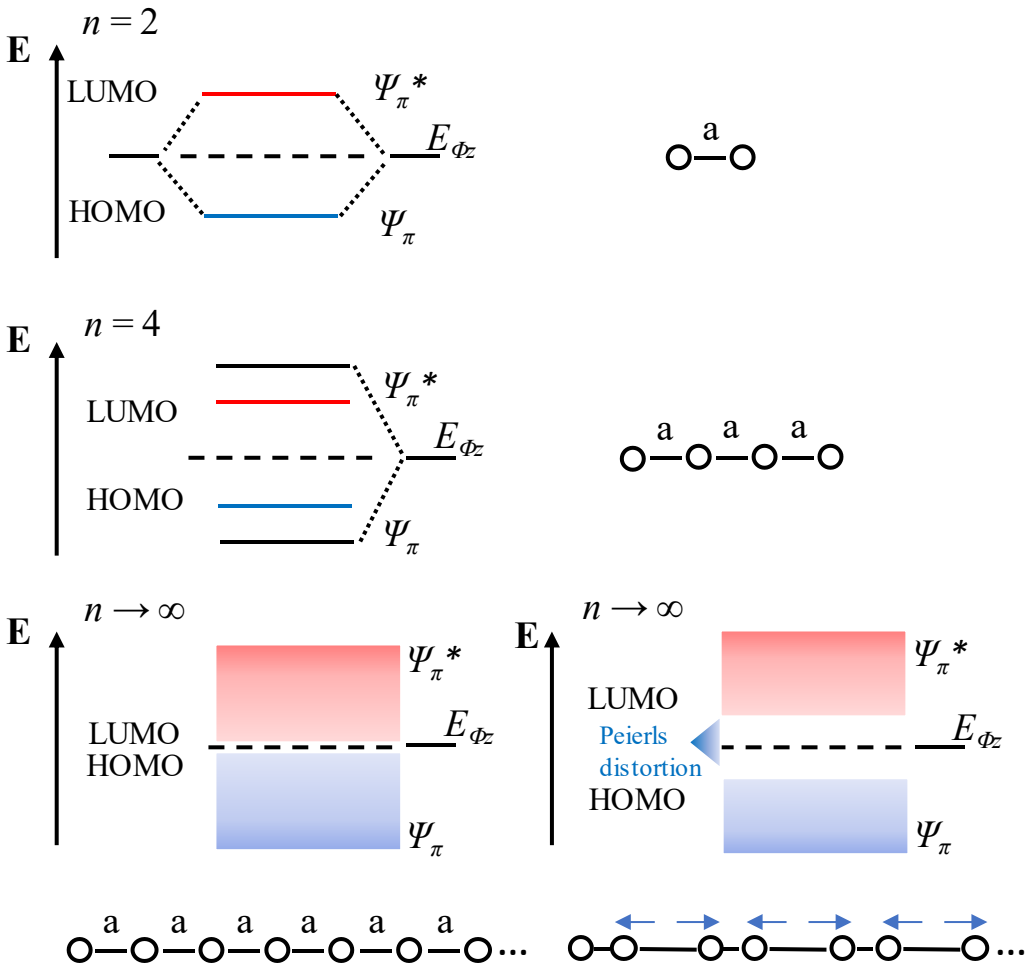


Figure 2.1: Formation of semiconductivity in organic π-conjugated systems[2]. *a* is the distance between two carbon atoms in the non-dimerized chain, Φ_z is the unhybridized atomic orbital p_z, Ψ_π and Ψ_π^* are the bonding and antibonding molecular orbital.

To enable the design and fabrication of organic semiconductors with tailor-made properties, side groups are usually added to the conjugated molecules. Adding the side groups can modify the mechanical and electrical properties such as solubility in organic solvents or the molecular packing in the solid state[5]. Organic semiconductors that are made from conjugated molecules and side groups can be split into two categories, namely polymers and small molecules. Polymers are made from a number of repeating molecular subunits, creating macromolecules with covalently bonded carbon backbones. In the polymer systems, the intermolecular binding mechanism is dominated by the van der Waals forces[6], resulting in relatively weak binding between molecules. The long molecular structure also means that the polymers tend to form spaghetti-like microstructures that are most-likely amorphous. Such

characteristics give rise to the enhanced mechanical flexibility, but also inferior charge transport due to the lack of intrinsic long-range order. In contrast, small-molecules can pack together neatly to form highly crystalline structures, which leads to better electrical properties but deteriorates the ability to be solution-processable.

2.1.2 Metal oxide semiconductors

In contrast to the conventional semiconductors which are based on covalent bonds, the chemical bonds of metal oxides exhibit a high degree of ionicity. The bonding between metal and oxygen atoms with significant ionic character can mainly be attributed to the charge transfer from the metal to the oxygen atoms due to the difference in electronegativity and ionisation energies of the metal and oxygen species. This charge transfer generates electrostatic potentials (known as Madelung potential), which consequently leads to the formation of the ionic bond between the metal and oxygen species. The large Madelung potential is also responsible for the formation of the large bandgap of metal oxides[7]. Most of the metal oxide semiconductors are oxides of heavy post-transition metal cations, e.g. indium, zinc and tin, which share the same orbital configuration of $(n-1)d^{10}ns^2$. In these metal oxides, it is the metal ns and oxygen 2p orbitals that contribute to the formation of the conduction band minimum (CBM) and the valence band maximum (VBM)[8]. As illustrated in **Figure 2.2**, the conduction bands are composed mainly of metal ns orbitals with some contribution from oxygen 2p orbitals, while the valence bands are dominated by oxygen 2p orbitals. The strong interaction between the metal ns orbitals with oxygen 2p orbitals gives rise to a highly dispersive CBM. In contrast, the large electronegativity and strong directivity of oxygen 2p character lead to a localising VBM. The highly dispersive nature of conduction band results in small effective mass for electrons and reasonably high electron mobility, while the localised valence band make it difficult for efficient hole transport. These band structure properties result in the predominantly electron-transporting or n-type characteristics of metal oxide semiconductors reported to date[9,10].

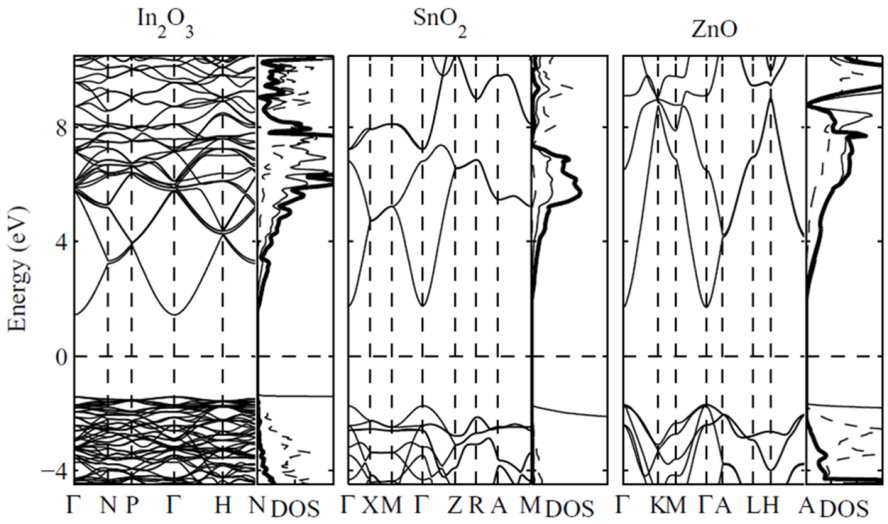


Figure 2.2: Band structures and partial density of states plots of In_2O_3, SnO_2, and ZnO obtained by screened-exchange local-density approximation method. The thick, dashed, and thin lines represent metal *s*, metal *p*, and oxygen *p* states, respectively. Taken from ref [8] with permission.

The electronic structure described above also explains another noteworthy property of metal oxides that is different from conventional semiconductors: the ability of retaining promising electron mobility even in the amorphous phase. In conventional semiconductor like silicon, electron mobility drops significantly from the crystalline state to the amorphous state. This is because the carrier pathway, which is composed of strongly directive sp^3 orbitals, is greatly affected by the structural disorder in the amorphous phase, resulting in degraded electron transport and reduced mobility. In the case of metal oxide, the electron transport pathway is formed by the overlaps between the neighbouring metal orbitals[11,12]. The spatially-extended and spherical metal ns orbitals overlap with each other in either ordered or disordered systems as long as the number of constituent cations overcome the percolation threshold[13,14]. This overlapping characteristic enables efficient electron transport pathways to be formed and hence high n-type mobility even when the metal oxides are in a non-crystalline state.

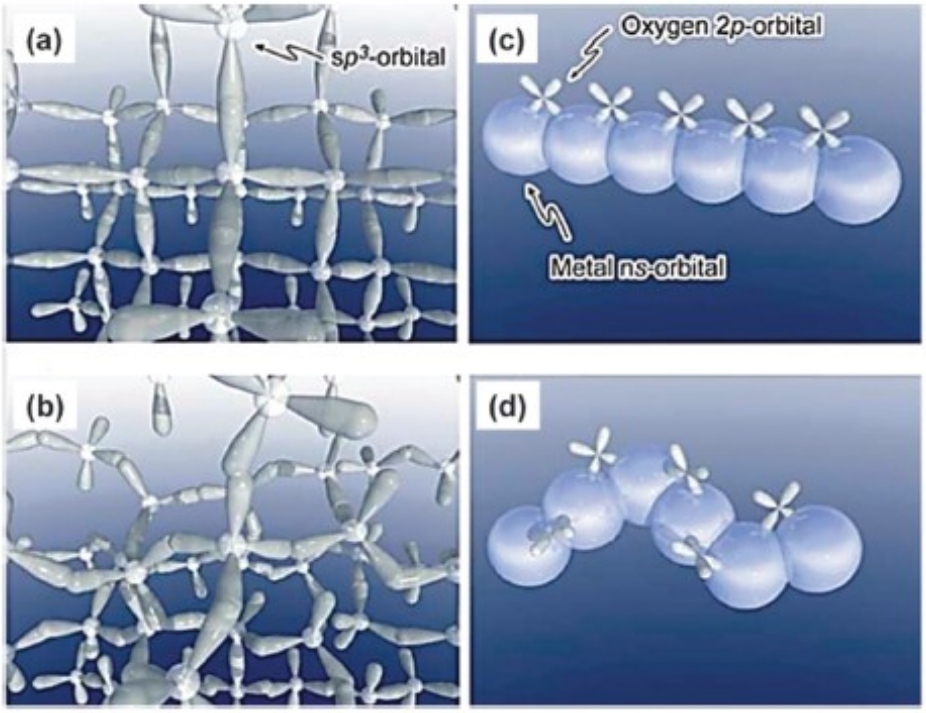


Figure 2.3: Schematic illustration of electron orbitals for carrier transport in (a) crystalline silicon; (b) amorphous silicon; (c) crystalline metal oxide and (d) amorphous metal oxide. Taken from ref [13] with permission.

Though the electronic band structure is favourable for charge transport, the large bandgap of metal oxides prevents the background thermal generation of charge carriers, resulting in very low intrinsic carrier density. This means most metals oxides to behave in general as insulators. However, some metals oxides can exhibit high n-type electrical conductivity even without any doping[7]. A widely accepted explanation of the high conductivity in these metal oxides is that the presence of native defects creates shallow donor levels inside the gap that supply the host with mobile carriers. This hypothesis is in accordance with some experimental observations that the conductivity in n-type metal oxides, such as ZnO and In_2O_3, can be enhanced when the materials are grown under oxygen-deficient or metal-rich conditions[15,16]. This implies that the non-stoichiometric compounds in oxides, e.g. oxygen vacancies or cation interstitials, potentially act as electron donors. However, theoretical calculations indicate that cation interstitials show a very low concentration due to the high formation energy[17]. This is consistent with some experiments indicating that abundant cation interstitials were observed only after artificial generation by high-energy electron irradiation[18,19]. All the results above tend to exclude the possibility of the cation interstitials being the origin of conductivity in undoped oxides. In contrast, oxygen vacancies are found to be an abundant point defect within the oxide system under equilibrium growth condition with

low formation energy[17]. These oxygen vacancies generally exist as deep levels within the bandgap and intrinsically might not be efficient electron donors. Nevertheless, it has been reported that the conductivity can arise from the transition of the oxygen vacancies from a deep, non-conductive ground state to a metastable conductive state upon photoexcitation[17,20]. The creation of shallow electron donor states by photoexcitation can be described by the following equation $V_O \rightarrow V_O^+ + e^-$ and $V_O^+ \rightarrow V_O^{2+} + e^-$. The calculated photon energies for the above two photoexcitation processes to occur are 1.6/1.8 eV for In_2O_3 and 2.8/2.4e V for ZnO, respectively[17,21]. The required photon energy in the visible light range allows for the above process to occur even in ambient background illumination. This oxygen vacancy photoexcitation is also widely considered as a possible reason for persistent photoconductivity (PPC) observed in metal oxide semiconductors as the required absorption energies in the visible range enable the sufficient and constant regeneration of the conductive oxygen vacancy state by the ambient illumination[17,21]. A more detailed discussion of PPC will be given in Chapter 5.

2.2 Charge Transport in Non-Traditional Semiconductors

Understanding the mechanism by which charge is transported is crucial to the development of semiconductor materials and devices. Non-traditional semiconductors produced from solution-processing methods usually contain significant portions of morphology disorder ranging from polycrystalline to amorphous. This non-crystallinity has a significant influence on charge transport. Conventional charge transport theory, which is built upon the crystal structure, might be invalid for these non-crystalline semiconductors. Research efforts therefore have been focused on understanding the actual charge transport mechanism in disordered semiconductors. Nowadays, there are several models for describing the charge transport phenomena in disordered semiconductor systems. However, the applicability might vary from case to case depending on the various parameters such as the degree of crystallinity and temperature. This section aims to provide a very brief overview of charge transport mechanism in disordered semiconductors. It starts by describing the difference in electronic structures between the crystalline and non-crystalline solids, which gives a foundation for further discussion of charge transport in these semiconductors. Following this, relevant models are discussed.

2.2.1 Electronic structure difference in crystalline and non-crystalline semiconductors

In highly-ordered crystalline solids, the electronic structure is determined by the interaction of electrons with the periodic potential of the crystal lattice. Charge carriers, in this system, can

be considered to be in a potential well with periodic boundary condition. Solving the Schrodinger equation with these boundary conditions results in an energy level distribution with two periodic bands in reciprocal space. These two bands are separated by a region where no solution for the Schrodinger equation exists. This region with no probability for charge carriers to exist is termed the band gap or the forbidden energy gap. For a state within the bands with an energy of E, the probability of being filled by electrons is governed by the Fermi-Dirac statistics and is given by the following equation:[22]

$$f(E) = \frac{1}{1 + \exp[(E - E_F)/k_B T]} \tag{2.1}$$

Where E_F is the Fermi level of the system, k_B is the Boltzmann constant and T is the temperature. For intrinsic semiconductors, E_F is located between the two energy bands, hence at $T = 0$ the lower band (valance band) is filled and the upper band (conduction band) is empty.

Unlike crystalline solids where the constant lattice parameters lead to a well-defined band structure with sharp edges and a distinct forbidden energy gap, Anderson argued that the disorder in the non-crystalline solids, e.g. impurities, lattice defects, variation in bond formation, creates the localised states beyond the bands within the band gap[23]. In contrast to the band states in which the wave function of an electron extends spatially over the entire solid crystal, localised states have wave functions which are confined to the finite regions and typically show exponential decay from localisation points. The localised states in non-crystalline materials form a continuous spectrum inside the energy gap, altering the sharp feature of bands and bandgap in crystalline solids. The short-range order in the non-crystalline solids, despite the strong structural disorder, allows the co-existence of the band states with the localised states. The band states in non-crystalline materials are referred to as the extended states. According to the band transport model, carriers can travel as waves in the extended state with high mobility but are immobile in the localised states with low mobility. This transport property forms conceptual borders between the localised states and the extended states, which are known as mobility edges. The region confined by the mobility edges is usually referred to as the mobility gap. The localised states near the mobility edges are called band tails or tail states. (Figure 2.4) In general, carriers in the delocalised states are considered to be trapped and do not contribute to charge transport. However, charge transport can happen via thermal excitation[24]. The delocalised/trap states therefore can be further classified into two categories depending on their relative positions to the mobility/band edge and the time scales of carrier localisation: (i) shallow traps, the localised states within $k_B T$ of the band-edge where carriers can be excited into/relaxed from the extended states via thermal excitation or (ii) deep traps,

the localised states that are greater than k_BT from the band-edge where carriers cannot be thermally activated.

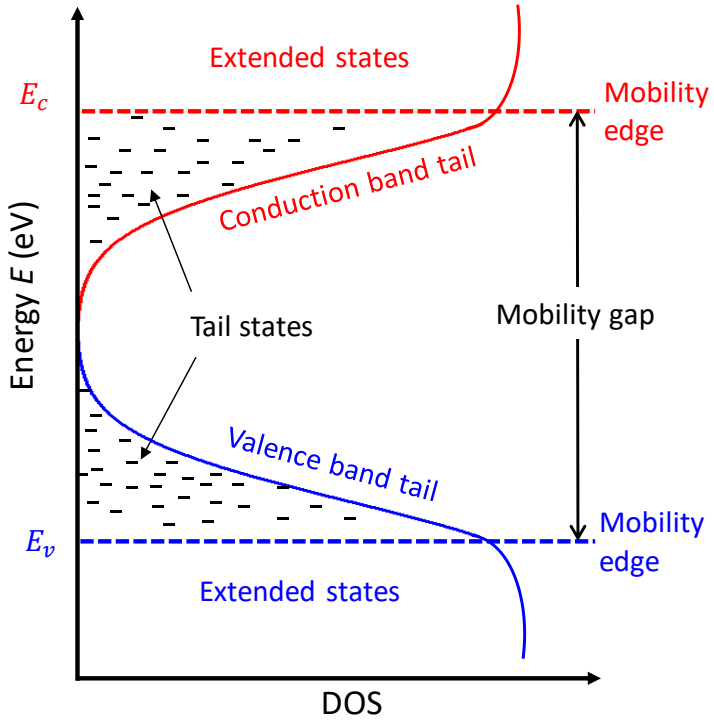


Figure 2.4: Schematic of density of states (DOS) in a non-crystalline semiconductor.

2.2.2 Band-like transport

Charge carriers travelling within the bands can be considered as Bloch waves through a set of delocalised states. The charge carriers wavefunction can be written as a delocalised wave packet with a well-defined momentum which can be scattered by impurities into a state with a different momentum. This dynamic, which described quantitatively by the semiclassical Boltzmann equation, is similar to the diffusion of a gas particle which periodically collides with other particles[25]. The effective mass of the charge carrier behaving as a particle in the bands is inversely proportional to the intermolecular coupling and is given by[26]

$$m^* = \frac{\hbar^2}{2|\tau|L^2} \tag{2.2}$$

Where τ is the electronic coupling (or transfer integral) and L is the distance between sites. The mobility, in this case, can be written as:

$$\mu = \frac{et_s}{m^*} \tag{2.3}$$

where t_s is the average time between collisions and e is the elementary charge. As the frequency of scattering event increases at higher temperature, t_s and hence μ decrease with increasing temperature. Such an inverse temperature dependence of mobility is the signature of band-like transport.

2.2.3 Hopping transport

Charge carriers in the localised states are not completely immobile. The localised carriers are able to travel between states via a mechanism known as hopping[27]. The basic concept of hopping model is that charge transport can take place between the localised trap states via phonon-induced tunnelling. Variable range hopping model is a model based on pure hopping mechanism for highly disordered systems at low temperature[28]. This model assumes that all charge transport happens by hopping from one localised state to another localised states with a variable range - either a large distance with a low activation energy, or a small distance with a high activation energy. The probability of hopping then is determined by the distance and the energy distribution of the localised states. According to the Miller-Abrahams jump-rate model, the probability of the hopping from state i to state j can as given by:[29,30]

$$P(R_{ij}) = P_0 \exp(-2\alpha R_{ij} - \frac{\Delta E_{ij}}{k_B T}) \quad (2.4)$$

Where P_0 is the hopping attempt frequency, α is the inverse of the wavefunction decay length, R_{ij} is the spatial distance between the two states and ΔE_{ij} is the energy difference of the states. This model was further developed by Bässler based on Monte Carlo simulation[4]. The simulation results of hopping between sites within a Gaussian distribution demonstrated the mobility has a temperature dependence as:

$$\mu \propto \exp(-\left(\frac{T_0}{T}\right)^2) \quad (2.5)$$

where T_0 is the characteristic temperature of the system. This result suggests that charge transport based on the hopping model exhibits an increase in mobility with increasing temperature.

2.2.4 Multiple trapping and release model

In reality, the polycrystalline and micro/nanocrystalline systems are disordered yet consisting of a region of high order and strong intramolecular interaction. These characteristics made the charge transport hard to explain by just the band-like transport which is for highly ordered system or hopping transport which is for highly disordered system. One of the more commonly-

used models for describing disordered semiconductors is the multi-trapping and release model[31], which merges transport in both extended states and localised states[32]. In this model, charge carriers can be either in extended states where they are mobile and contribute to the charge transport, or in localised states where they are trapped and not able to contribute to charge transport. The whole process is described as follows: (i) charge is induced into the extended states where it undergoes band-like transport until (ii) it is caught by localised/trap states near the band edge for a certain time and (iii) it is eventually released back to the conduction band via thermal excitation (**Figure 2.5c**). Since carriers are thermally excited to the conduction band, the mobility of the charge carriers can be described using an Arrhenius relationship as:[33]

$$\mu = \mu_0 \exp(-\frac{E_A}{k_B T}) \tag{2.6}$$

where μ_0 is a material-dependent pre-factor and E_A is the activation energy required for a carrier to move from a localised state to an extended state. Again, the mobility in this model shows an increase with increasing temperature.

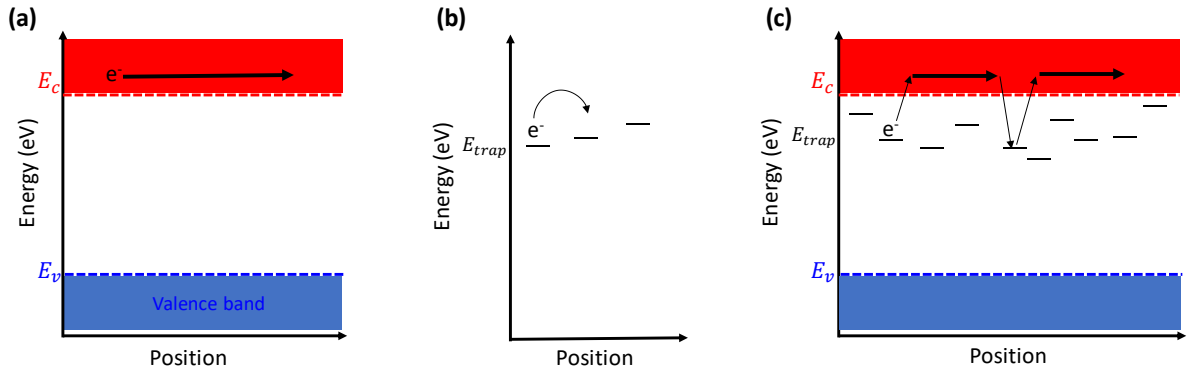


Figure 2.5: Schematic sketch of charge transport models. (a) Band-like transport. (b)Hopping between localised states. (c) Multiple trapping and release model.

2.3 Thin Film Transistors

The functionality of Field effect transistors (FETs) is usually considered as an electrically-controlled switch or amplifier. Thin film transistors (TFTs) are a subcategory of field effect transistors. The concept of thin film transistors was firstly demonstrated by Weimer in 1962[34]. Instead of using bulk materials as the active layer as well as the substrate like other well-demonstrated FETs such as metal-oxide-semiconductor field effect transistors (MOSFETs), TFTs utilise a thin film of semiconducting materials as active layer deposited on a supporting

substrate. The abundant options of supporting substrates and the variable active film processing conditions make flexible and transparent devices fabrication to be possible.

2.3.1 Thin Film Transistors Architecture

A thin film transistor typically consists of several components: a thin semiconducting film, a gate electrode, an insulting gate dielectric and two contact electrodes, namely the source and the drain. When an electric field is applied between the source and the drain, charge carriers typically flow at the dielectric-semiconductor interface within the area enclosed by the source and drain, i.e. the active channel area. Hence, the transistor channel width (W) and channel length (L) are defined by the shape and separation of the source and the drain electrodes.

The difference in device architecture can give rise to significant variation in TFT performance even with the same components. **Figure 2.6** shows four of the most commonly-used architectures for TFTs[10]. Depending on the relative position between the injecting source/drain electrodes, the semiconducting layer and the gate, these four architectures can be further classified into two types, namely staggered and coplanar configuration. In staggered configurations (**Figure 2.6a** and **d**), the source/drain electrodes and the gate are formed on opposite sides of the semiconducting layer while in coplanar configurations (**Figure 2.6b** and **c**) the source/drain electrodes and the gate are formed on the same side of the semiconducting layer. In coplanar configurations charges are injected directly from the electrode to the transistor channel in proximity to the dielectric-semiconductor interface, while in staggered configurations injected charges have to travel through the semiconductor bulk before reaching the actual channel. However, charge injection in staggered structures happens not only from the edge of the electrodes but also from the overlapping parts with the gate electrodes, resulting in a relatively larger injection area.[35] This explains why devices in the staggered configuration are usually found to exhibit better charge injection compared to those in the coplanar counterpart.

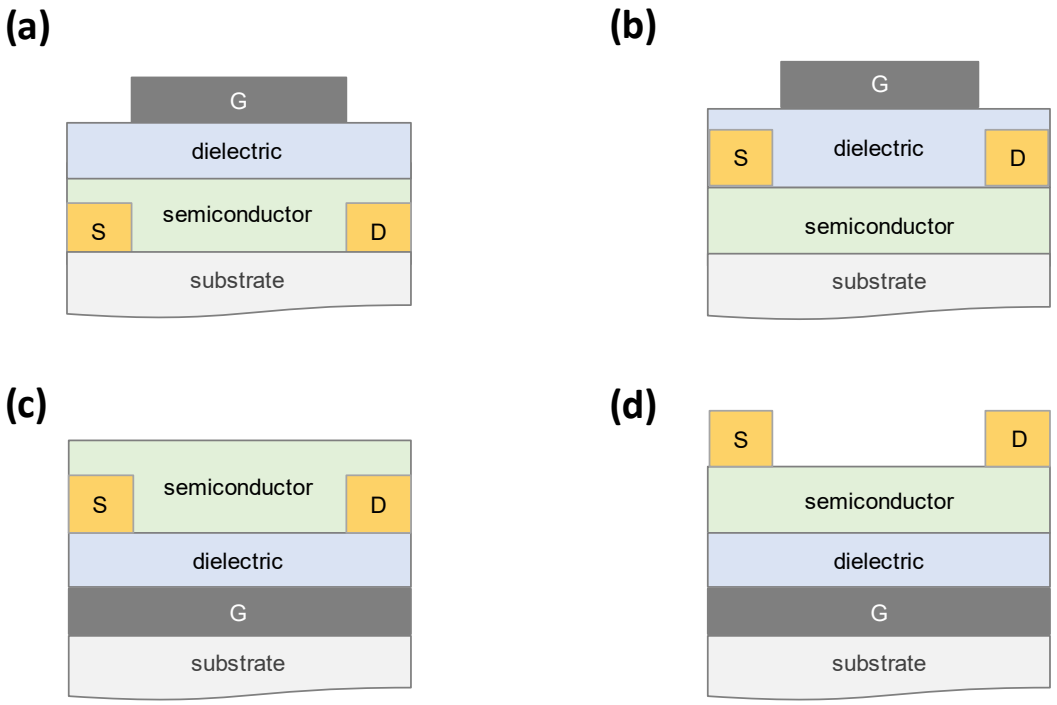


Figure 2.6: Schematic diagrams of four commonly used TFT architecture[10]; (**a**) top-gate, bottom-contact, (**b**) top-gate, top-contact, (**c**) bottom-gate, bottom-contact and (**d**) bottom-gate, top-contact. The diagram illustrates the position of the source (S), drain (D) and gate (G) electrodes relative to the semiconductor and dielectric.

2.3.2 Working Principle of TFTs

In normal transistor operation, a voltage is applied to the gate electrode and the drain electrode, while the source electrode is usually kept grounded. The potential difference between the source and the drain is referred to as the drain voltage (V_D) while the potential difference between the source and the gate is referred to as the gate voltage (V_G). If the potential difference between the source and the gate is larger than that between the drain and the gate, the source electrode works as the charge injection source. When a positive V_G is applied electrons are injected from the source and accumulated at the dielectric-semiconductor interface, i.e. the transistor channel. In this operation, the transistor is considered to be working in the electron accumulation mode, or n-channel mode. Similarly, when a negative V_G is applied holes are injected from the source and accumulated at the transistor channel, corresponding to a transistor working in the hole accumulation mode, or p-channel mode.

Figure 2.7 illustrates the basic operation regimes of a transistor. When no bias is applied to the drain, a transistor can be simply considered as a metal-insulator-semiconductor (MIS) diode. With a voltage applied to the gate electrode, charges of the opposite sign will be attracted from the grounded electrode and accumulated at the dielectric-semiconductor interface. The number

of accumulated charges is proportional to both the applied gate voltage and the capacitance of the gate dielectric. The accumulated charge carriers are mobile and current can flow under the influence of an external field. The current flow between the source and the drain is referred to as the drain current (I_D). However, not all the charge carriers within the channel are mobile and are able to contribute the drain current. Some will first fill deep carriers traps at the interface, contributing to a repulsive electric field. This results in a threshold voltage (V_{Th}) which has to be overcome before the additional charge carriers can become mobile. When a voltage greater than the threshold voltage is applied to the gate electrode and no voltage is applied to the drain electrode, the charge carrier concentration in the transistor channel is uniform as shown in **Figure 2.7a**. When a small V_D with the same sign as V_G is applied, carriers within the channel start flowing from the source electrode to the drain electrode. A linear gradient of charge density across the channel is thus formed and I_D is directly proportional to the applied drain voltage. Transistors working in such a condition are said to be working in the linear regime (**Figure 2.7b**). As V_D is increased, a point where $V_D = V_G - V_{Th}$ will be reached at which the transistor channel is "pinched off" (**Figure 2.7c**). Here a depletion region forms next to the drain electrode where no mobile charge carrier is present due to the potential difference between the gate and the drain below the threshold voltage. Charge carriers in this case can get swept across from the pinch-off point to the drain by the high electric field in the depletion region, forming a space-charge-limited current across this area. When V_D is further increased, the pinch-off point moves forward to the source leading to an expansion of the depletion region. Most of the additional voltage is dropped across the high-resistance depletion zone and the potential between the pinch-off point and the source remains V_G - V_{Th}. Therefore, I_D will not increase substantially with increasing V_D, and transistors in this condition are considered to be operating in the saturation regime (**Figure 2.7c**).

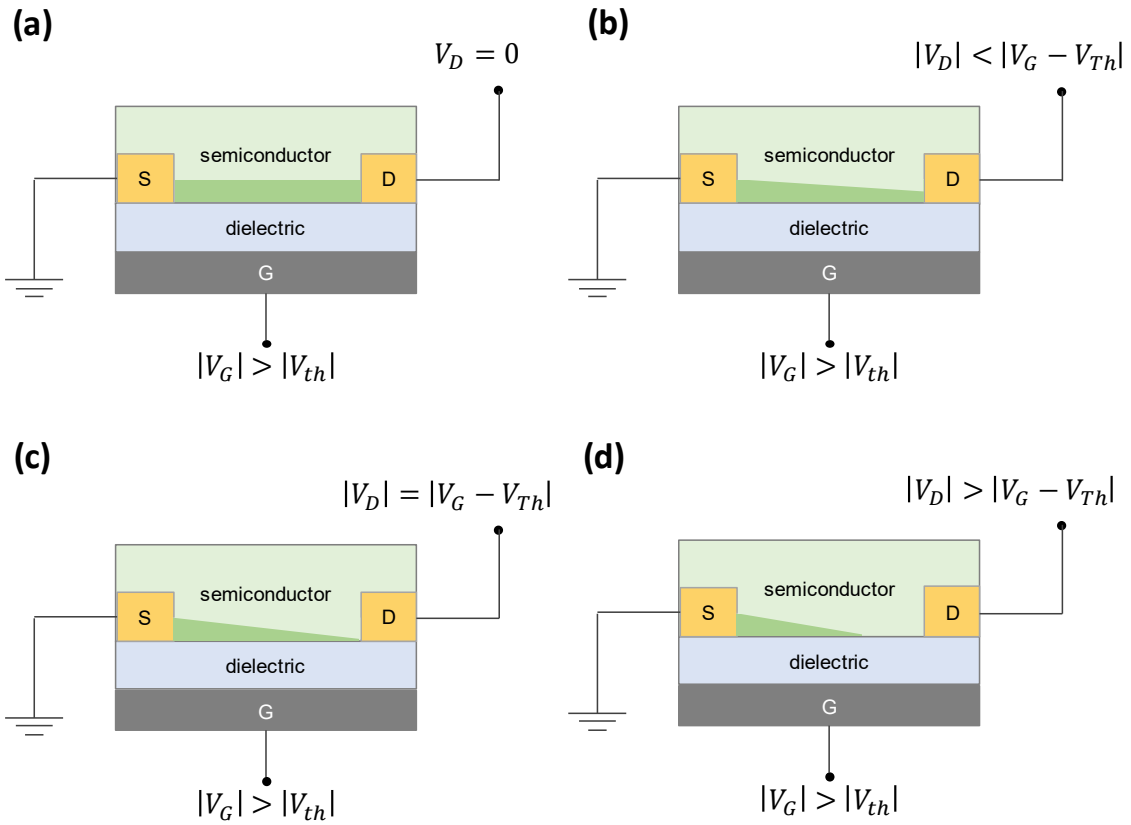


Figure 2.7: Schematic illustration of different operation regimes for a transistor; (**a**) No drain voltage is applied so the carrier concentration in the channel is uniform. (**b**) Transistor is working in the linear regime. (**c**) Transistor channel is pinched-off. (**d**) Transistor is working in the saturation regime.

2.3.3 Current-Voltage Characteristics

To mathematically describe the current-voltage characteristics of transistors is difficult. This is because of the presence of two electric field components within the transistor, one perpendicular to the transistor channel generated by the gate voltage and the other parallel to the current flow generated by the drain voltage. It can be done by using the square-law model based on the gradual channel approximation[36], which assumes the perpendicular field is much larger than the parallel one.

For a given gate voltage V_G greater than the threshold voltage, the capacitively-induced mobile charges can be described as:

$$Q_{mob} = C_i(V_G - V_{Th}) \tag{2.7}$$

where C_i is the geometric capacitance of the dielectric. The charge density within the transistor channel depends on the position along the channel. Taking this into account, the actual charge density at a distance x from the source should be expressed as:

$$Q(x) = C_i[V_G - V_{Th} - V(x)] \tag{2.8}$$

where *V(x)* is the channel potential at position *x*. The local electric field at this point is given by:

$$E_x = -\frac{dV(x)}{dx} \tag{2.9}$$

For a small segment *dx* within the channel, the local current I_x thus can be described as:

$$I_x = W\mu Q(x)E_x = W\mu C_i[V_G - V_{Th} - V(x)]\frac{dV(x)}{dx} \tag{2.10}$$

where *W* is the width of the channel and μ is the charge carrier mobility. Assuming the mobility is independent of the external electric field, the drain current within the channel can then be obtained by integration of the segment over the whole channel length *L*:

$$\int_0^L I_x dx = W\mu C_i \int_0^{V_D} [V_G - V_{Th} - V(x)]\, dV(x) \tag{2.11}$$

yielding:

$$I_D = \frac{W}{L}\mu C_i \left[(V_G - V_{Th})V_D - \frac{1}{2}{V_D}^2\right] \tag{2.12}$$

When the transistor is working in the linear regime, i.e. $|V_D| \ll |V_G|$, the quadratic term in Equation 2.12 can be omitted and the equation can be simplified as:

$$I_{D,lin} = \frac{W}{L}\mu C_i (V_G - V_{Th})V_D \tag{2.13}$$

When the transistor is working in saturation regime, the channel is pinched off and the drain current is independent of V_D. As the potential at the pinch-off point is always V_G - V_{Th}, the saturation drain current can then be obtained by substituting V_D with V_G - V_{Th} in Equation 2.12, yielding:

$$I_{D,sat} = \frac{W}{2L}\mu C_i (V_G - V_{Th})^2 \tag{2.13}$$

2.3.4 Key Parameters Extraction

In the transistor electrical characterisation two typical sets of current-voltage characteristics are usually recorded. The first one is a measurement of the drain current versus the drain voltage for different values of gate voltage. This is referred to as the output characteristics of a transistor (**Figure 2.8a**). The other one is a measurement of the drain current versus the gate voltage for different values of drain voltage. Typically, a high value and a low value of drain voltages are

chosen, which correspond to the device working in the linear and the saturation regimes, respectively. This is referred to as the transfer characteristics of a transistor (**Figure 2.8b**).

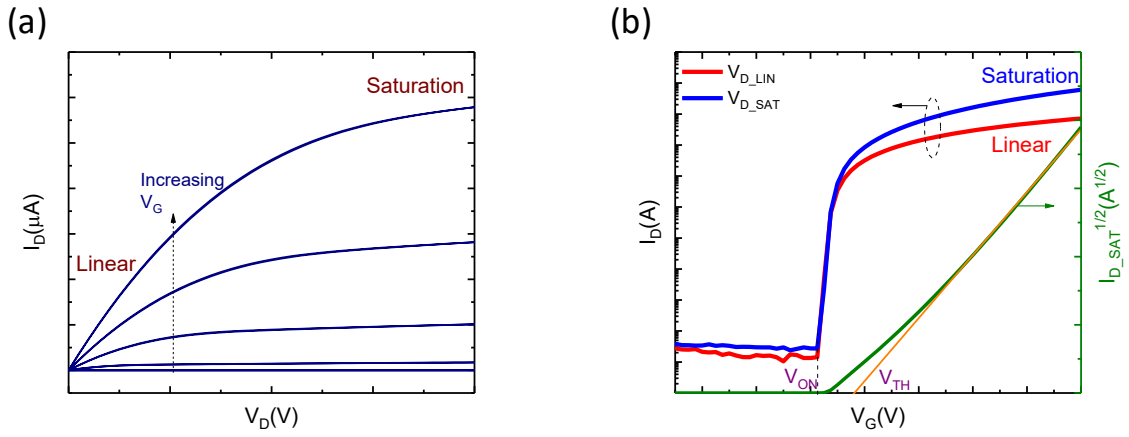


Figure 2.8: Representative I-V characteristics of an n-channel transistor; (**a**) Output characteristics. (**b**) Transfer characteristics.

The most commonly-used performance metrics for transistors are linear mobility, saturation mobility, threshold voltage, subthreshold swing and current on/off ratio. Most of these parameters can be extracted from the transfer characteristics.

The linear mobility μ_{lin} can be calculated from the gradient of I_D versus V_G by using the following equation:

$$\mu_{lin} = \frac{\partial I_{D,lin}}{\partial V_G} \cdot \frac{L}{W V_D C_i} \tag{2.14}$$

The saturation mobility μ_{sat}, on the other hand, can be calculated from either the second derivative of I_D versus V_G or the square-root of the first derivative by using the following equations:

$$\mu_{sat} = \frac{\partial^2 I_{D,sat}}{\partial {V_G}^2} \cdot \frac{L}{W C_i} \tag{2.15}$$

$$\mu_{sat} = \left(\frac{\partial I_{D,sat}}{\partial {V_G}^2}\right)^2 \cdot \frac{2L}{W C_i} \tag{2.16}$$

To extract these mobility values from experimental data, it can be simply done by performing numerical differentiation on I_D with respect to V_G from the corresponding transfer characteristics.

According to equation 2.13 the square root of $I_{D,sat}$ should be linearly proportional to V_G, the threshold voltage V_{Th} hence can be obtained by extrapolating the linear fit of the square root plot of $I_{D,sat}$ versus V_G the horizontal axis (**Figure 2.8b**).

The subthreshold swing *S.S.* represents the slope in the logarithmic plot of the transfer curve. It is defined by the following equation:

$$S.S. = \frac{\partial V_G}{\partial (log_{10} I_D)} \tag{2.17}$$

The S.S. indicates how rapidly the transistor can be switched from the off-state to the on-state hence a smaller value is desired in general.

The on/off ratio is defined as the ratio of the maximum drain current and the minimum drain current and can be calculated directly from the transfer characteristics. It is desirable for this value to be as large as possible to realise a clear switching function of a transistor.

2.4 Ambipolar Transistor

An Ambipolar transistor is a device in which both electrons and holes can be accumulated and conducted. This can enable the realisation of complementary-like inverter without complicated patterning techniques. From the perspective of circuit-level application this complementary-like inverter is desirable as it shows lower power dissipation, wider noise margin and higher operation robustness compared to its unipolar counterpart[37]. In addition, the ability of accumulating and conducting both electrons and holes in an ambipolar transistor enables the direct comparison of electron and hole transport within a single device and thus provide a way to improve the understating of the charge transport mechanisms and the device physics[38].

2.4.1 Routes to ambipolarity

Ambipolar transistor can be realised in several different ways, including the use of either single or a combination of two semiconductor materials. In the case of using single materials, the semiconductor is expected to intrinsically have a balanced hole and electron mobility. In addition, to achieve equally good electron and hole transport, the work function of the injecting electrodes need to be well aligned with the both the CBM and VBM (or LUMO and HOMO in organics) of the material to minimise the energetic barriers for hole and electron injection. Asymmetric electrodes are often used in the case of single-material ambipolar transistor to obtain a good energetic matching[39–41]. Instead of using a single material, ambipolarity can also be achieved by combining two semiconductor materials. Blending two semiconductors, which forms interpenetrating electron- and hole-transporting network within the same channel layer, is one of the more popular ways to achieve ambipolar behaviour[42–44]. Although this method provides a simple fabrication, it was found that often the field effect mobility in the blended

system is lower than single-component devices[45–47]. Another route to ambipolarity is using a bilayer structure. This structure was used in the first reported ambipolar organic transistors [48]. In this structure, it is expected that the electron transport occurs in the n-type semiconductor layer while the hole transport happens in the p-type semiconductor layer. The bilayer structure can hence be considered as two parallel-separated transistors with a common gate.

2.4.2 Operation of ambipolar transistor

Within an ambipolar transistor, the carriers present in the channel can be electrons, holes, or both simultaneously, depending on the biasing conditions. The transfer and output current-voltage characteristics therefore vary according to the potentials applied to the source, drain and gate electrodes relative to one another. The different working regimes of an ambipolar transistor are schematically presented in **Figure 2.9**.

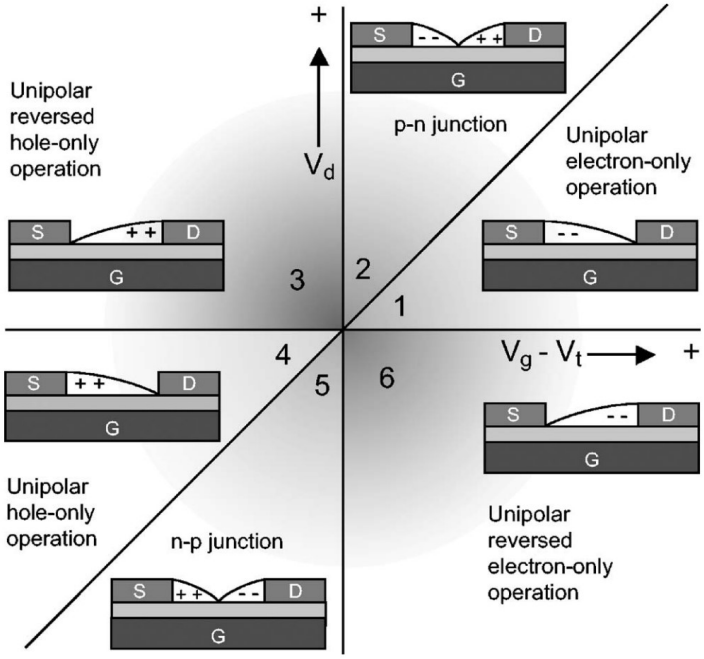


Figure 2.9: Schematic of all operating regimes for an ambipolar transistor as a function of drain gate biasing. Taken from ref[37] with permission.

A more detailed description of the working principle of an ambipolar transistor is presented here taking the device with a given positive drain voltage V_D as example (corresponding to the upper region in **Figure 2.9**). Prior to the description, it must be pointed out that the threshold voltage for electron accumulation in an ambipolar transistor is in general not equal to that for hole accumulation, i.e. $|V_{Th,e}| \neq |V_{Th,h}|$. This can be explained by the difference in injection barriers for electrons and holes. In addition, the density of trap states for electrons and holes is

unlikely to be the same, which also contributes to the difference in threshold voltage for the two carriers. For $V_G > V_{Th,e}$ and $V_G - V_{Th,e} \geq V_D$, electrons are injected from the source into the transistor channel and drift toward the drain (**Figure 2.10d**), which is identical to the normal n-channel unipolar transistor. The transistor under this condition is considered to be working in the unipolar regime. For $V_G > V_{Th,e}$ and $V_G - V_{Th,e} < V_D$, electrons are injected from the source and the transistor channel formed by the electron accumulation will be pinched-off like the normal unipolar transistor if $V_G - V_D \geq V_{Th,h}$ (**Figure 2.10c**). However, if $V_G - V_D < V_{Th,h}$ holes can be injected simultaneously from the drain and drift toward the source (**Figure 2.10b**). In this circumstance, both electrons and holes are present within the device contributing to the formation of transistor channel and hence the channel is no longer pinched-off. Such working regime is called the ambipolar regime. This is distinct from a unipolar transistor as the latter only allows the presence of one polarity of charges for any biasing conditions. For $V_G < V_{Th,e}$ and $V_G < V_D$, the potential difference between the gate and the drain is larger than that between the gate and the source. In this circumstance the drain can become the injection electrode, i.e. the effective "source", and holes are injected from the drain and drift to the source if $V_G - V_D < V_{Th,h}$ (**Figure 2.10a**). The transistor channel in this case is formed by the accumulation of holes and high current flow can be detected, unlike a unipolar n-channel transistor where the device will be in off-state due to the absence of electrons.

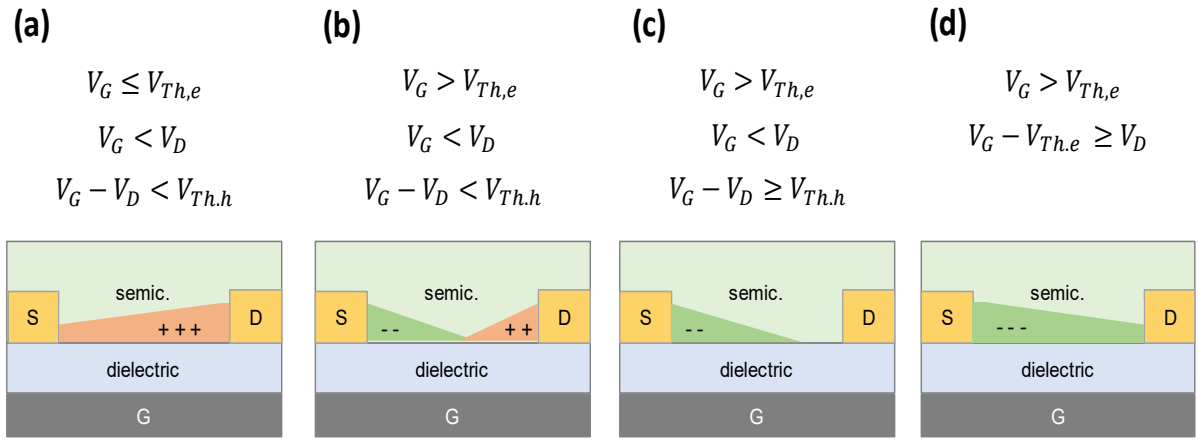


Figure 2.10: Schematic illustration of different operation regimes of an ambipolar transistor with a given positive drain voltage. (**a**) Unipolar regime with an inversed injection of holes from the drain to the source. (**b**) Ambipolar regime with electrons flowing from the source to the drain and holes flowing from the drain to the source. (**c**) Unipolar regime with a saturated (or pinched-off) channel for electrons transport. (**d**) Unipolar regime with electrons injected from the drain to the source.

2.5 Phototransistor

2.5.1 Operation principle of phototransistor

Absorption of light by semiconductors can lead to the photoexcitation of charge carriers, the conductivity and electrical characteristics of the semiconductors hence will be changed accordingly. This photo-responsive property of semiconductors can be exploited for light detection and forms the basis of photodetectors. There are several possible structures that can be used for a photodetector. The simplest structure is the photodiode/photoconductor in which a photoactive material is sandwiched by two metal electrodes (Figure 2.11**a** and **b**). The conductivity of such two-terminal device can be altered upon illumination. Photodetectors can also be realised in a phototransistor structure, where a gate electrode and a dielectric layer are added to the photoconductor structure, forming a three-terminal structure (Figure 2.11**c**). In this three-terminal device, the conductivity of the device can then be modulated by either the applied gate filed or the incident light. Compared to two-terminal devices the phototransistor structure provides an extra degree of freedom for device operation and tuneable optoelectronic properties.

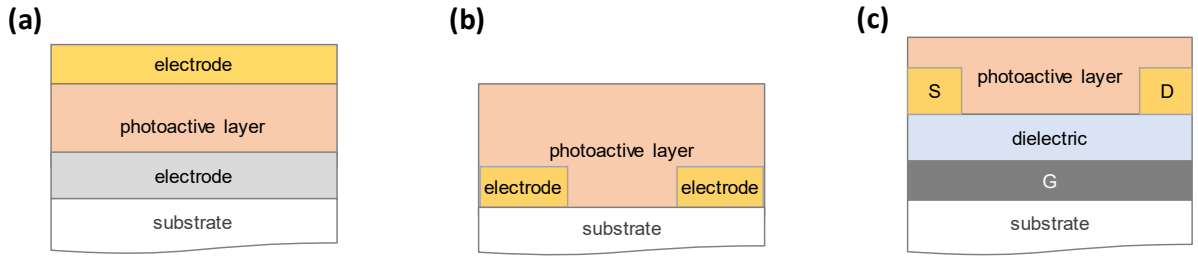


Figure 2.11: Schematic illustrations of different types of photodetectors. (a) Photodiode or photoconductor in vertical architecture. (b) Photoconductor in lateral architecture. (c) Phototransistor.

Just like normal transistors, a phototransistor should possess two operation regimes, namely linear regime and saturation regime[49]. These two operation regimes determine two different operation modes in phototransistor circuit, namely active mode and switch mode. In active mode, a phototransistor is working in linear regime and responds proportional to incident light intensity. In switch mode, a phototransistor operated in either cut-off regime or saturation regime exhibits different nonlinear current levels when varying illumination intensities. The non-linear response and saturation of channel current at high light intensity generate two output logic levels. Devices working in this mode acts as a digital switch. The existence of such two operation modes distinguishes phototransistors from photoconductors in the aspect of circuit

application. Having said that, one should note that there are many reports that show phototransistor-like photoconductor devices[50–58], i.e. three metal terminals and a gate dielectric. Despite the presence of field-effect modulation due to the gate bias, these devices, primarily based on highly conductivity materials such as graphene, typically exhibit no saturation in the drain current and low current on-off ratio, limiting the operation in active mode only. These devices therefore behave still like a photoconductor rather than a phototransistor.

2.5.2 Photogain/dark current trade-off

Another noteworthy property that makes phototransistors distinct from photodiodes is the presence of gain mechanism[22]. In conventional photodiodes, an absorbed photon can at maximum generate one electron-hole pair, corresponding to an external quantum efficiency (EQE) of 100%. In this circumstance, the devices are considered to be with no photogain. In phototransistors, the metal-semiconductor contacts allow continuous injection of charge carriers, and photodetectors of this kind can result in a high EQE level that exceeds 100%. The reason for this is that the majority carriers in a semiconductor can be quickly collected by the drain electrode under the certain conditions: (i) the minority carriers are trapped; and (ii) the majority charge carriers can be (re)injected from the metal contacts to achieve charge neutrality. Such a process continues until trapped carriers are released and recombined. Therefore, photocarriers with the same polarity as that of the majority carriers behave like circulating between two electrodes (e.g. from the source to drain contacts). This, in short, means upon illumination a photon can trigger a current flow by carrier circulation for many cycles, resulting in an EQE large than 100% and hence high photogain.

The gain mechanism in phototransistors (as well as photoconductors) is usually described as photoconductive gain[59]. It is defined as the ratio of photogenerated carrier life time to the carrier transit time. Based on this description, devices with high gain are usually obtained using materials with high carrier mobility as this results in a much shorter carrier transit time than carrier lifetime. However, these high mobility materials inevitably lead to high off currents even when the devices are not exposed to light (i.e., high dark current). High dark currents are undesirable for photodetectors as this causes a high level of shot noise and limits the detectivity of the devices [60]. Therefore, a trade-off between gain and dark current is commonly observed to exist in phototransistors dominated by photoconductive gain mechanism.

2.5.3 Phototransistor structure

The simplest way to construct phototransistors is by using a single-component as the active/channel layer for both light absorbing and charge transport (Figure 2.12**a**). In order to achieve high performance, this single layer should ideally possess several properties: (i) high mobility for large gain-bandwidth products, (ii) suitable bandgap for efficient gate modulation, (iii) high optical absorption for efficient photoexcitation and (iv) low trap state density for high subthreshold slope and low dark current[61]. Materials with potential to fulfil most of these requirements have been investigated including organics[62–64], transition-metal dichalcogenides (TMDs)[65–69], chalcogen-based inorganic nanomaterials[70–73] and black phosphorus[74–76]. However, a trade-off between the electrical modulation and the optical absorption due to the film thickness has been reported as a common issue for these single-component phototransistors[61]. A channel made of a thin layer exhibits better field-effect modulation and high on/off ratio but suffers from low optical absorption and hence limited photoresponse. On the contrary, a channel made of a bulk layer exhibits reduced on/off ratio and high off current but profits from enhanced photo absorption due to a longer optical path.

To overcome these issues one can employ a hybrid structure that decouples the photo absorption process from the charge transport (Figure 2.12**b**). In this structure a semiconductor layer with strong photo absorption property is employed as the light sensitizer for the channel layer with excellent charge transport property. This structure combines materials with good optical and electrical properties and allows the structural optimisation of both charge transport and photo absorption simultaneously. Based on this device concept, several attempts have been reported to obtain high-performance phototransistors with significantly enhanced photoresponse through the incorporation with well-performing light absorbing materials such as colloidal quantum dots (CQDs)[50,77–80] and metal halide perovskites[81–87]. It is also worth noting that the hybrid structure is not limited to solely enhancing photo absorption. For example, Adinolfi reported a photojunction field-effect transistor (photoJFET) based on a CQDs-MoO_3 hybrid structure[88]. This photoJFET exhibits high gain while breaking the trade-off of dark current/photo response/operation speed. The latter is attributed to the presence of a rectifying junction between the conductive top contact (MoO_3) and the actual channel (CQDs), allowing the phototransistor to be fully depleted causing extremely low dark current. Moreover, the hybrid concept has also been exploited to combine with the existing CMOS technologies for advanced imaging systems[89,90].

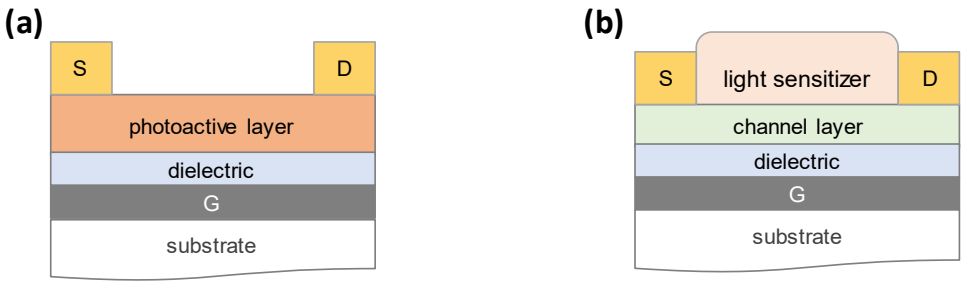


Figure 2.12: Schematic illustrations of two phototransistor structures. (**a**) Single layer structure. (**b**) Bilayer hybrid structure.

2.5.4 Characterisation of phototransistors

There are several figures of merit that can be used to evaluate the performance of photodetectors.

Photosensitivity (P) is defined as the ratio of photo-generated current to the dark current and is given as:

$$P = \frac{I_{ph}}{I_{dark}} = \frac{I_{illum} - I_{dark}}{I_{dark}} \tag{2.18}$$

where, I_{ph} is the photocurrent, I_{illum} is the channel current under illumination and I_{dark} is the drain current in the dark.

Responsivity (R) is defined as the ratio of photo-generated current to the incident optical power (P_{opt}). The magnitude of R can be calculated through the following equation:

$$R = \frac{I_{ph}}{P_{opt}} = \frac{I_{illum} - I_{dark}}{E_{opt} \cdot a} \tag{2.19}$$

where, a is the device area and E_{opt} is the optical power density (also termed as illumination intensity).

Photogain (G) defines the efficiency of optical power converted into measurable electrical current and can be calculated by the equation:

$$G = \frac{I_{ph}}{P_{opt}} \cdot \frac{hv}{q} \tag{2.20}$$

where hv is the photon energy, q is the elementary charge. In photodiodes an absorbed photon can generate at best one electron-hole pair, corresponding to the maximum obtainable gain of 1. In contrast, the Ohmic-like contact in phototransistors favours charge carriers to recirculate several times within the transistor channel, leading to photogain larger than unity. If the dominant gain mechanism in phototransistors can be explained by a trap-assisted model, the corresponding photoconductive gain (G_{pc}) can be expressed by[77]

$$G_{pc} = \frac{\tau}{t} \tag{2.21}$$

where τ is the photocarrier lifetime and t is the carrier transit time.

Specific detectivity (D^*) is another commonly adapted figure of merit to quantify the sensitivity of a photodetector with respect to noise and enable direct device comparison with different areas and geometries. The equation of D* is given as

$$D^* = \frac{\sqrt{a \cdot f_B}}{NEP} = \frac{\sqrt{a \cdot f_B} \cdot R}{S_{noise}} \tag{2.22}$$

where f_B is the bandwidth of the device and NEP is the noise equivalent power.

NEP is defined as the incident root mean square power required to produce a signal-to-noise ratio (SNR) of unity in a 1 Hz bandwidth, is a commonly used a figure of merit. It can be expressed as:

$$NEP = \frac{S_{noise}}{R} \tag{2.23}$$

where S_{noise} is noise spectral density and R is photoresponsivity.

The sources of electronic noise can be explained by many mechanisms such as thermal noise, dielectric noise or flicker noise[22]. Since all sources of noises are independent, their contributions to the total noise spectral are additive. However, a commonly-accepted assumption is that the shot noise from dark current is the dominant contribution[60]. Based on this assumption, the noise spectral density can be approximated as:

$$S_{noise} = \sqrt{2qI_{dark}} \tag{2.24}$$

where q is electron charge and I_{dark} is dark current. Under this circumstance, the expression of shot-noise limited detectivity D_s^* can be re-written as:

$$D_s^* = \frac{\sqrt{a} \cdot R}{\sqrt{2qI_{dark}}} \tag{2.25}$$

2.6 Integrated circuits

Integrated circuits are a major application of transistors in the microelectronic field. The elementary building block of most integrated circuits is the inverter, which is also referred to as NOT gate. This device can produce an output signal with the opposite logic level to an input signal.

At present there are two well-demonstrated technologies that enable the realisation of an inverter circuit, namely the unipolar and the complementary technology. The unipolar

inverter architecture consists of two transistors with the same channel polarity. This technology requires less complicated fabrication process but exhibits higher power consumption[91]. In contrast, the complementary inverter is constructed by a combination of n- and p-channel transistors. Inverters based on complementary technology have big advantages like a wide noise margin and low power dissipation, but the fabrication process is more complicated due to the fabrication of discrete n- and p-channel transistors within a scale of a few micrometres[92]. An alternative way to realise the complementary inverter is to replace the n- and p-channel transistor with two ambipolar transistors. The so-called complementary-like inverter can significantly simplify the fabrication process while retaining the major advantages of complementary technology. The schematic of the inverter based on all three technologies discussed above is shown in **Figure 2.13**.

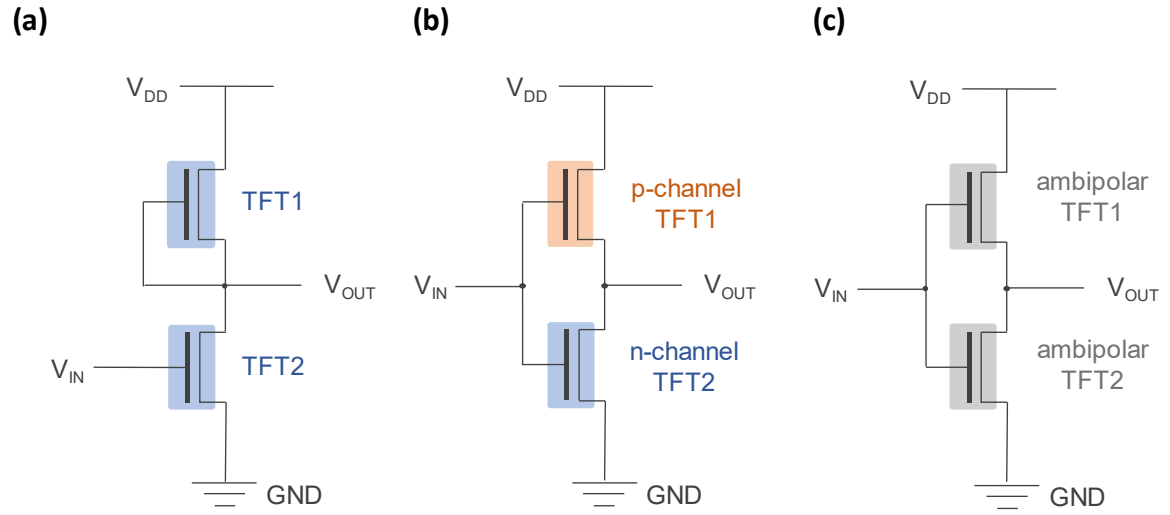


Figure 2.13: Schematic illustration of inverter circuit comprised of (**a**) two unipolar transistors with the same polarity, (**b**) two unipolar transistors with different polarities and (**c**) two ambipolar transistors.

Despite the difference in circuitry, the working principles of these inverters are similar. The two constituent transistors can be simply considered as two resistors connected in series, with the relative resistance difference which is determined by the input voltage V_{IN}. The output voltage V_{OUT}, which is the potential difference between TFT1 and TFT2, is changed according to the variation in V_{IN}. Taking the inverter in the first quadrant as an example (both the supply voltage V_{DD} and the input voltage V_{IN} are positive), when a low voltage is applied to V_{IN}, TFT2 is considered to be working in the depletion region with an extremely high resistance (Figure 2.14**a**). The supply voltage, therefore, drops mostly on TFT2 resulting in a high voltage in V_{OUT}.

Similarly, when the input voltage is set to be high, the resistance of TFT2 is relatively low and the supply voltage hence drops mostly on the TFT1, resulting in a low output signal V_{OUT} (Figure 2.14**b**).

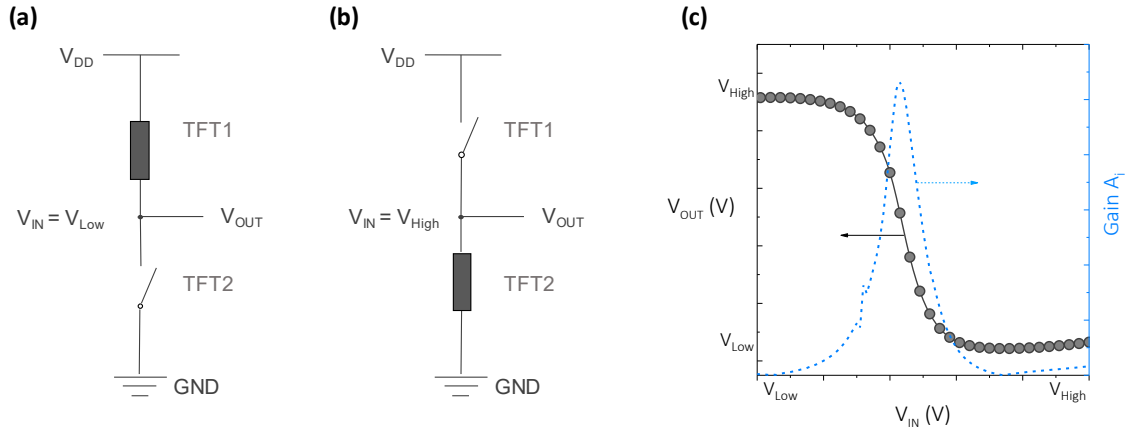


Figure 2.14: Schematic illustration of inverter operation using a voltage divider model. The open switch represents a high resistance and the resistor symbols represents a low resistance. (**a**) Inverter with a low V_{IN}. (**b**) Inverter with a high V_{IN}. (**c**) Representative transfer characteristics of an inverter working in the first quadrant.

The most important figure of merit for an inverter is the small signal gain A_i, which is also known as voltage amplification. It is defined as the slope of the inverter transfer characteristic (i.e. the plot of V_{OUT} versus V_{IN}). The maximum signal gain value $A_{i,max}$ is usually obtained at the point with the sharpest V_{OUT} voltage swing (Figure 2.14**c**). The high gain at this specific point means that a small change in V_{IN} can result in a large variation in V_{OUT} during a switching transient. From the viewpoint of microelectronic circuit, $A_{i,max}$ is usually obtained when the two constituent transistors are simultaneously working in the saturation regions[93]. In a practical integrated circuit, the output of an inverter is usually served as an input for a subsequent inverter. To enable the integrated circuit to function properly, the small signal gain is required to be larger than unity.

Bibliography

(1) Ouellette, R. J.; Rawn, D. *Organic Chemistry: Structure, Mechanism, and Synthesis*; 2014.

(2) Köhler, A.; Bässler, H. *Electronic Processes in Organic Semiconductors*; Wiley-VCH Verlag GmbH & Co. KGaA: Weinheim, Germany, 2015.

(3) Peierls, R. *Quantum Theory of Solids*; Oxford University Press, 1996.

(4) Bässler, H. Charge Transport in Disordered Organic Photoconductors a Monte Carlo Simulation Study. *Phys. status solidi* **1993**, *175* (1), 15–56.

(5) Wade, J.; Hollis, J. R.; Wood, S. *Printed Electronics*; IOP Publishing, 2018; Vol. 1.

(6) Mahan, G. D. Van Der Waals Forces in Solids. *J. Chem. Phys.* **1965**, *43* (5), 1569–1574.

(7) Kamiya, T.; Nomura, K.; Hosono, H. Origins of High Mobility and Low Operation Voltage of Amorphous Oxide TFTs: Electronic Structure, Electron Transport, Defects and Doping*. *J. Disp. Technol.* **2009**, *5* (12), 468–483.

(8) Facchetti, A.; Marks, T. J. *Transparent Electronics*; Facchetti, A., Marks, T. J., Eds.; John Wiley & Sons, Ltd: Chichester, UK, 2010.

(9) Fortunato, E.; Barquinha, P.; Martins, R. Oxide Semiconductor Thin-Film Transistors: A Review of Recent Advances. *Adv. Mater.* **2012**, *24* (22), 2945–2986.

(10) Thomas, S. R.; Pattanasattayavong, P.; Anthopoulos, T. D. Solution-Processable Metal Oxide Semiconductors for Thin-Film Transistor Applications. *Chem. Soc. Rev.* **2013**, *42* (16), 6910.

(11) Hosono, H. Ionic Amorphous Oxide Semiconductors: Material Design, Carrier Transport, and Device Application. *J. Non. Cryst. Solids* **2006**, *352* (9-20 SPEC. ISS.), 851–858.

(12) Nomura, K.; Kamiya, T.; Ohta, H.; Uruga, T.; Hirano, M.; Hosono, H. Local Coordination Structure and Electronic Structure of the Large Electron Mobility Amorphous Oxide Semiconductor In-Ga-Zn-O: Experiment and Ab Initio Calculations. *Phys. Rev. B - Condens. Matter Mater. Phys.* **2007**, *75* (3), 2–6.

(13) Nomura, K.; Ohta, H.; Takagi, A.; Kamiya, T.; Hirano, M.; Hosono, H. Room-Temperature Fabrication of Transparent Flexible Thin-Film Transistors Using Amorphous Oxide Semiconductors. *Nature* **2004**, *432* (7016), 488–492.

(14) Orita, M.; Ohta, H.; Hirano, M.; Narushima, S.; Hosono, H. Amorphous Transparent Conductive Oxide InGaO3(ZnO)m (m ≤ 4): A Zn 4s Conductor. *Philos. Mag. B Phys. Condens. Matter; Stat. Mech. Electron. Opt. Magn. Prop.* **2001**, *81* (5), 501–515.

(15) De Wit, J. H. W.; Van Unen, G.; Lahey, M. Electron Concentration and Mobility in In2O3. *J. Phys. Chem. Solids* **1977**, *38* (8), 819–824.

(16) Giles, N. C.; Bai, L.; Xu, C.; Boatner, L. A.; Garces, N. Y.; Luo, M.; Halliburton, L. E. Production of Native Donors in ZnO by Annealing at High Temperature in Zn Vapor. *Appl. Phys. Lett.* **2005**, *87* (17), 172108.

(17) Lany, S.; Zunger, A. Dopability, Intrinsic Conductivity, and Nonstoichiometry of Transparent Conducting Oxides. *Phys. Rev. Lett.* **2007**, *98* (4), 2–5.

(18) Look, D. C.; Hemsky, J. W.; Sizelove, J. R. Residual Native Shallow Donor in ZnO. *Phys. Rev. Lett.* **1999**, *82* (12), 2552–2555.

(19) Vlasenko, L. S.; Watkins, G. D. Optical Detection of Electron Paramagnetic Resonance for Intrinsic Defects Produced in ZnO by 2.5-MeV Electron Irradiation in Situ at 4.2 K. *Phys. Rev. B - Condens. Matter Mater. Phys.* **2005**, *72* (3), 1–12.

(20) Zhang, S. B.; Wei, S. H.; Zunger, A. Intrinsic N-Type versus p-Type Doping Asymmetry and the Defect Physics of ZnO. *Phys. Rev. B - Condens. Matter Mater. Phys.* **2001**, *63* (7), 1–7.

(21) Lany, S.; Zunger, A. Anion Vacancies as a Source of Persistent Photoconductivity in II-VI and Chalcopyrite Semiconductors. *Phys. Rev. B - Condens. Matter Mater. Phys.* **2005**, *72* (3), 1–13.

(22) Sze, S. M.; Ng, K. K. *Physics of Semiconductor Devices, 3rd Edition*; 2006.

(23) Anderson, P., W. Absence of Diffusion in Certain Random Lattices. *Phys. Rev.* **1958**, *109* (5), 1492–1506.

(24) Salleo, A. Electronic Traps in Organic Semiconductors. In *Organic Electronics*; Wiley-VCH Verlag GmbH & Co. KGaA: Weinheim, Germany, 2013; pp 341–380.

(25) Troisi, A. Charge Transport in High Mobility Molecular Semiconductors: Classical Models and New Theories. *Chem. Soc. Rev.* **2011**, *40* (5), 2347–2358.

(26) Ashcroft, N. W.; Mermin, D. *Solid State Physics*; Holt, Rinehart and Winston: New York, 1976.

(27) Waragai, K.; Akimichi, H.; Hotta, S.; Kano, H.; Sakaki, H. Charge Transport in Thin Films of Semiconducting Oligothiophenes. *Phys. Rev. B* **1995**, *52* (3), 1786–1792.

(28) Mott, N. F. Conduction in Non-Crystalline Materials. *Philos. Mag.* **1969**, *19* (160), 835–852.

(29) Monroe, D. Hopping in Exponential. *Phys. Rev. Lett.* **1985**, *54* (2), 146–149.

(30) Gr̈newald, M.; Movaghar, B.; Pohlmann, B.; Ẅrtz, D. Hopping Theory of Band-Tail Relaxation in Disordered Semiconductors. *Phys. Rev. B* **1985**, *32* (12), 8191–8196.

(31) Shur, M.; Hack, M.; Shaw, J. G. A New Analytic Model for Amorphous Silicon Thin-Film Transistors. *J. Appl. Phys.* **1989**, *66* (7), 3371–3380.

(32) Le Comber, P. G.; Spear, W. E. Electronic Transport in Amorphous Silicon Films. *Phys. Rev. Lett.* **1970**, *25* (8), 509–511.

(33) Vissenberg, M. C. J. M.; Matters, M. Theory of the Field-Effect Mobility in Amorphous Organic Transistors. *Phys. Rev. B* **1998**, *57* (20), 13.

(34) Paul K. Weimer. The TFT - A New Thin-Film Transistor. *Proc. IRE* **1962**, *50* (6), 1462–1469.

(35) Richards, T. J.; Sirringhaus, H. Analysis of the Contact Resistance in Staggered, Top-Gate Organic Field-Effect Transistors. *J. Appl. Phys.* **2007**, *102* (9), 094510.

(36) Brotherton, S. D. *Introduction to Thin Film Transistors: Physics and Technology of TFTs*; Springer Science & Business Media, 2013.

(37) Smits, E.; Anthopoulos, T.; Setayesh, S.; van Veenendaal, E.; Coehoorn, R.; Blom, P.; de Boer, B.; de Leeuw, D. Ambipolar Charge Transport in Organic Field-Effect Transistors. *Phys. Rev. B* **2006**, *73* (20), 205316.

(38) Zaumseil, J.; Sirringhaus, H. Electron and Ambipolar Transport in Organic Field-Effect Transistors. *Chem. Rev.* **2007**, *107*, 1296–1323.

(39) Zaumseil, J.; Friend, R. H.; Sirringhaus, H. Spatial Control of the Recombination Zone in an Ambipolar Light-Emitting Organic Transistor. *Nat. Mater.* **2006**, *5* (1), 69–74.

(40) Bird, M.; McKiernan, M. J.; Roberts, M.; McNeill, C. R.; Sirringhaus, H.; Zaumseil, J.; Friend, R. H.; Paul Ruden, P.; Smith, D. L. Quantum Efficiency of Ambipolar Light-Emitting Polymer Field-Effect Transistors. *J. Appl. Phys.* **2008**, *103* (6), 064517.

(41) Schmechel, R.; Ahles, M.; Von Seggern, H. A Pentacene Ambipolar Transistor: Experiment and Theory. *J. Appl. Phys.* **2005**, *98* (8).

(42) Meijer, E. J.; de Leeuw, D. M.; Setayesh, S.; van Veenendaal, E.; Huisman, B. H.; Blom, P. W. M.; Hummelen, J. C.; Scherf, U.; Kadam, J.; Klapwijk, T. M. Solution-Processed Ambipolar Organic Field-Effect Transistors and Inverters. *Nat. Mater.* **2003**, *2* (10), 678–682.

(43) Tada, K.; Harada, H.; Yoshino, K. Polymeric Bipolar Thin-Film Transistor Utilizing Conducting Polymer Containing Electron Transport Dye. *Japanese J. Appl. Physics, Part 2 Lett.* **1996**, *35* (7 SUPPL. B).

(44) Muccini, M.; Murgia, M.; Riess, W.; Karg, S.; Loi, M. A.; Rost, C. Light-Emitting Ambipolar Organic Heterostructure Field-Effect Transistor. *Synth. Met.* **2004**, *146* (3), 237–241.

(45) Anthopoulos, T. D. Electro-Optical Circuits Based on Light-Sensing Ambipolar Organic Field-Effect Transistors. *Appl. Phys. Lett.* **2007**, *91* (11), 113513.

(46) Anthopoulos, T. D.; Tanase, C.; Setayesh, S.; Meijer, E. J.; Hummelen, J. C.; Blom, P. W. M.; De Leeuw, D. M. Ambipolar Organic Field-Effect Transistors Based on a Solution-Processed Methanofullerene. *Adv. Mater.* **2004**, *16* (23–24), 2174–2179.

(47) Sirringhaus, H.; Brown, P. J.; Friend, R. H.; Nielsen, M. M.; Bechgaard, K.; Langeveld-Voss, B. M. W.; Spiering, A. J. H.; Janssen, R. A. J.; Meijer, E. W.; Herwig, P.; De Leeuw, D. M. Two-Dimensional Charge Transport in Self-Organized, High-Mobility Conjugated Polymers. *Nature* **1999**.

(48) Dodabalapur, a; Katz, H. E.; Torsi, L.; Haddon, R. C. Organic Heterostructure Field-Effect Transistors. *Science* **1995**, *269* (5230), 1560–1562.

(49) Betser, Y.; Ritter, D.; Liu, C. P.; Seeds, A. J.; Madjar, A. A Single-Stage Three-Terminal Heterojunction Bipolar Transistor Optoelectronic Mixer. *J. Light. Technol.* **1998**, *16* (4), 605–609.

(50) Konstantatos, G.; Badioli, M.; Gaudreau, L.; Osmond, J.; Bernechea, M.; de Arquer, P. G.; Gatti, F.; Koppens, F. H. L. Hybrid Graphene-Quantum Dot Phototransistors with Ultrahigh Gain. *Nat. Nanotechnol.* **2011**, *7* (6), 363–368.

(51) Lee, Y.; Kwon, J.; Hwang, E.; Ra, C. H.; Yoo, W. J.; Ahn, J. H.; Park, J. H.; Cho, J. H. High-Performance Perovskite-Graphene Hybrid Photodetector. *Adv. Mater.* **2015**, *27* (1), 41–46.

(52) Wang, Y.; Zhang, Y.; Lu, Y.; Xu, W.; Mu, H.; Chen, C.; Qiao, H.; Song, J.; Li, S.; Sun, B.; Cheng, Y. B.; Bao, Q. Hybrid Graphene-Perovskite Phototransistors with Ultrahigh Responsivity and Gain. *Adv. Opt. Mater.* **2015**, *3* (10), 1389–1396.

(53) Spina, M.; Lehmann, M.; Náfrádi, B.; Bernard, L.; Bonvin, E.; Gaál, R.; Magrez, A.; Forrõ, L.; Horváth, E. Microengineered CH3NH3PbI3 Nanowire/Graphene Phototransistor for Low-Intensity Light Detection at Room Temperature. *Small* **2015**, *11* (37), 4824–4828.

(54) Cho, N.; Li, F.; Turedi, B.; Sinatra, L.; Sarmah, S. P.; Parida, M. R.; Saidaminov, M. I.; Murali, B.; Burlakov, V. M.; Goriely, A.; Mohammed, O. F.; Wu, T.; Bakr, O. M. Pure Crystal Orientation and Anisotropic Charge Transport in Large-Area Hybrid Perovskite Films. *Nat. Commun.* **2016**, *7* (May), 1–11.

(55) Dang, V. Q.; Han, G. S.; Trung, T. Q.; Duy, L. T.; Jin, Y. U.; Hwang, B. U.; Jung, H. S.; Lee, N. E. Methylammonium Lead Iodide Perovskite-Graphene Hybrid Channels in Flexible Broadband Phototransistors. *Carbon N. Y.* **2016**, *105*, 353–361.

(56) Sun, Z.; Aigouy, L.; Chen, Z. Plasmonic-Enhanced Perovskite-Graphene Hybrid Photodetectors. *Nanoscale* **2016**, *8* (14), 7377–7383.

(57) Kwak, D.-H.; Lim, D.-H.; Ra, H.-S.; Ramasamy, P.; Lee, J.-S. High Performance Hybrid Graphene–CsPbBr $_{3-x}$ I $_x$ Perovskite Nanocrystal Photodetector. *RSC Adv.* **2016**, *6* (69), 65252–65256.

(58) Shao, Y.; Liu, Y.; Chen, X.; Chen, C.; Sarpkaya, I.; Chen, Z.; Fang, Y.; Kong, J.; Watanabe, K.; Taniguchi, T.; Taylor, A.; Huang, J.; Xia, F. Stable Graphene-Two-Dimensional Multiphase Perovskite Heterostructure Phototransistors with High Gain. *Nano Lett.* **2017**, *17* (12), 7330–7338.

(59) Gao, J.; Hegmann, F. A. Bulk Photoconductive Gain in Pentacene Thin Films. *Appl. Phys. Lett.* **2008**, *93* (22), 1–4.

(60) Gong, X.; Tong, M.; Xia, Y.; Cai, W.; Moon, J. S.; Cao, Y.; Yu, G.; Shieh, C.; Nilsson, B.; Heeger, A. J. High-Detectivity Polymer Photodetector with Spectral Response from 300 Nm to 1450 Nm. *Science (80-.).* **2009**, *325* (5948), 1665–1667.

(61) Kufer, D.; Konstantatos, G. Photo-FETs: Phototransistors Enabled by 2D and 0D Nanomaterials. *ACS Photonics* **2016**, *3* (12), 2197–2210.

(62) Hamilton, M. C.; Martin, S.; Kanicki, J. Thin-Film Organic Polymer Phototransistors. *IEEE Trans. Electron Devices* **2004**, *51* (6), 877–885.

(63) Tang, Q.; Li, L.; Song, Y.; Liu, Y.; Li, H.; Xu, W.; Liu, Y.; Hu, W.; Zhu, D. Photoswitches and Phototransistors from Organic Single-Crystalline Sub-Micro/Nanometer Ribbons. *Adv. Mater.* **2007**, *19* (18), 2624–2628.

(64) Jung, J. H.; Yoon, M. J.; Lim, J. W.; Lee, Y. H.; Lee, K. E.; Kim, D. H.; Oh, J. H. High-Performance UV-Vis-NIR Phototransistors Based on Single-Crystalline Organic Semiconductor-Gold Hybrid Nanomaterials. *Adv. Funct. Mater.* **2017**, *27* (6), 1604528.

(65) Zhang, W.; Huang, J. K.; Chen, C. H.; Chang, Y. H.; Cheng, Y. J.; Li, L. J. High-Gain Phototransistors Based on a CVD MoS2 Monolayer. *Adv. Mater.* **2013**, *25* (25), 3456–3461.

(66) Yin, Z.; Li, H.; Li, H.; Jiang, L.; Shi, Y.; Sun, Y.; Lu, G.; Zhang, Q.; Chen, X.; Zhang, H. Single-Layer MoS 2 Phototransistors. *ACS Nano* **2012**, *6* (1), 74–80.

(67) Kwon, J.; Hong, Y. K.; Han, G.; Omkaram, I.; Choi, W.; Kim, S.; Yoon, Y. Giant Photoamplification in Indirect-Bandgap Multilayer MoS2 Phototransistors with Local Bottom-Gate Structures. *Adv. Mater.* **2015**, *27* (13), 2224–2230.

(68) Lee, H. S.; Min, S. W.; Chang, Y. G.; Park, M. K.; Nam, T.; Kim, H.; Kim, J. H.; Ryu, S.; Im, S. MoS 2 Nanosheet Phototransistors with Thickness-Modulated Optical Energy

Gap. *Nano Lett.* **2012**, *12* (7), 3695–3700.

(69) Abderrahmane, A.; Ko, P. J.; Thu, T. V.; Ishizawa, S.; Takamura, T.; Sandhu, A. High Photosensitivity Few-Layered MoSe2 Back-Gated Field-Effect Phototransistors. *Nanotechnology* **2014**, *25* (36).

(70) Geohegan, D. B.; Wen, Z.; Wang, X.; Xiao, K.; Hu, P.; Yoon, M.; Feng, W.; Idrobo, J. C.; Wang, L.; Zhang, J.; Miyamoto, Y. Highly Responsive Ultrathin GaS Nanosheet Photodetectors on Rigid and Flexible Substrates. *Nano Lett.* **2013**, *13* (4), 1649–1654.

(71) Hu, P.; Wen, Z.; Wang, L.; Tan, P.; Xiao, K. Synthesis of Few-Layer GaSe Nanosheets for High Performance Photodetectors. *ACS Nano* **2012**, *6* (7), 5988–5994.

(72) Blakesley, J. C.; Castro, F. A.; Kylberg, W.; Dibb, G. F. A.; Arantes, C.; Valaski, R.; Cremona, M.; Kim, J. S.; Kim, J. S. Towards Reliable Charge-Mobility Benchmark Measurements for Organic Semiconductors. *Org. Electron. physics, Mater. Appl.* **2014**, *15* (6), 1263–1272.

(73) Shaygan, M.; Davami, K.; Kheirabi, N.; Baek, C. K.; Cuniberti, G.; Meyyappan, M.; Lee, J.-S. Single-Crystalline CdTe Nanowire Field Effect Transistors as Nanowire-Based Photodetector. *Phys. Chem. Chem. Phys.* **2014**, *16* (41), 22687–22693.

(74) Buscema, M.; Groenendijk, D. J.; Blanter, S. I.; Steele, G. A.; Van Der Zant, H. S. J.; Castellanos-Gomez, A. Fast and Broadband Photoresponse of Few-Layer Black Phosphorus Field-Effect Transistors. *Nano Lett.* **2014**, *14* (6), 3347–3352.

(75) Youngblood, N.; Chen, C.; Koester, S. J.; Li, M. Waveguide-Integrated Black Phosphorus Photodetector with High Responsivity and Low Dark Current. *Nat. Photonics* **2015**, *9* (4), 247–252.

(76) Wu, J.; Koon, G. K. W.; Xiang, D.; Han, C.; Toh, C. T.; Kulkarni, E. S.; Verzhbitskiy, I.; Carvalho, A.; Rodin, A. S.; Koenig, S. P.; Eda, G.; Chen, W.; Neto, A. H. C.; Özyilmaz, B. Colossal Ultraviolet Photoresponsivity of Few-Layer Black Phosphorus. *ACS Nano* **2015**, *9* (8), 8070–8077.

(77) Adinolfi, V.; Sargent, E. H. Photovoltage Field-Effect Transistors. *Nature* **2017**, *542* (7641), 324–327.

(78) Kufer, D.; Lasanta, T.; Bernechea, M.; Koppens, F. H. L.; Konstantatos, G. Interface Engineering in Hybrid Quantum Dot-2D Phototransistors. *ACS Photonics* **2016**, *3* (7), 1324–1330.

(79) Kufer, D.; Nikitskiy, I.; Lasanta, T.; Navickaite, G.; Koppens, F. H. L.; Konstantatos, G. Hybrid 2D-0D MoS 2 -PbS Quantum Dot Photodetectors. *Adv. Mater.* **2015**, *27* (1), 176–180.

(80) Hwang, D. K.; Lee, Y. T.; Lee, H. S.; Lee, Y. J.; Shokouh, S. H.; Kyhm, J.; Lee, J.; Kim, H. H.; Yoo, T.-H.; Nam, S. H.; Son, D. I.; Ju, B.-K.; Park, M.-C.; Song, J. D.; Choi, W. K.; Im, S. Ultrasensitive PbS Quantum-Dot-Sensitized InGaZnO Hybrid Photoinverter for near-Infrared Detection and Imaging with High Photogain. *NPG Asia Mater.* **2016**, *8* (1), e233–e233.

(81) Kang, D. H.; Pae, S. R.; Shim, J.; Yoo, G.; Jeon, J.; Leem, J. W.; Yu, J. S.; Lee, S.; Shin, B.; Park, J. H. An Ultrahigh-Performance Photodetector Based on a Perovskite–Transition-Metal-Dichalcogenide Hybrid Structure(SI). *Adv. Mater.* **2016**, *28* (35), 7799–7806.

(82) Park, Y.; Lee, S.; Park, H. J.; Baac, H. W.; Yoo, G.; Heo, J. Hybrid Metal-Halide Perovskite-MoS2 Phototransistor. *J. Nanosci. Nanotechnol.* **2016**, *16* (11), 11722–11726.

(83) Liu, F.; Wang, J.; Wang, L.; Cai, X.; Jiang, C.; Wang, G. Enhancement of Photodetection Based on Perovskite/MoS $_2$ Hybrid Thin Film Transistor. *J. Semicond.* **2017**, *38* (3), 034002.

(84) Huo, C.; Liu, X.; Wang, Z.; Song, X.; Zeng, H. High-Performance Low-Voltage-Driven Phototransistors through CsPbBr $_3$ -2D Crystal van Der Waals Heterojunctions. *Adv. Opt. Mater.* **2018**, *1800152*, 1800152.

(85) Xie, C.; You, P.; Liu, Z.; Li, L.; Yan, F. Ultrasensitive Broadband Phototransistors Based on Perovskite/Organic-Semiconductor Vertical Heterojunctions. *Light Sci. Appl.* **2017**, *6* (8), e17023.

(86) Chen, Y.; Chu, Y.; Wu, X.; Ou-Yang, W.; Huang, J. High-Performance Inorganic Perovskite Quantum Dot–Organic Semiconductor Hybrid Phototransistors. *Adv. Mater.* **2017**, *29* (44), 1–8.

(87) Zou, C.; Xi, Y.; Huang, C. Y.; Keeler, E. G.; Feng, T.; Zhu, S.; Pozzo, L. D.; Lin, L. Y. A Highly Sensitive UV–Vis–NIR All-Inorganic Perovskite Quantum Dot Phototransistor Based on a Layered Heterojunction. *Adv. Opt. Mater.* **2018**, *6* (14), 1–9.

(88) Adinolfi, V.; Kramer, I. J.; Labelle, A. J.; Sutherland, B. R.; Hoogland, S.; Sargent, E. H. Photojunction Field-Effect Transistor Based on a Colloidal Quantum Dot Absorber Channel Layer. *ACS Nano* **2015**, *9* (1), 356–362.

(89) Goossens, S.; Navickaite, G.; Monasterio, C.; Gupta, S.; Piqueras, J. J.; Pérez, R.; Burwell, G.; Nikitskiy, I.; Lasanta, T.; Galán, T.; Puma, E.; Centeno, A.; Pesquera, A.; Zurutuza, A.; Konstantatos, G.; Koppens, F. Broadband Image Sensor Array Based on Graphene–CMOS Integration. *Nat. Photonics* **2017**, *11* (6), 366–371.

(90) Mohammed, O. F.; Huang, B.; Liang, L.; Han, S.; Wu, J.; Bakr, O. M.; Huang, W.; Guan, X.; Chen, Q.; Yang, H.; Wang, Y.; Teh, D. B. L.; Yi, Z.; Xie, X.; Zhumekenov, A. A.; Bettinelli, M.; Fan, D.; Wu, T.; Ou, X.; Almutlaq, J.; All, A. H.; Liu, X.; Li, J.; Li, Y. All-Inorganic Perovskite Nanocrystal Scintillators. *Nature* **2018**, *561* (7721), 88–93.

(91) Gelinck, G. H.; Huitema, H. E. a; van Veenendaal, E.; Cantatore, E.; Schrijnemakers, L.; van der Putten, J. B. P. H.; Geuns, T. C. T.; Beenhakkers, M.; Giesbers, J. B.; Huisman, B.-H.; Meijer, E. J.; Benito, E. M.; Touwslager, F. J.; Marsman, A. W.; van Rens, B. J. E.; de Leeuw, D. M. Flexible Active-Matrix Displays and Shift Registers Based on Solution-Processed Organic Transistors. *Nat. Mater.* **2004**, *3* (2), 106–110.

(92) Dodabalapur, A.; Laquindanum, J.; Katz, H. E.; Bao, Z. Complementary Circuits with Organic Transistors. *Appl. Phys. Lett.* **1996**, *69* (27), 4227–4229.

(93) Adel S. Sedra; Kenneth C. Smith. *Microelectronic Circuits*; 2007.

Chapter 3 Experimental Methods

This chapter summarises the experimental methods and materials that were used to obtain the results summarized in the experimental Chapters 4-6. It starts with a discussion on the deposition techniques used for the device fabrication. There then follows a description on several material characterisation techniques such as atomic force microscopy, UV-Vis-NIR spectroscopy and scanning Kelvin probe, which are used for studying film morphology, optical absorption and surface potential, respectively. Finally, the electrical characterisation setup used for the transistor and phototransistor analysis, are introduced.

3.1 Device Fabrication Techniques

3.1.1 Substrate Preparation

In this study the devices were fabricated on two substrates, i.e. silicon wafers and glass slides. Silicon wafers, supplied by Active Business Company GmbH, were highly n-doped silicon (arsenic, resistivity <0.005 Ω ·cm) with a thermally-grown silicon dioxide layer (thickness =100 nm) on top. Glass substrates, supplied by Schott Borofloat®, were highly-transparent, chemically-durable and thermally-resistive borosilicate glass sheets.

The cleaning procedures for both substrates were the same. The substrates were cleaned by ultra-sonication in a sequence of solvents to remove surface contaminants. The sequence is as follow: de-ionised (DI) water with 3% v/v Decon 90 detergent, pure DI water, acetone and isopropanol (IPA). Each step last for 10 min and the residual solvent was dried by nitrogen flow. The cleaning procedure was completed by placing the substrates into an ultraviolet (UV) ozone cleaner (UVOCS® model T0606E) for 20 min to remove residual hydrocarbons from the substrate surface as well as to improve surface energy for better thin film formation.

3.1.2 Solution Deposition of Organic/Inorganic Materials

Within this thesis, all the soluble organic/inorganic materials were deposited using a conventional spin-coating technique, in which a fixed amount of solution is poured onto a spinning substrate surface to form a thin film. The required volume of solution depends on factors like solution viscosity and substrate surface energy. The cast solution spreads over the substrate surface due to centrifugal force in the early stage of the spinning process and excess solution is spun off. With the ongoing spinning process, the solvent starts evaporating and a solid thin film is eventually formed. The obtained film is then transferred to a hot plate to heat up for further evaporating excess solvent. The final thickness of the film is determined by a number of factors, such as the solution concentration, the spin speed and duration, solvent boiling point, ambient conditions etc. Therefore, spin-coating parameters always need to be optimised for different materials in order to obtain a smooth and uniform film with a desired thickness. The optimised deposition parameters for each material used in the thesis will be described in detail in the corresponding chapters.

3.1.3 Vacuum Deposition of Metal Contact

Metal contacts for transistors were deposited via thermal evaporation under high vacuum. The deposition process was carried out using a Kurt J. Lesker Mini SPECTROS^{TM} Deposition System. The system includes a chamber which is pumped down to the desired vacuum level by a turbo pump. Samples with shadow masks are loaded into a substrate holder at the top of the chamber while metals for evaporation are loaded into a source crucible at the bottom of the chamber connected to a heating element. The chamber is first pumped down to a relatively high vacuum (~5 x10^{-6} mbar) before the metal deposition. The source crucible is then heated up by applying an increasing current through it. The evaporation rate of the metal vapour is monitored by a crystal sensor mounted inside the chamber and controlled by a feedback routine of the system. The deposition rate of two metals used within this thesis, i.e. aluminium and gold, are typically specified at a rate of 0.05 nm/sec and 0.1 nm/sec, respectively. The deposition patterns are confined by the dedicated shadow masks placed in front of the sample substrates. The masks for source and drain electrodes outline a variety of transistor channel geometries, resulting in transistors with channel lengths and channel widths of 20-100 μm and 200-1500 μm, respectively.

3.1.4 Application of Self-Assembled Monolayers

Self-assembled monolayers (SAMs) are molecular assemblies that spontaneously-form on a surface via adsorption. SAMs have been widely employed in organic/inorganic electronics for various purposes including adjusting the work function of electrode, modifying surface energy, passivating surface and working as semiconducting materials[1–4]. Within this thesis, two types of SAMs were used for different purposes. Despite the difference in purpose, the applications of both SAMs were similarly via a dip-coating method. The substrates, prior to the deposition of SAMs, were exposed to UV Ozone treatment to remove impurities. The cleaned substrates were then submerged in a SAM solution for a specific time. The process was completed by rinsing the substrates with the same solvent as that of the solution to wash off the excess of SAMs. Detail information of each SAM application will be described individually in the experimental section of the corresponding chapters.

3.2 Material Characterisation

3.2.1 Atomic Force Microscopy

Atomic force microscopy (AFM) is a technique for studying surface topography of thin film samples. By using AFM 3-dimensional information of the measured surface can be obtained with a resolution up to the scale of an atomic lattice. In the present study, all the AFM measurement were carried out using an Agilent 5500 atomic force microscope in the ambient atmosphere.

The basic principle of AFM is to acquire topographic profiles of the measured samples by probing through the surface with an atomically sharp tip. A schematic illustration of an AFM system is shown in **Figure 3.1**. A sharp tip is attached to a free end of a cantilever. When the tip is close enough to the sample surface, the interaction between the probe tip and the sample surface causes the bending of the cantilever. This small displacement of the cantilever results in a change of deflection of a laser beam directed on the same end of the cantilever and is eventually recorded by a quadrant photodiode as a signal in volts.

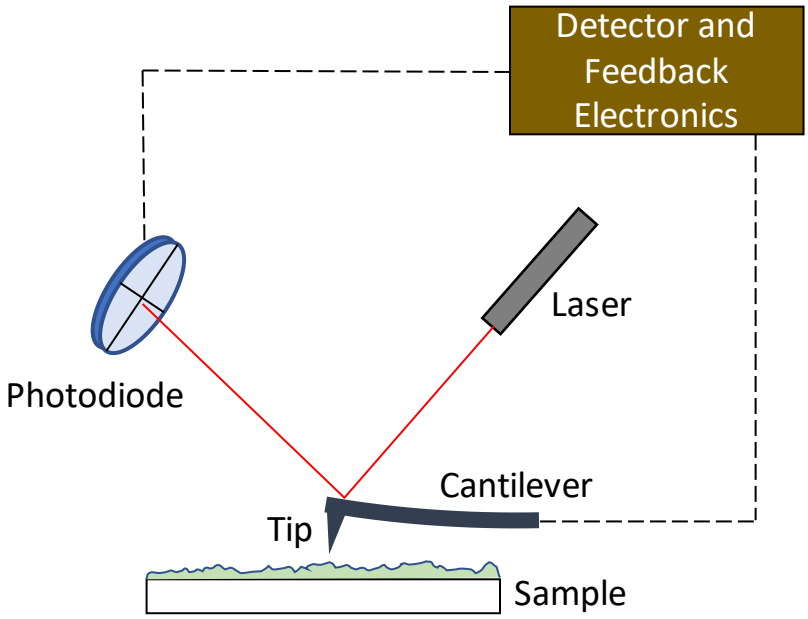


Figure 3.1: Schematic illustration of an AFM system.

In general, the AFM operation can be classified as several modes depending on the different operation regime. The mode used in this work is intermittent contact mode, which is also referred as tapping mode or AC mode. In this mode, the cantilever is driven to oscillate at its resonance frequency during the scan. This vibrating amplitude and phase will be changed by the tip-sample interaction when the tip is brought to the vicinity of the sample surface. To compensate the change a feedback system utilising a piezoelectric actuator is used to maintain

the cantilever at the set position. The adjustment can be used to evaluate the height of the corresponding sampling point. By scanning through all the sampling point, the topography of the sample surface can then be reconstructed. The advantage of tapping mode is the oscillation of cantilever in the vertical direction minimise the force in the lateral direction and hence reduce the likelihood of damage to both the sample and tip.

3.2.2 Ultraviolet-Visible-Near-infrared Spectroscopy

The ultraviolet-visible-near-infrared (UV-Vis-NIR) spectroscopy is a technique for studying the optical properties of the thin film such as transmittance, reflectance or absorbance. In addition, this technique can also be used for estimating the optical energy bandgaps of materials by Tauc plot analysis. Within this work, all measurements were performed by a Shimadzu UV-2600 spectrophotometer mounted with an ISR-2600 Plus integrating sphere. The basic principle of the UV-Vis measurement is using various monochromatic lights to illuminate the sample and comparing the intensity difference between the light transmitted (or reflected) from the object and the reference light. Samples are all deposited on quartz substrates due to its high transparency within the measuring spectrum (300-800 nm).

3.2.3 Scanning Kelvin Probe

Kelvin Probe (KP) is a technique for detecting the work function of conducting materials or surface potential of semiconducting materials in a non-contact non-destructive way. The Kelvin Probe system used in this work was a KP Technology Scanning Kelvin Probe System SKP5050.

The working principle of the Kelvin Probe is to evaluate the potentials difference between a material surface and a probe tip by detecting the electrical charges generated by capacitor effect. The capacitor is formed by the vibrating tip placed at a certain distance away from the sample and the conductive sample surface. When electrical contact is made, the equalisation of Fermi levels results in the generation of electrical charges on both surfaces of the vibrating capacitor. As the measured results are typically defined by the topmost layers of the measured surfaces, the obtained work function is extremely sensitive to surface conditions as well as atmospheric conditions such as temperature and humidity. In order minimise the environmental impacts all measurements presented in this work were performed in a dry nitrogen atmosphere and directly after sample preparation.

3.3 Electrical Characterisation

3.3.1 Current-Voltage Measurements

The performance of transistors is primarily assessed through the current-voltage measurement of the devices. Two types of current-voltage measurement are typically performed for TFT devices, i.e. transfer characterisation and output characterisation. For transfer characterisation the voltage applied to the drain electrode is held constant while the voltage applied to the gate electrode is swept across a range of values. For output characterisation the gate voltage is held constant while a sweep is performed on the drain voltage and repeated for multiple pre-set gate voltages. From these current-voltage characterisation key parameters for transistor analysis such as field effect mobility, subthreshold swing and current on/off ratio can be obtained. Within this work all the current-voltage measurements were performed using an Agilent B2902A Precision Source/Measure Unit (SMU) in combination with a probe station. The SMU is connected to the transistor electrodes via a set of micro-positioning needles in a probe station and BNC cables. When pre-set voltages are applied across the transistor electrodes, the corresponding current flow for each voltage is then recorded by the SMU and saved into a spreadsheet. For inverter characterisation, the two constituent transistors are connected via micro-positioning needles and interconnect cable to form the inverter circuit. A Keithley 4200-SCS Semiconductor Characterisation System (SCS) was used for this measurement and connected to the two transistors in a similar way as for the SMU. The SCS enables simultaneous data acquisition on the two constituent transistors. All the current-voltage characterisations presented in this thesis were performed under an inert gas atmosphere at room temperature in the dark. This is to avoid environmental impacts on the charge carrier transport within the transistor channel.

3.3.2 Light-Response Measurements

The light-response measurements presented in this thesis include two types of measurements, i.e. static measurement and dynamic measurement. The former records the static transistor current-voltage characteristics when the device is exposed to continuous illumination with various intensities while the latter while the latter records the dynamic current variation of the transistor under alternating illumination. To perform the static measurement, the transistor was fixed at a constant biasing condition using the setup as described in Section 3.3.1 and illuminated by an extra LED at a set distance away from the device. The variation in illumination intensities was achieved by changing the applied current on the LED driven by a

Keithley 2400 source-meter. The actual illumination intensity was calibrated by a Thorlabs S120UV power sensor placed at the same distance away from the LED as the transistor device. In dynamic measurement the variation in illumination was achieved by driving the LEDs with an Agilent 33220A function generator. The variation in channel current is first amplified by a Stanford Research Systems SR570 current preamplifier and subsequently recorded by an Agilent DSO6014A oscilloscope.

Bibliography

(1) Azzam, W.; Bashir, A.; Biedermann, P. U.; Rohwerder, M. Formation of Highly Ordered and Orientated Gold Islands : E Ff Ect of Immersion Time on the Molecular Adlayer Structure of Penta Fl Uorobenzenethiols (PFBT) SAMs on Au (111). **2012**, No. 111.

(2) Hamadani, B. H.; Corley, D. A.; Ciszek, J. W.; Tour, J. M.; Natelson, D. Controlling Charge Injection in Organic Field-Effect Transistors Using Self-Assembled Monolayers. *Nano Lett.* **2006**, *6* (6), 1303–1306.

(3) Kang, H.; Lee, N. S.; Ito, E.; Hara, M.; Noh, J. Formation and Superlattice of Long-Range-Ordered Self-Assembled Monolayers of Pentafluorobenzenethiols on Au(111). *Langmuir* **2010**, *26* (5), 2983–2985.

(4) Saudari, S. R.; Frail, P. R.; Kagan, C. R. Ambipolar Transport in Solution-Deposited Pentacene Transistors Enhanced by Molecular Engineering of Device Contacts. *Appl. Phys. Lett.* **2009**, *95*, 023301.

Chapter 4 High Speed Ultraviolet Phototransistors based on an Ambipolar Fullerene Derivative

Combining high charge carrier mobility with ambipolar transport in light absorbing organic semiconductors is highly desirable as it leads to enhanced charge photogeneration, and hence improved performance in various optoelectronic devices including solar cells and photodetectors. In this chapter the development of [6,6]-phenyl-C61-butyric acid methyl ester ($PC_{61}BM$)-based ultraviolet (UV) phototransistors with balanced electron and hole transport characteristics is presented. The balanced electron and hole transport within the single material channel is achieved by fine-tuning of the source-drain electrode work function using a self-assembled monolayer. Opto/electrical characterization of as-prepared ambipolar $PC_{61}BM$ phototransistors reveals promising photoresponse, particularly in the UVA region (315-400 nm), with maximum photosensitivity and responsivity of 9×10^3 and 3×10^3 A/W respectively. Lastly, the temporal response of the $PC_{61}BM$ phototransistors is found to be high with typical switching times of <2 ms, validating the potential of this ambipolar organic material for fast and sensitive UV photodetection.

4.1 Introduction

Organic thin film transistors (OTFTs) have been intensively studied due to their attractive characteristics that include mechanical flexibility and processing versatility that enables cost-effective manufacturing on inexpensive substrate materials.[1–5] Unlike existing silicon transistor technologies where p-type and n-type functionalities are achieved via diffusion or implantation of suitable dopants, charge transport in organic semiconductors, and their devices, is determined by the molecular structure and the ability to inject holes and/or electrons in the corresponding energy levels. This property has enabled the development of OTFTs that are able to transport holes and/or electrons, depending on the biasing conditions, within the same channel material.[6] These so-called ambipolar transistors have shown promise for a range of applications[7–10] as they combine multiple functions that include electrical switching, light-sensing and light emission.[11–15] To this end, organic phototransistors (OPTs) represent an important emerging technology as they offer light-sensing capabilities with electrical switching which makes them ideal for use as electro-optical transducer for signal-amplification. Such attractive characteristics are key for overcoming the noise level in conventional photodiode read-out circuit[16] as the tuneable gain mechanism controlled by the gate field (exclusive to transistor's three-terminal architecture) enables controllable sensitivity and low noise level compared to the conventional two-terminal photodiodes.[17] Moreover, the structural versatility of organic semiconductors with tailor-made properties allows the design for OPTs with desired functionality such as panchromatic sensitivity or wavelength selectivity.[18–22]

Methanofullerene derivatives such as the [6,6]-phenyl-C61-butyric acid methyl ester ($PC_{61}BM$) have been extensively used as electron-transporting materials in n-channel OTFTs,[23–26] in combination with p-type semiconductors to form heterostructure ambipolar OTFTs[27–29] as well as the electron acceptors in organic photovoltaics (OPVs).[30–34] Although a few early attempts have demonstrated ambipolar transport in $PC_{61}BM$ transistors, emphasis was placed on circuit applications.[7,35] This interesting combination of characteristics makes $PC_{61}BM$ a promising candidate for applications in the area of photodetectors and particularly phototransistors. Despite the promise, however, to date no ambipolar OPT based on $PC_{61}BM$ has been demonstrated.

This chapter presents the development of ambipolar $PC_{61}BM$ transistors with balanced electron and hole mobilities and their application as fast and highly sensitive UV photodetectors. Resulting devices were electrically characterised in the dark and under illumination with different light intensities and wavelengths. When illuminated with different

wavelengths of light, the OPTs are found to be visible blind with significant photoresponse observed only under UV illumination. The extracted figures of merit of $PC_{61}BM$-based OPTs are shown to be comparable to those reported for state-of-the-art silicon photodetectors. Finally, the $PC_{61}BM$ phototransistors show excellent dynamic response with turn-on and turn-off times of less than 2 ms. The present results highlight the potential of ambipolar $PC_{61}BM$ phototransistors as an alternative, and highly promising, UV photodetector technology.

4.2 Methods

4.2.1 Phototransistor Fabrication

Top-gate, bottom-contact (TG-BC) transistors were fabricated on 2 cm × 2 cm glass substrates. Prior to material deposition all substrates were cleaned by sonication in detergent solution (DECON90), deionized water, acetone and 2-propanol (IPA) for 10 minutes each. 40nm thick gold source and drain (S-D) contacts were thermally evaporated onto the substrates through shadow masks, resulting to transistors with channel length (L) and width (W) of 30 μm and 1 mm, respectively. The surfaces of the S-D contacts were then chemically modified with the functionalization of the pentafluorothiophenol (PFBT) self-assembling monolayer by immersing the substrates into a 1:100 vol % diluted solution of PFBT in IPA for 1 h at room temperature in air. The excess of PFBT was washed off with IPA. The $PC_{61}BM$ layer was then deposited by spin-casting from a chlorobenzene solution (20 mg/ml) at a spin speed of 1200 rpm for 60 s, followed by a 10-min annealing at 100 °C in nitrogen. The fluoropolymer CYTOP (Asahi Glass) was used as the gate dielectric layer and spin-coated directly onto the semiconducting layer at 2000 rpm for 60 s and dried in high vacuum (~10^{-7} bar) for 10 h. Device fabrication was completed with the thermal evaporation of 40-nm Al gate electrode through a shadow mask onto the CYTOP dielectric layer.

4.2.2 Material Characterization

Film absorption measurements were performed using a Shimadzu UV2600 UV-Vis spectrophotometer equipped with an ISR-2600 Plus integrating sphere. The samples for the UV-Vis measurement were made on quartz substrates, following an identical recipe of material deposition to that described previously in Section 4.2.1. The absorption spectrum was calculated from the measured transmittance and reflectance data. The surface morphologies of the various deposited films and the glass substrate were obtained using an Agilent 5500 atomic force microscope in intermitted contact mode. The work functions of Au electrode before and

after PFBT application were determined using a scanning Kelvin Probe (KP) system (KP Technology, SKP5050) using silver (Ag) as the reference work function material. The deposition of Au and the application of PFBT monolayer were performed using the same procedures as those described in Section 4.2.1.

4.2.3 Optoelectronic Characterization

Optoelectronic characterization was carried out by measuring the transfer and output characteristics of the fabricated transistors in a dark environment and under various illumination intensities using red-green-blue and UV light-emitting diodes (LEDs). Specifically, LEDs with electroluminescence (EL) emission peaks at 632, 525, 475 and 390 nm, were employed and driven using a Keithley 2400 source-meter. Electrical characterisation of all transistors was performed using an Agilent B2902A source-measure unit in dry nitrogen atmosphere. The illumination intensities (E_{opt}) generated by the LEDs driven at different current levels were measured by a Thorlabs S120UV power sensor.

4.2.4 Temporal Response Measurements

Dynamic characterization was performed by measuring the evolution of the channel current to an external optical stimulus (light pulse). To achieve this, the transistor was biased at fixed drain (V_D) and gate (V_G) voltages using an Agilent B2902A source-measurement unit as in electrical characterization and the variation in channel current was amplified by Stanford Research Systems SR570 current preamplifier and subsequently recorded by an Agilent DSO6014A oscilloscope. Optical pulses were generated using blue (λ_{max} = 475 nm) LED driven by an Agilent 33220A function generator.

4.3 Results and Discussion

4.3.1 Film Characterization

The absorption spectrum of the $PC_{61}BM$ layers deposited on quartz substrates were first investigated using a UV-Vis spectrophotometer (**Figure 4.1**). Evidently, the compound exhibits weak absorption in red region and moderate absorption in green-blue range. The weak absorption at longer wavelengths is attributed to the relatively wide band gap of $PC_{61}BM$ - a result of the peculiar electronic structure of C_{60}.[36] However, the absorption increases significantly in the UV-A region (<400 nm), hence making $PC_{61}BM$ a promising candidate for use in UV photodetectors.

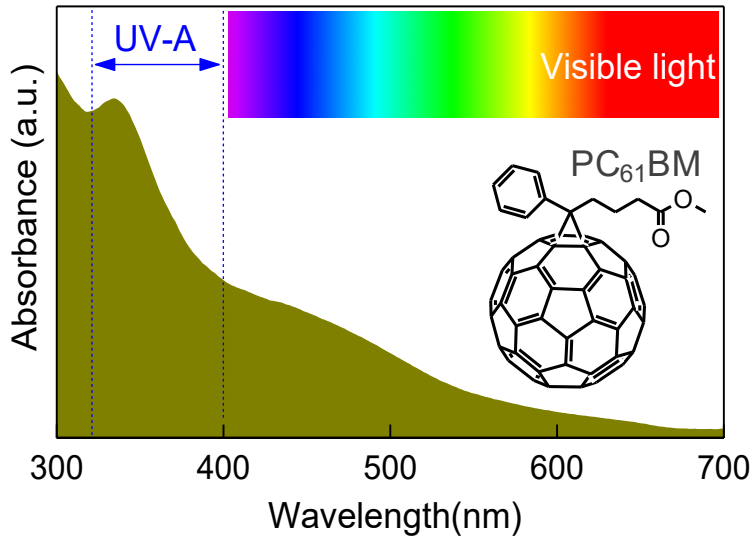


Figure 4.1: UV-Vis absorption spectrum of a $PC_{61}BM$ layer deposited on quartz substrate via spin coating. Inset shows the molecular structure of $PC_{61}BM$.

The surface topography of the $PC_{61}BM$ layers deposited on glass was investigated using atomic force microscopy (AFM) and is shown in **Figure 4.2 (a)**. The surface morphology of the bare glass surface is also shown for comparison. The $PC_{61}BM$ layer appears extremely smooth and uniform with a root-mean-square (RMS) roughness of ~0.26 nm, which is close to that of glass beneath (~0.22 nm). The similarity of the surface topographies of the two surfaces is further illustrated in the height histograms shown in **Figure 4.2 (b)** where no distinct differences can be observed. In the context of transistors, this feature is crucial for effective charge carrier accumulation and transport at the critical dielectric/semiconductor interface. This is particularly true for top-gate transistor architecture where the surface topography defines the morphology of the actual conducting channel.[37]

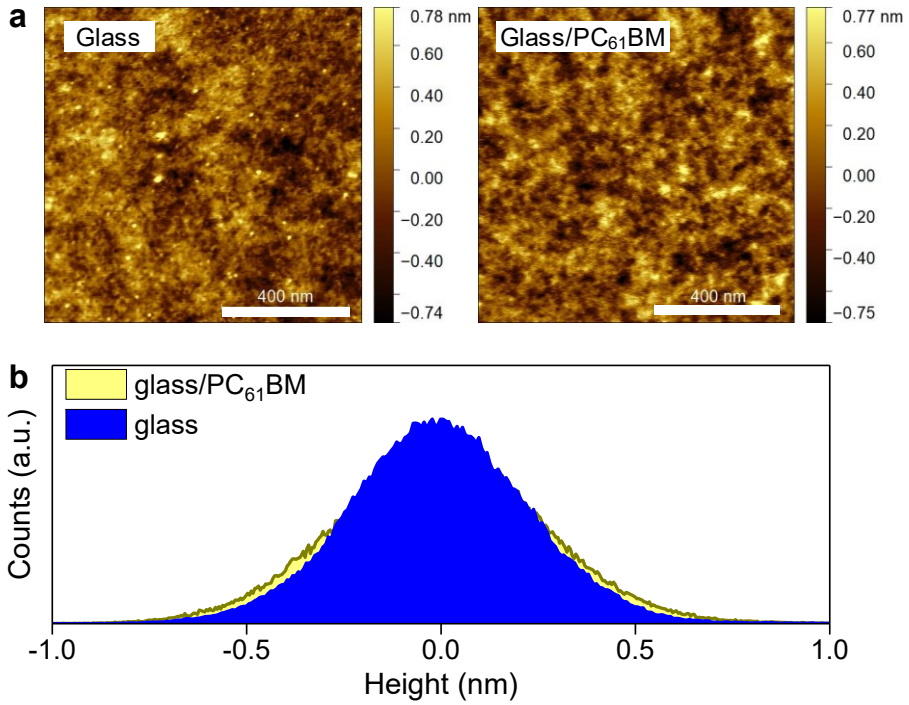


Figure 4.2: (**a**) AFM images of the surface topography of bare glass and $PC_{61}BM$ deposited on glass. The root-mean-square (RMS) surface roughness of the glass and glass/$PC_{61}BM$ samples are 0.22 and 0.26 nm, respectively. (**b**) Height distribution histogram extracted from the AFM images in (**a**).

4.3.2. Transistor Design and Electrical Characterisation

The charge transport properties of the $PC_{61}BM$ layers were investigated in TG-BC transistor architectures (**Figure 4.3a**). To achieve ambipolar transport, efficient injection of both electrons and holes from the S-D electrodes to the corresponding energy levels in the semiconductor, is essential. The latter requires good energy level alignment between the electrode(s) and the semiconductor. This can be, at least partially, accomplished using polar molecules that can self-assemble on the electrode's surface forming a highly-ordered dipole layer. Such self-assembled monolayers (SAMs) have been used as electrode work function modifiers, which under certain circumstances can lead to enhanced carrier injection.[38–41] Herein PFBT was chosen as the work function modifier for the Au S-D electrodes. **Figure 4.3b** shows the simplified energy-band diagram of $PC_{61}BM$ and Au electrode before and after PFBT application. The mismatch in the work function of Au and the HOMO of $PC_{61}BM$ before contact results in an injection barrier of ≈1.2 eV for holes. The actual mismatch, however, is known to further increase due to the formation of a strong dipole layer at the Au/$PC_{61}BM$ interface,[42] leading to a large injection barrier for holes. In an effort to address this issue, Au is treated with PFBT, which resulted to a reduction of the electrodes' work function by ≈1 eV (Au/PFBT in **Figure. 4.3b**). This shift towards the HOMO of $PC_{61}BM$ makes Au/PFBT a

potential hole-injecting electrode. Apart from charge injection, carrier trapping at the dielectric/semiconductor interface, which originates from impurities or certain chemical moieties,[43] is also known to limit the carrier mobility and presents an additional challenge for achieving balanced ambipolar charge transport. To address this issue the fluoropolymer CYTOP was selected as the gate dielectric. The formulation of this hydroxyl-free polymer is orthogonal to the underlying $PC_{61}BM$ and is known to lead to the formation of a trap-free semiconductor-dielectric interface for holes and electrons.[44,45]

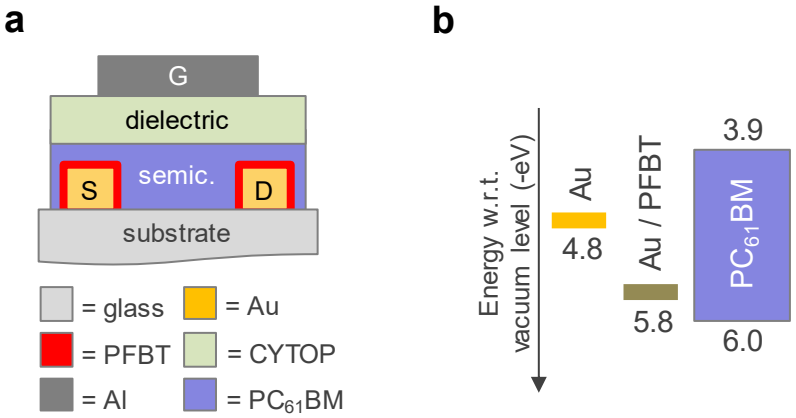


Figure 4.3: (**a**) A schematic of the top-gate, bottom-contact (TG-BC) transistor architecture developed in this study. (**b**) Energy level band diagram for $PC_{61}BM$, gold (Au) electrode and PFBT-treated Au electrode (Au/PFBT).

Figure 4.4 shows the transfer characteristics measured in the dark for a $PC_{61}BM$ transistor using negative and positive drain (V_D) and gate (V_G) voltages, respectively. In both bias modes the device exhibits typical V-shaped characteristics indicative of the injection of both hole and electron in the same transistor channel.

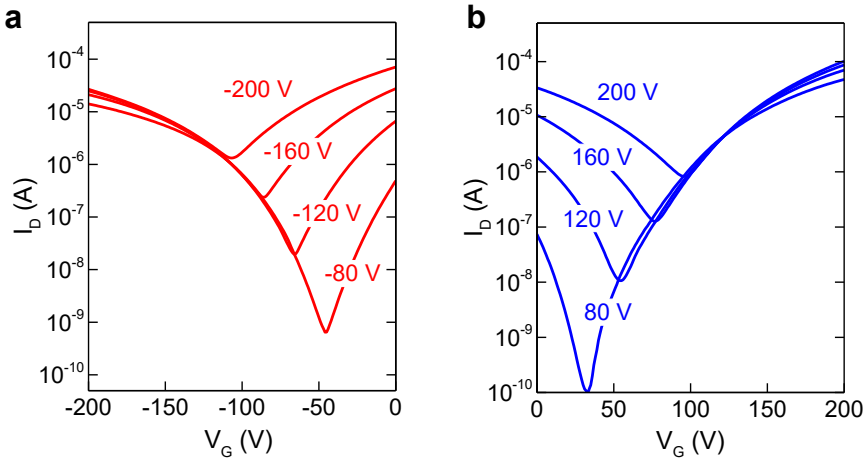


Figure 4.4: Transfer characteristics measured for a $PC_{61}BM$ transistor in (**a**) hole accumulation and (**b**) electron accumulation bias regimes.

The corresponding output characteristics of the same transistor in hole-enhancement and electron-enhancement bias regimes, respectively, are shown in **Figures 4.5**. At high V_G the transistor shows linear-to-saturation curves that resemble closely those of unipolar devices. At low V_G, however, a superlinear current increase is observed, especially in the high V_D region because of the injection of minority carriers[9], a feature that is absent in unipolar transistors. The nonlinear increase in the drain current (I_D) at small V_D indicates the presence of injection barriers from Au/PFBT S-D electrodes to $PC_{61}BM$ for both holes and electrons. Despite this, the extracted field-effect mobility for holes and electrons extracted in the linear region (V_D = ±80 V and V_G = ±200 V) are high and on the order of 0.06 and 0.14 cm^2/Vs, respectively. These measurements are extremely revealing as they provide direct evidence of the ambipolar nature of $PC_{61}BM$, a property that has remained elusive until now.

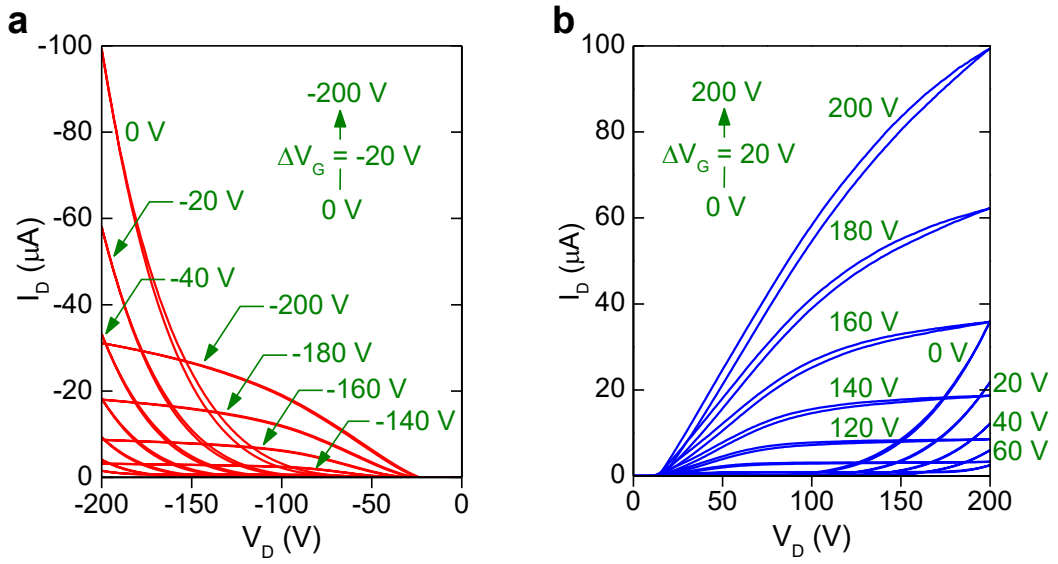


Figure 4.5: Output characteristics measured for the same $PC_{61}BM$ transistor obtained in (**a**) hole and (**b**) electron accumulation.

4.3.3. Optoelectronic Characterisation of $PC_{61}BM$ Transistors

Optoelectronic characterization of all transistors was carried out by illuminating the devices using a UV LED with an EL peak at 395 nm due to the strong absorption of $PC_{61}BM$ at this wavelength range (**Figure 4.6**).

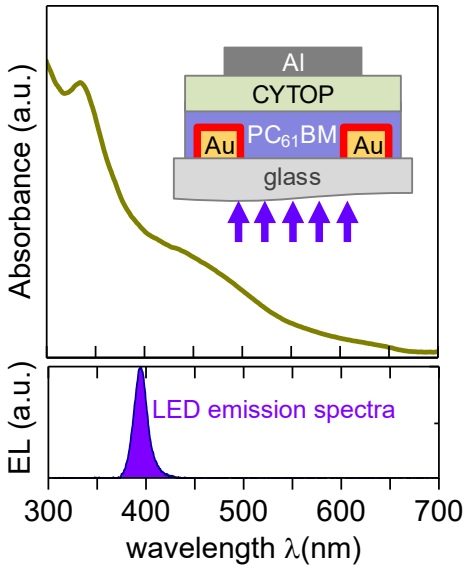


Figure 4.6: Absorption spectrum of $PC_{61}BM$ and EL spectrum of the UV LED used for optoelectronic characterisation of the devices. Inset: schematic of the TG-BC transistor architecture employed and the orientation of UV illumination.

The corresponding transfer and output curves of ambipolar $PC_{61}BM$ phototransistor in electron enhancement mode under different illumination intensity E_{opt}, are shown in **Figure 4.7**. The channel current of the device is found to increase with increasing light intensity, which is indicative of a strong photoresponse. The magnitude of the current increase depends on both the illumination intensity and applied V_G. These measurements suggest that additional charges are introduced in the channel upon optical stimulation. One possible photogeneration mechanism is via exciton formation within $PC_{61}BM$. These are then dissociated into free electrons and holes that drift to the corresponding electrodes (S or D) due to the applied electrical field (V_G, V_D).[46] Interestingly, the photocurrent enhancement occurs not only in the unipolar operating regime (i.e. V_G = 120 V; **Figure 4.7b**) but also in the ambipolar regime (V_G = 80 V for V_D > 150 V; **Figure 4.7c**) of the transistor. This observation supports the existence of an appreciable photoconductivity component within the channel region. Overall, the results demonstrate that the incident UV light has a strong gating effect that can modulate the channel current independently.

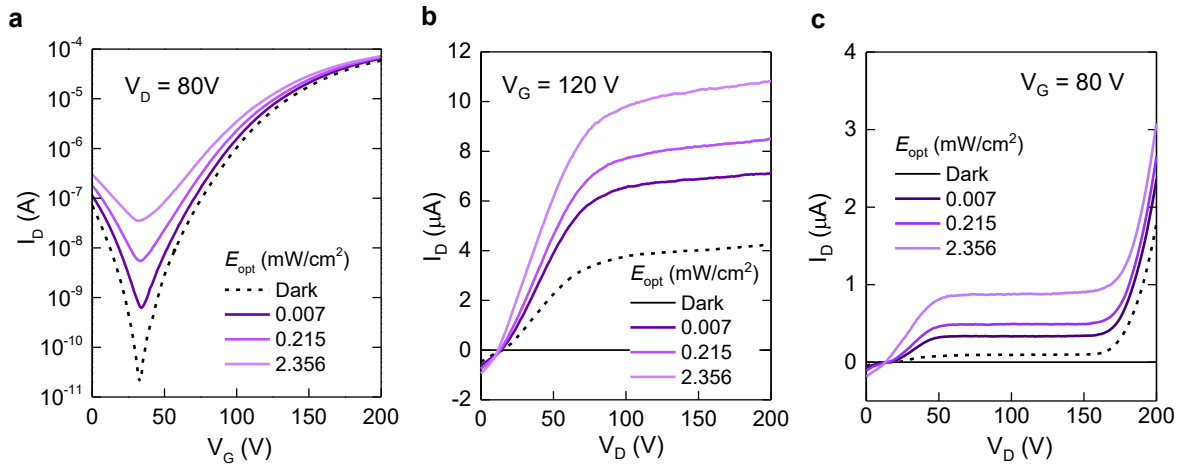


Figure 4.7: (**a**) Transfer characteristics of a $PC_{61}BM$ phototransistor measured at fixed V_D = 80 V (electron accumulation) in the dark and under UV illumination of different intensities. (**b**) Output characteristics measured for the same $PC_{61}BM$ transistor at V_G = 120 V (electron accumulation regime). (**c**) Output characteristics of the same $PC_{61}BM$ transistor measured at V_G = 80 V (ambipolar transport regime) under dark and UV illumination at various intensities.

The performance characteristics of the $PC_{61}BM$ phototransistors were further analysed by quantifying three important figures of merit for photodetector, i.e. photosensitivity P, responsivity R (in A/W) and specific detectivity D^* (in Jones) and plot them as a function of gate voltage V_G and incident optical power P_{opt}.

Photosensitivity, which is the ratio of photo-generated current to the dark current, represents the relative change in channel current with respect to the dark current. **Figure 4.8a** shows the evolution of P with V_G where a peak value of 9×10^3 is measured for an illumination intensity of 2.356 mW/cm^2 at V_G = 35 V. This is due to that fact that at this particular V_G bias the channel current is turn-off and I_{dark} becomes minimum, hence leading to a maximum P value. The decreasing P value with increasing V_G, on the other hand, indicates that at higher V_G the channel current is primarily due to injected charges with the photo-induced carriers becoming less and less dominant. However, the increasing P with increasing light intensity across the entire V_G range (**Figure 4.8b**) suggests that photo-generated carriers exist even at high V_G bias.

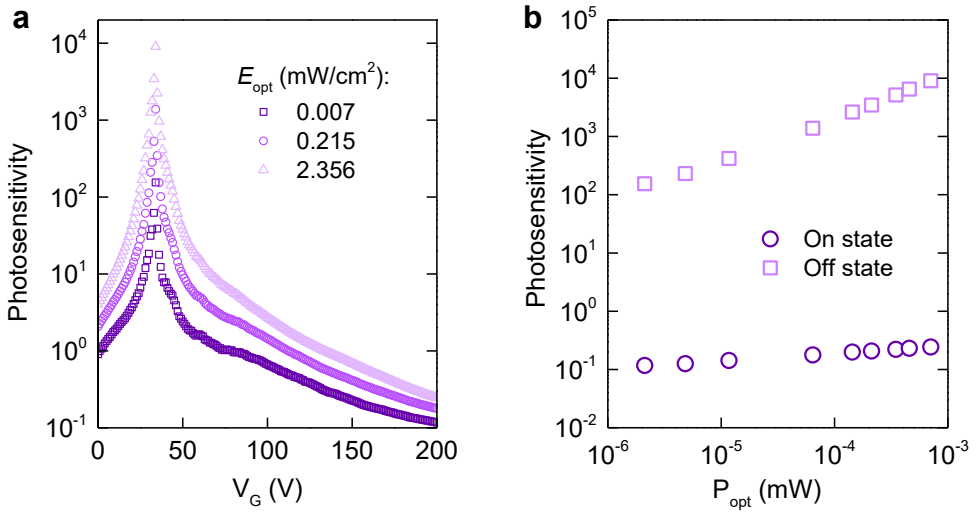


Figure 4.8: (**a**) Photosensitivity (P) versus V_G measured at a constant V_D = 80 V and at three different illumination intensities. (**b**) P versus incident optical power (P_{opt}) measured at two different channel biasing regimes: on-state (V_G = 200 V) and off-state (V_G = 35 V) at fixed V_D = 80 V.

Responsivity, which is the ratio of change in I_D against the incident P_{opt}, defines the efficiency of optical power converted into measurable electrical photocurrent. The dependence of R on V_G (**Figure 4.9a**) shows that the minimum value is achieved at the channel turn-off bias, which is opposite to that seen for P. The observed increase in R with increasing V_G is attributed to the improved charge photogeneration and transport across the channel. The log-log plot of R as a function of P_{opt} (**Figure 4.9b**) shows that for a given V_G the R decreases with increasing P_{opt}, which is again opposite to the P vs. P_{opt} trend. The effect is attributed most likely to enhanced photo-induced electron-hole recombination.[47] The maximum value for R of 3×10^3 A/W is obtained at the lowest light intensity of 0.007 mW/cm^2. Notably, this value is one order of magnitude higher than that reported for Si phototransistors (≈300 A/W) and highlights the potential of $PC_{61}BM$ phototransistors.[48]

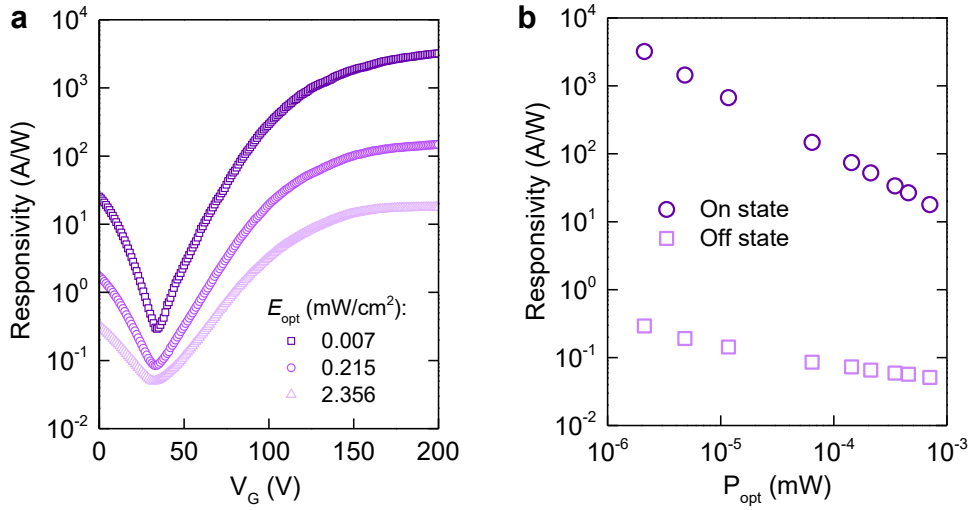


Figure 4.9: (**a**) Responsivity (R) versus V_G measured at a constant V_D = 80 V and at three different illumination intensities. (**b**) R versus incident optical power (P_{opt}) measured at two different channel biasing regimes: on-state (V_G = 200 V) and off-state (V_G = 35 V) at fixed V_D = 80 V.

The specific detectivity D^* describes the sensitivity of a photodetector with respect to noise and enables direct comparison of devices with different areas and geometries. A simple estimation of the specific detectivity according to **Equation 2.25** is the shot-noise limited detectivity D_s^*. The dependence of D_s^* on V_G shown in **Figure 4.10a** reveals two distinct regions: a peak value calculated at around V_G = 35 V, followed by a continuous increase and saturation for higher V_G. The sharp increase of D_s^* seen at V_G = 35 V is attributed to the low background noise level at that particular bias due to the supressed channel current. Specifically, the shot noise, which is proportional to I_{dark}, reaches the lowest level when the channel current is turn-off (V_G = 35 V), resulting in the observed maximum value of D_s^*. The upward trend of D_s^* with increasing V_G, on the other hand, is attributed to the improved current amplification due to the increase of the carrier mobility with increasing V_G. The downwards trend of D_s^* versus P_{opt} (**Figure 4.10b**), which is similar to that of the R, is evident in good agreement with **Equation 2.25**. Interestingly, devices characterised in the on-state exhibit a higher D_s^* at low P_{opt}, whereas those measured in the off-state show a higher D_s^* at high P_{opt}. This is believed to be due to the difference in the current amplification as a result of the different operating/illuminating regimes. A key conclusion that can be reached from these measurements is that in order to fully exploit the signal gain mechanism in these ambipolar $PC_{61}BM$ phototransistors the device needs to be operated at low P_{opt}. Only then, the maximum value for

D_s* of 1.3×10^{13} Jones can be achieved. It is noted that the latter is comparable to that measured for Si photodetectors (≈4×10^{12} Jones).[18]

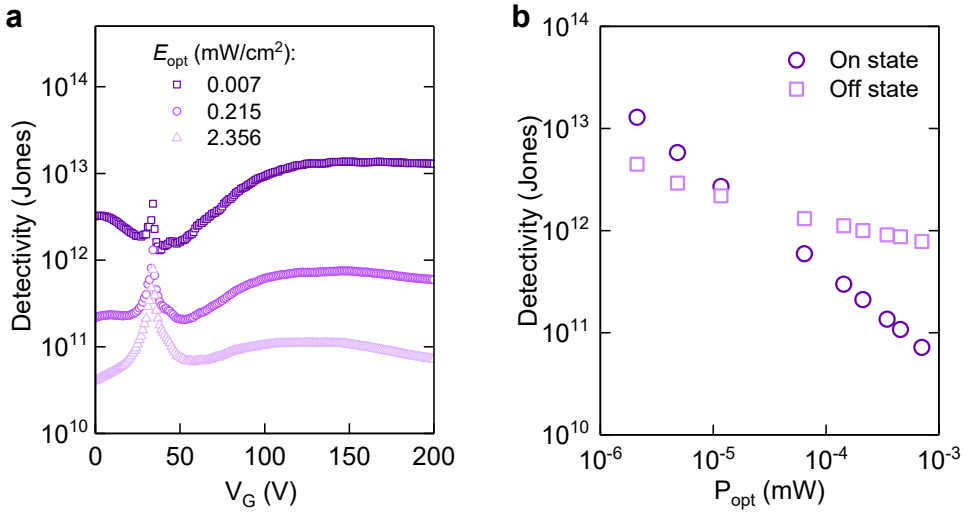


Figure 4.10: (**a**) Shot-noise limited specific detectivity (D_s*) versus V_G measured at three different illumination intensities and at a fixed V_D = 80 V. (**b**) D_s* versus P_{opt} measured for the same $PC_{61}BM$ phototransistor at two different channel biasing regimes: on-state (V_G = 200 V) and off-state (V_G = 35 V) at fixed V_D = 80 V.

In an effort to understand the different contributions in the photo-detection mechanism(s), the channel current of the transistors both in the off-state ($I_{D(Ph\text{-}OFF)}$) and on-state ($I_{D(Ph\text{-}ON)}$) is monitored as a function of P_{opt} (**Figure 4.11**). The result suggests two primary photodetection mechanisms, namely photovoltaic and photoconductive effects. These processes are similar to those observed in both inorganic[49] and organic[14,50] phototransistors, highlighting the similarities in the operating principles. In the case of photovoltaic effect, photo-generated carriers within the channel tend to lower the injection barrier and associated contact resistance as well as directly contribute to free charges in the channel. Both processes can lead to a measurable shift in the threshold voltage (V_{th}), resulting in a significant increase in channel current even under low illumination intensities. The photocurrent induced by the photovoltaic effect is given by[51]:

$$I_{pv} = g_m \Delta V_{th} = \frac{AkT}{q} \ln\left(1 + \frac{\eta q \lambda P_{opt}}{I_{\text{dark}}\, hc}\right) \tag{4.1}$$

where, g_m is the transconductance, ΔV_{TH} is the threshold voltage shift, A is the fitting parameter, η is the photogeneration quantum efficiency, I_{dark} is the dark current for minority carriers and hc/λ is the energy of the incident photons. In the case of photoconductive effect, photo-induced bound electrons and holes are separated and transferred directly by the external applied field,

the channel current therefore increases linearly with the incident power. The photocurrent caused by the photoconductive effect can be expressed as[52]:

$$I_{pc} = (q\mu_p pE)WD = BP_{opt} \quad (4.2)$$

where, μ_p is the hole mobility, p is the hole concentration, E is the electric field in the channel, W is the channel width, D is the depth of the absorption region, and B is the fitting parameter. In **Figure 4.11**, the photocurrents measured in both the on- and off-state for a fixed V_D of 80 V are plotted as a function of P_{opt}. Here symbols denote the experimental results while solid lines represent the fittings to the data using **Equation 4.1** and **4.2.** The fittings were performed assuming that the photocurrent is the result of a synergistic effect of the two mechanisms. The results indicate that the photoconductive effect dominates the device operation in the off-state while the photovoltaic effect becomes dominant in the on-state. This is an interesting finding as it provides direct evidence of the photogeneration mechanisms in ambipolar phototransistors.

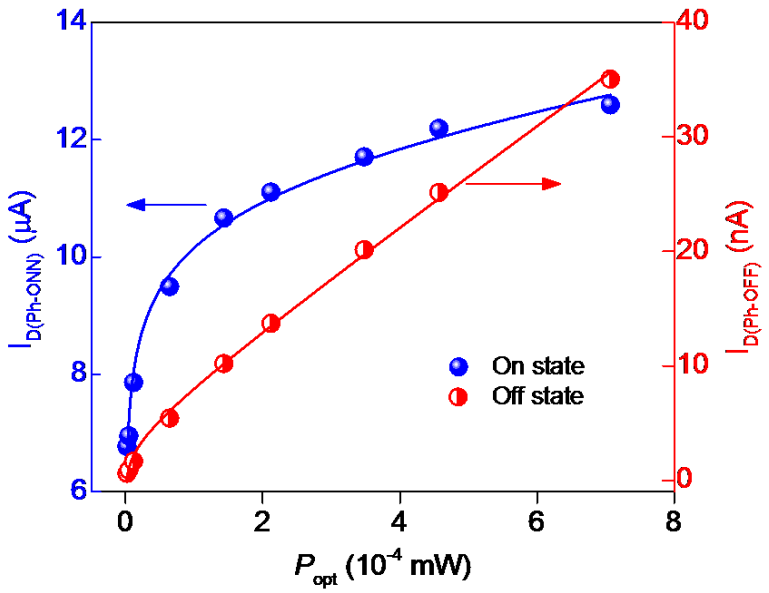


Figure 4.11: Evolution of the channel photocurrent as a function of incident optical power (P_{opt}) in measured for a $PC_{61}BM$ phototransistor in the on-state (V_G = 200 V) and in the off-state (V_G = 35 V) at a constant V_D = 80 V. The symbols represent experimental measured data whilst the solid lines are the fitting curves.

The detection capabilities of the ambipolar $PC_{61}BM$ phototransistor across a wider range of visible wavelengths have also been investigated. **Figure 4.12a** shows the absorption spectra of $PC_{61}BM$ together with the electroluminescence spectrum of the different LEDs employed as the light sources (with peak emission wavelengths of λ_B = 475 nm, λ_G = 525 nm, λ_R = 632 nm). The transfer characteristics of devices measured in the dark and under different illumination intensities with the different LEDs are shown in **Figure 4.12b**. A clear device

photoresponse is evident for all three wavelengths with the blue light-illuminated transistor exhibiting the highest response and the red-light illuminated one exhibiting the lowest response. The level of photoresponse appears to correlate with the overlap between the absorption of $PC_{61}BM$ and the EL emission of the individual LEDs (**Figure 4.12a**).

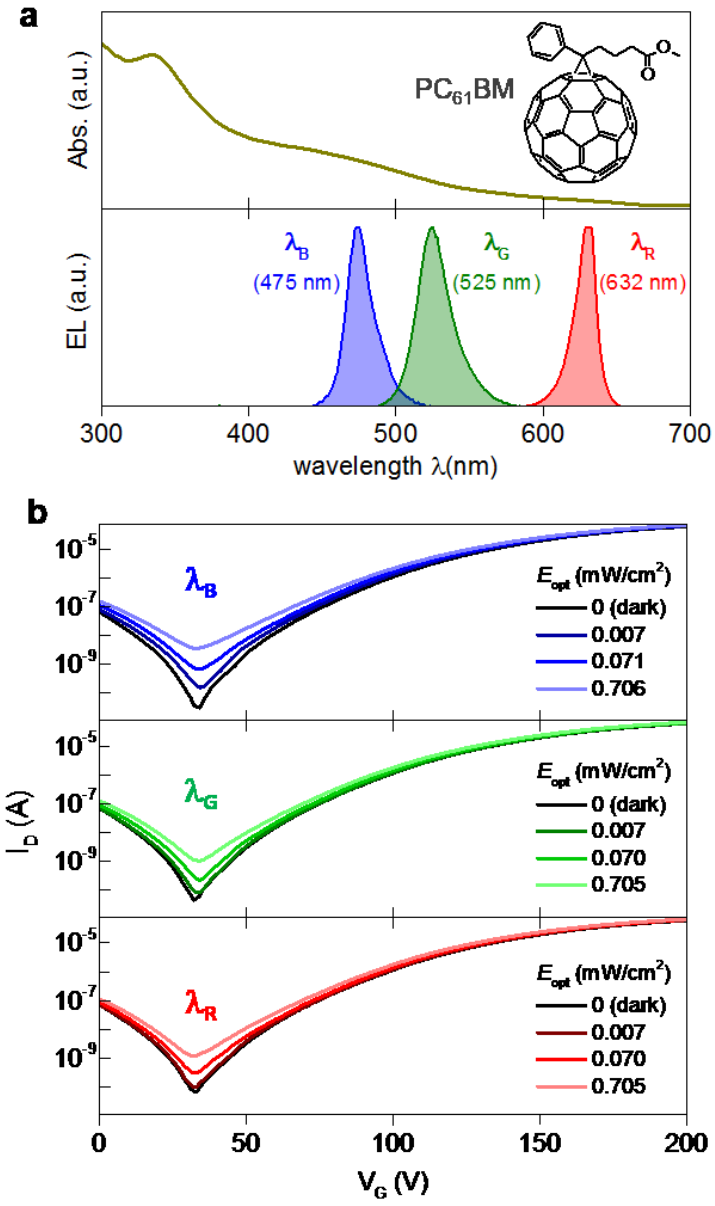


Figure 4.12: (**a**) Absorption and EL spectra of the $PC_{61}BM$ layer and for the three visible light LEDs used to perform the photoresponse measurements. (**b**) Transfer characteristics measured for a $PC_{61}BM$ phototransistor illuminated with blue light (λ_B = 475 nm), green light (λ_G = 525 nm) and red light (λ_R = 632 nm) at different intensities (P_{opt}). The black curves in each plot represent the transfer characteristics measured in dark at V_D = 80 V.

Quantitative analysis of the device response to different wavelengths was performed by calculating the P, R and D^* parameters (**Figure 4.13**) for all wavelengths at constant P_{opt} (0.7 mW/cm^2) and bias (V_D = 80 V and V_G = 35 V) conditions. Evidently, all three parameters improve as the wavelength of the incident light reduces from 632 nm (red) to 395 nm (UV-A). These demonstrate that $PC_{61}BM$ phototransistors function as filter-less UV-A (315-400 nm) photodetectors that combine high sensitivity with a simple device architecture.

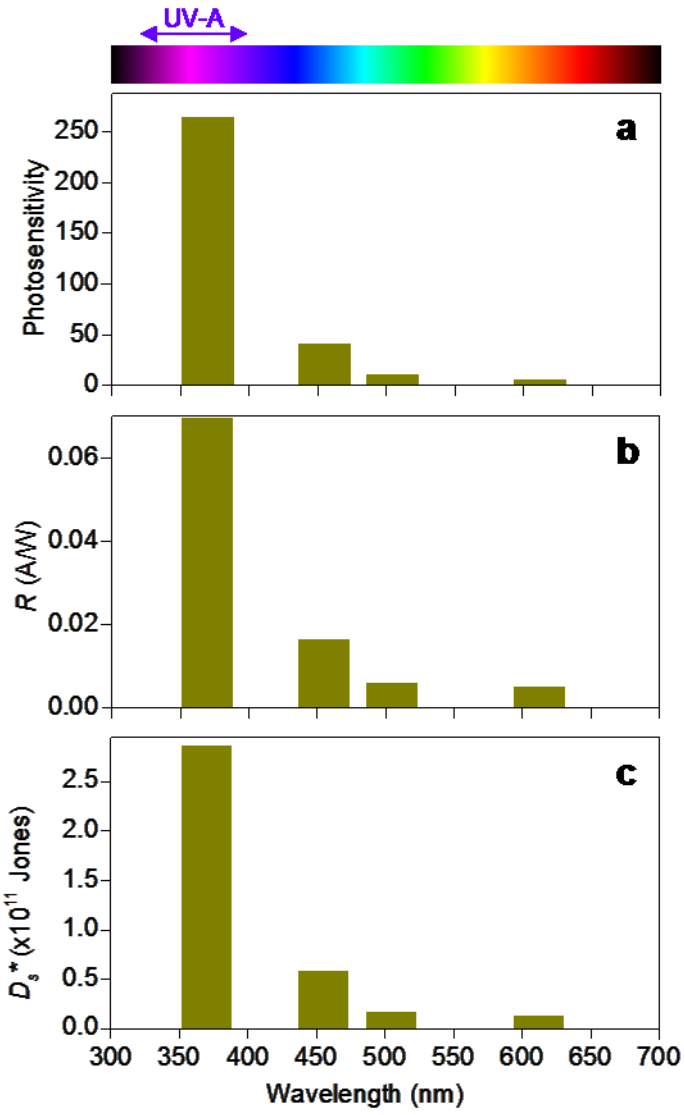


Figure 4.13: Calculated values for (**a**) P, (**b**) R, and (**c**) D_s^* for all four different wavelengths investigated. All parameters were calculated from the transfer characteristics of the same $PC_{61}BM$ phototransistor biased at V_G = 35 V, and V_D = 80 V, and illuminated with E_{opt} = 0.706 mW/cm^2.

4.3.4. Dynamic Operation of $PC_{61}BM$ Phototransistors

For the successful deployment of any emerging photodetector technology to commercial products the sensor should not only offer high sensitivity and spectra selectivity but also good temporal response. To measure the dynamic response of the present $PC_{61}BM$ phototransistor, the switching behaviour of optimized devices was investigated. This was achieved by exposing the devises to light pulses and monitoring the evolution of the channel current in real time using the measurement setup shown in **Figure 4.14a**. During the measurements the transistor was maintained at a constant bias of V_D = 80 V and V_G = 35 V. **Figure 4.14b** shows the temporal response of the channel current to a train of light pulses 10 ms long. The rise time, t_R, (current increasing from 10% to 90% of the maximum value) and the fall time, t_F, (current decreasing from 90% to 10% of its maximum value) were then calculated directly from **Figure 4.14c**, yielding values of t_R = 0.94 ms and t_F = 1.02 ms, respectively, as well as a total response time of ~2 ms. To this end it is noted that the latter value approaches the detection limit of the measurement setup because of the necessary trade-off between small-signal detection (nA) and the effective signal bandwidth of the current amplifier (CA). Despite this, however, the results show that the present $PC_{61}BM$ phototransistors are faster than most of the unipolar organic phototransistors reported to date and compare favourably to the ultrafast quantum dot (QD), low-dimensional and/or hybrid photodetectors.[53,54,63–67,55–62] The fast temporal response is attributed to the excellent ambipolar transport characteristics of $PC_{61}BM$, and the resulting efficient carrier generation and transport across the channel. Finally, the present results highlight the use of single organic ambipolar semiconductors as a promising approach to the development of fast phototransistors with tailored photoresponse.

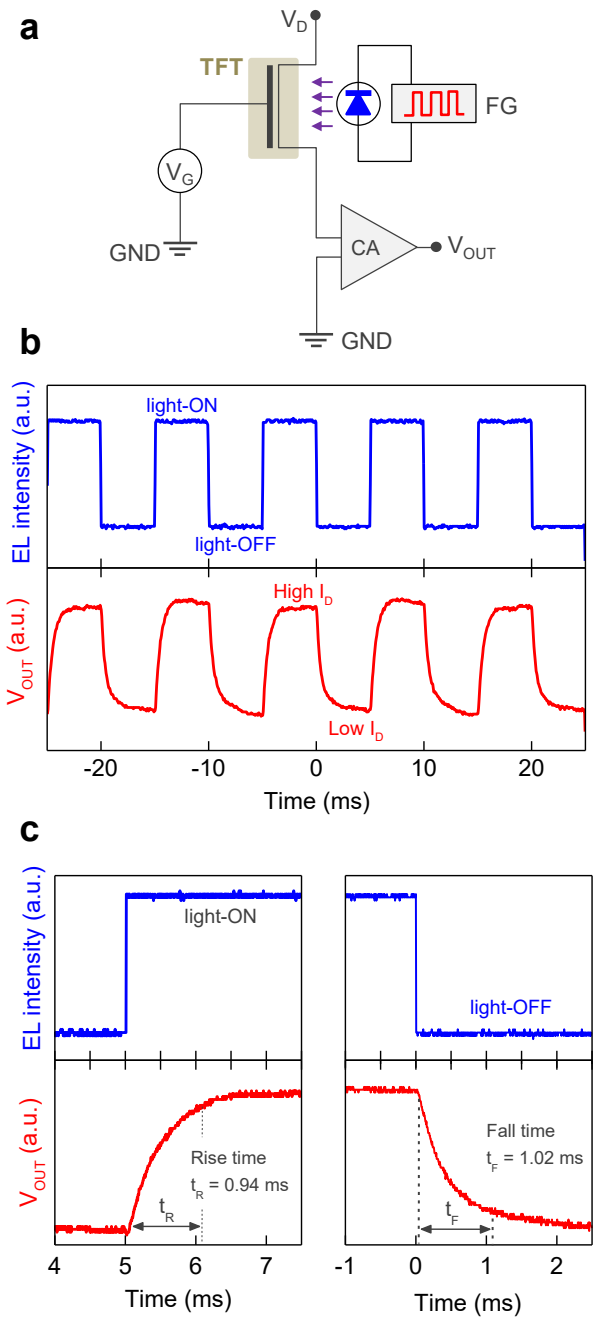


Figure 4.14: (**a**) Circuitry of the experimental setup used for the dynamic characterisation of the $PC_{61}BM$ phototransistors. A function generator (FG) is used to drive the LED. The channel current in the transistor, which is biased at $V_G = 35$ V and $V_D = 80$ V, is monitored in real time using a current amplifier (CA) and recorded as a voltage (V_{OUT}) using an oscilloscope. (**b**) Response of the channel current (red trace) to a train of blue ($\lambda_{max} = 475$ nm) light pulses with $E_{opt} = 0.744$ mW/cm^2 (blue trace). (**c**) Analysis of raise (t_R) and fall (t_F) times.

4.4 Conclusions

To summarize Chapter 4, UV-sensitive phototransistors based on the solution-processed methanofullerene $PC_{61}BM$ have been fabricated and characterised. The carefully engineered devices exhibit good ambipolar operation in the dark with electron and hole mobility values of 0.14 and 0.06 cm^2/Vs, respectively. Because of the light absorption characteristics of $PC_{61}BM$, the resulting devices exhibit large photoresponse particularly in the UV-A region of the electromagnetic spectrum. Importantly, the $PC_{61}BM$ phototransistors are able to operate at high frequencies with minimum response times of less than 2 ms, in spite of the long channel length (30 μm) employed - a temporal response difficult to achieve in conventional unipolar organic-based phototransistors. To this end, the performance parameters extracted under low illumination intensities are comparable with those of Si-based photodetectors, mainly because of the intrinsic gain mechanism associated with the three-terminal phototransistor architecture. This work highlights the use of single material ambipolar organic phototransistors as promising concept for the development of sensitive and fast photodetectors with tailored colour sensitivity.

Bibliography

(1) Drury, C. J.; Mutsaers, C. M. J.; Hart, C. M.; Matters, M.; de Leeuw, D. M. Low-Cost All-Polymer Integrated Circuits. *Appl. Phys. Lett.* **1998**, *73* (1), 108–110.

(2) Gelinck, G. H.; Huitema, H. E. a; van Veenendaal, E.; Cantatore, E.; Schrijnemakers, L.; van der Putten, J. B. P. H.; Geuns, T. C. T.; Beenhakkers, M.; Giesbers, J. B.; Huisman, B.-H.; Meijer, E. J.; Benito, E. M.; Touwslager, F. J.; Marsman, A. W.; van Rens, B. J. E.; de Leeuw, D. M. Flexible Active-Matrix Displays and Shift Registers Based on Solution-Processed Organic Transistors. *Nat. Mater.* **2004**, *3* (2), 106–110.

(3) Bao, Z. N.; Feng, Y.; Dodabalapur, A.; Raju, V. R.; Lovinger, A. J. High-Performance Plastic Transistors Fabricated by Printing Techniques. *Chem. Mater.* **1997**, *9* (24), 1299–1301.

(4) Forrest, S. R. The Path to Ubiquitous and Low-Cost Organic Electronic Appliances on Plastic. *Nature* **2004**, *428* (6986), 911–918.

(5) Dong, H.; Zhu, H.; Meng, Q.; Gong, X.; Hu, W. Organic Photoresponse Materials and Devices. *Chem. Soc. Rev.* **2012**, *41* (5), 1754–1808.

(6) Meijer, E. J.; de Leeuw, D. M.; Setayesh, S.; van Veenendaal, E.; Huisman, B. H.; Blom, P. W. M.; Hummelen, J. C.; Scherf, U.; Kadam, J.; Klapwijk, T. M. Solution-Processed Ambipolar Organic Field-Effect Transistors and Inverters. *Nat. Mater.* **2003**, *2* (10), 678–682.

(7) Anthopoulos, T. D.; De Leeuw, D. M.; Cantatore, E.; Setayesh, S.; Meijer, E. J.; Tanase, C.; Hummelen, J. C.; Blom, P. W. M. Organic Complementary-like Inverters Employing Methanofullerene-Based Ambipolar Field-Effect Transistors. *Appl. Phys. Lett.* **2004**, *85* (18), 4205–4207.

(8) Crone, B.; Dodabalapur, A.; Lin, Y. Y.; Filas, R. W.; Bao, Z.; LaDuca, A.; Sarpeshkar, R.; Katz, H. E.; Li, W. Large-Scale Complementary Integrated Circuits Based on Organic Transistors. *Nature* **2000**, *403* (6769), 521–523.

(9) Smits, E.; Anthopoulos, T.; Setayesh, S.; van Veenendaal, E.; Coehoorn, R.; Blom, P.; de Boer, B.; de Leeuw, D. Ambipolar Charge Transport in Organic Field-Effect Transistors. *Phys. Rev. B* **2006**, *73* (20), 205316.

(10) Wakahara, T.; D'Angelo, P.; Miyazawa, K.; Nemoto, Y.; Ito, O.; Tanigaki, N.; Bradley, D. D. C.; Anthopoulos, T. D. Fullerene/Cobalt Porphyrin Hybrid Nanosheets with Ambipolar Charge Transporting Characteristics. *J. Am. Chem. Soc.* **2012**, *134* (17), 7204–7206.

(11) Hepp, A.; Heil, H.; Weise, W.; Ahles, M.; Schmechel, R.; von Seggern, H. Light-Emitting Field-Effect Transistor Based on a Tetracene Thin Film. *Phys. Rev. Lett.* **2003**, *91* (15), 157406.

(12) Swensen, J. S.; Soci, C.; Heeger, A. J. Light Emission from an Ambipolar Semiconducting Polymer Field-Effect Transistor. *Appl. Phys. Lett.* **2005**, *87* (25), 253511.

(13) Smits, E. C. P.; Setayesh, S.; Anthopoulos, T. D.; Buechel, M.; Nijssen, W.; Coehoorn, R.; Blom, P. W. M.; De Boer, B.; De Leeuw, D. M. Near-Infrared Light-Emitting Ambipolar Organic Field-Effect Transistors. *Adv. Mater.* **2007**, *19* (5), 734–738.

(14) Marjanović, N.; Singh, T. B.; Dennler, G.; Günes, S.; Neugebauer, H.; Sariciftci, N. S.; Schwödiauer, R.; Bauer, S. Photoresponse of Organic Field-Effect Transistors Based on Conjugated Polymer/Fullerene Blends. *Org. Electron. physics, Mater. Appl.* **2006**, *7* (4), 188–194.

(15) Anthopoulos, T. D.; Wöbkenberg, P. H.; Bradley, D. D. C. Light-Sensing Ambipolar Organic Transistors for Optoelectronic Applications. *Proc. SPIE* **2008**, *6999*, 69990X.

(16) Kufer, D.; Konstantatos, G. Photo-FETs: Phototransistors Enabled by 2D and 0D Nanomaterials. *ACS Photonics* **2016**, *3* (12), 2197–2210.

(17) Baeg, K. J.; Binda, M.; Natali, D.; Caironi, M.; Noh, Y. Y. Organic Light Detectors: Photodiodes and Phototransistors. *Adv. Mater.* **2013**, *25* (31), 4267–4295.

(18) Gong, X.; Tong, M.; Xia, Y.; Cai, W.; Moon, J. S.; Cao, Y.; Yu, G.; Shieh, C.; Nilsson, B.; Heeger, A. J. High-Detectivity Polymer Photodetector with Spectral Response from 300 Nm to 1450 Nm. *Science (80-.).* **2009**, *325* (5948), 1665–1667.

(19) Arnold, M. S.; Zimmerman, J. D.; Renshaw, C. K.; Xu, X.; Lunt, R. R.; Austin, C. M.; Forrest, S. R. Broad Spectral Response Using Carbon Nanotube/Organic Semiconductor/C60 Photodetectors. *Nano Lett.* **2009**, *9* (9), 3354–3358.

(20) Antognazza, M. R.; Scherf, U.; Monti, P.; Lanzani, G. Organic-Based Tristimuli Colorimeter. *Appl. Phys. Lett.* **2007**, *90*, 163509.

(21) Nalwa, K. S.; Cai, Y.; Thoeming, A. L.; Shinar, J.; Shinar, R.; Chaudhary, S. Polythiophene-Fullerene Based Photodetectors: Tuning of Spectral Esponse and Application in Photoluminescence Based (Bio)Chemical Sensors. *Adv. Mater.* **2010**, *22* (37), 4157–4161.

(22) Gemayel, M. El; Treier, M.; Musumeci, C.; Li, C.; Mullen, K.; Samori, P. Tuning the Photoresponse in Organic Field-Effect Transistors. *J. Am. Chem. Soc.* **2012**, *134* (4), 2429–2433.

(23) Chikamatsu, M.; Nagamatsu, S.; Yoshida, Y.; Saito, K.; Yase, K.; Kikuchi, K. Solution-Processed n -Type Organic Thin-Film Transistors with High Field-Effect Mobility. *Appl. Phys. Lett.* **2005**, *87*, 203504.

(24) Kobayashi, S.; Takenobu, T.; Mon, S.; Fujiwara, A.; Iwasa, Y. Fabrication and Characterization of C60 Thin-Film Transistors with High Field-Effect Mobility. *Appl. Phys. Lett.* **2003**, *82* (25), 4581–4583.

(25) Waldauf, C.; Schilinsky, P.; Perisutti, M.; Hauch, J.; Brabec, C. J. Solution-Processed Organic n-Type Thin-Film Transistors. *Adv. Mater.* **2003**, *15* (24), 2084–2088.

(26) Wobkenberg, P. H.; Bradley, D. D. C.; Kronholm, D.; Hummelen, J. C.; de Leeuw, D. M.; Colle, M.; Anthopoulos, T. D. High Mobility N-Channel Organic Field-Effect Transistors Based on Soluble C60 and C70 Fullerene Derivatives. *Synth. Met.* **2008**, *158* (11), 468–472.

(27) Shkunov, M.; Simms, R.; Heeney, M.; Tierney, S.; McCulloch, I. Ambipolar Field-Effect Transistors Based on Solution-Processable Blends of Thieno[2,3-b]Thiophene Terthiophene Polymer and Methanofullerenes. *Adv. Mater.* **2005**, *17* (21), 2608–2612.

(28) Cho, S.; Yuen, J.; Kim, J. Y.; Lee, K.; Heeger, A. J. Ambipolar Organic Field-Effect Transistors Fabricated Using a Composite of Semiconducting Polymer and Soluble Fullerene. *Appl. Phys. Lett.* **2006**, *89*, 153505.

(29) Wei, Q.; Tajima, K.; Hashimoto, K. Bilayer Ambipolar Organic Thin-Film Transistors and Inverters Prepared by the Contact-Film-Transfer Method. *ACS Appl. Mater. Interfaces* **2009**, *1* (9), 1865–1868.

(30) Ma, W.; Yang, C.; Gong, X.; Lee, K.; Heeger, A. J. Thermally Stable, Efficient Polymer Solar Cells with Nanoscale Control of the Interpenetrating Network Morphology. *Adv. Funct. Mater.* **2005**, *15* (10), 1617–1622.

(31) Li, G.; Shrotriya, V.; Huang, J.; Yao, Y.; Moriarty, T.; Emery, K.; Yang, Y. High-Efficiency Solution Processable Polymer Photovoltaic Cells by Self-Organization of Polymer Blends. *Nat. Mater.* **2005**, *4* (11), 864–868.

(32) Kim, Y.; Cook, S.; Tuladhar, S. M.; Choulis, S. A.; Nelson, J.; Durrant, J. R.; Bradley, D. D. C.; Giles, M.; McCulloch, I.; Ha, C.-S.; Ree, M. A Strong Regioregularity Effect in Self-Organizing Conjugated Polymer Films and High-Efficiency Polythiophene:Fullerene Solar Cells. *Nat. Mater.* **2006**, *5* (3), 197–203.

(33) Hwang, I. W.; Soci, C.; Moses, D.; Zhu, Z.; Waller, D.; Gaudiana, R.; Brabec, C. J.; Heeger, A. J. Ultrafast Electron Transfer and Decay Dynamics in a Small Band Gap Bulk Heterojunction Material. *Adv. Mater.* **2007**, *19* (17), 2307–2312.

(34) Scharber, M. C.; Mühlbacher, D.; Koppe, M.; Denk, P.; Waldauf, C.; Heeger, A. J.; Brabec, C. J. Design Rules for Donors in Bulk-Heterojunction Solar Cells - Towards 10 % Energy-Conversion Efficiency. *Adv. Mater.* **2006**, *18* (6), 789–794.

(35) Anthopoulos, T. D.; Tanase, C.; Setayesh, S.; Meijer, E. J.; Hummelen, J. C.; Blom, P. W. M.; De Leeuw, D. M. Ambipolar Organic Field-Effect Transistors Based on a Solution-Processed Methanofullerene. *Adv. Mater.* **2004**, *16* (23–24), 2174–2179.

(36) Ball, J. M.; Bouwer, R. K. M.; Kooistra, F. B.; Frost, J. M.; Qi, Y.; Domingo, E. B.; Smith, J.; De Leeuw, D. M.; Hummelen, J. C.; Nelson, J.; Kahn, A.; Stingelin, N.; Bradley, D. D. C.; Anthopoulos, T. D. Soluble Fullerene Derivatives: The Effect of Electronic Structure on Transistor Performance and Air Stability. *J. Appl. Phys.* **2011**, *110*, 014506.

(37) Chua, L.; Zaumseil, J.; Chang, J.; Ou, E. C.-W.; Ho, P. K.-H.; Sirringhaus, H.; Friend, R. H. General Observation of N-Type Field-Effect Behaviour in Organic Semiconductors. *Nature* **2005**, *434* (7030), 194–199.

(38) Saudari, S. R.; Frail, P. R.; Kagan, C. R. Ambipolar Transport in Solution-Deposited Pentacene Transistors Enhanced by Molecular Engineering of Device Contacts. *Appl. Phys. Lett.* **2009**, *95*, 023301.

(39) De Boer, B.; Hadipour, A.; Mandoc, M. M.; Van Woudenbergh, T.; Blom, P. W. M. Tuning of Metal Work Functions with Self-Assembled Monolayers. *Adv. Mater.* **2005**, *17* (5), 621–625.

(40) Hong, J. P.; Park, A. Y.; Lee, S.; Kang, J.; Shin, N.; Yoon, D. Y. Tuning of Ag Work Functions by Self-Assembled Monolayers of Aromatic Thiols for an Efficient Hole Injection for Solution Processed Triisopropylsilylethynyl Pentacene Organic Thin Film Transistors. *Appl. Phys. Lett.* **2008**, *92*, 143311.

(41) Evans, S. D.; Ulman, A. Surface Potential Studies of Alkyl-Thiol Monolayers Adsorbed on Gold. *Chem. Phys. Lett.* **1990**, *170* (5–6), 462–466.

(42) Van Duren, J. K. J.; Mihailetchi, V. D.; Blom, P. W. M.; Van Woudenbergh, T.; Hummelen, J. C.; Rispens, M. T.; Janssen, R. A. J.; Wienk, M. M. Injection-Limited Electron Current in a Methanofullerene. *J. Appl. Phys.* **2003**, *94* (7), 4477–4479.

(43) Zaumseil, J.; Sirringhaus, H. Electron and Ambipolar Transport in Organic Field-Effect Transistors. *Chem. Rev.* **2007**, *107*, 1296–1323.

(44) Diemer, P. J.; Lamport, Z. A.; Mei, Y.; Ward, J. W.; Goetz, K. P.; Li, W.; Marcia, M.; Guthold, M.; Anthony, J. E.; Jurchescu, O. D.; Diemer, P. J.; Lamport, Z. A.; Mei, Y.; Ward, J. W.; Goetz, K. P.; Li, W.; Payne, M. M.; Guthold, M.; Anthony, J. E. Quantitative Analysis of the Density of Trap States at the Semiconductor-Dielectric Interface in Organic Field-Effect Transistors Quantitative Analysis of the Density of Trap States at the Semiconductor-Dielectric Interface in Organic Field-Effect Transis. *Org. Electron.* **2015**, *107*, 103303.

(45) Nugraha, M. I.; Hausermann, R.; Bisri, S. Z.; Matsui, H.; Sytnyk, M.; Heiss, W.; Takeya, J.; Loi, M. A. High Mobility and Low Density of Trap States in Dual-Solid-Gated PbS Nanocrystal Field-Effect Transistors. *Adv. Mater.* **2015**, *27* (12), 2107–2112.

(46) Hamilton, M. C.; Martin, S.; Kanicki, J. Thin-Film Organic Polymer Phototransistors. *IEEE Trans. Electron Devices* **2004**, *51* (6), 877–885.

(47) Bube, R. H. *Photoelectronic Properties of Semiconductors*; Cambridge University Press, 1992.

(48) Johnson, N. M.; Chiang, A. Highly Photosensitive Transistors in Single-Crystal Silicon Thin Films on Fused Silica. *Appl. Phys. Lett.* **1984**, *45* (10), 1102–1104.

(49) Madjar, A.; Herczfeld, P. R.; Paolella, A. Analytical Model for Optically Generated Currents in GaAs MESFETs. *IEEE Trans. Microw. Theory Tech.* **1992**, *40* (8), 1681–1691.

(50) Caranzi, L.; Pace, G.; Sassi, M.; Beverina, L.; Caironi, M. Transparent and Highly Responsive Phototransistors Based on a Solution-Processed, Nanometers-Thick Active Layer, Embedding a High-Mobility Electron-Transporting Polymer and a Hole-Trapping Molecule. *ACS Appl. Mater. Interfaces* **2017**, *9* (34), 28785–28794.

(51) Romero, M. A.; Martinez, M. A. G.; Herczfeld, P. R. An Analytical Model for the Photodetection Mechanisms in High-Electron Mobility Transistors. *IEEE Trans. Microw. Theory Tech.* **1996**, *44* (12 PART 1), 2279–2287.

(52) Takanashi, Y.; Takahata, K.; Muramoto, Y. Characteristics of InAlAs/InGaAs High-Electron-Mobility Transistors under Illumination with Modulated Light. *IEEE Trans. Electron Devices* **1999**, *46* (12), 2271–2277.

(53) Anthopoulos, T. D. Electro-Optical Circuits Based on Light-Sensing Ambipolar Organic Field-Effect Transistors. *Appl. Phys. Lett.* **2007**, *91* (11), 113513.

(54) Labram, J. G.; Wöbkenberg, P. H.; Bradley, D. D. C.; Anthopoulos, T. D. Low-Voltage Ambipolar Phototransistors Based on a Pentacene/PC 61BM Heterostructure and a Self-Assembled Nano-Dielectric. *Org. Electron. physics, Mater. Appl.* **2010**, *11* (7), 1250–

1254.

(55) Li, F.; Ma, C.; Wang, H.; Hu, W.; Yu, W.; Sheikh, A. D.; Wu, T. Ambipolar Solution-Processed Hybrid Perovskite Phototransistors. *Nat. Commun.* **2015**, *6*, 8238.

(56) Konstantatos, G.; Badioli, M.; Gaudreau, L.; Osmond, J.; Bernechea, M.; de Arquer, F. P. G.; Gatti, F.; Koppens, F. H. L. Hybrid Graphene–quantum Dot Phototransistors with Ultrahigh Gain. *Nat. Nanotechnol.* **2012**, *7* (6), 363–368.

(57) Yu, H.; Bao, Z.; Oh, J. H. High-Performance Phototransistors Based on Single-Crystalline n-Channel Organic Nanowires and Photogenerated Charge-Carrier Behaviors. *Adv. Funct. Mater.* **2013**, *23* (5), 629–639.

(58) Zhu, M.; Lv, S.; Wang, Q.; Zhang, G.; Lu, H.; Qiu, L. Enhanced Near-Infrared Photoresponse of Organic Phototransistors Based on Single-Component Donor–acceptor Conjugated Polymer Nanowires. *Nanoscale* **2016**, *8* (14), 7738–7748.

(59) Zhang, H.; Zhang, Y.; Song, X.; Yu, Y.; Cao, M.; Che, Y.; Wang, J.; Yang, J.; Dai, H.; Zhang, G.; Yao, J. High Performance PbSe Colloidal Quantum Dot Vertical Field Effect Phototransistors. *Nanotechnology* **2016**, *27* (42), 425204.

(60) Lee, H. S.; Min, S. W.; Chang, Y. G.; Park, M. K.; Nam, T.; Kim, H.; Kim, J. H.; Ryu, S.; Im, S. MoS 2 Nanosheet Phototransistors with Thickness-Modulated Optical Energy Gap. *Nano Lett.* **2012**, *12* (7), 3695–3700.

(61) Cho, M. Y.; Kim, S. J.; Han, Y. D.; Park, D. H.; Kim, K. H.; Choi, D. H.; Joo, J. Highly Sensitive, Photocontrolled, Organic Thin-Film Transistors Using Soluble Star-Shaped Conjugated Molecules. *Adv. Funct. Mater.* **2008**, *18* (19), 2905–2912.

(62) Kim, K. H.; Bae, S. Y.; Kim, Y. S.; Hur, J. A.; Hoang, M. H.; Lee, T. W.; Cho, M. J.; Kim, Y.; Kim, M.; Jin, J. Il; Kim, S. J.; Lee, K.; Lee, S. J.; Choi, D. H. Highly Photosensitive J-Aggregated Single-Crystalline Organic Transistors. *Adv. Mater.* **2011**, *23* (27), 3095–3099.

(63) Lucas, B.; El Amrani, A.; Chakaroun, M.; Ratier, B.; Antony, R.; Moliton, A. Ultraviolet Light Effect on Electrical Properties of a Flexible Organic Thin Film Transistor. *Thin Solid Films* **2009**, *517* (23), 6280–6282.

(64) Xu, H.; Li, J.; Leung, B. H. K.; Poon, C. C. Y.; Ong, B. S.; Zhang, Y.; Zhao, N. A High-Sensitivity near-Infrared Phototransistor Based on an Organic Bulk Heterojunction. *Nanoscale* **2013**, *5* (23), 11850–11855.

(65) Park, S.; Kim, S. J.; Nam, J. H.; Pitner, G.; Lee, T. H.; Ayzner, A. L.; Wang, H.; Fong, S. W.; Vosgueritchian, M.; Park, Y. J.; Brongersma, M. L.; Bao, Z. Significant Enhancement of Infrared Photodetector Sensitivity Using a Semiconducting Single-

Walled Carbon Nanotube/C60 Phototransistor. *Adv. Mater.* **2015**, *27* (4), 759–765.

(66) Luo, X.; Du, L.; Lv, W.; Sun, L.; Li, Y.; Peng, Y.; Zhao, F.; Zhang, J.; Tang, Y.; Wang, Y. Charge-Transport Interfacial Modification Enhanced Ultraviolet (UV)/near-UV Phototransistor with High Sensitivity and Fast Response Speed. *Synth. Met.* **2015**, *210*, 230–235.

(67) Wöbkenberg, P. H.; Labram, J. G.; Swiecicki, J.-M.; Parkhomenko, K.; Sredojevic, D.; Gisselbrecht, J.-P.; de Leeuw, D. M.; Bradley, D. D. C.; Djukic, J.-P.; Anthopoulos, T. D. Ambipolar Organic Transistors and Near-Infrared Phototransistors Based on a Solution-Processable Squarilium Dye. *J. Mater. Chem.* **2010**, *20* (18), 3673.

Chapter 5 Hybrid Inorganic Ambipolar Transistors with Dye Functionalization for Efficient and Fast Photo-Sensing Application

Metal oxides are attractive semiconducting materials for use in high carrier mobility thin-film transistors and integrated circuits. However, the wide optical bandgap and optical instability limit their photodetector applications. In this chapter, a novel hybrid heterostructure transistor based on indium oxide (In_2O_3) and copper thiocyanate (CuSCN) is presented. The presence of the p-n (CuSCN/In_2O_3) junction is found to enable ambipolar transistor operation, while maintaining a high optical transparency across the visible spectrum. The incorporation of a light-absorbing organic dye D102 in this transparent heterostructure enables the realization of phototransistors with remarkably enhanced photoresponse to green illumination as compared to the control In_2O_3/CuSCN bilayer device. More interestingly, the trilayer phototransistor exhibits high switching speed with a response time of ~1 ms. The fast switching behaviour is attributed to the synergistic effects of efficient charge transport across the In_2O_3/dye/CuSCN channel as well as the minimization of the oxygen-vacancy-related photoconductivity. The hybrid phototransistor developed here offers a universal approach to improve the speed of the oxide-based phototransistors for efficient and fast photo-sensing application.

5.1 Introduction

Solution processable metal oxides represent an attractive family of semiconducting materials for use in thin-film transistors and integrated circuits due to their high carrier mobility, low process temperature and excellent device parameter uniformity.[1–3] When it comes down to photodetector applications, however, the large optical bandgap of metal oxides limits their application majorly to ultraviolet (UV) photodetection.[4–6] Moreover, oxide-based photodetectors are known to exhibit unstable operating characteristics under continuous illumination.[7–10] This optical instability is observed even under visible illuminations, the energy of which is below the bandgap of metal oxides.[11,12] The phenomenon of sub-bandgap photo absorption is generally attributed to defect states located within the bandgap of metal oxide semiconductors.[11–18] For example, one widely-accepted explanation is that the deep and neutral oxygen vacancy states (V_O) can be ionised to shallow donor states (V_O") under visible light illumination, donating electrons to the conduction band of the metal oxide.[13,14] These ionised oxygen defects remain ionised due to the creation of an energy barrier against neutralisation by the outward relaxation of bonds surrounding the V_O sites,[14] resulting in materials remaining high conductivity even after the removal of light stimulation, i.e. so-called persistent photoconductivity (PPC).[14,19]

Although PPC has been reported to give rise to high optical detectivity in the oxide-based photodetector,[20,21] it can be problematic in practical applications. Such a phenomenon, which has proven to be able to maintain up to hours,[12,15,22] severely prolongs the device relaxation time and hence limits the operation speed of the oxide-based photodetectors. To eliminate the adverse effects from PPC, several studies have suggested a gate pulse method that can be implemented in three-terminal device architecture to effectively remove PPC.[18,23] This method, by applying a positive voltage pulse to the gate terminal, is thought to accelerate the recombination of electrons and ionised defect states, hence erase PPC immediately. Despite the success of eliminating PPC, this gate pulse method requires a more complicated operation scheme for the phototransistors. Alternatively, a few recent studies have reported fast oxide-based phototransistors by integrating n-type metal oxides with p-type semiconductors like poly (3-hexylthiophene) (P3HT), copper phthalocyanine (CuPc) and stannous oxide (SnO) to form a p-n heterojunction structure.[24–26] This heterojunction structure, which is initially designed for enhancing the photodetection of oxide-based devices in the visible light region, has been surprisingly found to enable the phototransistor to achieve fast device relaxation after the removal of illumination. The enhanced recovery process is believed to be due to the quick

recombination of the light-induced electrons and the holes inside the p-type capping layer. This hybrid method suggests a new routine towards fast photodetectors based on oxide semiconductors.

This chapter represents the development of a novel p-n heterostructure hybrid inorganic transistor based on indium oxide (In_2O_3) and copper thiocyanate (CuSCN). The presence of the p-n (CuSCN/In_2O_3) junction based on two large bandgap semiconductors enables ambipolar transistor operation, while maintaining high optical transparency across the visible electromagnetic spectrum (400-700 nm). More interestingly, it is found that the slow sub-bandgap photoconductivity from the oxide layer was effectively suppressed by the introduction of the p-n heterojunction. The ability of visible light detection is then enabled through the incorporation of a green light-absorbing organic dye D102 in the vicinity of the heterostructure during growth. The trilayer CuSCN/dye/In_2O_3 channel phototransistor shows a remarkably enhanced photoresponse to green light as compared with the control In_2O_3/CuSCN-based devices. In addition, the switching behaviour of the trilayer phototransistor is found to be very fast with a response time of ~1 ms. The latter is attributed to the synergistic effects of efficient charge transport across the multilayer channel and minimisation of the PPC by the p-n heterojunction. This hybrid transistor developed here provides an approach towards high-speed oxide-based phototransistor without the requirement of the additional gate pulse. In addition, due to the high optical transparency of the transistor channel, this hybrid structure is ideally compatible with other light absorbing materials to realise either wavelength-selective or panchromatic photodetectors.

5.2 Methods

5.2.1 Film deposition

The deposition of the In_2O_3 film was performed by a sol-gel based approach.[27] The solution was prepared by dissolving anhydrous indium nitrate ($In(NO_3)_3$) in 2-methoxyethanol (2ME) at a concentration of 20 mg/ml, followed by a 12-hour stirring at room temperature before use. The metal complex solute can be dissolved in the 2ME due to the organic ligands surrounding the central metal ion.[28] Within the solution it is then possible for a sol-gel to form as the precursor undergoes hydrolysis and polycondensation.[29] The solution was then deposited on a glass substrate via spin-casting at a spin speed of 4000 rpm for 30 seconds. After the deposition, the obtained film was annealed at 200 °C for 40 minutes in ambient atmosphere. The thermal

energy will help removing the residual solvent and ligands, and the formation of a thin In_2O_3 film.

To produce the CuSCN film, a solution was prepared by dissolving the CuSCN in dipropyl sulphide (DPS) at a concentration of 20mg/ml. The solution was deposited by spin-casting at a spin rate of 1200 rpm for 60 seconds, followed by a 10 minutes annealing at 80 °C in nitrogen.

D102 dye functionalization was performed by immersing the substrates with freshly deposited In_2O_3 film into a 50:50 vol. % mixed acetonitrile and tert-butanol solution at a concentration of 1mM for 30 minutes. Excess dye was washed off using deionised water, and the substrates were then dried in nitrogen at 80 °C for 10 minutes.

5.2.2 Film characterisation

Two thin film characterisation techniques were employed in this study. The film transmission/absorption spectra were investigated using a Shimadzu UV2600 UV-Vis spectrometer equipped with an ISR-2600Plus integrating sphere. Samples for the UV-Vis measurement were prepared on quartz substrates following the same material deposition process described above. The surface morphologies of the various deposited films were studied using an Agilent 5500 atomic force microscope (AFM) in intermitted contact mode. The samples for AFM measurement were prepared on glass substrates identical to that used for the transistor fabrication.

5.2.3 Transistor fabrication

Before the fabrication process, glass substrates (2 cm × 2 cm) were cleaned in a detergent solution (DECON90), deionised water, acetone and 2-propanol (IPA) using an ultrasonic bath for 10 minutes each. The cleaning process was followed by a 15 minutes UV-Ozone treatment to improve the wettability of the substrate surface. The active channel material deposition followed the same film deposition process as described in section 5.2.1. To produce the bilayer metal contacts, 20nm aluminium and 20nm gold were thermally evaporated onto the substrates through shadow masks. The shadow masks with specific source and drain(S-D) patterns define the dimension of transistors with channel length(L) and channel width(W) of 100μm and 1mm, respectively. The gate dielectric layer used here is a fluoropolymer CYTOP (Asahi Glass) and was spin-coated at 2000 rpm for 60 seconds, followed by a 10-hour drying in high vacuum ($\sim 10^{-7}$ bar). The geometric capacitance of the produced CYTOP dielectric was 2.1 nF/cm^2. The

device fabrication process was completed with the thermal evaporation of 100nm aluminium gate electrode on top of the CYTOP layer through a shadow mask.

5.2.4 Electrical and optoelectronic characterisation

Electrical characterisation of all transistors was carried out using an Agilent B2902A source/measure unit in dry nitrogen atmosphere. Optoelectronic characterisation was performed by measuring the transfer and/or output characteristics of the transistors in a dark environment and under illumination from a green light-emitting diode (LED) with an electroluminescence emission peak at 525 nm. The LED was driven using a Keithley 2400 Source Meter Unit. The various light intensities generated by the LED under different driving conditions were measured using a Thorlabs S120UV power sensor. The EQE spectral characterisation was carried out by measuring the photocurrent of the transistor under monochromatic illumination from a Xenon arc lamp in combination with a dual-grating monochromator. The illumination intensities were calibrated by the same Thorlabs S120UV power sensor. Dynamic characterisation was performed by measuring the temporal response of the transistor/logic circuit to an external optical stimulus (i.e. light pulse). The light pulses were generated by driving the LED with an Agilent 33220A function generator. In transistor dynamic characterisation, the transistor was biased at fixed drain and gate voltages using an Agilent B2902A source/measure unit and the variation in channel current was amplified by a Stanford Research Systems SR570 current preamplifier and recorded by an Agilent DSO6014A oscilloscope. In logic circuit demonstration, the two identical transistors were biased using a Keithley 4200-SCS semiconductor characterisation system and the variation in the output signal was recorded by the Agilent DSO6014A oscilloscope.

5.3 Hybrid Inorganic Transistor Based on CuSCN/In_2O_3 Heterostructure

5.3.1 Film characterisation

The optical property of the CuSCN/In_2O_3 bilayer film was first investigated using an ultraviolet-visible (UV-Vis) spectrophotometer. **Figure 5.1** shows a set of transmittance spectra measured from the pristine In_2O_3 film and the CuSCN/In_2O_3 bilayer film deposited on quartz substrate. The pristine In_2O_3 film exhibits extremely high transparency of over 90% across the range of visible wavelengths (300-700 nm). The decrease in transmittance in the CuSCN/In_2O_3 film stack can be attributed to the increase in the film thickness of the bilayer film stack. Nevertheless, the bilayer film remains reasonably highly transparent with over 85%

transparency across the visible wavelength range due to the large optical bandgap of both materials.[30,31]

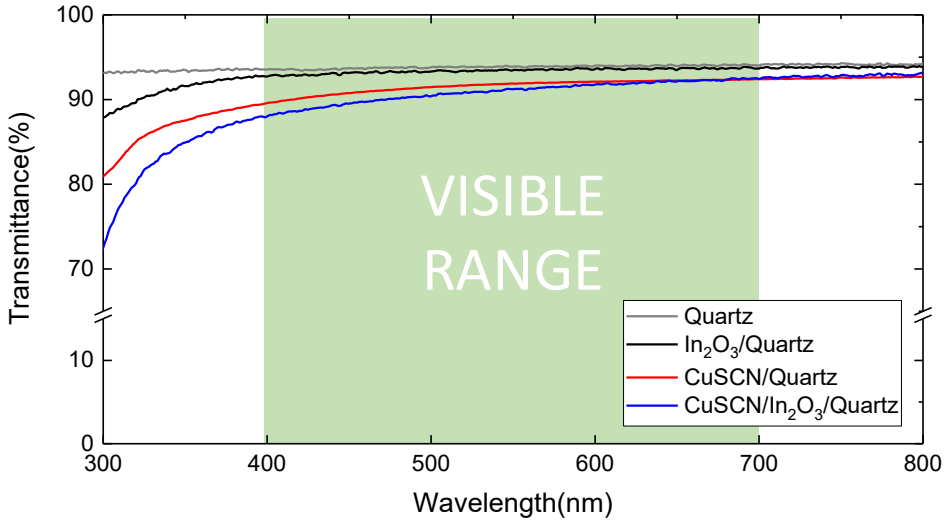


Figure 5.1: A set of UV-Vis transmittance spectra measured for In_2O_3 film and CuSCN/In_2O_3 bilayer film stack deposited on quartz substrate.

5.3.2 Transistor electrical characterisation

A hybrid inorganic transistor based on the CuSCN/In_2O_3 bilayer film was fabricated in a top-gate, middle-contact (TG-MC) configuration (**Figure 5.2a**). To achieve efficient injection for both electrons and holes from the source and drain electrodes to the corresponding energy level of the semiconductors, bilayer gold/aluminium electrodes were used. With the help of the bilayer electrodes, electrons are expected to be injected readily from the aluminium to the conduction band of In_2O_3 while holes are injected from the gold to the valence band of CuSCN, according to the energy-band diagram shown in **Figure 5.2b**. This device architecture, therefore, could ideally enable p-channel operation by the CuSCN layer with a hole-transporting channel formed at the interface between the CYTOP dielectric and the CuSCN, and n-channel operation by the In_2O_3 layer with an electron-transporting channel formed at the interface between the two semiconductors.

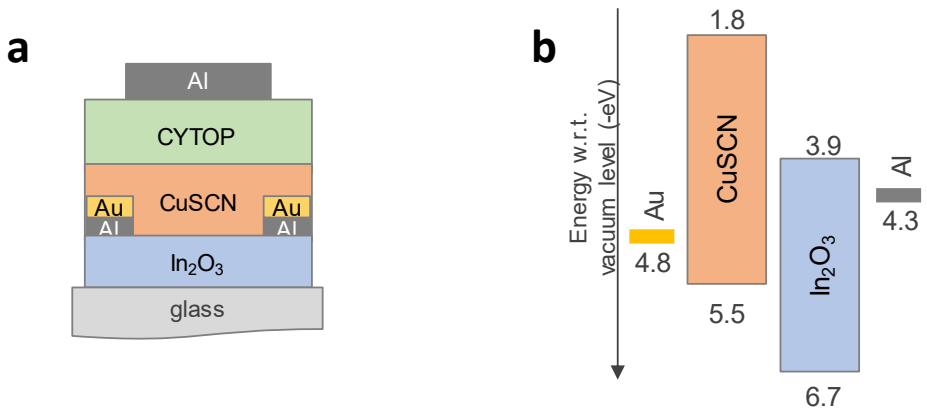


Figure 5.2: (**a**)A schematic of the top-gate, middle-contact transistor architecture developed in this study. (**b**) Energy level band diagram of In_2O_3, CuSCN, aluminium (Al) electrode and gold (Au) electrode.

The electrical properties of the fabricated transistor were investigated by measuring the transistor transfer characteristics in a dark environment. Since the middle-contact structure corresponds to the top-contact and bottom-contact for the In_2O_3 layer and the CuSCN layer respectively, control transistors based on sole In_2O_3 and sole CuSCN film with the corresponding configurations were also investigated for comparison. **Figure 5.3a** shows the transfer characteristics measured from the In_2O_3/CuSCN bilayer transistor with a positive drain voltage. The V-shape transfer characteristic, with one arm indicating electron accumulation and the other indicating hole accumulation, proves the ambipolar operation of this device architecture. One can notice that the transistor exhibits a severe imbalance in electron and hole transport, with higher current level and sharper slope in the electron accumulation region. This can be primarily attributed to the much higher electron mobility of In_2O_3 than the hole mobility of CuSCN, resulting in superior electron transport in the In_2O_3 layer than hole transport in the CuSCN layer. The difference in the mobility can also be seen in the transfer characteristics of the transistor with sole In_2O_3 and sole CuSCN film (as shown in **Figure 5.3 b** and **c**), even thought a less-efficient coplanar structure is employed in the In_2O_3 transistor. It is worth noting that a more balanced ambipolar transistor indeed can be obtained by altering the In_2O_3 deposition condition. However, this is achieved at the expense of sacrificing the high mobility of In_2O_3.

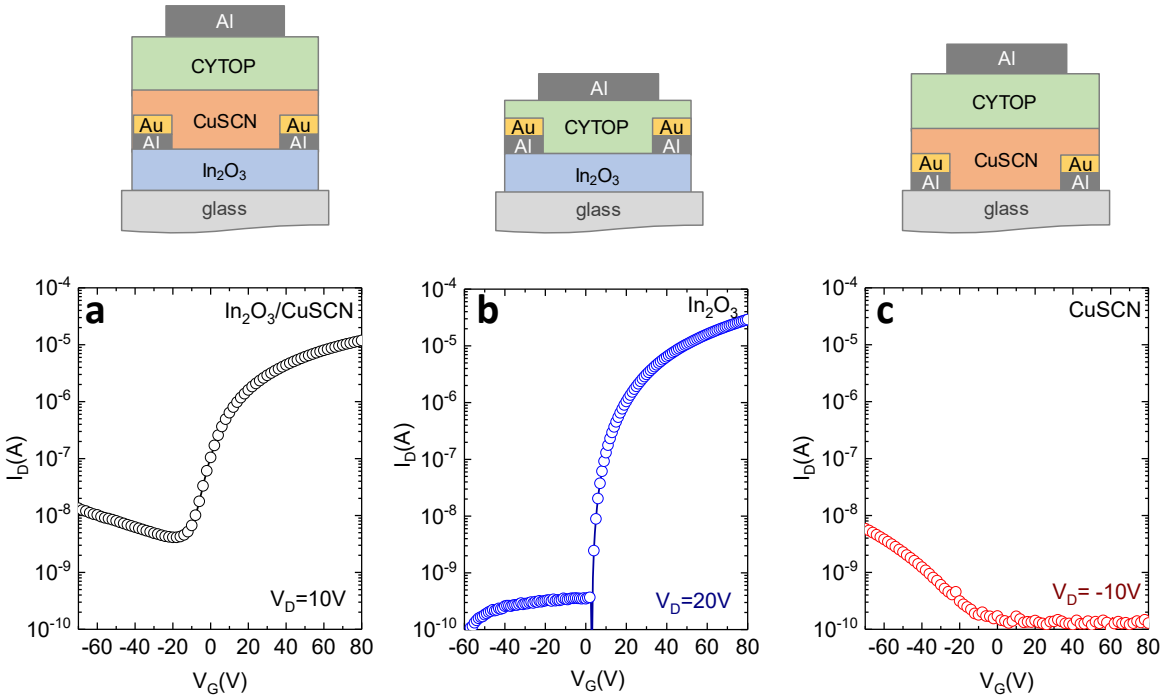


Figure 5.3: Transfer characteristics measured for transistor based on (**a**)CuSCN/In_2O_3 bilayer, (**b**) sole In_2O_3 film and (**c**)sole CuSCN film.

5.3.3 Transistor optoelectronic characterisation

Next, the optoelectronic property of the CuSCN/In_2O_3 bilayer transistor was investigated by illuminating the devices with a green LED light (EL peak at 525 nm). The obtained transfer characteristics are compared with those from the control In_2O_3 transistor (**Figure 5.4**). For the control device, the transfer characteristics under illumination show a negative shift on the threshold voltage and an increase in the drain current, indicating the occurrence of photo absorption under green light illumination, the photon energy of which is below the band gap of In_2O_3. This sub-bandgap photo absorption of the In_2O_3, as discussed above, is most likely attributed to the sub-gap states in the material, eventually resulting in persistent photoconductivity (PPC). In contrast, for the CuSCN/In_2O_3 bilayer device the variation in channel current under illumination is almost negligible, suggesting the sub-bandgap persistent photoconductivity originated from the In_2O_3 layer are effectively suppressed by the heterojunction structure. In the heterojunction structure, the additional photogenerated carriers (i.e. electrons) originated from the In_2O_3 tend to accumulate at the CuSCN/In_2O_3 interface under positive gate bias and could recombine immediately with holes in the CuSCN film, which lower the total photocarrier concentration and lead to the degradation of photoresponse to the green light. The suppression of PPC in the presented CuSCN/In_2O_3 bilayer device is particularly of interest as it could potentially enable photodetectors with faster response speed

and higher operation frequency to be made. In addition, this highly transparent device can be used practically as a stable, transparent driver circuit module which can completely avoid the influence of illumination stress.

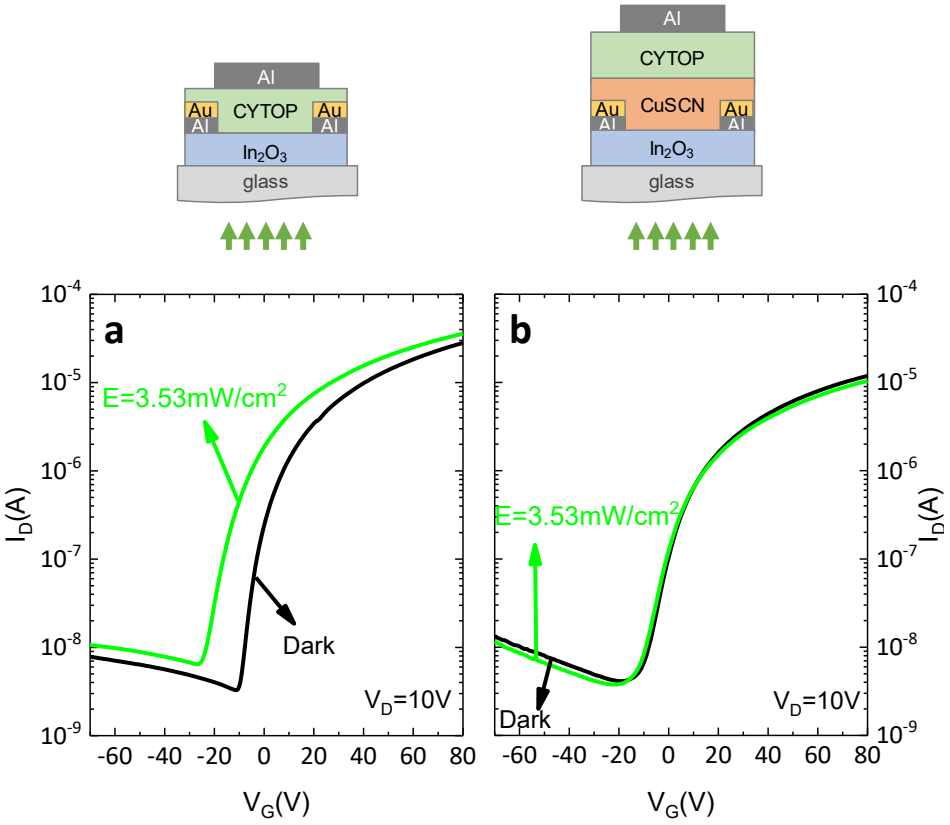


Figure 5.4: Optoelectronic characterisation of the transistor under the illumination of green LED with EL peak at 525 nm. Transfer characteristics obtained from (a) In_2O_3 transistor and (b) CuSCN/In_2O_3 bilayer transistor in the dark and under illumination. The black line indicates the I-V curve measured in the dark while the green one indicates that measured under an optical power density of 3.53 mW/cm^2.

5.4 Dye-Sensitized Hybrid Inorganic Phototransistor

Employing addition light-absorbing layer has proven to be an efficient way to extend the photo-sensing ability of oxide-based photodetectors to the visible light region. Several attempts on enhancing visible detection of oxide-based phototransistor by integrating with various materials such as low-dimensional nanomaterial, organic polymer, or organometal halide perovskite, have been reported.[25,32–34] Among all the materials, organic dye D102 is a strong candidate as the light sensitizer for metal oxides due to its successful demonstration in high efficiency dye-sensitized solar cells (DSSCs) [35,36] and high responsivity dye-sensitized oxide phototransistors[37,38]. This metal-free dye is able to bind to the surface of oxide film via its carboxylic anchoring group and to enhance the film absorption spectrum at the wavelength of

500nm. Therefore, D102 is used here as the light absorber to enable visible photodetection of the highly transparent CuSCN/In_2O_3 bilayer transistor. The functionalization of D102 was performed following the process as described in section 5.2.1.

5.4.1 Film characterisation

The influences of dye functionalization on the film properties were initially studied with two film characterisation techniques. Firstly, a UV-Vis spectrophotometer was used to investigate the presence of the D102 dye upon functionalization and the potential change in film absorption spectra (**Figure 5.5**). Compared with the pristine In_2O_3 film, the dye-sensitised D102/In_2O_3 film shows a new absorption peak at around 500 nm. The presence of the new absorption peak suggests the successful functionalization of dye D102 on the In_2O_3 film. For the CuSCN/D102/In_2O_3 trilayer film stack, a general increase in the absorption spectrum is observed across the whole wavelengths, which can be attributed to the increase in the total film thickness. However, the characteristic absorption peak from the D102 dye around 500 nm can still be observed. Such observation confirms that the dye D102 was not etched with sulphide solution during the deposition of CuSCN on top, confirming the successful introduction of dye D102 in between the CuSCN and In_2O_3 layer.

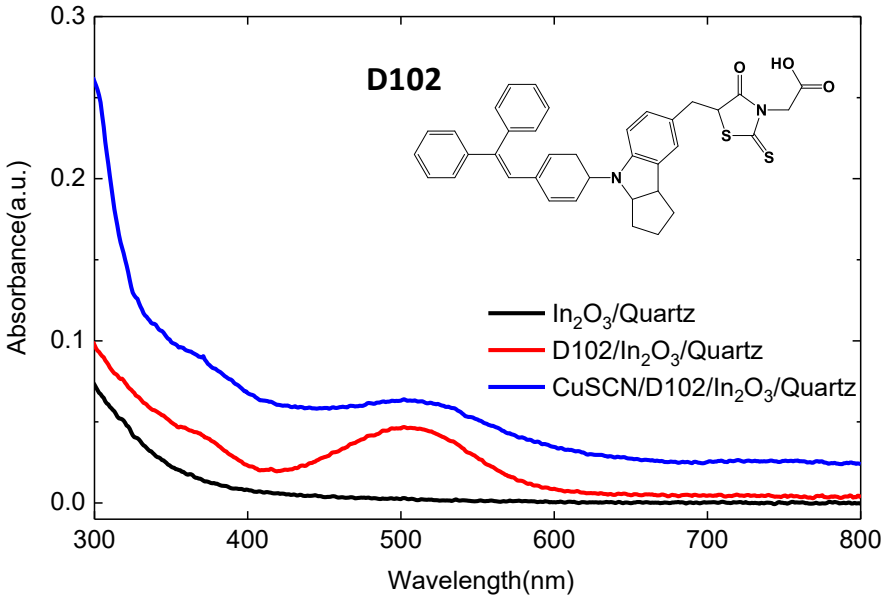


Figure 5.5: A set of UV-Vis absorption spectra measured for sole In_2O_3 film, dye-sensitised D102/In_2O_3 film and CuSCN/D102/In_2O_3 trilayer film stack deposited on quartz substrate. Inset shows the molecular structure of D102 dye.

The impact on the surface morphology of the films due to D102 functionalisation was studied with AFM in tapping mode. The representative topographical images and the corresponding statistic height distribution histograms are shown in **Figure 5.6**. The dye-sensitized D102/In_2O_3 film shows very similar topographical image as the pristine In_2O_3 film with similar root-mean-squared surface roughness of ~ 0.2 nm. This similarity can also be illustrated by the height distribution plots where no significant difference between the dye-sensitized D102/In_2O_3 film and pristine In_2O_3 film is observed. Such similarity in surface morphology can be explained by the fact that the D102 binds to the In_2O_3 surface via its carboxylic anchoring group and forms only a molecularly thin layer on the In_2O_3 surface[39]. Hence, no significant impact on the In_2O_3 surface morphology has been observed. On the other hand, the topographical images of CuSCN/In_2O_3 and CuSCN/D102/In_2O_3 film stack both appear elongated grains in oval-like shape, which are commonly observed in spin-cast CuSCN films from sulphide-based solutions.[40,41] Although similar oval-like gains are present in both film stacks, the grain length of CuSCN/D102/In_2O_3 trilayer film is found to be longer than that of CuSCN/ In_2O_3. Such difference is also illustrated in the height histogram where the CuSCN/D102/In_2O_3 trilayer film shows a wider height distribution with a larger root-mean-square roughness value (~1.8 nm) than that of CuSCN/In_2O_3 bilayer film (~1.3 nm). This variation in surface morphology is attributed to the fact that the top-most CuSCN films are deposited on different substrate materials, resulting in the difference in the grain growth of CuSCN film. This difference in surface morphology appears to support the conclusion that the functionalisation of a thin D102 layer in the trilayer film stack took place.

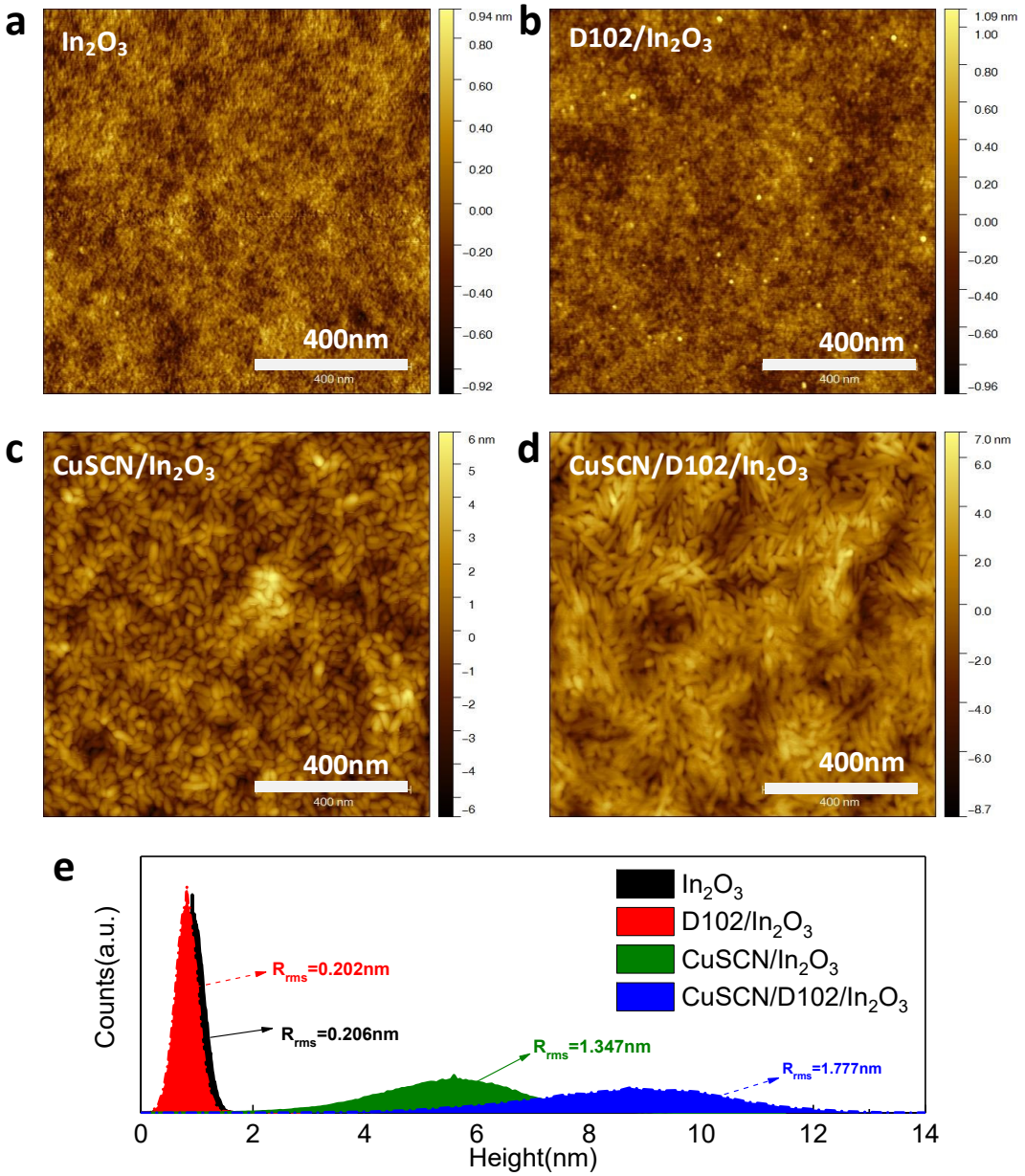


Figure 5.6: AFM images of the surface topography of (**a**) pristine In_2O_3 film, (**b**) dye-sensitised D102/In_2O_3 film, (**c**) bilayer CuSCN/In_2O_3 film and (**d**) trilayer CuSCN/D102/In_2O_3 film deposited on glass. (e)Height distribution extracted from the AFM images.

5.4.2 Trilayer transistor optoelectronic characterisation

Phototransistor based on the CuSCN/D102/In_2O_3 trilayer film was then fabricated in a TG-MC architecture. The transfer characteristics of the trilayer device were measured in the dark and under green illumination with various intensities as shown in **Figure 5.7b**. Compared with the control CuSCN/In_2O_3 bilayer device with negligible photoresponse (**Figure 5.7a**), the dye-sensitised trilayer device shows noticeable variation in the drain current under illumination, indicating a significantly enhanced photoresponse to the green illumination due to the

functionalization of the dye D102. Also, this photoresponse of the trilayer device shows different variation trend depending on device operation region, indicative of a strong dependence on the applied gate field. In negative V_G region, where the transistor is working in either depletion or hole accumulation mode, the drain current is found to increase with increasing illumination intensity. Such variation suggests that additional charges, most likely originated from the light absorber dye D102, are introduced in the transistor channel upon optical stimulation. Particularly, the amount of the photoinduced charge carriers under high-intensity illumination become comparable to the injected carriers by the gate field effect, resulting in the saturation in the drain current and hence weakened gate modulation. In positive V_G region, where the device is working in electron accumulation mode, an interesting founding is that the drain current under illumination is a bit lower than the dark current when the gate voltage is increased over a certain point. This negative photoresponse is most likely attributed to the enhanced scattering of electrons when the device is in the electron accumulation regime.[42,43] Similar phenomenon has also been reported by studies on other hybrid heterojunction phototransistors[34,44].

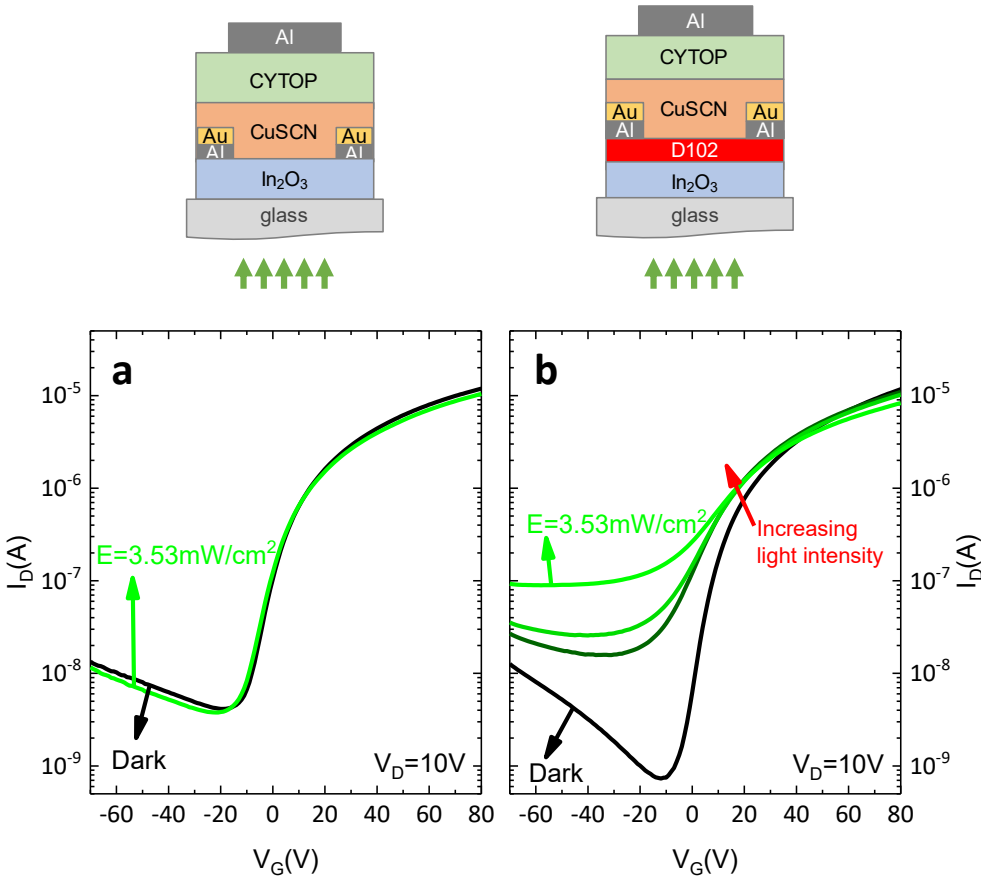


Figure 5.7: Optoelectronic characterisation of transistors with the illumination of green LED with EL peak at 525 nm. Transfer characteristics obtained from (**a**) CuSCN/In_2O_3 transistor and (**b**) CuSCN/D102/In_2O_3 transistor in the dark and under green illumination.

5.4.3 Spectral characterisation

To further explore the origin of the photogenerated carriers within the CuSCN/D102/In_2O_3 trilayer phototransistor, the spectral response of the device was investigated by illuminating the device with monochromatic light of different λ across a wide range of wavelengths at the same intensity. The corresponding external quantum efficiency (EQE) of the CuSCN/D102/In_2O_3 phototransistor can then be estimated following the equation:[45]

$$\eta = \frac{hc}{\lambda e} \cdot \frac{I_{ph}}{E_{opt} \cdot a} \tag{5.1}$$

where, I_{ph} is the photocurrent, E_{opt} is the illumination intensity, a is the device area, $hc/\lambda e$ is the photon energy in eV. The calculated EQE is plotted as a function of wavelength as shown in **Figure 5.8**. The EQE plot of the CuSCN/D102/In_2O_3 trilayer device exhibits a peak at around 500nm wavelength, which is coincident with the characteristic absorption peak of D102. This result is extremely revealing as it provides direct evidence of the photoresponse originating from the photoabsorption of dye D102 rather than the sub-bandgap absorption of In_2O_3.

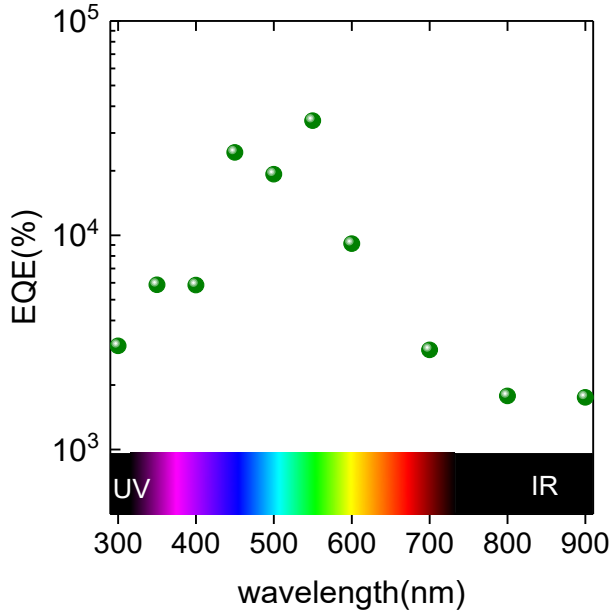


Figure 5.8: Spectral response of the CuSCN/D102/In_2O_3 trilayer phototransistor. EQE values were calculated from the transfer characteristics of the phototransistor biased at V_G = 20 V, V_D = 10 V and illuminated with wavelengths from 300 to 900 nm at fixed E_{opt} = 0.14 μW/cm^2.

With all the information presented so far, the mechanism for the carriers photogeneration within the CuSCN/D102/In_2O_3 trilayer phototransistor can be speculated. This mechanism, which should be similar to that in DSSCs, is attributed to the photoabsorption of dye D102, creating an excited state and free charge carriers. The difference in the energy level between D102 and CuSCN/In_2O_3 then allows electrons transfer from the LUMO of D102 to the conduction band of In_2O_3 and holes transfer from the HOMO of D102 to the valence band of CuSCN. This increases the carrier concentration within the transistor channel under illumination and hence the drain current. More importantly, unlike the dye-sensitised oxide phototransistor which suffers from a slow dye regeneration process through the slow back-transfer of electrons from the conduction band of oxide to the HOMO of dye,[37,46] the presence of a hole transporting channel by CuSCN in the trilayer device allows a more efficient dye-regenerating mechanism by hole transferring from the dye to the hole transporting layer.[47,48] Such an efficient dye-regeneration mechanism in principle should enable the phototransistor to exhibit much faster photo-switching behaviour.

5.4.4 Dynamic characterisation

To explore the operation speed of the CuSCN/D102/In_2O_3 trilayer phototransistor, the switching behaviour was studied by exposing the device to continuous green light pulses and monitoring the evolution of the channel current. A detailed description of the measurement setup is in section 5.2.3. **Figure 5.9a** shows the temporal response of the channel current to a train of light pulses 5 ms long. The rise time t_R and the fall time t_F were then calculated directly from current evolution yielding a rise time and a fall time of t_R = 0.53 ms and t_F = 0.60 ms, respectively, as well as a total response time of ~1 ms. It is worth noting that such response time in the millisecond scale already approaches the detection limit of the measurement setup due to the necessary trade-off between small-signal detection (nA) and the effective signal bandwidth of the current amplifier. This result, however, is still faster than most of the oxide-based phototransistors reported to date.[15,24–26,32,34,49] Here the fast response of the trilayer device is attributed to the suppression of PPC by heterojunction structure, and the efficient photocarrier generation and transport in the multilayer heterojunction structure.

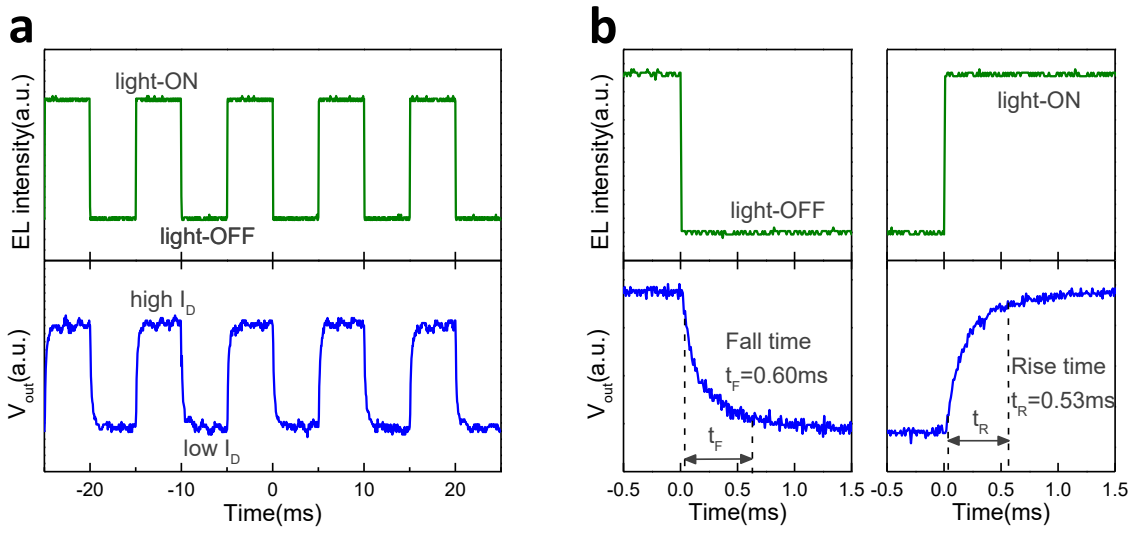


Figure 5.9: (**a**) Temporal response of the transistor channel current to a train of green light pulses. The transistor was biased at fixed V_G = -10 V and V_D = 10 V. (**b**) The enlarged channel current switch-on and -off behaviour for the rise and fall time analysis.

5.4.5 Gate-bias dependent figures of merit

To further quantitatively assess the performance metric of the CuSCN/D102/In_2O_3 trilayer phototransistor and identify the best operation condition for such device, three important figures of merit for photodetectors, i.e. the photosensitivity *P*, the responsivity *R* and the specific detectivity *D** were calculated from the transfer characteristics of the trilayer device. Since the photoresponse of the CuSCN/D102/In_2O_3 trilayer phototransistor exhibits a strong dependence on the applied gate field, these figures of merit should also be gate-dependent. The calculated *P*, *R* and *D** are plotted as a function of gate voltage (**Figure 5.10**). In **Figure 5.10a**, the photosensitivity *P* shows a peak at around V_G = -10V, revealing the highest ratio of photogenerated current to the dark current is obtained when the transistor is working in depletion mode. Such a peak value of photosensitivity can be explained by the fact that at this particular V_G the transistor channel is turned-off with the lowest drain current in the dark. The responsivity *R* (**Figure 5.10b**), on the other hand, exhibits a peak value at around V_G = 20V corresponding to the transistor operated in the electron accumulation mode. This peak value of *R* can be attributed to the improved photocarrier transport in In_2O_3 layer due to the high electron mobility and the strong gate field effect. However, as discussed in 5.4.2, the strong gate field can also lead to an enhanced electron scattering, which offsets the gain mechanism of transistor in the accumulation mode, resulting in a dramatic drop of the responsivity at V_G > 20 V. In the

case of the specific detectivity *D** (**Figure 5.10c**), a peak is found at around V_G = -10 V under the highest illumination intensity, which is similar to the photosensitivity. This similarity can be explained by the fact that a shot-noise-limit assumption is used here for noise analysis. Under this assumption, the noise level is proportional to the drain current in the dark and reaches its lowest value when the transistor is in depletion mode. However, it is noticeable that the peak value of specific detectivity shows a positive shift with decreasing light intensity. This is believed to be due to the signal amplification in the transistor accumulation mode becoming more prominent in the case of low light intensity.

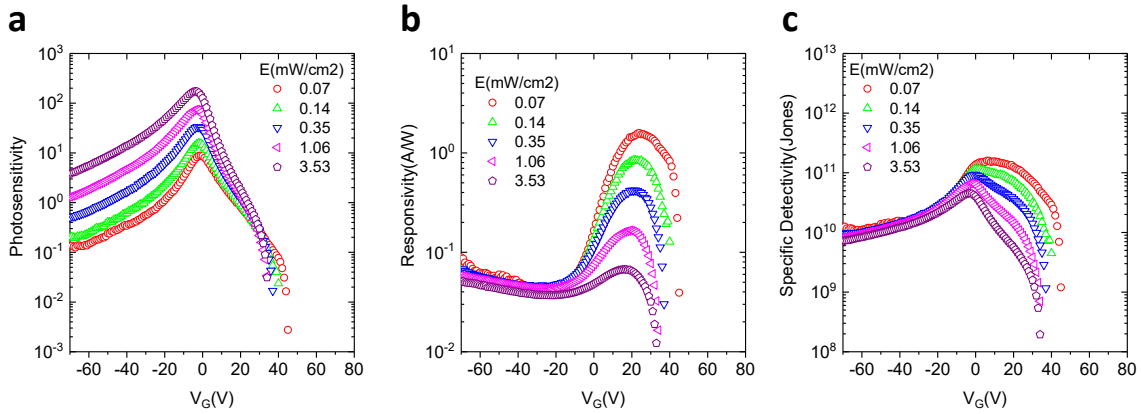


Figure 5.10: Gate-voltage dependent figures of merit (**a**) photosensitivity, (**b**) responsivity and (**c**) specific detectivity measured at V_D = -10 V under different illumination intensities.

5.4.6 Illumination dependent figures of merit

From the above gate-dependent analysis, two optimal gate biasing conditions, i.e. V_G = -10 V and V_G = 20 V, can be identified which can give rise to the best performance metric for the CuSCN/D102/In_2O_3 trilayer device as a photodetector. However, it is also noticed that the illumination intensity might affect device performance. Such effects relevant to the illumination intensity were then further investigated with the phototransistor fixed at the two optimal biasing conditions. The output characteristics of the transistor biased at these two V_G under various illumination intensities are shown in **Figure 5.11**. In both V_G cases, the drain currents of the phototransistor are found to be significantly modulated by the illumination intensity across the whole V_D range, suggesting that the illumination intensity has an equivalent modulation effect on the transistor channel as the gate field.

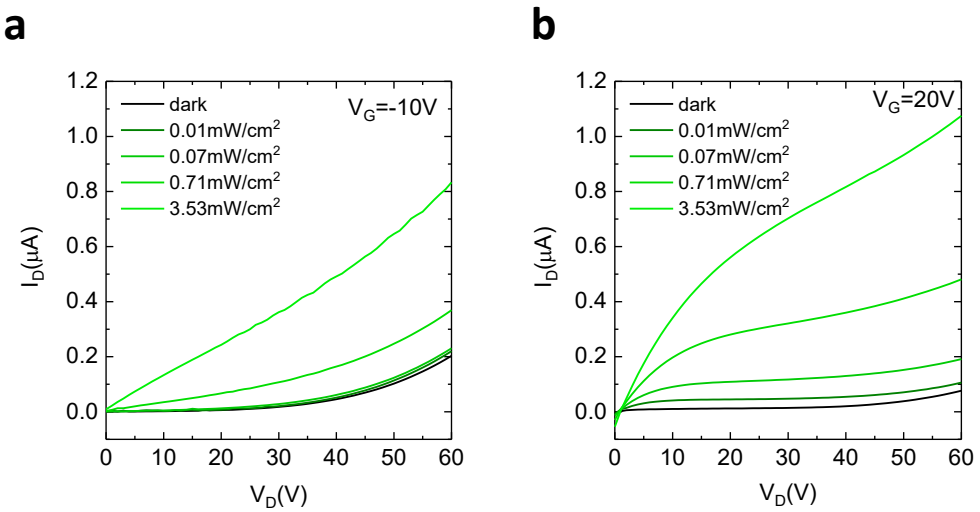


Figure 5.11: Output characteristics of the trilayer phototransistor measured in the dark and under illumination with various intensities at fixed gate bias (**a**) V_G = -10V and (**b**) V_G = 20V.

To make a direct comparison of phototransistor working at the two optimal biasing conditions, the amount of photocurrent increment was plotted as a function of the incident light intensity (**Figure 5.12**). The larger slope of the device at V_G = -10V suggests that the device in the depletion mode is more sensitive to the light intensity variation. The higher photocurrent level of the device at V_G = 20V, on the other hand, indicates a higher optical power conversion efficiency of the device working in the accumulation region.

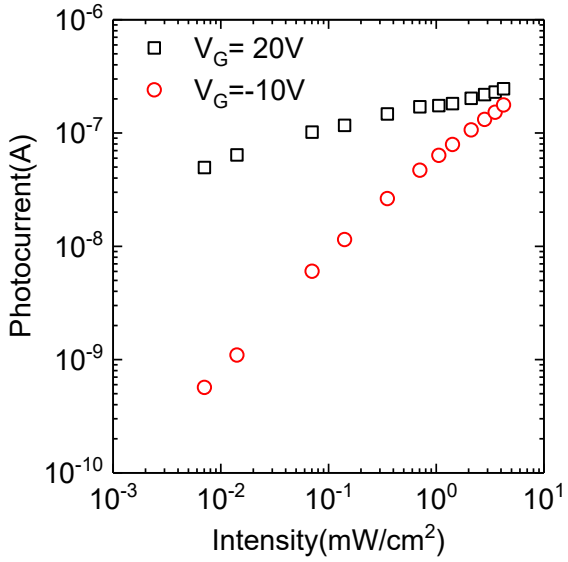


Figure 5.12: Evolution of the channel photocurrent as a function of incident light intensity measured for the device fixed at two optimal gate biasing conditions (V_G = 20 V and V_G = -10 V) and a constant V_D = 10 V.

A more quantitative analysis was also carried out by calculating the photosensitivity *P*, the responsivity *R* and the specific detectivity *D** at these two V_G as a function of incident light intensity (**Figure 5.13**). The photosensitivity (**Figure 5.13a**) exhibits an increase with increasing light intensity and the maximum value of 197 at V_G = -10 V under the highest illumination of 4.23mW/cm^2. In contrast, the responsivity (**Figure 5.13b**) and the specific detectivity (**Figure 5.13c**) show a decrease with light intensity and the maximum value of 7 A/W and 6.1×10^{11} Jones respectively at V_G = 20 V under the lowest illumination intensity of 0.01mW/cm^2. The sublinear increase in photosensitivity at high light intensity suggests a decrease in photogeneration efficiency under strong illumination intensities. This is in good agreement with the downward trend of both the responsivity and the specific detectivity. The decrease in efficiency of photocarrier generation is attributed most likely to the enhanced photocarrier recombination at high light intensity.[50] Such an efficiency decrease is even more prominent in the plots for V_G=20 V due to the current amplification mechanism of the transistor at the accumulation region. Interestingly, the difference in the gate-dependent amplification mechanism as well as the intensity-dependent photogeneration efficiency results in the phototransistor in accumulation mode with a higher specific detectivity under low light illumination, and the transistor in depletion mode with a higher specific detectivity under high light intensity.

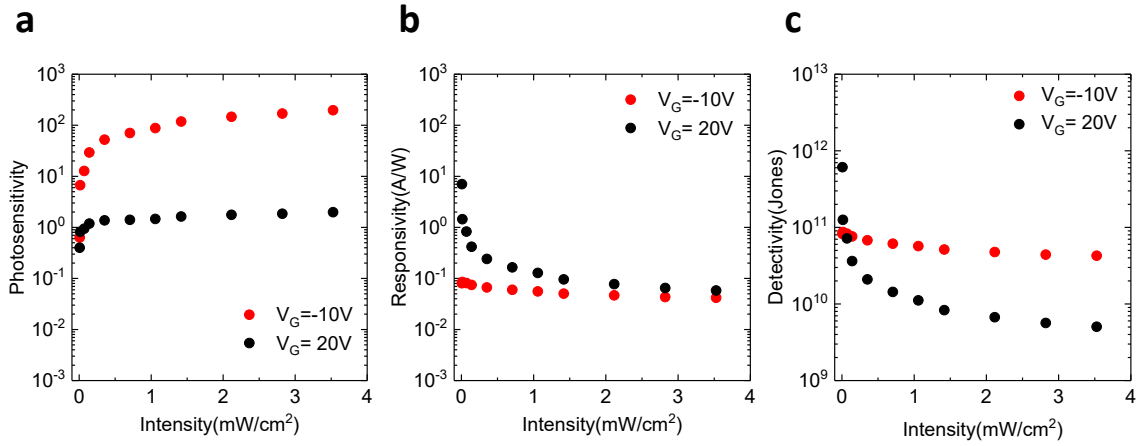


Figure 5.13: Illumination-intensity dependent figures of merit (**a**) photosensitivity, (**b**) responsivity and (**c**) specific detectivity measured for the device at two optimal gate biasing conditions (V_G = 20 V and V_G = -10 V) at a constant V_D = 10 V.

A conclusion can be reached for all the performance metric analysis above is that the present phototransistor in the depletion mode is more suitable for normal/high light detection due to the suppressed background noise, while device biased in the electron accumulation mode is more appropriate for low light detection because of signal amplification mechanism.

5.5 Opto-Electronic Circuits

In section 5.4 a phototransistor based on the CuSCN/D102/In_2O_3 trilayer structure with the ability of green light detection and fast switching speed has been demonstrated. As a further step to demonstrate the potential of this trilayer device in practical circuit application, a simple electro-optical, NOT gate was fabricated. The circuit was constructed by two identical transistors connected in a way similar to the complementary layout (**Figure 5.14a**). The operation principle of this electro-optical circuit is described briefly here. When the optical signal A_{IN} is high (light on), the impedance of TFT2 reduces to a level much lower than that of the TFT1 due to the photocarrier generation within the TFT2 transistor channel. The supplied voltage V_{DD}, therefore, is dropped mostly on TFT1. The circuit output voltage (V_{OUT}), which is identical to the voltage drop on TFT2, therefore is in a low state. When the A_{IN} is low (light off), the impedance of TFT2 becomes comparable to that of TFT1, pulling a larger voltage drop on TFT2. V_{OUT} in the circumstance is set to a high state. This electro-optical circuit enables the inversion between A_{IN} state and V_{OUT} state to occur for either binary state of A_{IN}, which is in good agreement with the truth table of a standard NOT gate as listed in **Figure 5.14c**. A representative set outputs of the circuit to green optical stimulus are shown in **Figure 5.14d**. It is worth noting that such a result was obtained on an operating frequency of 10Hz and still shows two clear binary V_{OUT} states. This circuit result here proves the potential of using the present phototransistors for fast photo-sensing application.

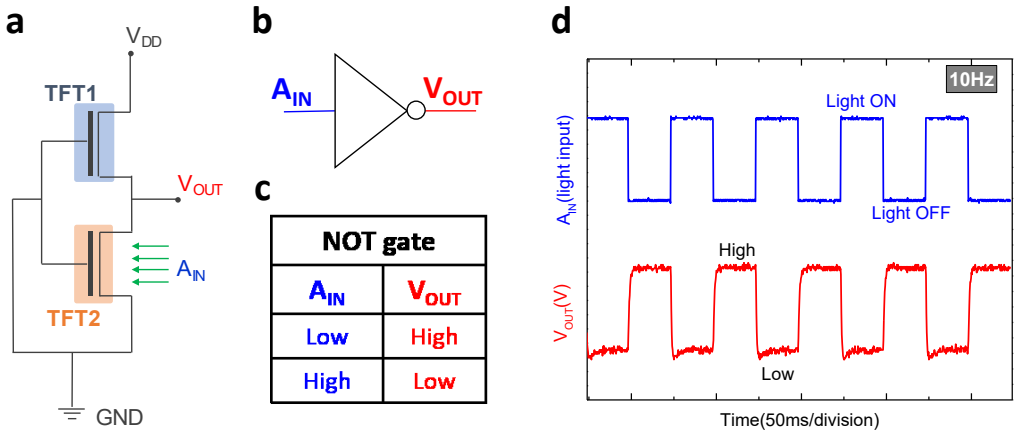


Figure 5.14: (**a**) Circuitry of the electro-optical NOT gate. (**b**) the symbolic representation of the NOT gate. (**c**) The truth table of the NOT gate. (**d**) Optical input A_{IN} pulsed at a frequency of 10Hz and the corresponding evolution of the circuit output voltage V_{OUT}.

5.6 Conclusions

To summarise Chapter 5, phototransistors based on the CuSCN/D102/In_2O_3 trilayer were fabricated and studied. This work starts with the development of a hybrid heterojunction transistor based on a CuSCN/In_2O_3 bilayer, which exhibits high optical transparency and ambipolar transistor operation. The presence of the p-n (CuSCN/In_2O_3) heterojunction was found to suppress the intrinsic PPC associated with the In_2O_3 layer. Organic dye D102 was then incorporated in-between this heterojunction to enable visible light sensitization/detection. The resulting CuSCN/dye/In_2O_3 trilayer channel phototransistors show a remarkably enhanced photoresponse to green illumination. Importantly, the trilayer phototransistors exhibit fast switching behaviour with a response time of ~1 ms, which is faster than the fast majority of oxide-based phototransistors. Such a fast response time is attributed to the minimisation of PPC from the oxide layer and efficient photocarrier transport within the trilayer channel. This work highlights the use of a hybrid heterostructure as a promising method to improve the speed of oxide-based phototransistors for fast photo-sensing application.

Bibliography

(1) Nomura, K.; Ohta, H.; Takagi, A.; Kamiya, T.; Hirano, M.; Hosono, H. Room-Temperature Fabrication of Transparent Flexible Thin-Film Transistors Using Amorphous Oxide Semiconductors. *Nature* **2004**, *432* (7016), 488–492.

(2) Fortunato, E.; Barquinha, P.; Martins, R. Oxide Semiconductor Thin-Film Transistors: A Review of Recent Advances. *Adv. Mater.* **2012**, *24* (22), 2945–2986.

(3) Kizu, T.; Aikawa, S.; Mitoma, N.; Shimizu, M.; Gao, X.; Lin, M. F.; Nabatame, T.; Tsukagoshi, K. Low-Temperature Processable Amorphous In-W-O Thin-Film Transistors with High Mobility and Stability. *Appl. Phys. Lett.* **2014**, *104* (15), 1–6.

(4) Kind, H.; Yan, H. Q.; Messer, B.; Law, M.; Yang, P. D. Nanowire Ultraviolet Photodetectors and Optical Switches. *Adv. Mater.* **2002**, *14* (2), 158–160.

(5) Zhang, D.; Li, C.; Han, S.; Liu, X.; Tang, T.; Jin, W.; Zhou, C. Ultraviolet Photodetection Properties of Indium Oxide Nanowires. *Appl. Phys. A Mater. Sci. Process.* **2003**, *77* (1), 163–166.

(6) Zhai, T.; Fang, X.; Liao, M.; Xu, X.; Zeng, H.; Yoshio, B.; Golberg, D. A Comprehensive Review of One-Dimensional Metal-Oxide Nanostructure Photodetectors. *Sensors* **2009**, *9* (8), 6504–6529.

(7) Melnick, D. A. Zinc Oxide Photoconduction, an Oxygen Adsorption Process. *J. Chem. Phys.* **1957**, *26* (5), 1136–1146.

(8) Takahashi, Y.; Kanamori, M.; Kondoh, A.; Minoura, H.; Ohya, Y. Photoconductivity of Ultrathin Zinc Oxide Films. *Jpn. J. Appl. Phys.* **1994**, *33*, 6611–6615.

(9) Studenikin, S. A.; Golego, N.; Cocivera, M. Density of Band-Gap Traps in Polycrystalline Films from Photoconductivity Transients Using an Improved Laplace Transform Method. *J. Appl. Phys.* **1998**, *84* (9), 5001–5004.

(10) Studenikin, S. A.; Golego, N.; Cocivera, M. Optical and Electrical Properties of Undoped ZnO Films Grown by Spray Pyrolysis of Zinc Nitrate Solution. *J. Appl. Phys.* **1998**, *83* (4), 2104–2111.

(11) Li, Q. H.; Gao, T.; Wang, Y. G.; Wang, T. H. Adsorption and Desorption of Oxygen Probed from ZnO Nanowire Films by Photocurrent Measurements. *Appl. Phys. Lett.* **2005**, *86* (12), 1–3.

(12) Moazzami, K.; Murphy, T. E.; Phillips, J. D.; Cheung, M. C. K.; Cartwright, A. N. Sub-Bandgap Photoconductivity in ZnO Epilayers and Extraction of Trap Density Spectra. *Semicond. Sci. Technol.* **2006**, *21* (6), 717–723.

(13) Janotti, A.; Van De Walle, C. G. Oxygen Vacancies in ZnO. *Appl. Phys. Lett.* **2005**, *87* (12), 1–3.

(14) Lany, S.; Zunger, A. Anion Vacancies as a Source of Persistent Photoconductivity in II-VI and Chalcopyrite Semiconductors. *Phys. Rev. B - Condens. Matter Mater. Phys.* **2005**, *72* (3), 1–13.

(15) Görrn, P.; Lehnhardt, M.; Riedl, T.; Kowalsky, W. The Influence of Visible Light on Transparent Zinc Tin Oxide Thin Film Transistors. *Appl. Phys. Lett.* **2007**, *91* (19), 193504.

(16) Takechi, K.; Nakata, M.; Eguchi, T.; Yamaguchi, H.; Kaneko, S. Comparison of Ultraviolet Photo-Field Effects between Hydrogenated Amorphous Silicon and Amorphous InGaZnO4 Thin-Film Transistors. *Jpn. J. Appl. Phys.* **2009**, *48* (1), 2–5.

(17) Ryu, B.; Noh, H. K.; Choi, E. A.; Chang, K. J. O-Vacancy as the Origin of Negative Bias Illumination Stress Instability in Amorphous In-Ga-Zn-O Thin Film Transistors. *Appl. Phys. Lett.* **2010**, *97* (2), 2008–2011.

(18) Lee, S.; Nathan, A.; Jeon, S.; Robertson, J. Oxygen Defect-Induced Metastability in Oxide Semiconductors Probed by Gate Pulse Spectroscopy. *Sci. Rep.* **2015**, *5* (1), 14902.

(19) Lany, S.; Zunger, A. Dopability, Intrinsic Conductivity, and Nonstoichiometry of Transparent Conducting Oxides. *Phys. Rev. Lett.* **2007**, *98* (4), 2–5.

(20) Soci, C.; Zhang, A.; Xiang, B.; Dayeh, S. A.; Aplin, D. P. R.; Park, J.; Bao, X. Y.; Lo, Y. H.; Wang, D. ZnO Nanowire UV Photodetectors with High Internal Gain. *Nano Lett.* **2007**, *7* (4), 1003–1009.

(21) Liu, J. S.; Shan, C. X.; Li, B. H.; Zhang, Z. Z.; Yang, C. L.; Shen, D. Z.; Fan, X. W. High Responsivity Ultraviolet Photodetector Realized via a Carrier-Trapping Process. *Appl. Phys. Lett.* **2010**, *97* (25).

(22) Bao, J.; Shalish, I.; Su, Z.; Gurwitz, R.; Capasso, F.; Wang, X.; Ren, Z. Photoinduced Oxygen Release and Persistent Photoconductivity in ZnO Nanowires. *Nanoscale Res. Lett.* **2011**, *6* (1), 404.

(23) Jeon, S.; Ahn, S. E.; Song, I.; Kim, C. J.; Chung, U. I.; Lee, E.; Yoo, I.; Nathan, A.; Lee, S.; Robertson, J.; Kim, K. Gated Three-Terminal Device Architecture to Eliminate Persistent Photoconductivity in Oxide Semiconductor Photosensor Arrays. *Nat. Mater.* **2012**, *11* (4), 301–305.

(24) Ruan, D.-B.; Liu, P.-T.; Chen, Y.-H.; Chiu, Y.-C.; Chien, T.-C.; Yu, M.-C.; Gan, K.-J.; Sze, S. M. Photoresponsivity Enhancement and Extension of the Detection Spectrum for Amorphous Oxide Semiconductor Based Sensors. *Adv. Electron. Mater.* **2019**, *1800824*,

1800824.

(25) Zan, H.-W.; Chen, W.-T.; Hsueh, H.-W.; Kao, S.-C.; Ku, M.-C.; Tsai, C.-C.; Meng, H.-F. Amorphous Indium-Gallium-Zinc-Oxide Visible-Light Phototransistor with a Polymeric Light Absorption Layer. *Appl. Phys. Lett.* **2010**, *97* (20), 203506.

(26) Li, J.; Zhou, F.; Lin, H. P.; Zhu, W. Q.; Zhang, J. H.; Jiang, X. Y.; Zhang, Z. L. Enhanced Photosensitivity of InGaZnO-TFT with a CuPc Light Absorption Layer. *Superlattices Microstruct.* **2012**, *51* (4), 538–543.

(27) Lin, Y.-H.; Faber, H.; Labram, J. G.; Stratakis, E.; Sygellou, L.; Kymakis, E.; Hastas, N. A.; Li, R.; Zhao, K.; Amassian, A.; Treat, N. D.; McLachlan, M.; Anthopoulos, T. D. High Electron Mobility Thin-Film Transistors Based on Solution-Processed Semiconducting Metal Oxide Heterojunctions and Quasi-Superlattices. *Adv. Sci.* **2015**, *2* (7), 1500058.

(28) Jeong, S.; Moon, J. Low-Temperature, Solution-Processed Metal Oxide Thin Film Transistors. *J. Mater. Chem.* **2012**, *22* (4), 1243–1250.

(29) Park, S.; Kim, K.-H.; Jo, J.-W.; Sung, S.; Kim, K.-T.; Lee, W.-J.; Kim, J.; Kim, H. J.; Yi, G.-R.; Kim, Y.-H.; Yoon, M.-H.; Park, S. K. In-Depth Studies on Rapid Photochemical Activation of Various Sol-Gel Metal Oxide Films for Flexible Transparent Electronics. *Adv. Funct. Mater.* **2015**, *25* (19), 2807–2815.

(30) Girtan, M.; Folcher, G. Structural and Optical Properties of Indium Oxide Thin Films Prepared by an Ultrasonic Spray CVD Process. *Surf. Coatings Technol.* **2003**, *172* (2–3), 242–250.

(31) Jaffe, J. E.; Kaspar, T. C.; Droubay, T. C.; Varga, T.; Bowden, M. E.; Exarhos, G. J. Electronic and Defect Structures of CuSCN. *J. Phys. Chem. C* **2010**, *114* (19), 9111–9117.

(32) Yang, J.; Kwak, H.; Lee, Y.; Kang, Y. S.; Cho, M. H.; Cho, J. H.; Kim, Y. H.; Jeong, S. J.; Park, S.; Lee, H. J.; Kim, H. MoS2-InGaZnO Heterojunction Phototransistors with Broad Spectral Responsivity. *ACS Appl. Mater. Interfaces* **2016**, *8* (13), 8576–8582.

(33) Pei, Z.; Lai, H. C.; Wang, J. Y.; Chiang, W. H.; Chen, C. H. High-Responsivity and High-Sensitivity Graphene Dots/a-IGZO Thin-Film Phototransistor. *IEEE Electron Device Lett.* **2015**, *36* (1), 44–46.

(34) Du, S.; Li, G.; Cao, X.; Wang, Y.; Lu, H.; Zhang, S.; Liu, C.; Zhou, H. Oxide Semiconductor Phototransistor with Organolead Trihalide Perovskite Light Absorber. *Adv. Electron. Mater.* **2017**, 1600325.

(35) Schmidt-Mende, L.; Bach, U.; Humphry-Baker, R.; Horiuchi, T.; Miura, H.; Ito, S.;

Uchida, S.; Grätzel, M. Organic Dye for Highly Efficient Solid-State Dye-Sensitized Solar Cells. *Adv. Mater.* **2005**, *17* (7), 813–815.

(36) Le Bahers, T.; Pauporté, T.; Scalmani, G.; Adamo, C.; Ciofini, I. A TD-DFT Investigation of Ground and Excited State Properties in Indoline Dyes Used for Dye-Sensitized Solar Cells. *Phys. Chem. Chem. Phys.* **2009**, *11* (47), 11276–11284.

(37) Pattanasattayavong, P.; Rossbauer, S.; Thomas, S.; Labram, J. G.; Snaith, H. J.; Anthopoulos, T. D. Solution-Processed Dye-Sensitized ZnO Phototransistors with Extremely High Photoresponsivity. *J. Appl. Phys.* **2012**, *112* (7).

(38) Mottram, A. D.; Lin, Y. H.; Pattanasattayavong, P.; Zhao, K.; Amassian, A.; Anthopoulos, T. D. Quasi Two-Dimensional Dye-Sensitized In2O3 Phototransistors for Ultrahigh Responsivity and Photosensitivity Photodetector Applications. *ACS Appl. Mater. Interfaces* **2016**, *8* (7), 4894–4902.

(39) Park, H.; Bae, E.; Lee, J. J.; Park, J.; Choi, W. Effect of the Anchoring Group in Ru-Bipyridyl Sensitizers on the Photoelectrochemical Behavior of Dye-Sensitized TiO2 Electrodes: Carboxylate versus Phosphonate Linkages. *J. Phys. Chem. B* **2006**, *110* (17), 8740–8749.

(40) Pattanasattayavong, P.; Yaacobi-Gross, N.; Zhao, K.; Ndjawa, G. O. N.; Li, J.; Yan, F.; O'Regan, B. C.; Amassian, A.; Anthopoulos, T. D. Hole-Transporting Transistors and Circuits Based on the Transparent Inorganic Semiconductor Copper(I) Thiocyanate (CuSCN) Processed from Solution at Room Temperature. *Adv. Mater.* **2013**, *25* (10), 1504–1509.

(41) Wijeyasinghe, N.; Regoutz, A.; Eisner, F.; Du, T.; Tsetseris, L.; Lin, Y. H.; Faber, H.; Pattanasattayavong, P.; Li, J.; Yan, F.; McLachlan, M. A.; Payne, D. J.; Heeney, M.; Anthopoulos, T. D. Copper(I) Thiocyanate (CuSCN) Hole-Transport Layers Processed from Aqueous Precursor Solutions and Their Application in Thin-Film Transistors and Highly Efficient Organic and Organometal Halide Perovskite Solar Cells. *Adv. Funct. Mater.* **2017**, *27* (35), 1–13.

(42) Ghatak, S.; Pal, A. N.; Ghosh, A. Nature of Electronic States in Atomically Thin MoS2 Field-Effect Transistors. *ACS Nano* **2011**, *5* (10), 7707–7712.

(43) Schießl, S. P.; Faber, H.; Lin, Y. H.; Rossbauer, S.; Wang, Q.; Zhao, K.; Amassian, A.; Zaumseil, J.; Anthopoulos, T. D. Hybrid Modulation-Doping of Solution-Processed Ultrathin Layers of ZnO Using Molecular Dopants. *Adv. Mater.* **2016**, *28* (20), 3952–3959.

(44) Kufer, D.; Nikitskiy, I.; Lasanta, T.; Navickaite, G.; Koppens, F. H. L.; Konstantatos, G.

Hybrid 2D-0D MoS 2 -PbS Quantum Dot Photodetectors. *Adv. Mater.* **2015**, *27* (1), 176–180.

(45) Sze, S. M.; Ng, K. K. *Physics of Semiconductor Devices, 3rd Edition*; 2006.

(46) Wu, H. C.; Huang, Y. C.; Ding, I. K.; Chen, C. C.; Yang, Y. H.; Tsai, C. C.; Chen, C. D.; Chen, Y. T. Photoinduced Electron Transfer in Dye-Sensitized SnO2nanowire Field-Effect Transistors. *Adv. Funct. Mater.* **2011**, *21* (3), 474–479.

(47) Bach, U.; Lupo, D.; Comte, P.; Moser, J. E.; Weissörtel, F.; Salbeck, J.; Spreitzer, H.; Grätzel, M. Solid-State Dye-Sensitized Mesoporous TiO2 Solar Cells with High Photon-to-Electron Conversion Efficiencies. *Nature* **1998**, *395* (6702), 583–585.

(48) Kroeze, J. E.; Hirata, N.; Schmidt-Mende, L.; Orizu, C.; Ogier, S. D.; Carr, K.; Grätzel, M.; Darrant, J. R. Parameters Influencing Charge Separation in Solid-State Dye-Sensitized Solar Cells Using Novel Hole Conductors. *Adv. Funct. Mater.* **2006**, *16* (14), 1832–1838.

(49) Ghaffarzadeh, K.; Lee, S.; Nathan, A.; Robertson, J.; Jeon, S.; Kim, S.; Kim, C.; Chung, U.-I.; Lee, J.-H. Light-Bias Induced Instability and Persistent Photoconductivity in In-Zn-O/Ga-In-Zn-O Thin Film Transistors. *SID Symp. Dig. Tech. Pap.* **2011**, *42* (1), 1154–1157.

(50) Bube, R. H. *Photoelectronic Properties of Semiconductors*; Cambridge University Press, 1992.

Chapter 6 Tuneable, high-performance perovskite-organic heterojunction phototransistors

Metal-halide perovskites (MHPs) promise to revolutionise large-area photodetection technologies due to their high absorption coefficients, long diffusion lengths, low trap densities and versatile processing. However, successful extraction of photogenerated carriers from the MHPs layer and their conversion to electrical signals remain challenging due to the interdependency of the photogain and dark current. This chapter describes the development of hybrid perovskite-organic heterojunction phototransistors by integrating MHP into a series of organic semiconductor transistor channels to form either "straddling-gap" type-I or "staggering" type-II heterojunctions. Characterisation of the phototransistors shows that with preferential edge-on molecular orientation, "straddling-gap" type-I heterojunction structure results in more efficient photocarrier circulation, while transforming the heterojunction type by varying the organic composition leads to tuneable photoresponse. The results provide important insights into the charge-transfer dynamics, which can help the development of advanced device designs with "on-demand" optoelectronic properties. In addition, a novel evaluation method for phototransistors is proposed by using a photo-inverter circuitry. This circuit-based methodology is used to assess the phototransistors' amplification as well as to assert transistors' functionality for both linear and saturation operations.

6.1 Introduction

Among several emerging semiconducting materials metal-halide perovskites (MHPs) stand out as a strong candidate for implementation in photodetection[1], owing to their attractive material properties such as remarkable absorption coefficients[2], long-lived photocarriers[3] and tuneable optical bandgaps[4]. Together with simple processing requirements, this has led to their rapid emergence over the past years, not only for revolutionised energy generation[5,6] but also for innovative optoelectronic applications[7–9]. Despite their promising features, phototransistors based on process-friendly semiconducting MHPs (i.e. solution-grown polycrystalline films) have not been widely reported[10–12]. The reason behind this could be attributed to inter-grain boundary scattering[13] and/or intragrain defect recombination[14]. Furthermore, several groups have reported that the ionic nature of MHPs appears to cause difficulties for gating the transistor channel at room temperature[15,16]. Research efforts have since been put into devices based on single crystals[17], single-crystalline layers[18] and monolayer flakes[19]. However, the rather complex process protocols to form single-crystalline materials are less scalable, hence posing a great challenge to high-throughput, large-area manufacturing[9]. On the other hand, hybrid heterostructures that combine materials with advantageous optical and electrical properties in a phototransistor serve as an excellent platform to enhance photoresponse[1]. Noteworthy state-of-the-art demonstrations with this approach have extensively enriched the field of photodetection, such as enhancing infrared detection for Si electronics with colloidal quantum dots[20], wide-dynamic-range photocarrier integration[21], and combined with existing CMOS technologies for advanced imaging systems[22,23]. Numerous attempts using MHPs in a similar manner have also been reported, but their mediocre performance is usually mitigated by employing a highly conductive channel material, resulting in a photoconductor, rather than a phototransistor, with an apparent trade-off between photogain and dark current levels.

This chapter presents a conceptual heterojunction phototransistors architecture employing MHPs as the light absorber and two organic semiconductors (OSC) as well as their blend as the conducting channel materials. Using a range of experimental characterisation techniques, the dynamics behind photogenerated charge transfer process and the mechanisms of photoresponse in the present hybrid phototransistors are deciphered. The enhanced photoresponse is attributed to more efficient photocarrier circulation in a "straddling gap" type-I heterojunction between the MHP and OSC, rather than the conventional concept of employing an energetically-favourable "staggering gap" type-II heterojunction[21,24]. By combining two phototransistors, photo-inverters are demonstrated with the ability to provide a photo-

modulated output voltage, and to evaluate the intrinsic amplification of the phototransistor. More importantly, a photo-inverter requires the phototransistors of interest to function in both linear and saturation modes, which are essential for a three terminal device to operate as a transistor, not simply a gate-tuneable photoconductor as the latter is limited to linear operation mode not capable of complete circuit applications. Not only will the knowledge acquired from this work help to provide tailorable, on-demand optoelectronic sensors, but the large library of MHP and OSC materials could also address many other optoelectronic applications, by pursuing this hybrid approach to electrically active layers in semiconductor devices.

6.1.1 Review of perovskite-based phototransistors

Perovskites, in general, refer to a class of compounds with $CaTiO_3$-like crystalline structure. These perovskite compounds share a same chemical formula of ABX_3, where A and B are cations and X is an anion. The cation A can be either an inorganic ion (e.g. Cs^+, Rb^+) or an organic ion (e.g. methylammonium $CH_3NH_3^+$, formamidinium $CH(NH_2)_2^+$), the cation B is a bivalent transition metal ion (e.g. Pb^{2+}, Sn^{2+}, Ge^{2+}, Mn^{2+}), and X is a halide ion (e.g. Cl^-, Br^-, I^-).[8] In particular, metal-halide perovskites (MHPs) have emerged as compelling materials in optoelectronic applications since they combine the advantages of organic and inorganic semiconductors such as tuneable energy bandgap that can be controlled by the halide ratio, low-cost processability similar to organic semiconductors and low exciton binding energy resembling that of inorganic semiconductors.[7,25,26]

Despite the promising features, there have been only a few reports on phototransistors based on single-component MHPs[10–12]. In this structure, a perovskite thin film is required to fulfil both high field effect mobility and high responsivity. However, getting functional perovskite-only transistor channel with reasonable charge carrier mobility at room temperature is found to be difficult. For example, Li *et al.*[10] reported a phototransistor based on a solution-processed polycrystalline $CH_3NH_3PbI_3$ film with field-effect mobility of 0.1 $cm^2/V{\cdot}s$ when the device was under strong illumination of 10 mW/cm^2. However, the performance of the phototransistor in the dark was poor, exhibiting an extremely low drain current below 0.5 nA and small on/off ratio of less than one order of magnitude. These poor device performance parameters could largely limit its functionality as an electrical switch, especially in a low-light condition. The reason behind this could be attributed to strong defect recombination[14]. To address this issue and improve the device performance research efforts hence have been put on optimising crystalline structure as well as film morphology[11,12,18,19,27]. For example, Cho *et al.*[11]

reported a perovskite phototransistor with enhanced mobility of 2.1 $cm^2/V{\cdot}s$ using an orientationally pure crystalline $CH_3NH_3PbI_3$ film with unique crystal orientation and low trap-state density. The enhancement in mobility was observed for charge transport along the crystal orientation.

An alternative solution to overcome this obstacle is to adopt a hybrid structure that combines MHPs with other functional channel materials that possess excellent electronic transport properties. Numerous attempts have been reported by incorporating MHPs with a wide range of materials such as graphene[28–37], transition-metal dichalcogenides (TMDs)[38–41] carbon nanotubes[42,43] and organics[24,44,45]. Among all these materials, graphene has been most extensively studied due to its ultrahigh carrier mobility ($\sim 10^4$ $cm^2/V{\cdot}s$)[46,47]. The first graphene/perovskite heterojunction phototransistor was reported by Lee *et al.* and showed a responsivity of 180 A/W with a solution-processed $CH_3NH_3PbI_3$ film[28]. The photoresponse in this graphene/perovskite hybrid structure is explained by photogating effect that enhances the photoconductive gain. The responsivity of graphene/perovskite hybrid phototransistors was further enhanced by research efforts on micro/nanostructure engineering on perovskites layers to reduce bulk recombination. For example, Wang *et al.* reported a graphene/perovskite hybrid phototransistor by forming a thin layer of dispersive $CH_3NH_3PbI_3$ island on top of the graphene layer[29]. The resulting devices showed a high responsivity of 6.0×10^5 A/W. Spina *et al.* employed $CH_3NH_3PbI_3$ nanowire in a heterostructure with graphene[30] and obtained a device with responsivity as high as 2.6×10^6 A/W. Shao *et al.* covered a graphene monolayer with a 2D multiphase perovskite film[34], achieving a phototransistor with responsivity of $\sim 10^5$ A/W. Based on similar design principles of hybrid with high-mobility channel materials, several attempts that combined perovskite with other highly conductive materials (e.g. carbon nanotubes[42,43] and PEDOT:PSS[24]) have been reported. Phototransistor obtained through these approaches commonly exhibit ultrahigh responsivities $>10^4$ A/W under low illumination intensities (i.e. at the level of nW~μW /cm^2).

In spite of the promising values of responsivity, devices based on channel materials with ultrahigh mobility also induce several issues, which are not ideal for phototransistor operation. Due to the absence of bandgap these semimetal-like materials (e.g., graphene, carbon nanotubes and PEDOT:PSS) possess high mobility at the expense of tuneability of channel conductivity[48], causing poor current-voltage modulation[49] and leading to a transistor channel that cannot be switched off. As a result, a high level of dark current[35] and/or limited detectivity[28] is observed from these approaches. More critically, devices based on semimetal-like materials usually show no saturation of channel current. The latter constrains these devices

to operate in active mode only. Therefore, the devices based on semimetal-like materials, even though they are configured in a three-terminal structure, should be termed as a photoconductor, rather than a phototransistor, with an inevitable trade-off between photogain and dark current levels (as discussed in Section 2.5.2).

6.1.2 Perovskite-organic heterojunction phototransistors

In this chapter, MHP-OSC heterojunction phototransistors (HJPTs) with high responsivity are presented using organic materials with field-effect mobilities in the range of 0.3 to 1 $cm^2/V \cdot s$. This result is particularly of interest as it demonstrates a new route towards photodetectors with high responsivity. Since the responsivity is defined as the ratio of photogenerated current to incident optical power, increasing the level of photocurrent is the key to obtain high responsivity. The concept of using high-mobility materials as aforementioned is to enlarge photocurrent by enhancing charge carrier circulation in a transistor channel. In this scenario, devices with moderate mobility should only exhibit moderate responsivity for a given number of photogenerated carriers involved in this circulation process. The demonstration of high values of responsivity using the approach present in this chapter indicates that the enlargement in photocurrent is attributed to other factors rather than enhanced photocarrier circulation through high-conductivity materials. Indeed, the responsivity improvement is attributed to the improved efficiency of preserving photocarriers that are involved in carrier circulation, which is realised by engineering a type-I straddling MHP/OSC heterojunction. A comparison of phototransistor performance of the present work and all other perovskite-based phototransistors is summarised in **Table 6.1**. Compared to the results collected from the literature, the work present here has demonstrated one of the highest responsivities among all the reported PT-type phototransistors (i.e. devices worked like a proper phototransistor with ability of operating in both active mode and switch mode), and this value is found to be even comparable to some of the PC*-type devices (i.e. device configured in a transistor structure but worked like a photoconductor).

Table 6.1: Summary of performance metrics of perovskite-based phototransistors.

Feature	Materials	Type‡	Mobility ($cm^2V^{-1}s^{-1}$)	Responsivity (AW^{-1})	@light intensity	Gain/EQE	Detectivity (Jones)	Ref
Perovskite/Organic	FACs/ C_8-BTBT	PT	0.33	1.7×10^4	7 μW/cm^2 (475 nm)	4.5×10^4	2.2×10^{14}	**This work**
Perovskite/Organic	FACs/ Blend 1:1	PT	0.42	1.1×10^4	7 μW/cm^2 (475 nm)	2.9×10^4	4.9×10^{14}	
Perovskite/Organic	FACs/ C_{16}-IDTBT	PT	1.02	3.2×10^3	7 μW/cm^2 (475 nm)	8.4×10^3	3.8×10^{13}	
Pure perovskite	$CH_3NH_3PbI_3$	PT	0.18	320	10 mW/cm^2 (white)			10
Orientationally pure crystalline perovskite	$CH_3NH_3PbI_3$	PT	2.1	6.1	0.5 mW/cm^2 (white)			11
2D layered Perovskite	$(C_6H_5C_2H_4NH_3)_2SnI_4$	PT	1.2	1.9×10^4	5 μW/cm^2 (447nm)	5.3×10^4		12
NGQD-perovskite blend/mrGO bilayer	mrGO/NGQDs-$CH_3NH_3PbI_3$	PT		1.92×10^4	23.6 μW/cm^2 (660 nm)	1.0×10^4	2.7×10^{13}	50
APTES-doped TMD/Perovskite	APTES/MoS_2/ $CH_3NH_3PbI_3$	PT		1.94×10^6	4.63 pW (520 nm)		1.29×10^{12}	51
2D TMD/Perovskite	MoS_2/ $CH_3NH_3PbI_3$	PT	5.24	1.1	4 mW/cm^2 (638 nm)		9×10^{10}	39
TMD/Perovskite	MoS_2/CH3NH3 I	PT	19.7	1.1×10^4	0.3 mW/cm^2			40
Perovskite QDs/Organic	$CsPbBr_3$ QDs/DNTT	PT		1.7×10^4	0.003 mW/cm^2 (460 nm)	6.7×10^4	2.0×10^{14}	44
Organic/ Perovskite QDs	DPPDTT/$CsPbI_3$ QDs	PT	0.05	110	0.008 mW/cm^2 (405nm)		2.9×10^{13}	45
Perovskite/CQDs	$CH_3NH_3PbI_3$/PbSe QDs	PT	0.16	1.2	0.3 mW/cm^2 (300 nm)	4.96	3.3×10^7	52
Perovskite QDs/ CQDs	$CsPbBr_3$/PbS QDs	PT	4083	4.5×10^5	0.3 mW/cm^2 (808 nm)		7×10^{12}	53
Graphene/Perovskite bilayer	ODTS/Graphene/$CH_3NH_3PbI_3$	PC*		180	1 μw (520 nm)	5×10^2	10^9	28
Graphene/Perovskite (island) bilayer	Graphene/ $CH_3NH_3PbBr_2I$	PC*		6.0×10^5	1.052 nW (405 nm)	2.01×10^9		29
Graphene/Perovskite (nanowire)	Graphene/ $CH_3NH_3PbI_3$	PC*		2.6×10^6	65 nW/cm^2 (633 nm)	4×10^6		30
Graphene/Perovskite on flexible substrate	Graphene/ $CH_3NH_3PbI_3$	PC*		115	~0 (515 nm)		3×10^{12}	31
Plasmonic-enhanced Graphene/Perovskite (island)	AuNP/Graphene/$CH_3NH_3PbI_3$	PC*	0.14	2.1×10^3	14 μW/cm^2 (532 nm)			32
Graphene/Perovskite (nanocrystal)	Graphene/CsPbBrI	PC*		8.2×10^8	0.07 μW/cm^2 (405 nm)		2.4×10^{16}	33
Graphene/2D multiphase Perovskite	hBN/Graphene/ $(BA)_2(MA)_{n-1}Pb_nI_{3n+1}$	PC*	16000	10^5	42 pW (532 nm)		$3.3x10^{10}$	34
Graphene/ Organic/ Perovskite	Graphene/P3HT /CH_3NH_3PbICl	PC*	2120	3.4×10^9	14.15 nW/cm^2 (598 nm)	8.9×10^9		36
Graphene/SVD Perovskite	ODTS/Graphene/ $CH_3NH_3PbI_3$	PC*	212	1.73×10^7	133 nW/cm^2 (white)	10^6	2×10^{15}	37
Graphene nanoribbon/Perovskite QDs/IGZO	GNR/$CsPbI_3$ QDs/IGZO	PC*	13	2.3×10^5	0.1 mW/cm^2 (300 nm)	5×10^3	7.5×10^{14}	54
2D TMD/Perovskite VDWH	CsPbBrs-MoS_2	PC*	0.08	13.1	1.4 mW/cm^2 (442 nm)			41
CNT/Perovskite(nanowire)	CNT/ $CH_3NH_3PbI_3$	PC*		7.7×10^5	6.25 nW/cm^2 (533 nm)	1.5×10^6		42
SWNTs-Perovskite blend	SWNTs-CH_3NH_3PbICl	PC*	595	1.17×10^4	10 mW/cm^2 (white)	8×10^3	3.68×10^{14}	43
Organic/Perovskite bilayer	PEDOT: PSS/CH_3NH_3PbICl	PC*	5.6	2×10^9	14.15 nW/cm^2 (598 nm)	4×10^9	1.7×10^{14}	24

‡ Perovskite-based phototransistors listed here are classified into two types, i.e. PT-type and PC*-type. PT-type devices are referred to those worked like a proper phototransistor, with ability to operate in both active mode and switch mode. PC*-type devices are those followed a transistor three-terminal structure but not able to be working in the switch mode due to the absence of drain current saturation. Such devices worked more like a photoconductor even though weak gate effect is observed.

6.2 Methods

6.2.1 Preparation of metal-halide perovskites and organic semiconductors

To form the mixed-cation lead mixed anion perovskite precursor solutions, caesium iodide (CsI, Alfa Aesar), formamidinium iodide (FAI, GreatCell Solar), methylammonium iodide (MAI, GreatCell Solar), lead iodide (PbI_2, TCI) and lead bromide ($PbBr_2$, Alfa Aesar) were prepared in the way corresponding to the exact stoichiometry for the desired $FA_{0.83}Cs_{0.17}PbI_{2.7}Br_{0.3}$ compositions in a mixed organic solvent of anhydrous N,N-dimethylformamide (DMF, Sigma-Aldrich) and dimethyl sulfoxide (DMSO, Sigma-Aldrich) in a ratio of DMF : DMSO = 4 : 1. The perovskite precursor concentration used was 0.2 M for making HJPTs and carrying out the UV-Vis measurement whilst for the rest of characterisations and measurements in this work the concentration for the perovskite solution was 1.0 M. For organic semiconductors, C_{16}-IDTBT was prepared using previously reported procedures in ref.[55] whilst C_8-BTBT was purchased from 1-Material and used as received. The organic solutions were prepared by dissolving C_{16}-IDTBT and C_8-BTBT in tetralin and chlorobenzene, respectively, and stirred for 12 h before use. The blend solutions were prepared by mixing the C_{16}-IDTBT and C_8-BTBT solutions at desired ratios. The concentration for all organic solutions was 10 mg/ml.

6.2.2 Fabrication of perovskite heterojunction phototransistors and bilayer structures

TG-BC HJPTs were fabricated on glass substrates. The substrates were cleaned with acetone and isopropanol in a sonication bath for 8~10 min for each step. 40 nm thick Au source and drain electrodes (channel width/length: 1000 μm/30 μm) were evaporated through shadow masks under high vacuum (~10^{-6} mbar). The perovskite light-absorbing layer was first deposited using a spin coater with the following processing parameters: starting at 1000 rpm (ramping time of 5 sec) for 10 sec and then 5000 rpm (ramping time of 5 sec from 1000 rpm) for 30 sec. 10 sec before the end of the spinning process, a solvent-quenching method was used by dropping 100 μL toluene onto the perovskite wet films. The organic semiconductors were deposited from as-prepared solutions via spin coating at 2000 rpm for 30 sec and thermally annealed at 100 °C for 5 min. Following semiconductor depositions, a Teflon based material (AF2400, Dupont) dissolved in a Fluorinertt electronic liquid (FC-43, 3 M) at a concentration of 25 mg/ml was used as the gate dielectric and deposited via spin-cast (500 rpm for 20 sec followed by 1000 rpm for 30 sec) to produce a ~330 nm thick dielectric layer. The AF2400 gate dielectric was annealed at 50 °C for 30 min. The TG-BC HJPTs were completed by thermal evaporation of 50 nm thick Al gate electrodes through shadow masks under high

vacuum (~10^{-6} mbar). The entire transistor fabrication process was carried out in a nitrogen-filled glove box. For perovskite-organic diodes and Mott-Schottky analysis, the samples were using the same cleaning, film-deposition and metal-evaporation processes, except for i) 20 nm Au bottom electrodes evaporated for perovskite-organic diodes; ii) ITO-coated glass used for carrying out impedance spectroscopy in order to perform Mott-Schottky analysis.

6.2.3 Film characterisation

The ultraviolet-visible (UV-Vis) absorbance measurements were performed using a Shimadzu UV-2600 UV-Vis spectrophotometer. The samples were prepared on quartz substrates using the same deposition parameters described in section 6.2.2 for perovskite and organic thin film deposition. Atomic force microscopy (AFM) study was carried out using an Agilent 5500 atomic force microscope in intermitted contact mode.

Grazing-incidence wide-angle X-ray scattering (GIWAXS) measurements were conducted by Dr. Ruipeng Li on CMS beamline at NSLS II, Brookhaven National Lab. The X-ray with the energy of 13.5 keV shone on the as-cast films at incident angles of 0.1°. The high incident angle of 0.1° allows the X-ray to penetrate through the top organic layer into the bottom perovskites layer. A Photon Science CCD detector was placed 227 mm away from the sample and recorded for 10 s for each film. The data analysis was performed by SciAnalysis programme.

6.2.4 Electrical and optoelectronic characterisations.

Electrical characterisation of transistors and diode was carried out using an Agilent B2902A Precision Source/Measure Unit (SMU) and a homemade probe station in a nitrogen-filled glove box. The SMU was connected to the transistor/diode electrodes via a set of metallic needles held by micropositioners (EB-700, EVERBEING). Characterisation of inverter circuit was carried out using a Keithley 4200 Semiconductor Characterisation System (SCS) in combination with the same probe station. The interconnection of two constituent transistors and the connection to the SCS were achieved via micro-positioning needles and BNC cables.

Optoelectronic characterisation was carried out by measuring the current-voltage characteristics of the fabricated devices in dark environment and under various illumination intensities using light-emitting diodes (LEDs). Specifically, LEDs with electroluminescence emission peaks at 475, 525 and 632 nm were employed. The various illumination intensities were achieved by driving the LEDs with different currents using a Keithley 2400 source-meter.

The actual illumination optical powers were calibrated by a Thorlabs 120UV power sensors prior to the measurement.

6.2.5 Photodetectors simulation

The performance of the present HJPTs was analytically compared with that of other photodetector architectures. The comparison was performed by plotting the photogain as a function of dark current density for the present HJPTs as well as simulated photodetectors and photoconductors.

The plots of photogain and dark current density for the HJPTs can be extracted from the current-voltage (I-V) characteristics of phototransistors at a constant drain voltage (V_D) of -40 V in the dark and under illumination of ~7 μW cm^{-2} at 475 nm. The dark current density can be converted from the HJPTs drain current in the dark while the photogain can be calculated through the following equation:

$$G = \frac{I_{ph}}{E_{opt} \cdot A} \cdot \frac{hv}{e} \tag{6.1}$$

where, I_{ph} is the photocurrent, E_{opt} is the optical power density, A is the device area enclosed by the transistor channel length L and channel width W, hv is the photon energy, e is the elementary charge.

For the simulated photoconductor, the dark current can be expressed based on an intuitive model from the drift current equation:[20,56]

$$I_{dark} = \frac{W}{L} \cdot D \cdot N_A \cdot \mu \cdot e \cdot V_{appl} \tag{6.2}$$

where D is the channel thickness, N_A is the carrier concentration, μ is the carrier mobility, V_{appl} is the applied voltage. Since the gain mechanism that dominates photoconductors is generally explained by the trap-assisted photoconductivity[57,58], the photogain can be estimated by

$$G_{pc} = \frac{\tau}{t} \tag{6.3}$$

where τ is the photocarrier lifetime (also known as the trap lifetime) and t is the carrier transit time within the channel, which is given by $t = L^2/\mu V_{appl}$. Therefore, the photoconductor exhibits a linear relationship between photogain and dark current. The gain can be increased by using materials with high mobility to decrease the transit time. The latter, however, increase the dark current. The simulation of photoconductor in this work was carried out using the same device dimensions as the present HJPTs and the following parameters that resemble MHP-like properties[15,16]: carrier lifetime of 1 μs, carrier concentration of 10^{17} cm^{-3}, mobility of 0.6 cm^2 V^{-1} s^{-1}, film thickness of 500 nm, and applied voltages (V_{appl}) ranging from 0.2 V to 10^3 V.

On the other hand, photodiode as a passive element could only generate a maximum photogain of 1 under the condition of reaching an external quantum efficiency of 100 %[56].

6.2.6 Photoluminescence spectroscopy

Steady-state photoluminescence (SSPL) and time-resolved photoluminescence (TRPL) measurements were conducted by by Dr. Nobuya Sakai from University of Oxford. SSPL spectra were recorded using an excitation wavelength of 510 nm and slit widths of 5 mm on a commercial spectrofluorometer (Horiba, Fluorolog). Time-resolved PL measurements were acquired using a time-correlated single photon counting (TCSPC) setup (FluoTime 300 PicoQuant GmbH). Film samples were photoexcited using a 507nm laser head (LDH-P-C-510, PicoQuant GmbH) pulsed at frequencies between 0.2 MHz.

6.2.7 Time-resolved microwave conductivity

Time-resolved microwave conductivity (TRMC) measurements were by Prof. John Labram and his colleagues at Oregon State University. In the TRMC measurent system, a microwave-frequency oscillatory electric signal is generated using a Sivers IMA VO4280X/00 voltage-controlled oscillator (VCO). The signal has an approximate power of 16 dBm and a tuneable frequency between 8 GHz and 15 GHz. The oscillatory signal is incident on an antenna inside a WR90 copper-alloy waveguide. The microwaves emitted from the antenna pass through an isolator and an attenuator before they are incident on a sample cavity. The cavity supports a TE_{102} mode formed by a short section of WR90 waveguide and an ITO-coated glass window that allows optical access to the sample. The sample is mounted inside the cavity at a maximum of the electric-field component of the standing microwaves, using a PLA sample holder. Microwaves reflected from the cavity are directed through an isolator and then to a zero-bias Schottky diode detector (Fairview Microwave SMD0218). The detector outputs a voltage linearly-proportional to the amplitude of the incident microwaves, which is then amplified by a Femto HAS-X-1-40 high-speed amplifier. The amplified signal is detected by a Textronix TDS 3032C digital oscilloscope. A Continuum Minilite II pulsed Nd:YAG laser is used to illuminate the sample. The laser pulse has a wavelength of 532 nm, a full-width at half-maxima of approximately 5 nm and a maximum fluence incident on the sample of ~10^{15} cm^{-2}. An external trigger link is employed to trigger the oscilloscope ~50 ns before the laser fires. Changes in the detector voltage under illumination can then be used to extract the relevant TRMC parameters: $\phi\Sigma\mu_{\mathrm{TRMC}}$.

6.2.8 Transient photoconductivity

Transient photoconductivity (TPC) measurements were conducted by by Dr. Jongchul Lim from University of Oxford. A Nd:YAG pulsed laser excitation source pumped at 10 Hz with FWHM = 3.74 ns was set to 470 nm with a range of fluences in order to vary the charge carrier densities of FACs. A bias of 24 V is applied on one of the in-plane electrodes. A variable resistor is connected in series with the samples. The voltage drop on this resistor was monitored through an oscilloscope with a high internal resistance (1 MΩ) connected in parallel to determine the change of the potential across the two in-plane Au electrodes. Transient photoconductivity was calculated using the following equation, $\sigma_{\mathrm{TPC}} = \frac{V_r}{R_r \times (V_{appl} - V_r)} \times \frac{l}{w \times t}$, where R_r is resistance for the variable resistor, V_r is the potential drop measured across the resistor, V_{appl} is applied voltage, l is channel length, w is channel width, and t is film thickness. For sample preparation, the as-deposited films were scribed to have a 5-mm channel width and coated with a layer of 200-nm poly(methyl methacrylate) (PMMA) whilst the channel length is defined by two thermally-evaporated Au electrodes with a distance of 4 mm.

6.2.9 Impedance spectroscopy

The impedance spectroscopy (IS) technique was carried out using an Autolab PGSTAT302N potentiostat with a FRA32M module to perform the Mott-Schottky analysis. In the IS measurement, the AC perturbation was set to 10 mV. The illumination was supplied by a LED light source with a flux of ~12 lumens. The room conditions were of ~20-30% humidity and 295-300 K temperature.

6.3 Results and Discussion

6.3.1 Heterojunction Phototransistor Configuration

The present HJPT configured in top-gate bottom-contact (TG-BC) features a staggered structure as shown in **Figure 6.1a**. The design of the present HJPT sandwiches the light-absorbing layer MHP between the source-drain (S-D) contacts and the OSC transistor channel. This structure has proven to be able to combine excellent gate-modulated field effect with efficient photoinduced carrier extraction from the light absorber into the transistor channel[21]. The perovskite light absorber employed here is a mixed-cation mixed-anion MHP, $FA_{0.83}Cs_{0.17}PbI_{2.7}Br_{0.3}$ (FACs, FA = formamidinium)[4]. The transistor channel materials imployed here are two high-mobility p-type OSCs (**Figure 6.1b**), namely [1]benzothieno[3,2-*b*]benzothiophene based small-molecule derivative (C_8-BTBT)[59] and the indacenodithiophene-co-benzothiadiazole copolymer (C_{16}-IDTBT)[55], as well as their blends. Since C_8-BTBT and C_{16}-IDTBT possess different highest occupied molecular orbital (HOMO) levels (5.5 eV for C_8-BTBT[60] and 5.1 eV for C_{16}-IDTBT[61,62]) and the valence band (VB) for FACs is around 5.4 eV[4], the OSC materials chosen to construct HJPTs could form either straddling-gap type-I heterojunctions (C_8-BTBT) or staggered-gap type-II heterojunctions (C_{16}-BTBT)[56] with FACs (**Figure 6.1c**). These two different heterojunction configurations can be used to understand how to best facilitate photoinduced carriers transferring/circulating from the absorber to the channel in hybrid-type phototransistors.

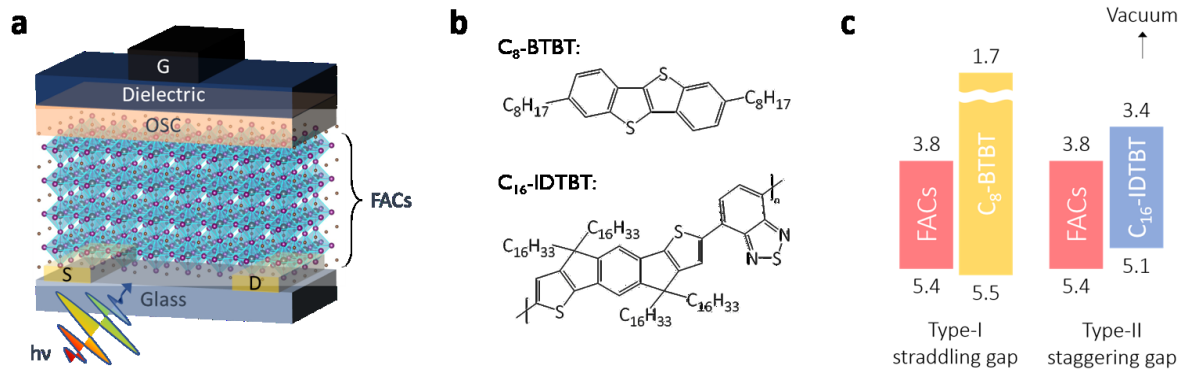


Figure 6.1: (**a**) Schematic of HJPT configured in a staggered BC-TG architecture. A MHP ($FA_{0.83}Cs_{0.17}PbI_{2.7}Br_{0.3}$, FACs)/OSC heterostructure is employed as a dual function transistor channel. Incident light absorbed upon the FACs layer can trigger the photodetection functionality in HJPTs. (**b**) Chemical structures of a small molecule C_8-BTBT and a copolymer C_{16}-IDTBT employed as the OSC layer. (**c**) Energy band alignments of type-I and type-II heterojunctions for FACs/C_8-BTBTand FACs/C_{16}-IDTBT, respectively.

6.3.2 Film Characterisations

Figure 6.2 shows the ultraviolet-visible (UV-vis) absorption spectra for FACs, C_8-BTBT, C_{16}-IDTBT and a blend film composed of C_8-BTBT and C_{16}-IDTBT in a ratio of 1:1 (abbreviated as blend 1:1). The absorption edge for FACs appears slightly below 800 nm while C_8-BTBT and C_{16}-IDTBT/blend 1:1 start at ~400 nm and ~730 nm, respectively.

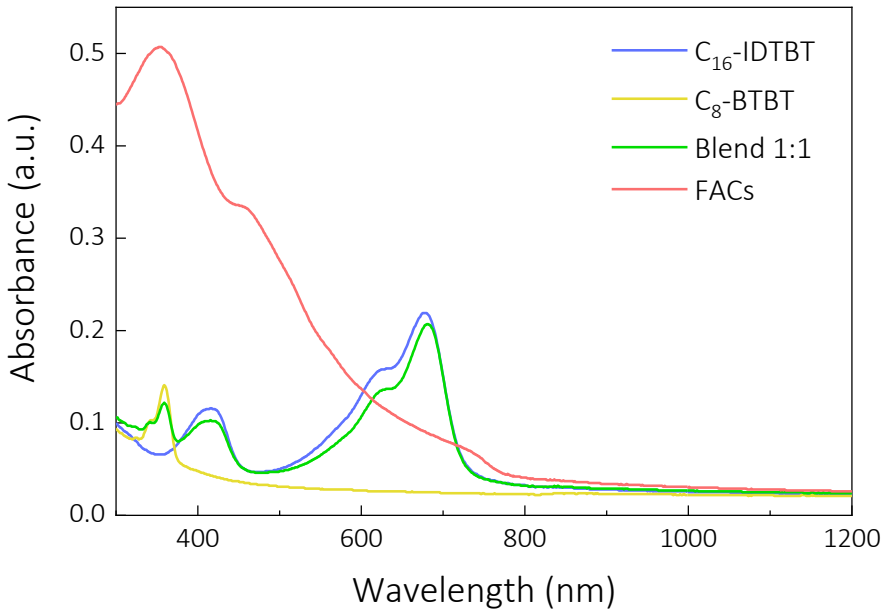


Figure 6.2: Ultraviolet–visible (UV-vis) absorption spectrum for C_{16}-IDTBT, C_8-BTBT, an organic blend of C_8-BTBT:C_{16}-IDTBT in a ratio of 1:1 (blend 1:1) and FACs.

Figures 6.3a-d show surface topographic images acquired using atomic force microscopy (AFM) for the hetero FACs/OSC bilayer stacks and the pristine FACs film. The height distribution extracted from the AFM data is presented in **Figure 6.3e**. Apart from clear grain-like surface features, the pristine FACs film exhibits two distinct peaks in its height distribution. This is attributed to the co-existence of thick perovskite-rich areas as well as thin perovskite-deficient regions in the FACs film. On the other hand, for all the FACs/OSC bilayer stacks only one Gaussian-like distribution is observed regardless of what OSC compositions were used. Therefore, in the bilayer stacks the OSCs formed conformal coatings with excellent coverage over the grainy FACs layer below. The latter is critical for long-range carrier-transport pathways in laterally-structured devices like transistors[63].

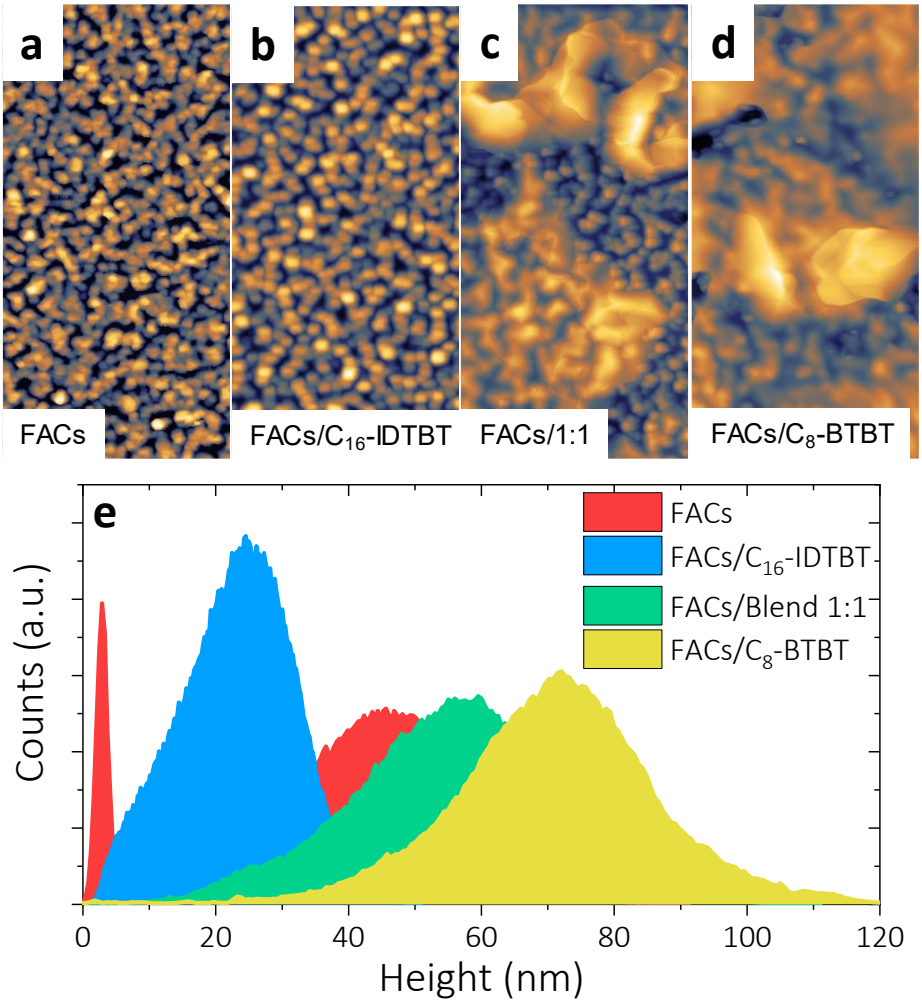


Figure 6.3: Representative AFM topographic images for different MHP/OSC bilayer stacks: (**a**) FACs; (**b**) FACs/ C_{16}-IDTBT (top-right); (**c**) FACs/blend 1:1; (**d**) FACs/C_8-BTBT. (**e**) Corresponding height distributions derived from the AFM results (**a**)-(**d**).

Figure 6.4 shows grazing-incidence wide-angle X-ray scattering (GIWAXS) patterns for the pristine OSC films and the FACs/OSC bilayers, which resemble the actual film stack in the present perovskite HJPTs. X-ray incident angle of 0.1° was used for studying both the pristine OSC films (1st row in **Figure 6.4**) and the bilayer stacks (2nd row in **Figure 6.4**) in the GIWAXS measurement. The GIWAXS pattern for the pristine C_8-BTBT film shows the (001) peak at q = 0.25 $Å^{-1}$ and a series of (00L) peaks along out-of-plane (q_z) direction (L = 1, 2, 3…), presenting a typical edge-on orientation[64]. This property is important for efficient in-plane, lateral charge transport, in particular for transistor applications. On the other hand, the pristine C_{16}-IDTBT thin film shows both (200) peak at q = 0.48 $Å^{-1}$ and (010) peak at q = 1.65 $Å^{-1}$ along q_z direction, corresponding to the backbone stacking and π-π stacking of the polymer chain, respectively. This result reveals the coexistence of edge-on and face-on orientations in the pristine C_{16}-IDTBT film. The blend 1:1 film shares a similar structure with the pristine C_8-

BTBT, suggesting the same orientation for C_8-BTBT in the blend and C_{16}-IDTBT being amorphous. The FACs layer introduces ring-like features at higher *q* space. At low q space, the FACs/C_8-BTBT and FACs/blend 1:1 bilayer stacks share similar scattering features with the corresponding pristine OSC films. The GIWAXS patterns do not exhibit any pronounced OSC structural features in the FACs/C_{16}-IDTBT sample, indicating that C_{16}-IDTBT forms an amorphous-like layer on top of FACs.

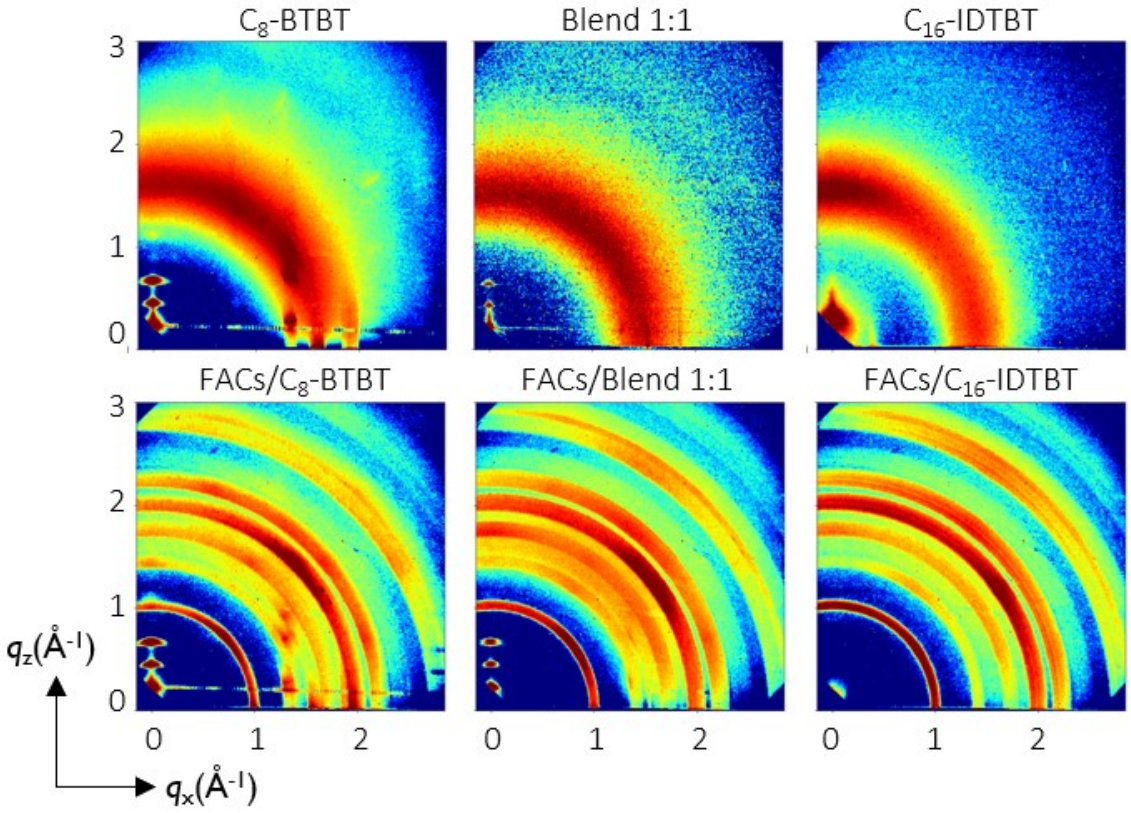


Figure 6.4: GIWAXS patterns for the pristine OSC films and FACs/OSC bilayer stacks.

6.3.3 Phototransistor Optoelectronic Characterisations

To examine the optoelectronic properties of the HJPTs, five types of FACs HJPTs with different OSC compositions were fabricated, namely pure C_8-BTBT (1:0), pure C_{16}-IDTBT (0:1), and three C_8-BTBT:C_{16}-IDTBT blends (i.e., C_8-BTBT:C_{16}-IDTBT = 3:1, 1:1 and 1:3). All the fabricated HJPTs were first measured in the dark as normal transistors and the transistor performance parameters are summarised in **Table 6.2**.

Table 6.2: Transistor performance of FACs/OSC HJPTs.

Composition (C_8-BTBT:C_{16}-IDTBT)	Mobility ($cm^2V^{-1}s^{-1}$)	Threshold voltage V_{TH} (V)	Turn-on voltage V_{ON} (V)	On/off ratio	Subthreshold swing S.S. (V/dec)
1:0	0.33	-4.1	-1.6	2.5×10^3	9.4
3:1	0.05	-6.4	-4.0	2.0×10^3	6.5
1:1	0.42	-7.3	-3.6	4.3×10^3	3.5
1:3	0.57	-5.6	-2.8	9.2×10^3	4.1
0:1	1.02	-6.6	-3.4	2.4×10^4	4.8

The optoelectronic characterisation was then performed by exposing these HJPTs to illuminations of three LED light sources with EL peaks centred at 632 nm(red) ,525 nm(green) and 475 nm(blue) under three different intensities. The corresponding transfer characteristics are shown in **Figures 6.5 - 6.9**. Under illumination, an increase in the drain current (I_D) was observed for all HJPTs indicative of photocarrier generation. In the HJPT with C_8-BTBT only (**Figure 6.5**), the photoresponse appears to consist of two components, i.e. transistors turned on at more positive V_G and a significant increase in the I_D at the off-state. I_D at the off-state was increased by an order of magnitude even under the illumination of the lowest intensity of 7 $\mu W/cm^2$. The observation of a more positive turn-on voltage (V_{ON}) is attributed to a change in the flat band voltage caused by the photogenerated carriers accumulated at the back channel side[65]. Moreover, the fact that an apparent increase was observed in the off-current is evidencing the back-channel charge accumulation. Similar to pristine C_8-BTBT, the blend 3:1 HJPT (**Figure 6.6**) shows photoresponse consisting of a positive shift of V_{ON} and an increased I_D at the off-state. However, compared to the pristine C8BTBT device, the increase in I_D at the off-state is less prominent with a maximum increment of one order of magnitude observed under the highest incident light intensity of 705 $\mu W/cm^2$. In the blend 1:1 HJPT (**Figure 6.7**), no significant increase in I_D at the off-state is observed and the photoresponse can be mainly recognised by a shift of V_{ON} toward the positive V_G. This photoresponse is close to the phenomenon described in an ideal hybrid phototransistor consisting of a channel semiconductor and a light absorber, with the highest photoresponse around V_{ON} and suppressed

photoinduced channel current at the transistor's off-state[1]. Such a characteristic is due to the fact that photogenerated carriers were mostly transferred from the absorber to the channel with the presence of larger amount of C_{16}-IDTBT. In the blend 1:3 HJPT (**Figure 6.8**), the photoresponse is similar to that of blend 1:1 but the magnitude of the curve shift become less apparent. In the pristine C_{16}-IDTBT HJPT (**Figure 6.9**), I_D modulation by light is further less prominent. Such observation indicates the inefficiency of photogenerated carriers to transport and circulate in the C_{16}-IDTBT channel as compared to the carriers that are induced and modulated by the gate bias. Moreover, the carriers injected by applying large gate bias at transistor on-state are generally several orders of magnitude higher than the photoinduced carriers. This explains why the magnitude of the increased current levels (i.e., photoresponse) at transistor on-state is found to be less prominent compared to that in the off-state for all the HJPTs.

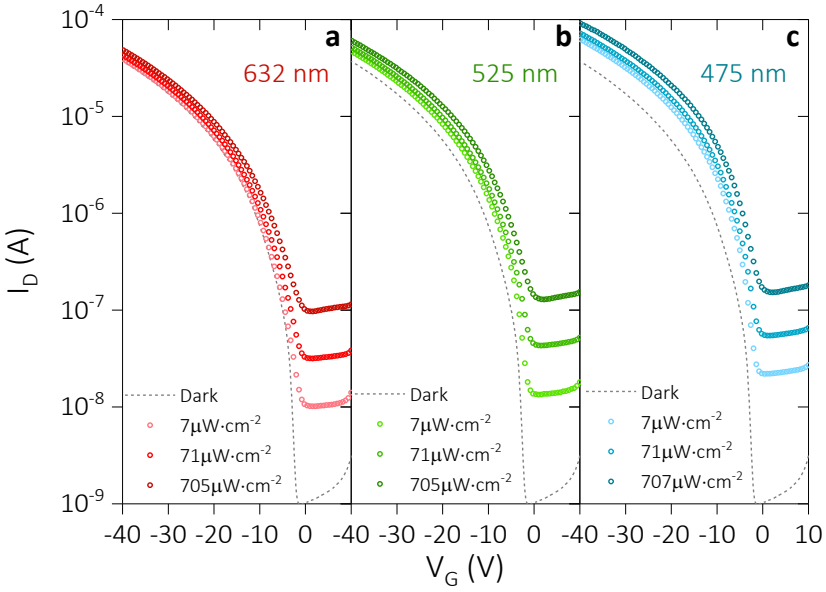


Figure. 6.5: Transfer characteristics of a FACs/OSC HJPT with C_8-BTBT only measured in dark and under illumination of (**a**) red light (λ_{peak}= 632 nm), (**b**) green light (λ_{peak}= 525 nm) and (**c**) blue light (λ_{peak}= 475 nm) with three different power densities. The device was operated at a constant drain voltage (V_D) of -40 V

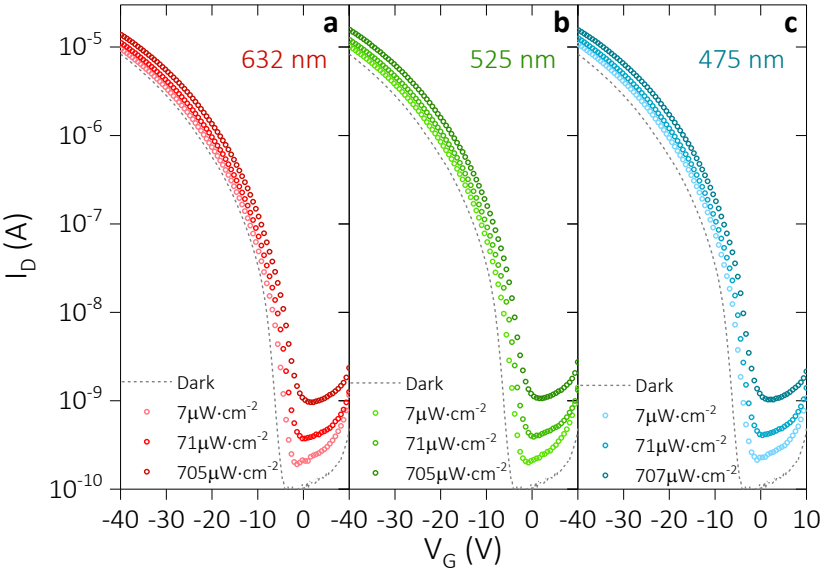


Figure 6.6: Transfer characteristics of a FACs/OSC HJPT with a blend of C_8-BTBT and C_{16}-IDTBT in a ratio of 3:1 measured in dark and under illumination of (**a**) red light (λ_{peak}= 632 nm), (**b**) green light (λ_{peak}= 525 nm) and (**c**) blue light (λ_{peak}= 475 nm) with three different power densities. The device was operated at a constant drain voltage (V_D) of -40 V.

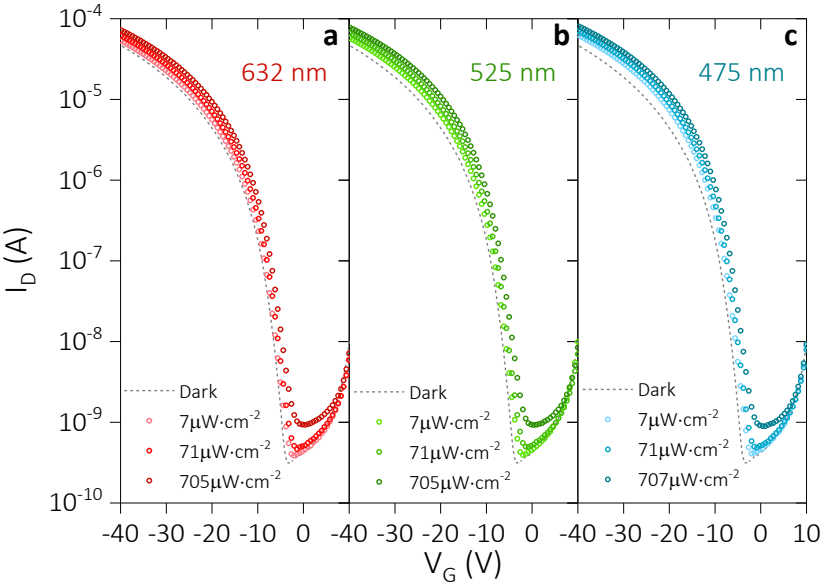


Figure 6.7: Transfer characteristics of a FACs/OSC HJPT with a blend of C_8-BTBT and C_{16}-IDTBT in a ratio of 1:1 measured in dark and under illumination of (**a**) red light (λ_{peak}= 632 nm), (**b**) green light (λ_{peak}= 525 nm) and (**c**) blue light (λ_{peak}= 475 nm) with three different power densities. The device was operated at a constant drain voltage (V_D) of -40 V.

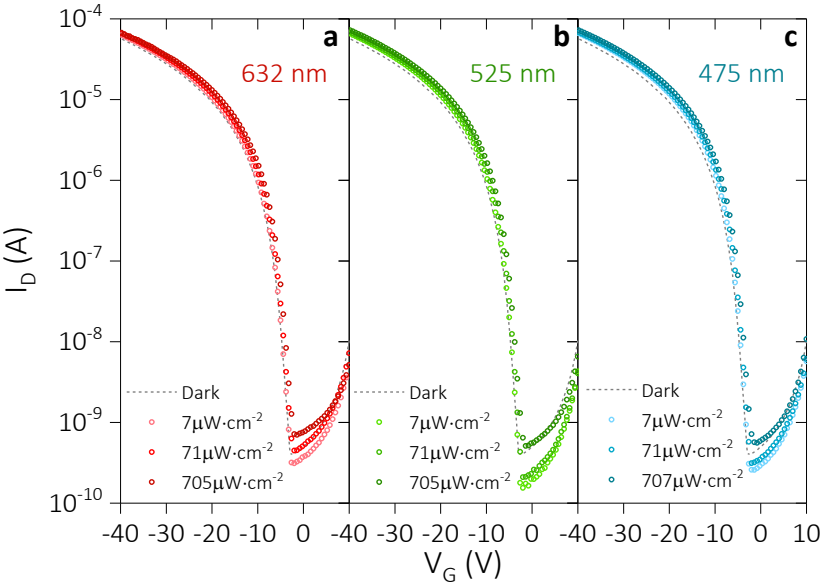


Figure 6.8: Transfer characteristics of a FACs/OSC HJPT with a blend of C_8-BTBT and C_{16}-IDTBT in a ratio of 1:3 measured in dark and under illumination of (**a**) red light (λ_{peak}= 632 nm), (**b**) green light (λ_{peak}= 525 nm) and (**c**) blue light (λ_{peak}= 475 nm) with three different power densities. The device was operated at a constant drain voltage (V_D) of -40 V.

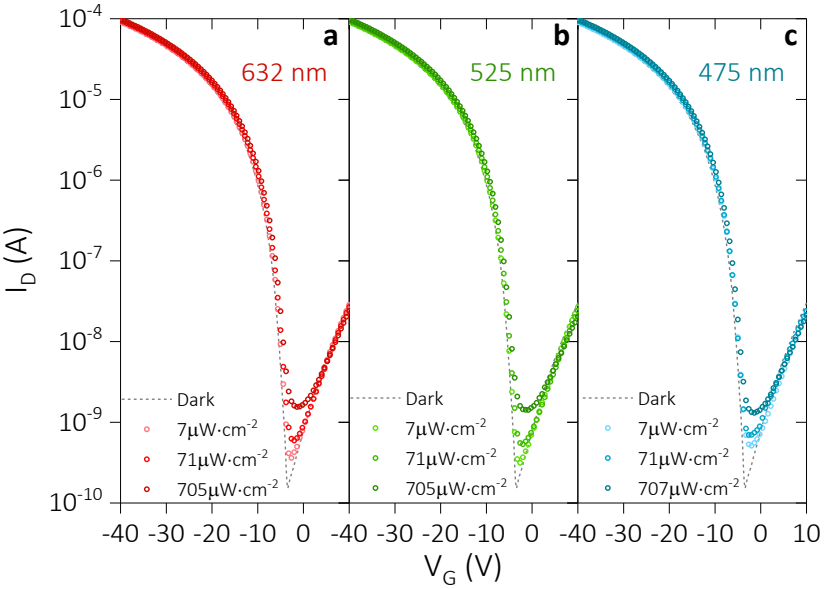


Figure 6.9: Transfer characteristics of a FACs/OSC HJPT with C_{16}-IDTBT only measured in dark and under illumination of (a) red light (λpeak= 632 nm), (b) green light (λpeak= 525 nm) and (c) blue light (λpeak= 475 nm) with three different power densities. The device was operated at a constant drain voltage (VD) of -40 V.

The photoresponse of these five types of HJPTs also shows different wavelength dependence. In the C_8-BTBT based HJPTs a strong wavelength dependence was observed, with a more significant photoresponse under blue illumination and a less significant photoresponse under red illumination. This wavelength dependence of photoresponse in the C_8-BTBT dominant HJPTs is coincident with the absorption spectrum of FACs which has a higher absorption coefficient at shorter wavelengths (as shown in **Figure 6.2**), indicating the efficient photocarrier transport and circulation within the C_8-BTBT/FACs heterojunction. In contrast, the wavelength dependence becomes less prominent with the increasing amount of C_{16}-IDTBT. Such a difference in wavelength dependence again confirms the inefficiency of photogenerated carriers transport and circulation in the C_{16}-IDTBT dominated devices.

Figure. 6.10 summarises the calculated gate-dependent responsivity for the HJPTs under the illumination of three LED light sources with illumination intensity of 7 $\mu W/cm^2$. A maximum responsivity over 10^4 A/W appears to be readily achievable with most of the present HJPTs operated at the transistors' on-state (V_G = -40V). Among different OSC compositions, the C_8-BTBT based HJPT exhibits the highest responsivity of 2×10^4 A/W. Yet, another noticeable feature for the HJPTs is the responsivity measured at/near the transistors' off-state (i.e., low dark-current levels) that exhibits significant difference from one another. The difference in responsivity of the HJPTs indicates that adjusting the C_8-BTBT to C_{16}-IDTBT composition can deliver tuneable, 'on-demand'-like responsivity using the HJPT approach, extending the HJPT's suitability for a variety of optoelectronic applications[20–22]. The responsivity achieved in the HJPT approach is almost among the highest reported to date for MHP based phototransistors. Since the HJPTs with C_8-BTBT and/or C_{16}-IDTBT can only deliver field-effect mobility <1 $cm^2/V \cdot s$ (as shown in **Table 6.2**) the reason for this outstanding performance should be attributed other factors rather than excessive channel carrier density like that in a photoconductor.

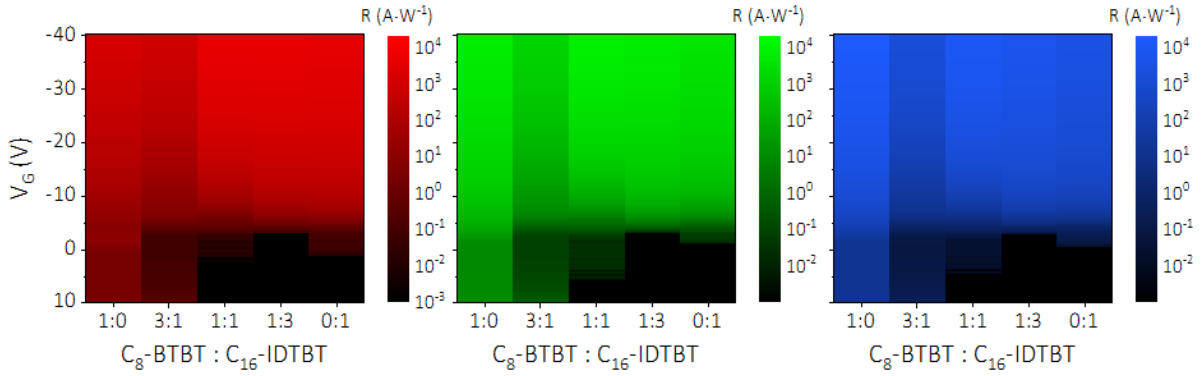


Figure 6.10: Gate-voltage dependent responsivity (R) measured at VD = -40 V from HJPTs based on C_8-BTBT, C_{16}-IDTBT and different blend ratios between them under different light sources: 632 nm (left); 525 nm (middle); 475 nm (right), all under ~5 µW cm-2 incident optical power density.

An important feature of a phototransistor that sets this technology apart from photodiodes is their intrinsic ability to deliver tuneable, high-level gain. Compared to photodiodes, the high responsivity for phototransistors and photoconductors is almost inevitably accompanied by higher dark current densities, hence introducing a high level of noise. The latter is detrimental to signal distinguishing and amplification, as well as diminishing the potential for deploying readout-free circuitry. In **Figure 6.11**, we plot the relation between photogain and dark current density for the HJPTs as well as simulated photodetectors and photoconductors (see section 6.2.5). The HJPTs approach can result in high photogain (with the highest photogain reaching ~4.5×10^4) at low dark current levels[20]. Such a result is comparable to the state-of-the-art hybrid-type phototransistors[20] and surpasses the simulated single-component MHP photoconductor model (light purple line shown in **Figure 6.11**) by several orders of magnitude. Ideally, if a pseudo-photoconductor is set to operate at V_{appl} = 40 V with the same aforementioned parameters, it will require an extremely-long carrier lifetime of ~20 ms in order to achieve such a high photogain of 4×10^4. Moreover, a noticeable feature that appears between the off-state and the subthreshold region, is that the devices based on C_8-BTBT and 3:1 blend explicitly exhibit photogain plateau, i.e. slow decrease in photogain; when operating outside this regime, i.e. towards the high-gain region, both follow a power-law increase as the HJPTs based on the other OSC compositions. As such, for those devices based on C_8-BTBT and 3:1 blend the photogain levels maintain even when the dark current density starts decreasing as the transistor further enters the deep-subthreshold operation (i.e., close to off-state).

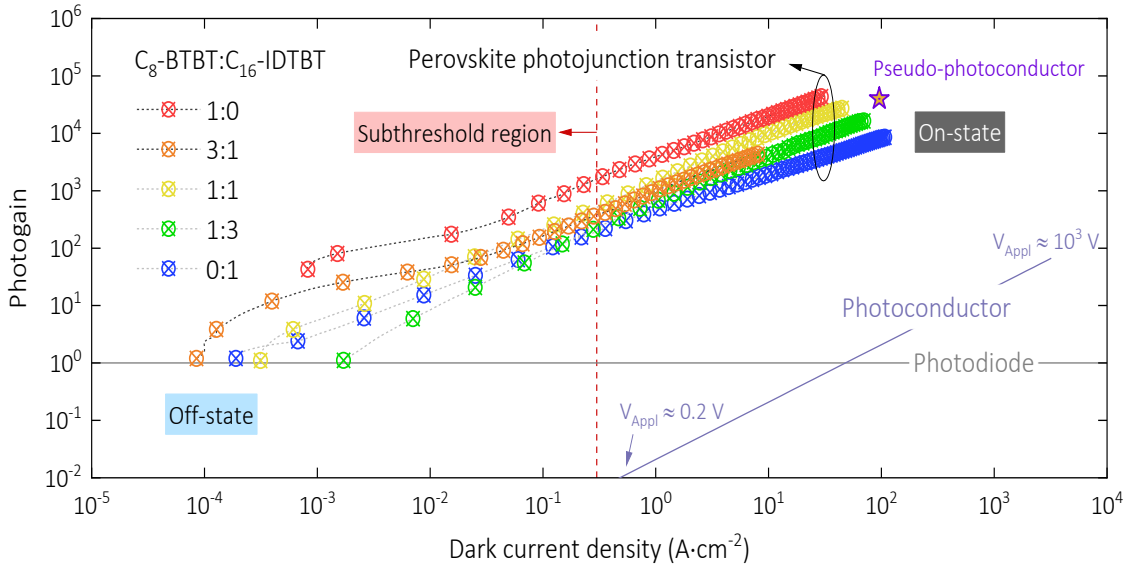


Figure 6.11: Photogain as a function of dark current density for HJPTs with different OSCs at ~5 μW cm^{-2} incident power from a 475-nm LED light source. For comparison, a photoconductor model is calculated based on the same channel dimension using the drift current equation with applied voltages (V_{appl}) ranging from 0.2 V to 10^3 V. A pseudo-photoconductor modelled to achieve a high-gain level (~4 × 10^4) is set to operate at V_{appl} = 40 V using the same parameters for the drift current equation but requires a carrier lifetime of 20 ms. The theoretical limit for the photogain from a photodiode is drawn for reference.

6.3.4 Characterisation of Current Noise in HJPTs

To further quantify the performance of the HJPTs with respect to noise, two noise-related figures of merit, i.e. noise-equivalent power (NEP) and specific detectivity D* of HJTPs, were analysed via the current noise characterisation. By performing the current noise measurement, the spectral noise density of the devices, which is critical for the NEP and D* analysis, can be determined.

In general, the sources of noise within an electronic device can be explained by many mechanisms such as thermal noise, dielectric noise or flicker noise[56], the total noise spectral therefore is affected by multiple factors. A commonly-accepted assumption is that the shot noise from dark current is the dominant contribution[66]. This shot-noise-based assumption provides a simple way to estimate the noise spectrum density, but it might also lead to a severe underestimation[7,67]. The noise spectral density in this study therefore was obtained following a previously-reported approach[68]. This approach estimates the noise spectrum density based on Fourier analysis on the acquired device dark current waveform. The dark current waveforms of HJPTs with three different OSC compositions (i.e. C_8-BTBT, C_{16}-IDTBT and a blend film

composed of C_8-BTBT and C_{16}-IDTBT in a ratio of 1:1) were recorded when the devices were biased at a fixed V_D of -40V. The waveforms acquired in a sampling rate of 1 kHz are shown in **Figure 6.12**.

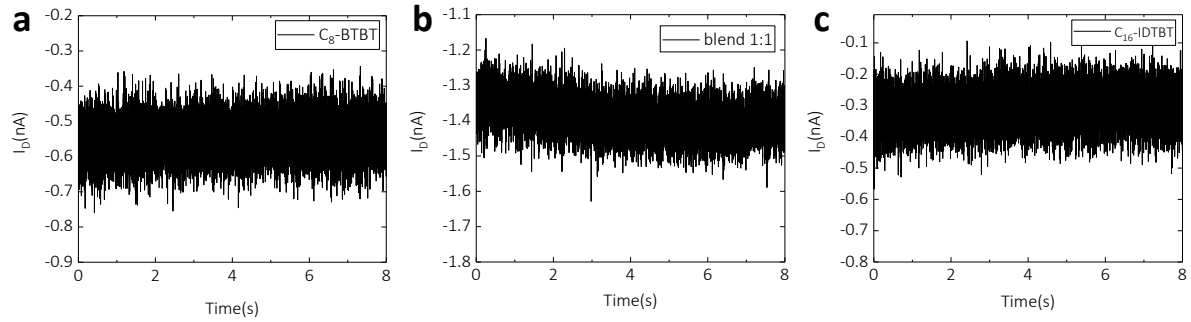


Figure 6.12: The dark current waveforms of FACs/OSC HJPTs with (**a**) pristine C_8-BTBT, (**b**) blend in a ratio of 1:1 and (**c**) pristine C_{16}-IDTBT measured at a constant drain voltage (V_D) of -40 V.

By applying a Fourier transform to the dark current waveform, the noise spectral density was obtained as shown in **Figure 6.13**. The corresponding *NEP* can then be calculated via **Equation 2.22** and the specific detectivity (D^*) can be obtained via **Equation 2.23**. The calculated *NEP* and D^* values at a modulation frequency of 1 Hz for the devices with different OSC compositions are summarised in **Table 6.3**. Since the responsivity of the present HJPTs under the illumination of three LED light sources (λ_{peak}= 475, 525, 632 nm) can reach ~10^4 A/W, this corresponds to an *NEP* of 10^{-17} W $Hz^{-1/2}$ and a D^* of 10^{14} Jones. We note that such high D^* value is already two orders of magnitude higher than the value reported for Si-based photodetectors[66].

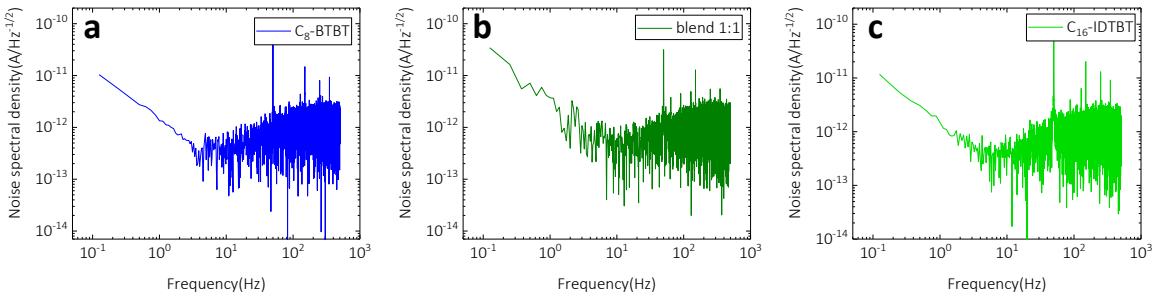


Figure 6.13: Analysis of noise spectral density of the HJPTs based on the Fourier transform of dark current waveform shown in Figure 6.12.

Table 6.3: HJPTs figures of merit from current noise characterisation.

composition	R(AW^{-1})	I_n(pA)	NEP(W·Hz$^{-1/2}$)	D*(Jones)
C_8-BTBT	1.7×10^{4}	1.3	7.8×10^{-17}	2.2×10^{14}
Blend 1:1	1.1×10^{4}	3.7	3.5×10^{-17}	4.9×10^{14}
C_{16}-IDTBT	3.2×10^{3}	1.5	4.5×10^{-16}	3.8×10^{13}

6.3.5 Spectroscopic Analysis of Photoinduced Charge Carriers

The most peculiar characteristic in the present HJPTs is their tuneable photoresponse characteristic at/near the transistor off-states. This operation regime has no/little gate field to attract photoinduced carriers to cross the heterojunctions between the FACs and OSCs. Therefore, a series of spectroscopic studies, which do not involve direct out-of-plane field-effect, on the FACs/OSC bilayer stacks were carried out in order to elucidate the driving force behind this tuneable photoresponse characteristic.

Fig. 6.14 shows the results of FACs/C_8-BTBT, FACs/blend 1:1 and FACs/C_{16}-IDTBT obtained from time-resolved and steady-state photoluminescence (TRPL and SSPL) studies, respectively. Compared to FACs/C_8-BTBT, the shorter PL decay and the quenched PL signal observed from the FACs/C_{16}-IDTBT sample suggest the photocarriers in FACs have been effectively transferred to the C_{16}-IDTBT. On the other hand, the FACs/blend 1:1 sample share similar PL characteristics with the FACs/C_{16}-IDTBT one, suggesting that the OSC material in a C_8-BTBT/C_{16}-IDTBT blend in direct contact with FACs is mostly C_{16}-IDTBT. These observations in fact, are in line with the pronounced vertical phase separation for small molecule and polymer blends reported previously[62,63], where they show that C_8-BTBT mostly form in the upper part of a blend layer when mixed with C_{16}-IDTBT.

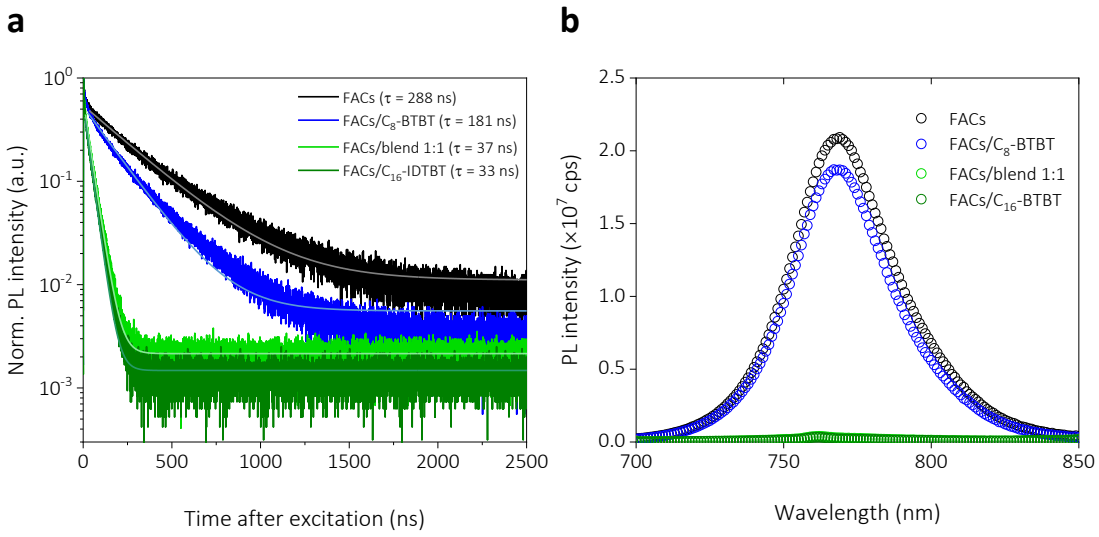


Figure 6.14: Photoluminescence (PL) spectroscopy results for FACs and FACs/OSC bilayer stacks: (**a**) time-resolved PL (TRPL) study and (**b**) steady-state PL (SSPL) study. In (**a**) the time constant τ for each sample was extracted using the rate based on mono-exponential decay.

To further probe the nature of charge-transfer between the FACs and OSC layers, the bilayer stacks were studied using time-resolved microwave conductivity (TRMC). TRMC enables one to evaluate a proxy for the sum of electron and hole mobilities without the need to form a device or deposit electrical contacts[69,70]. **Figure 6.15a** shows the TRMC figure of merit $\phi\Sigma\mu_{\mathrm{TRMC}} = \phi(\mu_e + \mu_h)$ for pristine FACs and FACs/OSC bilayer stacks as a function of optical fluence, where ϕ is the charge-generation efficiency, and μ_e and μ_h are the electron and hole mobilities, respectively. From **Figure 6.15a**, one can evaluate $\phi\Sigma\mu_{\mathrm{TRMC}}$ = 0.8 cm^2 V^{-1} s^{-1} for the pristine FACs film, $\phi\Sigma\mu_{\mathrm{TRMC}}$ = 0.61, 0.15 and 0.2 cm^2 V^{-1} s^{-1} for the FACs/C_8-BTBT, FACs/C_{16}-IDTBT and FACs/blend 1:1 bilayer stacks, respectively. Both the pristine FACs and FACs/C_8-BTBT bilayer have an approximately three to four-fold increase in $\phi\Sigma\mu_{\mathrm{TRMC}}$ as compared to the FACs/C_{16}-IDTBT and FACs/blend 1:1 bilayer stacks. $\phi\Sigma\mu_{\mathrm{TRMC}}$ as determined by the TRMC technique is representative of local sum of electron and hole mobilities, in the plane of the substrate, averaged over the whole sample. In an attempt to draw an analogy between spectroscopic analysis and HJPT operation from the viewpoint of the in-plane charge transport, transient photoconductivity (TPC) measurement was carried out to determine long-range lateral mobility $\phi\Sigma\mu_{\mathrm{TPC}}$ [71,72] The results as shown in **Figure 6.15b** show that the long-range lateral mobility $\Sigma\mu_{\mathrm{TPC}}$ are 0.69, 0.52, 0.19 and 0.22 cm^2 V^{-1} s^{-1} (at the lowest excitation density of 1.57×10^{17} cm^{-3}) for the pristine FACs, FACs/C_8-BTBT, FACs/C_{16}-IDTBT and FACs/blend 1:1, respectively. Notably, these long-range mobilities of the pristine FACs

and FACs/OSC bilayers are in good agreement with the average local mobilities determined by TRMC.

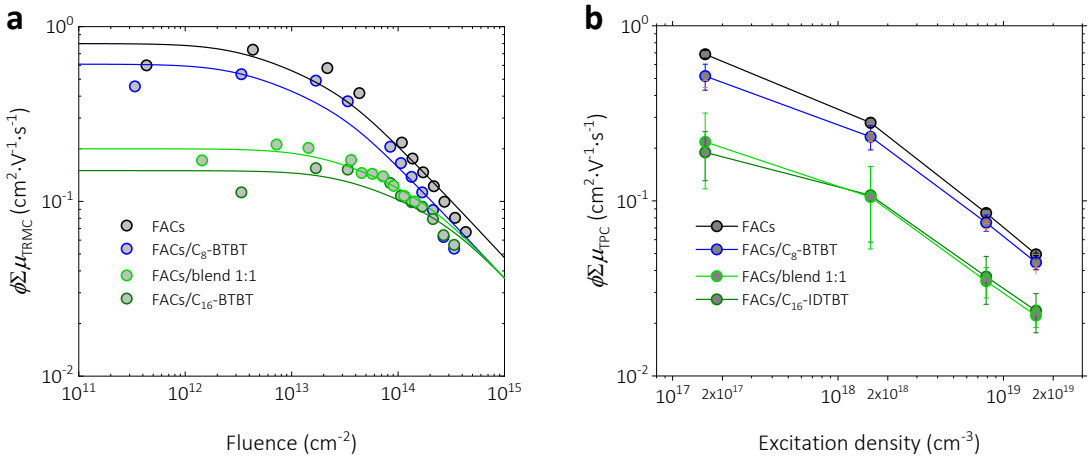


Figure 6.15: (**a**) Time resolved microwave conductivity (TRMC) figure of merit $\phi\Sigma\mu_{TRMC}$, plotted as a function of incident optical fluence for FACs and FACs/OSC bilayer stacks on quartz substrates. (**b**) Transient photoconductivity (TPC) long-range lateral mobility $\phi\Sigma\mu_{TPC}$, plotted as a function of excitation density by varying incident laser fluences for FACs and FACs/OSCs bilayer stacks.

To summarise the spectroscopic analysis presented in **Figures 6.14&15**, the results are considered as convincing evidence that upon illumination, photoinduced charges are readily transferred from FACs to C_{16}-IDTBT or a C_8-BTBT:C_{16}-IDTBT blend, but less readily from FACs to C_8-BTBT. In making this claim, the sum of mobility of charge carriers in the FAC film is assumed to be higher than in the OSCs[73], hence allowing us to interpret a lower measured mobility being representative of a greater proportion of carriers in the OSC versus the FACs film. The observed difference in charge-transfer is hypothesised to be due to the energetic levels between FACs and OSCs (**Figure 6.1c**) and the differences in morphology at the interface between the OSC and FAC, as observed in the GIWAXS data (**Figure 6.4**), in which C_8-BTBT molecules form an edge-on orientation. The latter is not as beneficial as face-on orientation to help vertical charge transfer, as widely reported in the field of organic photovoltaics[74].

6.3.6 Mott-Schottky Analysis and Perovskite-Organic Contact Diodes

To elucidate the relationship between i) the efficient circulation of photocarrier, and ii) high responsivity and high photogain, Mott-Schottky analysis was carrier out on the FACs/OSCs bilayer stacks. This is in order to gain insight into how the photoinduced charge profiles are

distributed in proximity to various FACs/OSCs heterointerfaces in a dark environment and upon light illumination. In the meantime, perovskite-organic contact diodes were also fabricated by sandwiching three different FACs/OSC bilayer stacks between Au-Au electrodes to interrogate their optoelectronic characteristics (**Figure 6.16**). For both the FACs/C_{16}-IDTBT and FACs/blend 1:1 devices, typical diode I-V characteristics are observed in the dark (**Figure 6.16a** and **b**) whilst upon light illumination, clear photoresponse arise at the low dark current region. The FACs/C_8-BTBT device on the other hand, exhibits less-rectifying I-V curves in the dark as a sign of forming a bilayer dielectric stack (**Figure 6.16c**), rather than a diode. Upon light illumination the symmetric I-V curve remains with a rising current level under both positive and negative biasing conditions due to the straddling type-I heterojunction that forms the non-rectifying junction between the HOMO level of C_8-BTBT and the VB edge of FACs.

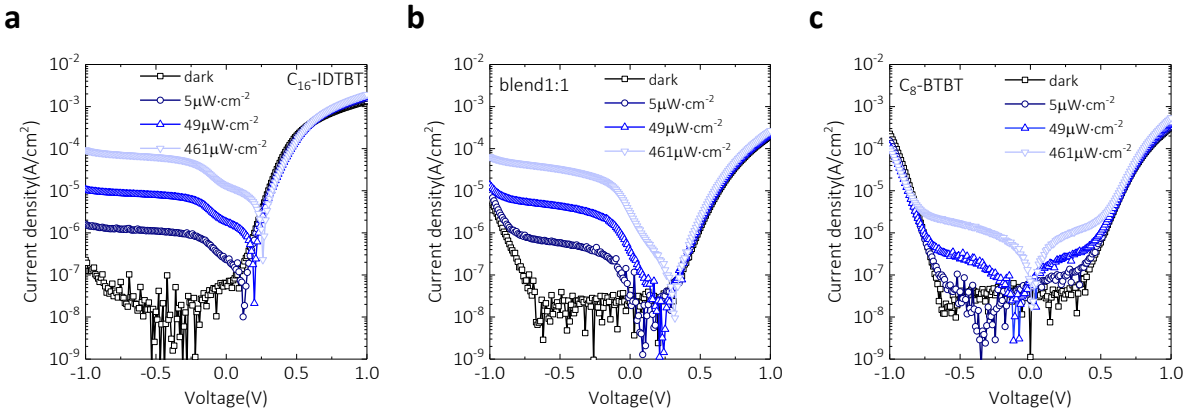


Figure 6.16: Current voltage characteristics of diodes based on FACs/OSC heterostructure measured in the dark and under different illumination intensities using a green LED light source (λ_{peak}= 525 nm): (**a**) FACs/C_8-BTBT, (**b**) FACs/Blend 1:1 and (**c**) FACs/C_{16}-IDTBT. The FACs/OSC stacks were sandwiched by two symmetric Au electrodes.

To enhance the transparency for illumination from the glass side, the experimental film stacks for Mott-Schottky analysis were made on ITO-coated glass with the composition of glass/ITO/FACs/OSC/Au. The Mott-Schottky analysis was carried out at an intermediate frequency of ~5 kHz, the effects of series resistance and surface as well as interface dipoles can be minimised during operation[75–77]. **Figure 6.17** shows the Mott-Schottky results for FACs/ C_{16}-IDTBT, FACs/blend 1:1 and FACs/C_8-BTBT, respectively. In the dark, both the FACs/C_{16}-IDTBT and FACs/blend 1:1 samples (**Figure. 6.17a** and **b**) exhibit two distinct regions in their Mott-Schottky plots: i) a transition region with an uprising trend (going from forward to reverse bias); ii) a flat region with constant capacitance levels. For the former, this is the operation regime where charge depletion takes place whilst the latter indicates combined

geometric capacitance from bulk dielectric polarisation of the FACs/OSC bilayer stacks[76]. For the FACs/C_8-BTBT sample (**Figure. 6.17c**), only one distinct region with a constant capacitance level is observed during the entire operational regime. This characteristic indicates the FACs/C_8-BTBT bilayer forms a dielectric stack. Such a result is in line with the electrical characterisation obtained from the attempt to make a FACs/C_8-BTBT diode (**Figure 6.16c**).

However, under illumination, the FACs/C_{16}-IDTBT (**Figure 6.17a**) and FACs/blend 1:1 (**Figure. 6.17b**) samples exhibit charge polarity inversion behaviour with a depletion region for p-type charge carriers at low forward bias corresponding to the decrease in the capacitance (i.e., higher C^{-2}). This is followed by the accumulation of the oppositely charged carriers (i.e. n-type) associated with the increase in the capacitance. Under large reverse bias, the Mott-Schottky plots for both FACs/C_{16}-IDTBT and FACs/blend 1:1 returns to a high capacitance level. For the latter, the true enhancement on bulk dielectric polarisation in FACs still need to be clarified because to evidence such enhancement taking place one needs to exclude the effect caused by the accumulation of surface/interface dipoles, which results in a high capacitance level under light[76]. Nevertheless, the clear charge polarity inversion when entering the reverse bias regime (**Figure 6.17a** and **b**) is a direct indication that negatively charged carriers (i.e., electrons) are left behind after positively charge carriers (i.e., holes) are transferred to the OSC layers. This result is supported by the spectroscopic data (**Figure 6.14** and **Figure 6.15**). On the other hand, in **Figure 6.17c** upon illumination the FACs/C_8-BTBT sample exhibit high capacitance levels measured under very low biasing conditions (see **Figure 6.17c** inset, from -0.1 V to 0.1 V), but outside this regime, extremely low capacitance was measured. For the latter, the most plausible reason being that this bilayer dielectric stack could not withhold any charge carriers as a result of capacitance lost, hence the effect of series resistance being manifest. The two different capacitance levels outside ±0.1 V also correspond to different charge extraction efficiencies. This result agrees with the I-V characteristics of the FACs/C_8-BTBT diode, i.e., higher current levels (corresponding to higher capacitance levels) at positive bias than negative bias.

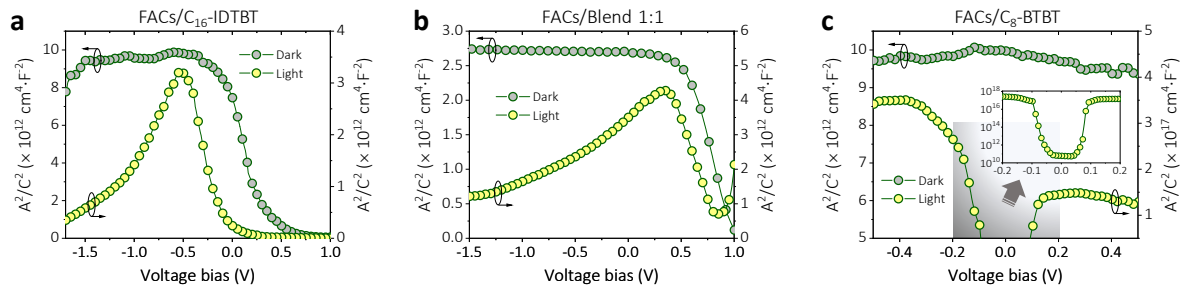


Figure 6.17: Mott-Schottky plots for different FACs/OSC bilayer stacks: (**a**) FACs/C_{16}-IDTBT; (**b**) FACs/blend 1:1; (**c**) FACs/C_8-BTBT. The impedance spectroscopy measurements were carried out with an AC perturbation of 10 mV at 5 kHz in the dark (grey-filled dark green circles) as well as under a white-light LED illumination source (~2.61 mW cm^{-2}; data shown in yellow-filled bright green circles).

6.3.7 Charge Transfer Mechanism

From the information presented so far, the proposed photoinduced charge transfer mechanisms in the HJPTs under illumination for different transistor operation regimes can be summarised in **Figure 6.18**.

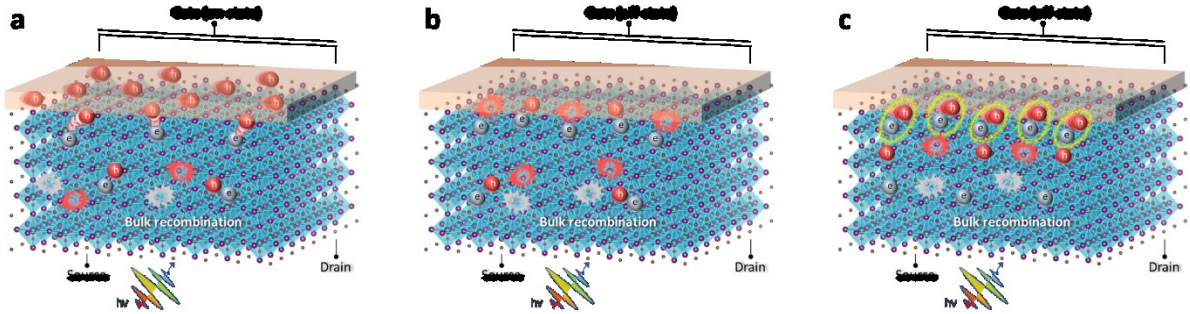


Figure 6.18: Schematic illustration of photocarriers' charge transfer mechanisms for HJPTs under different operational regimes: (**a**) photocarriers being swept into a transistor channel under strong influence of gate-induced field at a HJPT's on-state; (**b**) at/near the off-state FACs/C_{16}-IDTBT-dominant HJPTs under a weak accumulation or depletion operation whilst majority p-type photocarriers being transferred from FACs to OSC due to favourable energetic alignment; (**c**) at/near the off-state photoinduced carriers accumulated at the heterointerfaces in the FACs/C_8-BTBT HJPTs, being attributed to the formation of a type-I heterojunction between FACs/C_8-BTBT and a preferential edge-on molecular orientation in C_8-BTBT. The latter helps to transport photocarriers along the edge-on π-π stacking on the back-channel side of C_8-BTBT.

When a HJPT operates in the on-state, photoinduced charge carriers are pulled across the heterojunction between FACs and OSCs by the applied gate field, regardless of which type of heterojunctions FACs/OSCs are formed (**Figure 6.18a**). For the off-state of HJPTs based on

FACs/C_{16}-IDTBT and FACs/C_{16}-IDTBT-dominant blends (e.g. C_8-BTBT:C_{16}-IDTBT = 1:3), the photocarriers transferred from FACs to OSCs are still able to be transported in a transistor channel due to the formation of a type-II heterojunction (**Figure 6.18b**). However, their weak photoresponse at/near the off-states indicates the inefficiency of such a mechanism for a hybrid phototransistor. On the other hand, the pronounced photoresponse at/near the off-state obtained from the FACs/C_8-BTBT HJPTs can be related to the observation of the largest increase of the capacitance at zero bias. The latter suggests strong formation of photoinduced carriers accumulated at the FACs/C_8-BTBT interfaces[76] and can be depicted as a photocarrier-rich region that forms next to p-type C_8-BTBT (**Figure 6.18c**). Such interpretation coincides with the spectroscopic data as upon light illumination, no significant charge transfer from FACs to C_8-BTBT was observed. The latter is attributed not only to the type-I heterojunction formation between FACs and C_8-BTBT, but also to the evident edge-on orientation of C_8-BTBT, which helps those photoinduced carriers to transport along the heterointerfaces of FACs and C_8-BTBT and be manifested as photocurrent. Importantly, this assumption is supported by the fact that the pristine FACs transistor is only able to provide a fraction of channel current (I_D) under the same flux of incident light (**Figure 6.19**).

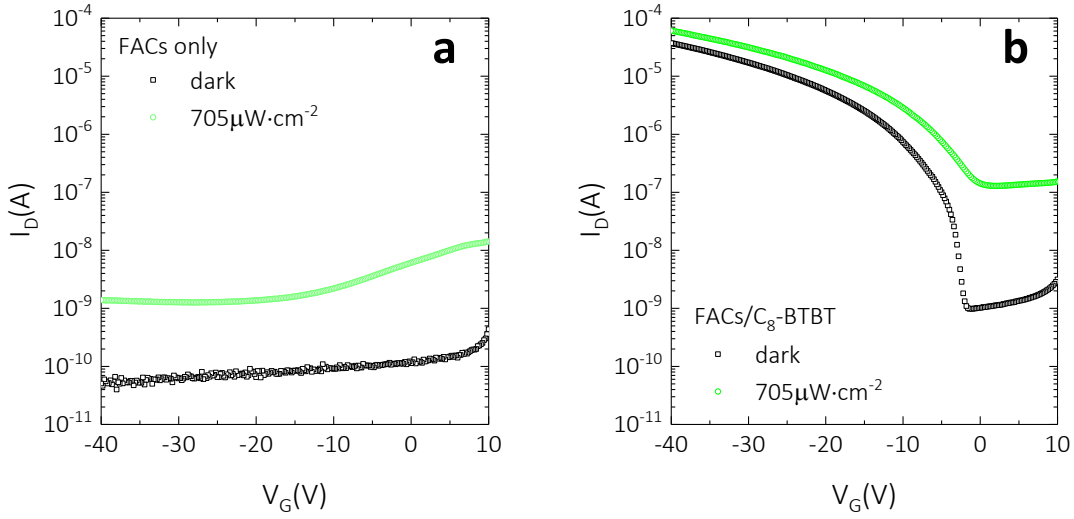


Figure 6.19: Transfer characteristics of phototransistors with (a) FACs only and (b) FACs/C8-BTBT heterojunction measured in dark and under green illumination (λpeak= 525 nm) of 705 μW cm-2. Both devices were operated at a constant VD = -40 V.

6.3.8 Assessing Performance Metrics via A Photo-Inverter

Key performance metrics for phototransistors, such as responsivity, noise-equivalent power, and specific detectivity, are traditionally assessed relative to those defined for photodiodes.

These figures of merit characterise the efficiency of photodetectors related to the process of photon-electron conversion. However, being an active device, phototransistor enables not only photodetection but also controllable signal amplification. Unique properties in phototransistors such as tuneability of photoresponse and current/voltage amplification cannot be assessed through those performance metrics set for traditional two terminal photodetectors. Since phototransistors combine detection and amplification into a single element, it is more informative to consider their utility as a circuit element. Here a simple circuit route that uses a photo-inverter to assess a phototransistor's performance metric, which is in a manner more applicable for optoelectronic circuit design, is proposed. To demonstrate this concept, a PMOS-like photo-inverter served as a common-source amplifier was fabricated using two identical FACs HJPTs (**Figure 6.20**).

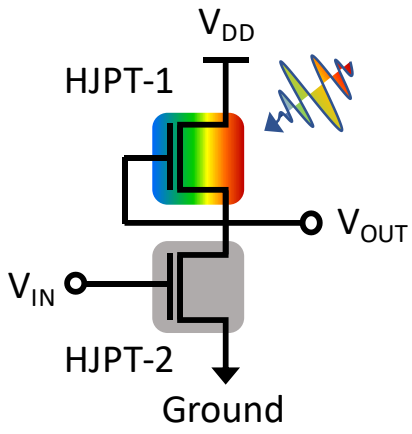


Figure 6.20: Schematic of a PMOS-like HJPT photo-inverter to resemble a common-source amplifier for assessing phototransistor performance metric.

The operation of this photo-inverter can be simply explained by a voltage divider model[78]. The resistance difference between the constituent phototransistors, namely HJPT-1 and HJPT-2, determines the voltages dropped on HJPT-1 and HJPT-2, and hence the level of circuit output signal (V_{OUT}). The resistance of the depletion load HJPT-1 is controlled by the illumination intensity, while that of the electrical switch HJPT-2 is controlled by the electrical input signal (V_{IN}). To fulfil the function of signal inversion, it requires pronounced photoresponse from the optical load and excellent current-voltage modulation from the electrical switch, respectively. Since the photo-inverter configuration is composed of two identical HJPTs, it requires the constituent devices with both good electrical switching and high photoresponse. In this regard, the proposed photo-inverter circuit is considered as a unique method for phototransistor performance evaluation. In this circuit configuration, one can

directly evaluate the intrinsic amplification (A_i) of the composed optoelectronic elements (e.g. HJPT-1 and HJPT-2) for amplifying input signals[79] as the latter is the main advantage for using an active electronic component like phototransistors. Moreover, A_i is an important criterion to separate a phototransistor from a photoconductor as the need for saturation in I_D to achieve high A_i.

Figure 6.21 shows the photo-inverters based on FACs/C_8-BTBT and FACs/C_{16}-IDTBT in the operation regime that corresponds to the lower dark current levels. The sharp voltage swing for both photo-inverters is a result of good current-voltage modulation from HJPT-2. Using a range of light intensities to illuminate HJPT-1, significant difference arises in the photo-inverters' transfer characteristics (V_{OUT} versus V_{IN}). In the case of FACs/C_{16}-IDTBT, the output signal (V_{OUT}) is observed to be only half of the power supply (V_{DD}) under low-power illumination. This is attributed to rather weak photoresponse from HJPT-1, and a pronounced signal inversion was only observed under stronger light intensities (**Figure 6.21a**). In contrast, the stronger photoresponse of the FACs/C_8-BTBT HJPT-1 allows high V_{OUT} can be achieved at low V_{IN} (i.e. signal inversion) under the lowest incident light intensity (**Figure 6.21b**).

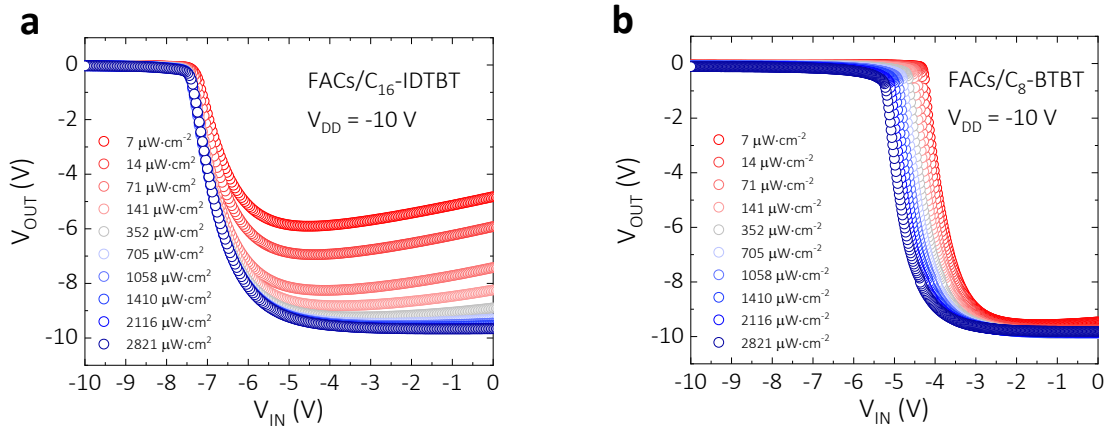


Figure 6.21: Inverter transfer characteristics measured under different incident light intensities for photo-inverters composed of HJPTs using (**a**) FACs/C_{16}-IDTBT and (**b**) FACs/C_8-BTBT.

The positions of V_{IN} for the maximum amplification ($A_{i,max}$) remains relatively close to one another under different illumination intensities in the FACs/C_{16}-IDTBT photo-inverter (**Figure 6.22a**); whilst for the FACs/C_8-BTBT a clear shift towards more negative V_{IN} is observed to achieve $A_{i,max}$ (**Figure 6.22b**). The latter implies a change of device characteristics (i.e., a transistor's threshold voltage) under light illumination. More importantly, with this unipolar configuration the present HJPTs are able to deliver a high $A_{i,\,max}$ of ~15, especially if

one considers that this is achieved without any advanced device engineering and only based on the use of a very low-k gate dielectric material[80].

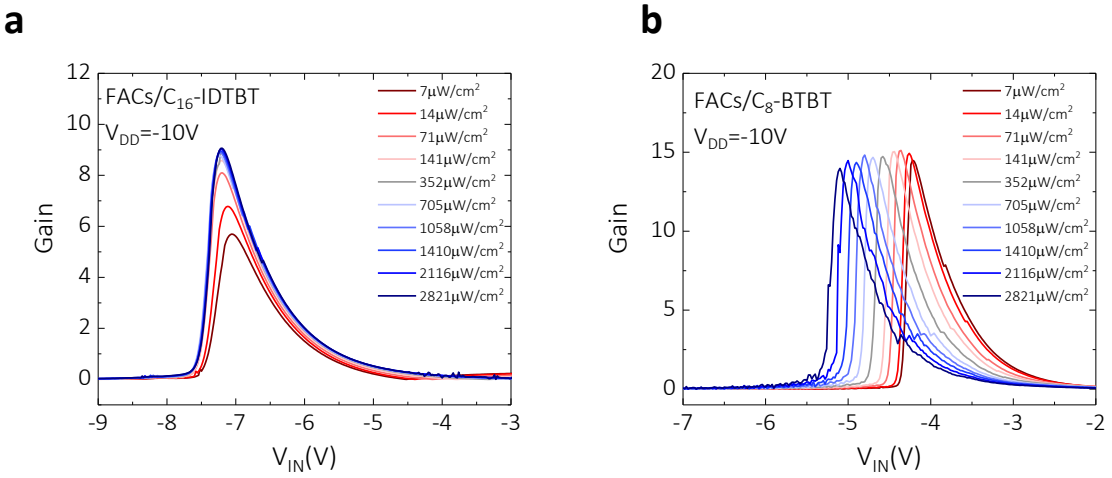


Figure 6.22: Corresponding intrinsic amplification (A_i) obtained for (**a**) FACs/C_{16}-IDTBT and (**b**) FACs/C_8-BTBT.

Furthermore, plotting V_{OUT} as a function of optical power density under different V_{IN} (**Figure 6.23a** and **b**), the FACs/C_8-BTBT photo-inverter can operate as an electro-optical optical switch/sensor[81,82] offering higher tune-ability/sensitivity using either electrical or optical signals (or both) as compared to the FACs/C_{16}-IDTBT configuration. All the results from the photo-inverter analysis are in line with the observation from HJPTs' transfer characteristics where the FACs/C_8-BTBT HJPT exhibits a stronger photoresponse.

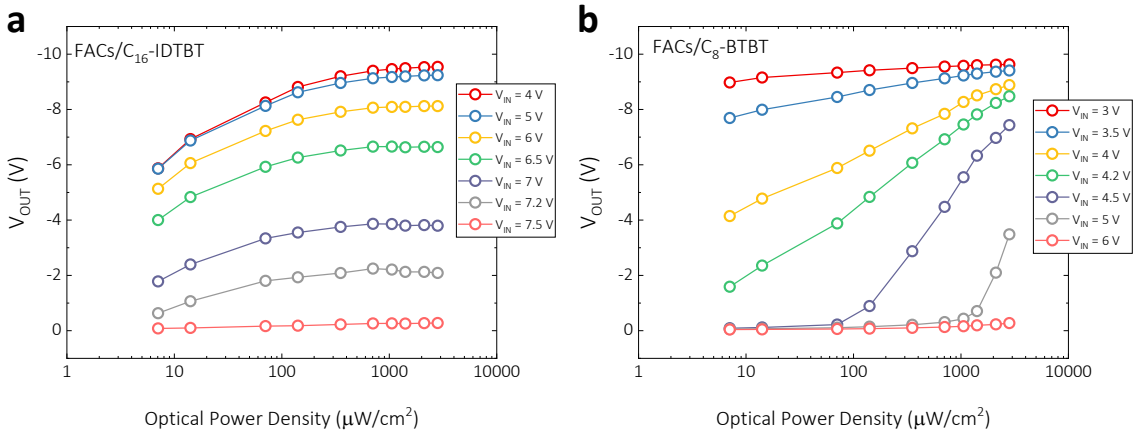


Figure 6.23: Effect of incident optical power density on VOUT measured at a fixed voltage supply VDD of -10 V for different VIN biases for the (**a**) FACs/C_{16}-IDTBT photo-inverter and (**b**) FACs/C_8-BTBT photo-inverter.

6.4 Conclusions

In this chapter a new concept of a hybrid phototransistor incorporating a MHP into a series of OSCs as the channel material, was investigated. Resulting phototransistors are characterised by a straddling-gap type-I heterojunction and exhibit state-of-the-art photogain of 4.5×10^4. Using a variety of characterisations techniques, highly efficient photocarrier transfer is found to transport through preferential edge-on molecular orientation at the MHP/OSC heterointerfaces. By tuning MHP/OSC interfaces from straddling-gap to staggering-gap heterojunction configurations, the ability to tune optoelectronics of phototransistors in an 'on-demand' manner is demonstrated. Next, a new method to assess phototransistors is proposed by using a photo-inverter circuit to evaluate their amplification and essential functionality in order to be operated in both linear and saturation modes as a transistor. The improved insights into the photocarrier dynamics and its dependence on material properties and operational conditions provide both essential knowledge and thorough understanding for designing and developing perovskite-organic based optoelectronic devices and systems.

Bibliography

(1) Kufer, D.; Konstantatos, G. Photo-FETs: Phototransistors Enabled by 2D and 0D Nanomaterials. *ACS Photonics* **2016**, *3* (12), 2197–2210.

(2) De Wolf, S.; Holovsky, J.; Moon, S. J.; Löper, P.; Niesen, B.; Ledinsky, M.; Haug, F. J.; Yum, J. H.; Ballif, C. Organometallic Halide Perovskites: Sharp Optical Absorption Edge and Its Relation to Photovoltaic Performance. *J. Phys. Chem. Lett.* **2014**, *5* (6), 1035–1039.

(3) Alcocer, M. J. P.; Leijtens, T.; Herz, L. M.; Petrozza, A.; Snaith, H. J. Electron-Hole Diffusion Lengths Exceeding Trihalide Perovskite Absorber. *Science (80-.).* **2013**, *342* (October), 341–344.

(4) McMeekin, D. P.; Sadoughi, G.; Rehman, W.; Eperon, G. E.; Saliba, M.; Horantner, M. T.; Haghighirad, A.; Sakai, N.; Korte, L.; Rech, B.; Johnston, M. B.; Herz, L. M.; Snaith, H. J. A Mixed-Cation Lead Mixed-Halide Perovskite Absorber for Tandem Solar Cells. *Science (80-.).* **2016**, *351* (6269), 151–155.

(5) Snaith, H. J. Present Status and Future Prospects of Perovskite Photovoltaics. *Nat. Mater.* **2018**, *17*, 372–376.

(6) Green, M. A.; Ho-Baillie, A.; Snaith, H. J. The Emergence of Perovskite Solar Cells. *Nat. Photonics* **2014**, *8* (7), 506–514.

(7) García de Arquer, F. P.; Armin, A.; Meredith, P.; Sargent, E. H. Solution-Processed Semiconductors for next-Generation Photodetectors. *Nat. Rev. Mater.* **2017**, *2* (3), 16100.

(8) Stranks, S. D.; Snaith, H. J. Metal-Halide Perovskites for Photovoltaic and Light-Emitting Devices. *Nat. Nanotechnol.* **2015**, *10* (5), 391–402.

(9) Lin, Y.-H.; Pattanasattayavong, P.; Anthopoulos, T. D. Metal-Halide Perovskite Transistors for Printed Electronics: Challenges and Opportunities. *Adv. Mater.* **2017**, *29* (46), 1702838.

(10) Li, F.; Ma, C.; Wang, H.; Hu, W.; Yu, W.; Sheikh, A. D.; Wu, T. Ambipolar Solution-Processed Hybrid Perovskite Phototransistors. *Nat. Commun.* **2015**, *6*, 8238.

(11) Cho, N.; Li, F.; Turedi, B.; Sinatra, L.; Sarmah, S. P.; Parida, M. R.; Saidaminov, M. I.; Murali, B.; Burlakov, V. M.; Goriely, A.; Mohammed, O. F.; Wu, T.; Bakr, O. M. Pure Crystal Orientation and Anisotropic Charge Transport in Large-Area Hybrid Perovskite Films. *Nat. Commun.* **2016**, *7* (May), 1–11.

(12) Chen, C.; Zhang, X.; Wu, G.; Li, H.; Chen, H. Visible-Light Ultrasensitive Solution-Prepared Layered Organic–Inorganic Hybrid Perovskite Field-Effect Transistor. *Adv. Opt. Mater.* **2017**, *5* (2), 2–6.

(13) de Quilettes, D. W.; Vorpahl, S. M.; Stranks, S. D.; Nagaoka, H.; Eperon, G. E.; Ziffer, M. E.; Snaith, H. J.; Ginger, D. S. Impact of Microstructure on Local Carrier Lifetime in Perovskite Solar Cells. *Science (80-.).* **2015**, *348* (6235), 683–686.

(14) Wu, X.; Trinh, M. T.; Niesner, D.; Zhu, H.; Norman, Z.; Owen, J. S.; Yaffe, O.; Kudisch, B. J.; Zhu, X. Y. Trap States in Lead Iodide Perovskites. *J. Am. Chem. Soc.* **2015**, *137* (5), 2089–2096.

(15) Goedel, K.; Friend, R. H.; Sadhanala, A.; Thomas, T. H.; Nair, B.; Yang, B.; Docampo, P.; Giesbrecht, N.; Huang, W.; Senanayak, S. P.; Sirringhaus, H.; McNeill, C. R.; Moya, X.; Gann, E.; Guha, S. Understanding Charge Transport in Lead Iodide Perovskite Thin-Film Field-Effect Transistors. *Sci. Adv.* **2017**, *3* (1), e1601935.

(16) Labram, J. G.; Fabini, D. H.; Perry, E. E.; Lehner, A. J.; Wang, H.; Glaudell, A. M.; Wu, G.; Evans, H.; Buck, D.; Cotta, R.; Echegoyen, L.; Wudl, F.; Seshadri, R.; Chabinyc, M. L. Temperature-Dependent Polarization in Field-Effect Transport and Photovoltaic Measurements of Methylammonium Lead Iodide. *J. Phys. Chem. Lett.* **2015**, *6* (18), 3565–3571.

(17) Fang, Y.; Dong, Q.; Shao, Y.; Yuan, Y.; Huang, J. Highly Narrowband Perovskite Single-Crystal Photodetectors Enabled by Surface-Charge Recombination. *Nat. Photonics* **2015**, *9* (10), 679–686.

(18) Feng, J.; Gong, C.; Gao, H.; Wen, W.; Gong, Y.; Jiang, X.; Zhang, B.; Wu, Y.; Wu, Y.; Fu, H.; Jiang, L.; Zhang, X. Single-Crystalline Layered Metal-Halide Perovskite Nanowires for Ultrasensitive Photodetectors. *Nat. Electron.* **2018**, *1* (7), 404–410.

(19) Leng, K.; Abdelwahab, I.; Verzhbitskiy, I.; Telychko, M.; Chu, L.; Fu, W.; Chi, X.; Guo, N.; Chen, Z.; Chen, Z.; Zhang, C.; Xu, Q. H.; Lu, J.; Chhowalla, M.; Eda, G.; Loh, K. P. Molecularly Thin Two-Dimensional Hybrid Perovskites with Tunable Optoelectronic Properties Due to Reversible Surface Relaxation. *Nat. Mater.* **2018**, *17* (10), 908–914.

(20) Adinolfi, V.; Sargent, E. H. Photovoltage Field-Effect Transistors. *Nature* **2017**, *542* (7641), 324–327.

(21) Pierre, A.; Gaikwad, A.; Arias, A. C. Charge-Integrating Organic Heterojunction Phototransistors for Wide-Dynamic-Range Image Sensors. *Nat. Photonics* **2017**, *11* (3), 193–199.

(22) Goossens, S.; Navickaite, G.; Monasterio, C.; Gupta, S.; Piqueras, J. J.; Pérez, R.;

Burwell, G.; Nikitskiy, I.; Lasanta, T.; Galán, T.; Puma, E.; Centeno, A.; Pesquera, A.; Zurutuza, A.; Konstantatos, G.; Koppens, F. Broadband Image Sensor Array Based on Graphene–CMOS Integration. *Nat. Photonics* **2017**, *11* (6), 366–371.

(23) Mohammed, O. F.; Huang, B.; Liang, L.; Han, S.; Wu, J.; Bakr, O. M.; Huang, W.; Guan, X.; Chen, Q.; Yang, H.; Wang, Y.; Teh, D. B. L.; Yi, Z.; Xie, X.; Zhumekenov, A. A.; Bettinelli, M.; Fan, D.; Wu, T.; Ou, X.; Almutlaq, J.; All, A. H.; Liu, X.; Li, J.; Li, Y. All-Inorganic Perovskite Nanocrystal Scintillators. *Nature* **2018**, *561* (7721), 88–93.

(24) Xie, C.; You, P.; Liu, Z.; Li, L.; Yan, F. Ultrasensitive Broadband Phototransistors Based on Perovskite/Organic-Semiconductor Vertical Heterojunctions. *Light Sci. Appl.* **2017**, *6* (8), e17023.

(25) Nagiri, R. C. R.; Meredith, P.; Armin, A.; Lin, Q.; Burn, P. L. Electro-Optics of Perovskite Solar Cells. *Nat. Photonics* **2014**, *9* (2), 106–112.

(26) Hodes, G.; Kronik, L.; Cahen, D.; Egger, D. A.; Brenner, T. M. Hybrid Organic—inorganic Perovskites: Low-Cost Semiconductors with Intriguing Charge-Transport Properties. *Nat. Rev. Mater.* **2016**, *1* (1), 1–16.

(27) Yu, W.; Li, F.; Yu, L.; Niazi, M. R.; Zou, Y.; Corzo, D.; Basu, A.; Ma, C.; Dey, S.; Tietze, M. L.; Buttner, U.; Wang, X.; Wang, Z.; Hedhili, M. N.; Guo, C.; Wu, T.; Amassian, A. Single Crystal Hybrid Perovskite Field-Effect Transistors. *Nat. Commun.* **2018**, *9* (1), 5354.

(28) Lee, Y.; Kwon, J.; Hwang, E.; Ra, C. H.; Yoo, W. J.; Ahn, J. H.; Park, J. H.; Cho, J. H. High-Performance Perovskite-Graphene Hybrid Photodetector. *Adv. Mater.* **2015**, *27* (1), 41–46.

(29) Wang, Y.; Zhang, Y.; Lu, Y.; Xu, W.; Mu, H.; Chen, C.; Qiao, H.; Song, J.; Li, S.; Sun, B.; Cheng, Y. B.; Bao, Q. Hybrid Graphene-Perovskite Phototransistors with Ultrahigh Responsivity and Gain. *Adv. Opt. Mater.* **2015**, *3* (10), 1389–1396.

(30) Spina, M.; Lehmann, M.; Náfrádi, B.; Bernard, L.; Bonvin, E.; Gaál, R.; Magrez, A.; Forrõ, L.; Horváth, E. Microengineered CH3NH3PbI3 Nanowire/Graphene Phototransistor for Low-Intensity Light Detection at Room Temperature. *Small* **2015**, *11* (37), 4824–4828.

(31) Dang, V. Q.; Han, G. S.; Trung, T. Q.; Duy, L. T.; Jin, Y. U.; Hwang, B. U.; Jung, H. S.; Lee, N. E. Methylammonium Lead Iodide Perovskite-Graphene Hybrid Channels in Flexible Broadband Phototransistors. *Carbon N. Y.* **2016**, *105*, 353–361.

(32) Sun, Z.; Aigouy, L.; Chen, Z. Plasmonic-Enhanced Perovskite-Graphene Hybrid Photodetectors. *Nanoscale* **2016**, *8* (14), 7377–7383.

(33) Kwak, D.-H.; Lim, D.-H.; Ra, H.-S.; Ramasamy, P.; Lee, J.-S. High Performance Hybrid Graphene–CsPbBr $_{3-x}$ I $_x$ Perovskite Nanocrystal Photodetector. *RSC Adv.* **2016**, *6* (69), 65252–65256.

(34) Shao, Y.; Liu, Y.; Chen, X.; Chen, C.; Sarpkaya, I.; Chen, Z.; Fang, Y.; Kong, J.; Watanabe, K.; Taniguchi, T.; Taylor, A.; Huang, J.; Xia, F. Stable Graphene-Two-Dimensional Multiphase Perovskite Heterostructure Phototransistors with High Gain. *Nano Lett.* **2017**, *17* (12), 7330–7338.

(35) Qian, L.; Sun, Y.; Wu, M.; Xie, D.; Ding, L.; Shi, G. A Solution-Processed High-Performance Phototransistor Based on a Perovskite Composite with Chemically Modified Graphenes(SI). *Adv. Mater.* **2017**, *29* (22).

(36) Xie, C.; Yan, F. Perovskite/Poly(3-Hexylthiophene)/Graphene Multiheterojunction Phototransistors with Ultrahigh Gain in Broadband Wavelength Region. *ACS Appl. Mater. Interfaces* **2017**, *9* (2), 1569–1576.

(37) Chang, P. H.; Liu, S. Y.; Lan, Y. B.; Tsai, Y. C.; You, X. Q.; Li, C. S.; Huang, K. Y.; Chou, A. S.; Cheng, T. C.; Wang, J. K.; Wu, C. I. Ultrahigh Responsivity and Detectivity Graphene-Perovskite Hybrid Phototransistors by Sequential Vapor Deposition. *Sci. Rep.* **2017**, *7* (March), 1–10.

(38) Kang, D. H.; Pae, S. R.; Shim, J.; Yoo, G.; Jeon, J.; Leem, J. W.; Yu, J. S.; Lee, S.; Shin, B.; Park, J. H. An Ultrahigh-Performance Photodetector Based on a Perovskite–Transition-Metal-Dichalcogenide Hybrid Structure(SI). *Adv. Mater.* **2016**, *28* (35), 7799–7806.

(39) Park, Y.; Lee, S.; Park, H. J.; Baac, H. W.; Yoo, G.; Heo, J. Hybrid Metal-Halide Perovskite-MoS2 Phototransistor. *J. Nanosci. Nanotechnol.* **2016**, *16* (11), 11722–11726.

(40) Liu, F.; Wang, J.; Wang, L.; Cai, X.; Jiang, C.; Wang, G. Enhancement of Photodetection Based on Perovskite/MoS $_2$ Hybrid Thin Film Transistor. *J. Semicond.* **2017**, *38* (3), 034002.

(41) Huo, C.; Liu, X.; Wang, Z.; Song, X.; Zeng, H. High-Performance Low-Voltage-Driven Phototransistors through CsPbBr $_3$ -2D Crystal van Der Waals Heterojunctions. *Adv. Opt. Mater.* **2018**, *1800152*, 1800152.

(42) Spina, M.; Náfrádi, B.; Tóháti, H. M.; Kamarás, K.; Bonvin, E.; Gaal, R.; Forró, L.; Horváth, E. Ultrasensitive 1D Field-Effect Phototransistors: CH3NH3PbI3nanowire Sensitized Individual Carbon Nanotubes. *Nanoscale* **2016**, *8* (9), 4888–4893.

(43) Li, F.; Wang, H.; Kufer, D.; Liang, L.; Yu, W.; Alarousu, E.; Ma, C.; Li, Y.; Liu, Z.;

Liu, C.; Wei, N.; Wang, F.; Chen, L.; Mohammed, O. F.; Fratalocchi, A.; Liu, X.; Konstantatos, G.; Wu, T. Ultrahigh Carrier Mobility Achieved in Photoresponsive Hybrid Perovskite Films via Coupling with Single-Walled Carbon Nanotubes. *Adv. Mater.* **2017**, *29* (16).

(44) Chen, Y.; Chu, Y.; Wu, X.; Ou-Yang, W.; Huang, J. High-Performance Inorganic Perovskite Quantum Dot–Organic Semiconductor Hybrid Phototransistors. *Adv. Mater.* **2017**, *29* (44), 1–8.

(45) Zou, C.; Xi, Y.; Huang, C. Y.; Keeler, E. G.; Feng, T.; Zhu, S.; Pozzo, L. D.; Lin, L. Y. A Highly Sensitive UV–vis–NIR All-Inorganic Perovskite Quantum Dot Phototransistor Based on a Layered Heterojunction. *Adv. Opt. Mater.* **2018**, *6* (14), 1–9.

(46) Bao, Q.; Loh, K. P. Graphene Photonics, Plasmonics, and Broadband Optoelectronic Devices. *ACS Nano* **2012**, *6* (5), 3677–3694.

(47) Novoselov, K. S.; Fal'Ko, V. I.; Colombo, L.; Gellert, P. R.; Schwab, M. G.; Kim, K. A Roadmap for Graphene. *Nature* **2012**, *490* (7419), 192–200.

(48) Murali, R. Graphene Transistors. *Graphene Nanoelectron. From Mater. to Circuits* **2012**, *9781461405* (7), 51–91.

(49) Meric, I.; Han, M. Y.; Young, A. F.; Ozyilmaz, B.; Kim, P.; Shepard, K. L. Current Saturation in Zero-Bandgap, Top-Gated Graphene Field-Effect Transistors. *Nat. Nanotechnol.* **2008**, *3* (11), 654–659.

(50) Qian, L.; Sun, Y.; Wu, M.; Xie, D.; Ding, L.; Shi, G. A Solution-Processed High-Performance Phototransistor Based on a Perovskite Composite with Chemically Modified Graphenes. *Adv. Mater.* **2017**, *29* (22), 1–7.

(51) Kang, D. H.; Pae, S. R.; Shim, J.; Yoo, G.; Jeon, J.; Leem, J. W.; Yu, J. S.; Lee, S.; Shin, B.; Park, J. H. An Ultrahigh-Performance Photodetector Based on a Perovskite–Transition-Metal-Dichalcogenide Hybrid Structure. *Adv. Mater.* **2016**, *28* (35), 7799–7806.

(52) Yu, Y.; Zhang, Y.; Zhang, Z.; Zhang, H.; Song, X.; Cao, M.; Che, Y.; Dai, H.; Yang, J.; Wang, J.; Zhang, H.; Yao, J. Broadband Phototransistor Based on $CH_3NH_3PbI_3$ Perovskite and PbSe Quantum Dot Heterojunction. *J. Phys. Chem. Lett.* **2017**, *8* (2), 445–451.

(53) Yu, Y.; Zhang, Y.; Song, X.; Zhang, H.; Cao, M.; Che, Y.; Dai, H.; Yang, J.; Zhang, H.; Yao, J. High Performances for Solution-Pocessed 0D–0D Heterojunction Phototransistors. *Adv. Opt. Mater.* **2017**, *5* (24), 1–6.

(54) Liu, X.; Kuang, W.; Ni, H.; Tao, Z.; Huang, Q.; Chen, J.; Liu, Q.; Chang, J.; Lei, W. A

Highly Sensitive and Fast Graphene Nanoribbon/CsPbBr3quantum Dot Phototransistor with Enhanced Vertical Metal Oxide Heterostructures. *Nanoscale* **2018**, *10* (21), 10182–10189.

(55) Watkins, S. E.; Heeney, M.; Salleo, A.; Gysel, R.; Ashraf, S.; McCulloch, I.; Kirkpatrick, J.; Anthopoulos, T.; Zhang, W.; McGehee, M.; Smith, J. Indacenodithiophene Semiconducting Polymers for High-Performance, Air-Stable Transistors. *J. Am. Chem. Soc.* **2010**, *132* (33), 11437–11439.

(56) Sze, S. M.; Ng, K. K. *Physics of Semiconductor Devices, 3rd Edition*; 2006.

(57) Konstantatos, G.; Badioli, M.; Gaudreau, L.; Osmond, J.; Bernechea, M.; de Arquer, F. P. G.; Gatti, F.; Koppens, F. H. L. Hybrid Graphene–quantum Dot Phototransistors with Ultrahigh Gain. *Nat. Nanotechnol.* **2012**, *7* (6), 363–368.

(58) Kufer, D.; Nikitskiy, I.; Lasanta, T.; Navickaite, G.; Koppens, F. H. L.; Konstantatos, G. Hybrid 2D-0D MoS 2 -PbS Quantum Dot Photodetectors. *Adv. Mater.* **2015**, *27* (1), 176–180.

(59) Ebata, H.; Izawa, T.; Miyazaki, E.; Takimiya, K.; Ikeda, M.; Kuwabara, H.; Yui, T. Highly Soluble [1]Benzothieno[3,2-b]Benzothiophene (BTBT) Derivatives for High-Performance, Solution-Processed Organic Field-Effect Transistors. *J. Am. Chem. Soc.* **2007**, *129* (51), 15732–15733.

(60) Kim, C. H.; Kymissis, I. Graphene-Organic Hybrid Electronics. *J. Mater. Chem. C* **2017**, *5* (19), 4598–4613.

(61) Venkateshvaran, D.; Nikolka, M.; Sadhanala, A.; Lemaur, V.; Zelazny, M.; Kepa, M.; Hurhangee, M.; Kronemeijer, A. J.; Pecunia, V.; Nasrallah, I.; Romanov, I.; Broch, K.; McCulloch, I.; Emin, D.; Olivier, Y.; Cornil, J.; Beljonne, D.; Sirringhaus, H. Approaching Disorder-Free Transport in High-Mobility Conjugated Polymers. *Nature* **2014**, *515* (7527), 384–388.

(62) Paterson, A. F.; Treat, N. D.; Zhang, W.; Fei, Z.; Wyatt-Moon, G.; Faber, H.; Vourlias, G.; Patsalas, P. A.; Solomeshch, O.; Tessler, N.; Heeney, M.; Anthopoulos, T. D. Small Molecule/Polymer Blend Organic Transistors with Hole Mobility Exceeding 13 Cm2V−1s−1. *Adv. Mater.* **2016**, *28* (35), 7791–7798.

(63) Panidi, J.; Paterson, A. F.; Khim, D.; Fei, Z.; Han, Y.; Tsetseris, L.; Vourlias, G.; Patsalas, P. A.; Heeney, M.; Anthopoulos, T. D. Remarkable Enhancement of the Hole Mobility in Several Organic Small-Molecules, Polymers, and Small-Molecule:Polymer Blend Transistors by Simple Admixing of the Lewis Acid p-Dopant B(C 6 F 5) 3. *Adv. Sci.* **2018**, *5* (1), 1700290.

(64) H, S.; P, B.; R, F.; M, N.; K, B.; B, L.-V.; A, S.; R, J.; E, M.; P, H.; D, D. L.; Fewer, S. Two-Dimensional Charge Transport in Self-Organized, High-Mobility Conjugated Polymers. *Nature* **1999**, *401* (6754), 685–688.

(65) Schießl, S. P.; Faber, H.; Lin, Y. H.; Rossbauer, S.; Wang, Q.; Zhao, K.; Amassian, A.; Zaumseil, J.; Anthopoulos, T. D. Hybrid Modulation-Doping of Solution-Processed Ultrathin Layers of ZnO Using Molecular Dopants. *Adv. Mater.* **2016**, *28* (20), 3952–3959.

(66) Gong, X.; Tong, M.; Xia, Y.; Cai, W.; Moon, J. S.; Cao, Y.; Yu, G.; Shieh, C.; Nilsson, B.; Heeger, A. J. High-Detectivity Polymer Photodetector with Spectral Response from 300 Nm to 1450 Nm. *Science (80-.).* **2009**, *325* (5948), 1665–1667.

(67) Fang, Y.; Armin, A.; Meredith, P.; Huang, J. Accurate Characterization of Next-Generation Thin-Film Photodetectors. *Nat. Photonics* **2019**, *13* (1), 1–4.

(68) Liu, C.-H.; Chang, Y.-C.; Norris, T. B.; Zhong, Z. Graphene Photodetectors with Ultra-Broadband and High Responsivity at Room Temperature. *Nat. Nanotechnol.* **2014**, *9* (4), 273–278.

(69) Oga, H.; Saeki, A.; Ogomi, Y.; Hayase, S.; Seki, S. Improved Understanding of the Electronic and Energetic Landscapes of Perovskite Solar Cells: High Local Charge Carrier Mobility, Reduced Recombination, and Extremely Shallow Traps. *J. Am. Chem. Soc.* **2014**, *136* (39), 13818–13825.

(70) Hutter, E. M.; Gélvez-Rueda, M. C.; Osherov, A.; Bulović, V.; Grozema, F. C.; Stranks, S. D.; Savenije, T. J. Direct–indirect Character of the Bandgap in Methylammonium Lead Iodide Perovskite. *Nat. Mater.* **2017**, *16* (1), 115–120.

(71) Leijtens, T.; Stranks, S. D.; Eperon, G. E.; Lindblad, R.; Johansson, E. M. J.; McPherson, I. J.; Rensmo, H.; Ball, J. M.; Lee, M. M.; Snaith, H. J. Electronic Properties of Meso-Superstructured and Planar Organometal Halide Perovskite Films: Charge Trapping, Photodoping, and Carrier Mobility. *ACS Nano* **2014**, *8* (7), 7147–7155.

(72) Lim, J.; Hörantner, M. T.; Sakai, N.; Ball, J. M.; Mahesh, S.; Noel, N. K.; Lin, Y. H.; Patel, J. B.; McMeekin, D. P.; Johnston, M. B.; Wenger, B.; Snaith, H. J. Elucidating the Long-Range Charge Carrier Mobility in Metal Halide Perovskite Thin Films. *Energy Environ. Sci.* **2019**, *12* (1), 169–176.

(73) Herz, L. M. Charge-Carrier Mobilities in Metal Halide Perovskites: Fundamental Mechanisms and Limits. *ACS Energy Lett.* **2017**, *2* (7), 1539–1548.

(74) Rand, B. P.; Cheyns, D.; Vasseur, K.; Giebink, N. C.; Mothy, S.; Yi, Y.; Coropceanu, V.; Beljonne, D.; Cornil, J.; Brédas, J. L.; Genoe, J. The Impact of Molecular Orientation

on the Photovoltaic Properties of a Phthalocyanine/Fullerene Heterojunction. *Adv. Funct. Mater.* **2012**, *22* (14), 2987–2995.

(75) Almora, O.; Aranda, C.; Mas-Marzá, E.; Garcia-Belmonte, G. On Mott-Schottky Analysis Interpretation of Capacitance Measurements in Organometal Perovskite Solar Cells. *Appl. Phys. Lett.* **2016**, *109* (17), 173903.

(76) Almora, O.; Aranda, C.; Garcia-Belmonte, G. Do Capacitance Measurements Reveal Light-Induced Bulk Dielectric Changes in Photovoltaic Perovskites? *J. Phys. Chem. C* **2018**, *122* (25), 13450–13454.

(77) Lopez-Varo, P.; Jiménez-Tejada, J. A.; García-Rosell, M.; Ravishankar, S.; Garcia-Belmonte, G.; Bisquert, J.; Almora, O. Device Physics of Hybrid Perovskite Solar Cells: Theory and Experiment. *Adv. Energy Mater.* **2018**, *8* (14), 1702772.

(78) Adel S. Sedra; Kenneth C. Smith. *Microelectronic Circuits*; 2007.

(79) Lee, S.; Nathan, A. Subthreshold Schottky-Barrier Thin-Film Transistors with Ultralow Power and High Intrinsic Gain. *Science (80-.).* **2016**, *354* (6310), 302–304.

(80) Paterson, A. F.; Lin, Y.-H.; Mottram, A. D.; Fei, Z.; Niazi, M. R.; Kirmani, A. R.; Amassian, A.; Solomeshch, O.; Tessler, N.; Heeney, M.; Anthopoulos, T. D. The Impact of Molecular P-Doping on Charge Transport in High-Mobility Small-Molecule/Polymer Blend Organic Transistors. *Adv. Electron. Mater.* **2018**, *4* (10), 1700464.

(81) Labram, J. G.; Wöbkenberg, P. H.; Bradley, D. D. C.; Anthopoulos, T. D. Low-Voltage Ambipolar Phototransistors Based on a Pentacene/PC 61BM Heterostructure and a Self-Assembled Nano-Dielectric. *Org. Electron. physics, Mater. Appl.* **2010**, *11* (7), 1250–1254.

(82) Anthopoulos, T. D. Electro-Optical Circuits Based on Light-Sensing Ambipolar Organic Field-Effect Transistors. *Appl. Phys. Lett.* **2007**, *91* (11), 113513.

Chapter 7 Conclusions

In this thesis different approaches toward high-performance phototransistors based on solution-processed semiconductors have been reported. This chapter aims to summarise the key findings from each experimental chapter and indicate possible future directions for research in this field.

In Chapter 4, UV-sensitive phototransistors based on the solution-processed methanofullerene $PC_{61}BM$ have been fabricated and characterised. The carefully engineered devices exhibit good ambipolar operation in the dark with electron and hole mobility values of 0.14 and 0.06 cm^2/Vs, respectively. Because of the light absorption characteristics of $PC_{60}BM$, the resulting devices exhibit large photoresponse particularly in the UV-A region of the electromagnetic spectrum. Importantly, the $PC_{60}BM$ phototransistors are able to operate at high frequencies with minimum response times of less than 2 ms, in spite of the long channel length (30 μm) employed - a temporal response difficult to achieve in conventional unipolar organic-based phototransistors. To this end, the performance parameters extracted under low illumination intensities are comparable with those of Si-based photodetectors, mainly because of the intrinsic gain mechanism associated with the three-terminal phototransistor architecture. This work highlights the use of single material ambipolar organic phototransistors as a promising concept for the development of sensitive and fast photodetectors with tailored colour sensitivity.

In Chapter 5, phototransistors based on the CuSCN/D102/In_2O_3 trilayer were fabricated and studied. This work starts with the development of a hybrid heterojunction transistor based on a CuSCN/In_2O_3 bilayer, which exhibits high optical transparency and ambipolar transistor operation. The presence of the p-n (CuSCN/In_2O_3) heterojunction was found to suppress the intrinsic PPC associated with the In_2O_3 layer. Organic dye D102 was then incorporated in-between this heterojunction to enable visible light sensitisation/detection. The resulting CuSCN/dye/In_2O_3 trilayer channel phototransistors show a remarkably enhanced response to green illumination. Importantly, the trilayer phototransistors exhibit fast switching behaviour with a response time of ~1 ms, which is faster than the most of oxide-based phototransistors. Such a fast response time is attributed to the minimisation of PPC from the oxide layer and efficient photocarrier transport within the trilayer channel. This work highlights the use of a

hybrid heterostructure as a promising method to improve the speed of oxide-based phototransistors for fast photo-sensing application.

In Chapter 6, a new concept of hybrid phototransistor incorporating a MHP into a series of OSCs as the channel material, was investigated. Resulting phototransistors are characterised by a straddling-gap type-I heterojunction and exhibit state-of-the-art photogain of 4.5×10^4. Using a variety of characterisations techniques, highly efficient photocarrier transfer is found to transport through preferential edge-on molecular orientation at the MHP/OSC heterointerfaces. By tuning MHP/OSC interfaces from straddling-gap to staggering-gap heterojunction configurations, the ability to tune optoelectronics of phototransistors in an 'on-demand' manner is demonstrated. Next, a new method to assess phototransistors is proposed by using a photo-inverter circuit to evaluate their amplification and essential functionality in order to be operated in both linear and saturation modes as a transistor. The improved insights into the photocarrier dynamics and its dependence on material properties and operational conditions provide both essential knowledge and thorough understanding for designing and developing perovskite-organic based optoelectronic devices and systems.

The results presented in this thesis show improved the performance and understanding of phototransistors based on solution-processed semiconductors. Two device concepts have been demonstrated that can enhance the phototransistor performance. The first outcome is the demonstration of using ambipolar phototransistor architecture to enhance the speed of the phototransistor. The ambipolar characteristic can be achieved by either using ambipolar organic materials to form single-component ambipolar organic phototransistor (Chapter 4); or using p-n heterojunction to form heterostructure ambipolar phototransistors. The latter has been exploited in Chapter 5 to demonstrate the fastest oxide-based phototransistor reported to date. Whist in this thesis the ability of photodetection in the heterojunction device is enabled by the incorporation with organic dye only, the high optical transparency of the CuSCN/In_2O_3 heterojunction could allow this structure to be incorporated easily with other light sensitizers. Another important development in this thesis is the demonstration of hybrid perovskite-organic phototransistor with enhanced photoresponse in Chapter 6. Although the concept of hybrid structure has been widely implemented with a range of materials, the strength of using such a structure is generally attributed to the extra degree of freedom for optimisation due to the separation of transport and sensitization. One important finding in this thesis is that the interface between the transport layer and the sensitiser also plays an important role in efficient photocarrier transfer, which is the key to a high-performance phototransistor, and could give rise to tuneable optoelectronic properties. This finding provides a useful guideline for interface

engineering that can further optimise the performance of hybrid phototransistors. The improved understanding of photocarrier dynamics in the hybrid structures, in combination with the ever-evolving material and device engineering, is believed to be the key to break through the current technology bottlenecks for photodetectors including the noise/gain/bandwidth trade-off.

Appendix A Content Reuse Permission

A1. Copyrights for Chapter 1

SPRINGER NATURE LICENSE
TERMS AND CONDITIONS

Nov 28, 2019

This Agreement between Imperial Collge London -- Wentao Huang ("You") and Springer Nature ("Springer Nature") consists of your license details and the terms and conditions provided by Springer Nature and Copyright Clearance Center.

License Number	4717680445838
License date	Nov 28, 2019
Licensed Content Publisher	Springer Nature
Licensed Content Publication	Nature
Licensed Content Title	Fully integrated wearable sensor arrays for multiplexed in situ perspiration analysis
Licensed Content Author	Wei Gao et al
Licensed Content Date	Jan 27, 2016
Type of Use	Thesis/Dissertation
Requestor type	academic/university or research institute
Format	electronic
Portion	figures/tables/illustrations
Number of figures/tables /illustrations	1
High-res required	no
Will you be translating?	no
Circulation/distribution	1 - 29
Author of this Springer Nature content	no
Title	Solution Processable Semiconductors for Opto-Electronic Application
Institution name	n/a
Expected presentation date	Nov 2019
Portions	Figure 1

A2. Copyrights for Chapter 2

JOHN WILEY AND SONS LICENSE
TERMS AND CONDITIONS

Nov 28, 2019

This Agreement between Imperial Collge London -- Wentao Huang ("You") and John Wiley and Sons ("John Wiley and Sons") consists of your license details and the terms and conditions provided by John Wiley and Sons and Copyright Clearance Center.

License Number	4717270080494
License date	Nov 27, 2019
Licensed Content Publisher	John Wiley and Sons
Licensed Content Publication	Wiley Books
Licensed Content Title	Transparent Electronics: From Synthesis to Applications
Licensed Content Author	Antonio Facchetti Tobin Marks
Licensed Content Date	May 1, 2010
Licensed Content Pages	1
Type of use	Dissertation/Thesis
Requestor type	University/Academic
Format	Electronic
Portion	Figure/table
Number of figures/tables	1
Original Wiley figure/table number(s)	Figure 1.2
Will you be translating?	No
Title of your thesis / dissertation	Solution Processable Semiconductors for Opto-Electronic Application
Expected completion date	Nov 2019
Expected size (number of pages)	160

SPRINGER NATURE LICENSE
TERMS AND CONDITIONS

Nov 28, 2019

This Agreement between Imperial Collge London -- Wentao Huang ("You") and Springer Nature ("Springer Nature") consists of your license details and the terms and conditions provided by Springer Nature and Copyright Clearance Center.

License Number	4717680699447
License date	Nov 28, 2019
Licensed Content Publisher	Springer Nature
Licensed Content Publication	Nature
Licensed Content Title	Room-temperature fabrication of transparent flexible thin-film transistors using amorphous oxide semiconductors
Licensed Content Author	Kenji Nomura et al
Licensed Content Date	Nov 25, 2004
Type of Use	Thesis/Dissertation
Requestor type	academic/university or research institute
Format	electronic
Portion	figures/tables/illustrations
Number of figures/tables /illustrations	1
High-res required	no
Will you be translating?	no
Circulation/distribution	1 - 29
Author of this Springer Nature content	no
Title	Solution Processable Semiconductors for Opto-Electronic Application
Institution name	n/a
Expected presentation date	Nov 2019
Portions	Figure 1

American Physical Society
Reuse and Permissions License

28-Nov-2019

This license agreement between the American Physical Society ("APS") and Wentao Huang ("You") consists of your license details and the terms and conditions provided by the American Physical Society and SciPris.

Licensed Content Information

License Number:	**RNP/19/NOV/020730**
License date:	28-Nov-2019
DOI:	10.1103/PhysRevB.73.205316
Title:	Ambipolar charge transport in organic field-effect transistors
Author:	Edsger C. P. Smits et al.
Publication:	Physical Review B
Publisher:	American Physical Society
Cost:	USD $ 0.00

Request Details

Does your reuse require significant modifications: No

Specify intended distribution locations:	United States,UK & Commonwealth (excluding Canada)
Reuse Category:	Reuse in a thesis/dissertation
Requestor Type:	Academic Institution
Items for Reuse:	Figures/Tables
Number of Figure/Tables:	1
Figure/Tables Details:	FIG. 2. A sketch of all operating regimes for a typical ambipolartransistor as a function of drain and gate biasing.
Format for Reuse:	Electronic

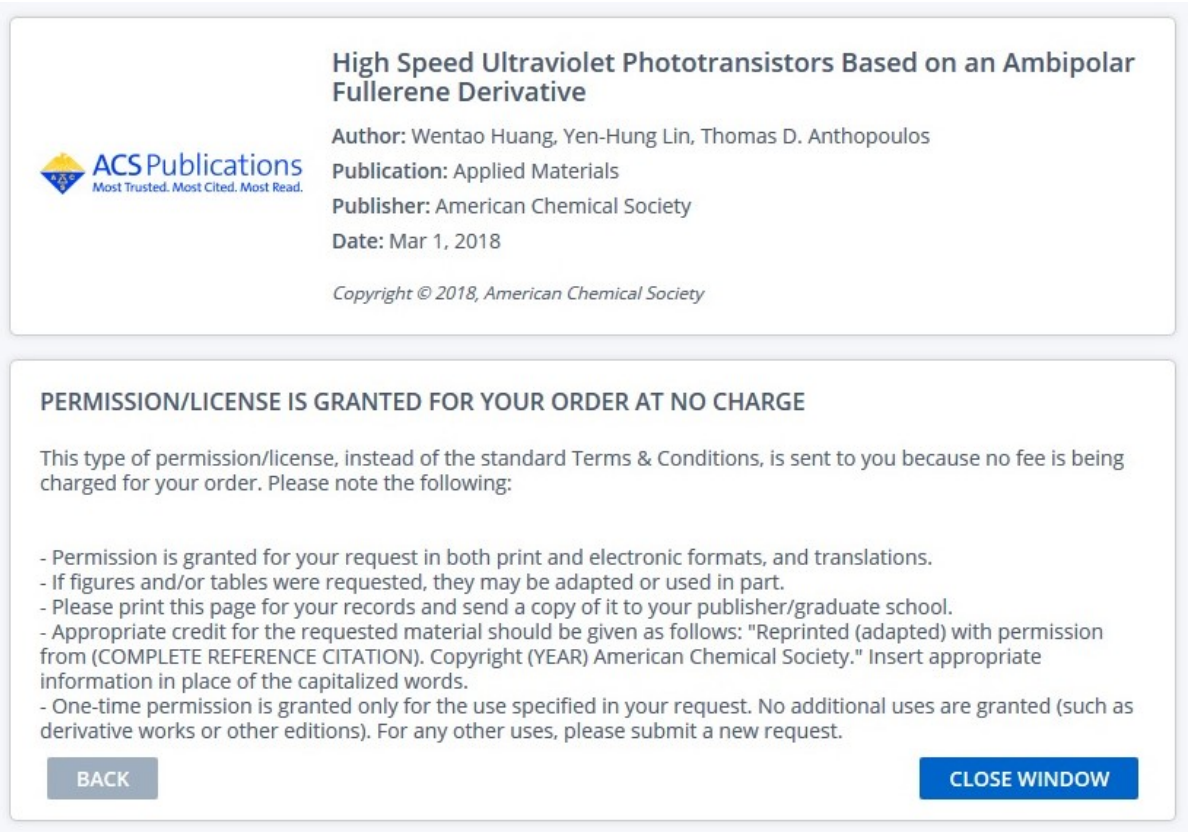
Information about New Publication:

University/Publisher:	Imperial College London
Title of dissertation/thesis:	Solution Processable Semiconductor for Opto-Electronic Applications
Author(s):	Wentao Huang
Expected completion date:	Nov. 2019

License Requestor Information

Name:	Wentao Huang
Affiliation:	Individual
Email Id:	wentao.huang13@imperial.ac.uk
Country:	United Kingdom

A3. Copyrights for Chapter 4



High Speed Ultraviolet Phototransistors Based on an Ambipolar Fullerene Derivative

Author: Wentao Huang, Yen-Hung Lin, Thomas D. Anthopoulos

Publication: Applied Materials

Publisher: American Chemical Society

Date: Mar 1, 2018

Copyright © 2018, American Chemical Society

PERMISSION/LICENSE IS GRANTED FOR YOUR ORDER AT NO CHARGE

This type of permission/license, instead of the standard Terms & Conditions, is sent to you because no fee is being charged for your order. Please note the following:

- Permission is granted for your request in both print and electronic formats, and translations.
- If figures and/or tables were requested, they may be adapted or used in part.
- Please print this page for your records and send a copy of it to your publisher/graduate school.
- Appropriate credit for the requested material should be given as follows: "Reprinted (adapted) with permission from (COMPLETE REFERENCE CITATION). Copyright (YEAR) American Chemical Society." Insert appropriate information in place of the capitalized words.
- One-time permission is granted only for the use specified in your request. No additional uses are granted (such as derivative works or other editions). For any other uses, please submit a new request.

BACK CLOSE WINDOW